# MANGANESE TITANIUM PEROVSKITES AS ANODES FOR SOLID OXIDE FUEL CELLS

**Alejandro Ovalle**

**A Thesis Submitted for the Degree of PhD**
**at the**
**University of St. Andrews**

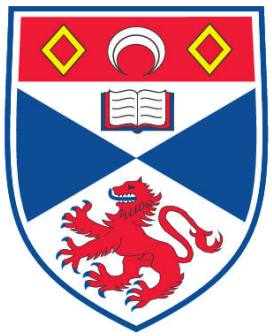

**2008**

**Full metadata for this item is available in**
**Research@StAndrews:FullText**
**at:**
**http://research-repository.st-andrews.ac.uk/**

**Please use this identifier to cite or link to this item:**
**http://hdl.handle.net/10023/567**

**This item is protected by original copyright**

# Manganese Titanium Perovskites as Anodes for Solid Oxide Fuel Cells

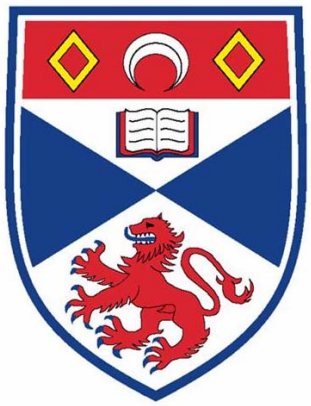

A thesis submitted for the degree of Ph.D. by

**Alejandro Ovalle**

February 2008

School of Chemistry
University of St. Andrews

Supervised by Prof. John T S Irvine

# Declaration

I, Alejandro Ovalle-López, hereby certify that this thesis, which is approximately 25,000 words in length, has been written by me, that it is the record of work carried out by me and that it has not been submitted in any previous application for a higher degree.

Date 20-02-2008 signature of candidate

I was admitted as a research student in October 2003 and as a candidate for the degree of PhD in October 2004; the higher study for which this is a record was carried out in the University of St Andrews between 2003 and 2006.

Date 20-02-2008 signature of candidate

I hereby certify that the candidate has fulfilled the conditions of the Resolution and Regulations appropriate for the degree of Doctor of Philosophy in the University of St Andrews and that the candidate is qualified to submit this thesis in application for that degree.

Date 20-02-2008 signature of supervisor

In submitting this thesis to the University of St Andrews I wish access to it to be subject to the following conditions: for a period of 1 year from the date of submission, the thesis shall be withheld from use; I understand, however, that the title and abstract of the thesis will be published during this period of restricted access; and that after the expiry of this period the thesis will be made available for use in accordance with the regulations of the University Library for the time being in force, subject to any copyright in the work not being affected thereby, and a copy of the work may be made and supplied to any bona fide library or research worker, that my thesis will be electronically accessible for personal or research use, and that the library has the right to migrate my thesis into new electronic forms as required to ensure continued access to the thesis. I have obtained any third-party copyright permissions that may be required in order to allow such access and migration.

Date 20-02-2008 signature of candidate

“En lo que faltaba de camino, les fue contando el licenciado las excelencias de la espada, con tantas razones demostrativas y con tantas figuras y demostraciones matemáticas, que todos quedaron enterados de la bondad de la ciencia (...)”.

**El ingenioso hidalgo Don Quijote de la Mancha**
**Vol. II, Capítulo XIX**

“During the remainder of the journey the licentiate held forth to them on the excellences of the sword, with such conclusive arguments, and such figures and mathematical proofs, that all were convinced of the value of the science (...)”.

**Don Quixote, Vol. II, Chapter XIX**

**Miguel de Cervantes Saavedra (1547-1616)**

# Acknowledgments

There are many people I would like to thank for their help and support during my PhD.

First of all I would like to thank my supervisor, Professor John Irvine for the support and guidance over the years and for giving me the chance to perform interesting and stimulating research. A special thanks goes to Bobby Cathcart, George Anthony and Brian Walker for their readiness to fix and optimise our fuel cell setup and to Sylvia Williamson for her technical advice.

Thanks to all the past and present members of the JTSI group. Special thanks go to Jesús Canales-Vázquez, Juan Carlos Ruiz-Morales, Paul Connor, Martin Smith and John Bradley for their help, advice and patience with all the aspects of my work. Thanks to Angela Kruth, Abul Kalam Azad, Sneh Jain, Flaviano García-Alvarado, Laura León-Reina, Alodia Orera, Edwin Raj, Julie Nairn, Pierrot Attedikou and Maarten Verbraeken for their help and some nice moments outside the lab.

Thanks to my friends here in St Andrews, especially Alvaro, Sandra, Cristina Lucas, Cristina Jiménez, Jose, Susana, Kevin, Cristian, Gil, Fede, Karen, Till and Juan Carlos. With you everything was easier. Thanks to Nigel Dickie for nice sailing moments and beautiful house by the Tay.

Back in Spain I would like say thanks to Prof. Lorenzo Pueyo, Prof. Santiago García-Granda and Prof. Jesús Angel Blanco (Universidad de Oviedo) for their advice and help when I needed it.

A Andrés, Clara, Monti, Miguel y Nuria por acordaros siempre de mi. Gracias.

A mis padres, hermanos, abuela y 3 guapísimas sobrinas por estar siempre ahí apoyándome y dándome cariño. Gracias a vosotros esto ha sido posible.

And last but not least to Belén for her love and make my life easier.

# Abstract

A new family of perovskite titanates with formulae $La_{4+n}Sr_{8-n}Ti_{12-n}Mn_nO_{38}$ and $La_4Sr_8Ti_{12-n}Mn_nO_{38-\delta}$ have been investigated as potential fuel electrode materials for SOFCs.

The series $La_{4+n}Sr_{8-n}Ti_{12-n}Mn_nO_{38}$ present layered domains within their structure. As such layers appear to have a large negative effect over the electrochemical properties only a few compounds have been characterised.

The series $La_4Sr_8Ti_{12-n}Mn_nO_{38-\delta}$ present a rhombohedral (R-3c) unit cell at room temperature which becomes cubic when increasing the temperature up to 900°C both in air and in reducing conditions. The primitive volume correlates with the oxygen content for the reduced samples. TGA and magnetic studies have revealed that the Mn present is mainly as $Mn^{+3}$. Preliminary HRTEM investigations have revealed that some crystallographic shears distributed randomly within a perovskite matrix remain in the structure, which implies that the oxygen overstoichiometry is compatible with rhombohedral distortions in the oxygen sublattice. Mn substitution does not have a large impact on the bulk conductivity of the phases studied, which remains close to the values observed in other related titanates, although the grain boundary contributions are largely improved. Relatively low polarisation resistances were observed under both hydrogen and methane conditions for the lowest n compounds of the series. The anodic overpotential for n=1 was fairly low to those reported in the literature for other materials and especially for titanate-based anodes, i.e. a value of 55mV at $0.5A/cm^2$, at $950^oC$, under wet hydrogen was obtained. Additionally, a value 72mV was obtained in the same conditions under methane. These values indicate that the use of Mn as dopant for perovskite-related titanates enhanced electrochemical performance of these anodes, especially at high temperatures.

# Table of contents


Declaration ii
Acknowledgments iv
Abstract v
Table of contents vi

**1 Introduction**

1.1. Introduction 1

1.2. The fuel cell 2

1.2.1. Definition of a fuel cell 2
1.2.2. History 2
1.2.3. Types of fuel cells 3

1.3. The Solid Oxide Fuel Cell (SOFC) 6

1.3.1. Principle of operation 7
1.3.2. SOFC Thermodynamics 8
1.3.3. SOFC Kinetics 9
1.3.4. SOFC components 12
1.3.4.1. Electrolyte 12
1.3.4.2. Cathode (air electrode) 14
1.3.4.3. Anode (fuel electrode) 15
1.3.4.4. Interconnects 17
1.3.5. SOFC designs 18

1.4. Perovskites 20

1.5. Aims of the thesis 29

1.6. References 30

**2 Experimental techniques**

2.1. Introduction 37

2.2. Experimental 37

2.2.1. Synthesis preparation 37
2.2.2. X-ray diffraction 38
2.2.3. Neutron diffraction 39
2.2.4. TGA 43
2.2.5. Magnetic measurements 44
2.2.6. SEM 49
2.2.7. TEM 51
2.2.8. AC Impedance 52
2.2.9. Four terminal measurements 57
2.2.10. Fuel cell tests 60

2.3 References 61

**3 Structural characterisation**

3.1. Introduction 62

3.2. $La_{4+n}Sr_{8-n}Ti_{12-n}Mn_nO_{38}$ series 63

3.2.1. Synthesis preparation 63
3.2.2. XRD 63
3.2.3. TGA 64
3.2.4. TEM 65

3.3. $La_4Sr_8Ti_{12-n}Mn_nO_{38-\delta}$ series 67

3.3.1. Synthesis preparation 67
3.3.2. X-Ray and Neutron diffraction 68
3.3.3. TGA 107
3.3.4. SEM 110
3.3.5. TEM 112

3.4. Conclusions 114

3.5. References 116

**4 Electrical and magnetic characterisation**

4.1. Introduction 117

4.2. AC impedance spectroscopy 118

4.3. Magnetic studies 136

4.4 $pO_2$ measurements 143

4.5. Conclusions 149

4.6. References 152

**5 Fuel cell tests**

5.1. Introduction 153

5.2. Fuel cell tests 153

5.3. Summary 168

5.4. Conclusions 170

5.5. References 172

**6 Conclusions and future work**

6.1. Conclusions 173
6.2. Future work 176

# 1

# Introduction

## 1.1. Introduction

The use of fossil fuels, which currently provide the bulk of our energy, releases greenhouse gases into the atmosphere. Due to factors such as population growth and changes in lifestyle, the demand for energy has increased to levels where the burning of fossil fuels is releasing enough greenhouse gases into the atmosphere to begin to directly affect our climate system.

To help lessen the effects of climate change, we must reduce the level of greenhouse gases emitted. This can be achieved by generating our energy from sources that emit low or even zero levels of greenhouse gases, such as renewable energy. We can also make sure that we use energy as efficiently as possible.

The energy industry still relies on finite, diminishing sources of fossil fuel such as coal, oil and gas. In 2005, approximately 74 per cent of the UK's electricity was generated from fossil fuel sources, just over 19 per cent from nuclear sources, and just over 4 per cent from renewable sources.[1]

As part of its goal to reduce emissions, the UK Government has set a target for the generation of electricity from renewable energy sources. By 2010, 10 per cent of UK electricity should come from renewable sources.

Fuel cell technology has been much proclaimed in recent years as a keystone of the future energy economy. In association with the hydrogen economy, it has been strongly promoted by the governments of most of the world's leading industrialised nations.[2]

## 1.2. The fuel cell

### 1.2.1. Definition

A fuel cell is an electrochemical device that converts chemical energy, from a reaction between a fuel and an oxidant, to electrical energy without combustion. Unlike a battery, a fuel cell will continuously produce electricity as long as fuel is supplied to it. They offer a clean, pollution free technology to electrochemically generate electricity at high efficiencies as they are not limited by Carnot's cycle. The basic physical structure of a fuel cell consists of an electrolyte layer in contact with a porous anode and cathode on either side, Figure 1.1. Different fuels can be used, such as hydrogen, ethanol, biomass or natural gas. Oxygen or air can be used as oxidant.

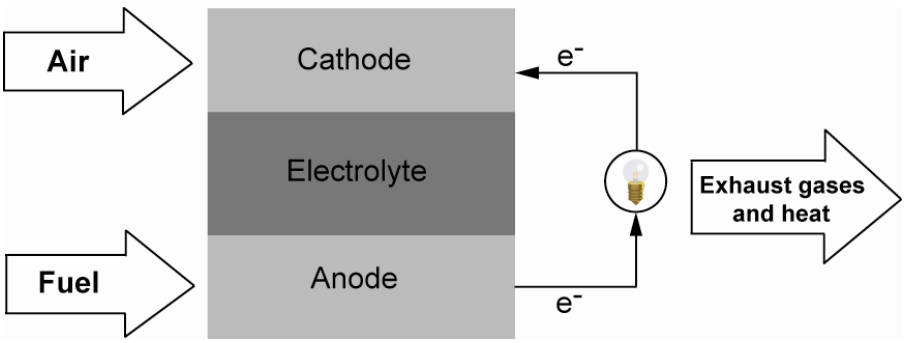


**Figure 1.1 Schematic representation of a fuel cell.**

### 1.2.2. History[3, 4]

Sir William Grove discovered the basic operating principle of fuel cells by reversing water electrolysis to generate electricity from hydrogen and oxygen[5] in 1839. The term "fuel cell' was coined by the chemists Ludwig Mond and Charles Langer[6] in 1889 as they attempted to build the first practical device using air and industrial coal gas. In 1897 Nernst used yttrium-doped zirconia (YSZ) as the electrolyte in the Nernst-Lamp.[7] YSZ as an electrolyte even today represents the

basis for the Solid Oxide Fuel Cell (SOFC) in stationary energy production. The next major chapter in the fuel cell story was written by an engineer at Cambridge University, Dr Francis Thomas Bacon. This device which he named the 'Bacon Cell' was in essence the first alkaline fuel cell (AFC). However it was not until 1959 that Bacon first demonstrated a practical five-kilowatt fuel cell system.

Also in the late 1950s, The National Aeronautics and Space Administration (NASA) began to build a compact electricity generator for use on space missions. NASA soon came to fund hundreds of research contracts involving fuel cell technology. Fuel cells now have a proven role in the space program, after supplying electricity to several space missions.

In the 1980s focus on pollution and the demand for higher efficiency in the exploitation of fossil resources initiated a new wave of fuel cell developments. At present several types of fuel cells are approaching the consumer market within a limited number of years. The primary challenges are cost and durability, to be solved by materials selection and design engineering.

### 1.2.3. Types of fuel cells[8, 9]

Fuel cells are classified primarily by the kind of electrolyte they employ. Today five types of fuel cells are commonly known:

- alkaline fuel cell (AFC)
- molten carbonate fuel cell (MCFC)
- phosphoric acid fuel cell (PAFC)
- polymer electrolyte membrane fuel cell (PEMFC)
- solid oxide fuel cell (SOFC)

Table 1.1 shows a summary of these fuel cell types. Details of each are also presented below. SOFCs will be presented in next section.

| | AFC | MCFC | PAFC | PEMFC | SOFC |
|---|---|---|---|---|---|
| Electrolyte | KOH | Carbonate | $H_3PO_4$ | Polymer | YSZ |
| Operating temperature(ºC) | 100-250 | 650 | 200 | 80 | 600-1000 |
| Electrical Efficiency (%) | 35-55 | 60 | 40 | 35-45 | 60 |
| Charge Carrier | $HO^-$ | $CO_3^{2-}$ | $H^+$ | $H^+$ | $O^{2-}$ ($H^+$) |
| Catalyst | Ni | Ni | Pt | Pt | Perovskites |
| Main Cell Components | C-based | Stainless Steel | Graphite -based | C-based | Ceramic |

**Table 1.1 Currently developed types of fuel cells and their characteristics.[10]**

#### 1.2.3.1. Alkaline Fuel Cell (AFC)

These fuel cells use concentrated KOH as electrolyte and they operate between 100 and 250ºC. The electrolyte is retained in a matrix (usually asbestos), and a wide range of electrocatalysts can be used such as Ni, Ag, metal oxides, spinels, and noble metals. Alkaline fuel cells can achieve power generating efficiencies of up to 70 percent. The main drawback of this type of fuel cell is that they are very susceptible to carbon contamination, so require high purity $H_2$ and $O_2$. They have been used by NASA on space missions.

#### 1.2.3.2. Molten Carbonate Fuel Cell (MCFC)

The electrolyte in this fuel cell is usually a combination of alkali carbonates, which is retained in a ceramic matrix of $LiAlO_2$. They require carbon dioxide and oxygen to be delivered to the cathode. The fuel cell operates at 600 to 700°C where the alkali carbonates form a highly conductive molten salt, with $CO_3^{2-}$ ions providing ionic conduction. They achieve electrical efficiencies in the range of 35-55%. The higher operating temperature places severe demands on the corrosion stability and life of cell components.

#### 1.2.3.3. Phosphoric Acid Fuel Cell (PAFC)

PAFCs were the first commercial fuel cells in electric power industry. Phosphoric acid concentrated is used for the electrolyte in this fuel cell, which operates at 150 to 220°C with efficiencies ranging from 40 to 80% in the case of steam co-generation. At lower temperatures, phosphoric acid is a poor ionic conductor, and CO poisoning of the Pt electrocatalyst in the anode becomes severe. One of the main advantages to this type of fuel cell, besides the nearly 80% cogeneration efficiency, is that it can use impure hydrogen as fuel. Another advantage is they can tolerate a CO concentration of about 1.5 percent, which broadens the choice of fuels. The main drawbacks are the use of Pt catalyst affecting the costs of fabrication and the corrosive nature of phosphoric acid that affects the choice of materials.

#### 1.2.3.4. Polymer Electrolyte Membrane Fuel Cell (PEMFC)

The PEM fuel cell is also known as the proton conducting membrane or solid polymer fuel cell (SPFC).

In these fuel cells the electrolyte is a proton conductor, usually a fluorinated sulphonic acid polymer (Nafion® 117) or related, which acts as a solid ion exchange membrane. The electrodes consist of Pt supported on carbon within a polymer matrix. These fuel cells operate at 80-120ºC with efficiencies of 35-45%. PEM fuel cells are used primarily for transportation and some stationary applications. Due to their fast start-up time, low sensitivity to orientation, and favourable power-to-weight ratio, PEM fuel cells are particularly suitable for use in passenger vehicles, such as cars and buses. The most important companies in transportation such as BMW, Toyota, Daimler-Chrysler, Fiat, Ford, General Motors, Renault or Ballard systems, have developed fuel cell buses and fuel cell duty vehicles working with PEM fuel cells since 1995.[11-14]

### 1.3. The Solid Oxide Fuel Cell (SOFC)

Solid oxide fuel cells use a solid ceramic inorganic oxide as the electrolyte, generally yttria-stabilised zirconia (YSZ) which acts as a conductor of oxide ions. They are the most efficient devices yet invented for conversion of chemical fuels directly into electrical power.[15] Efficiencies up to 85% can be achieved with SOFCs considering co-generation of power provided by the production of steam as by-product. They operate at elevated temperatures, typically between 800-1000°C. Because of these high temperatures of operation natural gas can be reformed within the cell stack eliminating the need of an external reformer. The elevated operating temperature of the SOFC also leads to production of heat as a by-product in addition to the electrical power. This high quality heat can be used in various ways, for example in combined heat and power systems, or to drive a gas turbine to generate more electricity.

On the other hand, the use of high temperatures has negative effects such as limitations in long lifetime operations. There is an increasing interest in finding new, alternative oxide ion conducting electrolytes such as ceria or lanthanum gallate that can be used at lower temperatures, e.g. 600-700°C, but with improved stability.

There also exists the possibility of SOFCs operating with a proton conductor electrolyte. The protonic conductivity may be higher than the oxide ion conductivity in the intermediate temperature range.

Solid oxide fuel cells are particularly suited to combined heat and power (CHP) applications, ranging from less than 1 kW to several MW, which covers individual households, larger residential units and business and industrial premises, providing all the power and hot water from a single system.

This section briefly reviews the thermodynamics and kinetics on SOFCs as well as the materials currently used for the different cell components. Emphasis is placed on the anode, its chemistry, research and development aspects.

### 1.3.1. Principles of operation

The operating principle of the solid oxide fuel cell is shown in Figure 1.2. Like all fuel cells, the SOFC consists of three main components: a cathode (or air electrode), an anode (or fuel electrode) and an electrolyte.

Most SOFCs are based on the concept of an oxygen ion conducting electrolyte through which the oxide ions migrate from the cathode side to the anode side where they react with the fuel to generate an electrical voltage, water and heat (if hydrogen is the fuel). SOFCs must operate at high temperatures to enable diffusion of $O^{2-}$ through the electrolyte.

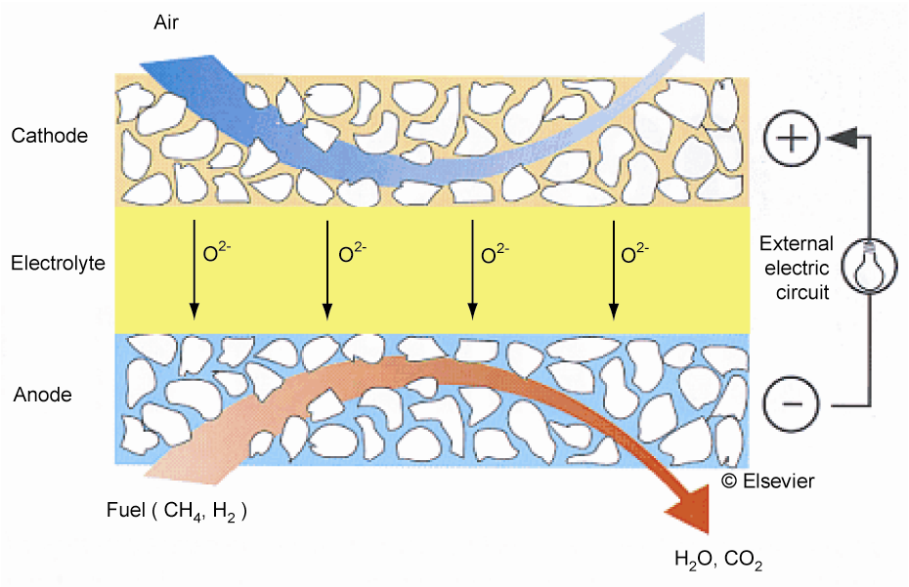


**Figure 1.2 Schematic representation of a solid oxide fuel cell (SOFC).**

Considering as fuels $H_2$ or $CH_4$ the electrode reactions are:

Anode: $H_2 + O^{2-} \rightarrow H_2O + 2e^-$

$CH_4 + 4\ O^{2-} \rightarrow 2\ H_2O + CO_2 + 8e^-$

Cathode: $½\ O_2 + 2e^- \rightarrow O^{2-}$

And the overall reactions are:

$H_2$ as a fuel: $H_2 + ½\ O_2 \rightarrow H_2O + \Delta E$

$CH_4$ as a fuel: $CH_4 + 2\ O_2 \rightarrow 2\ H_2O + CO_2 + \Delta E$

### 1.3.2. SOFC Thermodynamics

The maximum electrical energy available from a fuel cell is determined by the Gibbs free energy difference across the electrolyte membrane, ΔG.

$$\Delta G = - nFE \qquad [1.1]$$

where n denotes the number of electrons participating in the reaction and F is the Faraday's constant.

This determines the equilibrium voltage of the cell, *E*, through the Nernst equation. E is the open circuit voltage, OCV, and when $H_2$ is the fuel is given in terms of the various partial pressures by:

$$E = -\frac{\Delta G}{2F} = -\frac{\Delta G^{\circ}}{2F} - \frac{RT}{2F}\ln\frac{P_{H_2O}}{P_{H_2}\cdot P_{O_2}^{1/2}} = E^{\circ} + \frac{RT}{2F}\ln\frac{P_{H_2}\cdot P_{O_2}^{1/2}}{P_{H_2O}} \qquad [1.2]$$

Here, E° is the ideal standard potential and has a value of 1.229 V at a pressure of 1 bar and a temperature of 25°C.

If the fuel is $CH_4$ there is an analogous relationship:

$$E = E^{\circ} + \frac{RT}{8F}\ln\frac{P_{CH_4}\cdot P_{O_2}^{2}}{P_{H_2O}^{2}\cdot P_{CO_2}} \qquad [1.3]$$

The Nernst equation provides a relationship between the ideal standard potential (E°) for the cell reaction and the ideal equilibrium potential (E) at other temperatures and partial pressures of reactants and products. Once the ideal potential at standard conditions is known, the ideal voltage can be determined at other temperatures and pressures through the use of these equations.

At the temperatures of interest for SOFC applications, the standard potentials for oxidation, E°, are similar for methane (full oxidation to $CO_2$ and $H_2O$) and for $H_2$; i.e. 1.01 V for $H_2$ and 1.05 V for $CH_4$ at 973 K.[16] The Nernst potentials for $H_2$ and

$CH_4$ were calculated[17] from equations 1.2 and 1.3 as a function of conversion at 973 K, Figure 1.3. For these calculations, the methane was assumed to react directly to $CO_2$ and $H_2O$, with no intermediate products. That means the thermodynamic efficiency of a fuel cell operating directly on methane fuel can be significantly higher than in hydrogen.

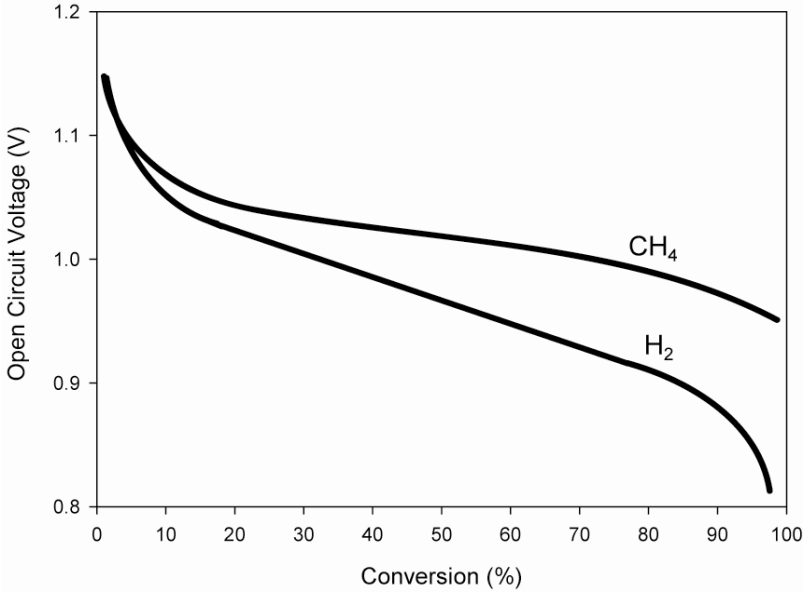


**Figure 1.3 Theoretical open-circuit potential as a function of conversion to total oxidation of hydrogen and methane at 973 K. Adapted from McIntosh and Gorte.[17]**

### 1.3.3. SOFC Kinetics

Thermodynamics describe reactions at equilibrium and the maximum energy release for a given reaction. However the actual cell potential is decreased from its equilibrium potential because of irreversible losses in the electrodes and in the electrolyte, as shown in Figure 1.4. The losses are called polarisation, overpotential, or overvoltage and they are a function of current density. For YSZ electrolytes, the losses are purely ohmic and are equal to the product of the current and the electrolyte resistance. For the electrodes we have a more complex situation. Basically, three different kinetics effects for polarisation have to be considered: activation polarisation, ohmic loss or ohmic polarisation and concentration polarisation.

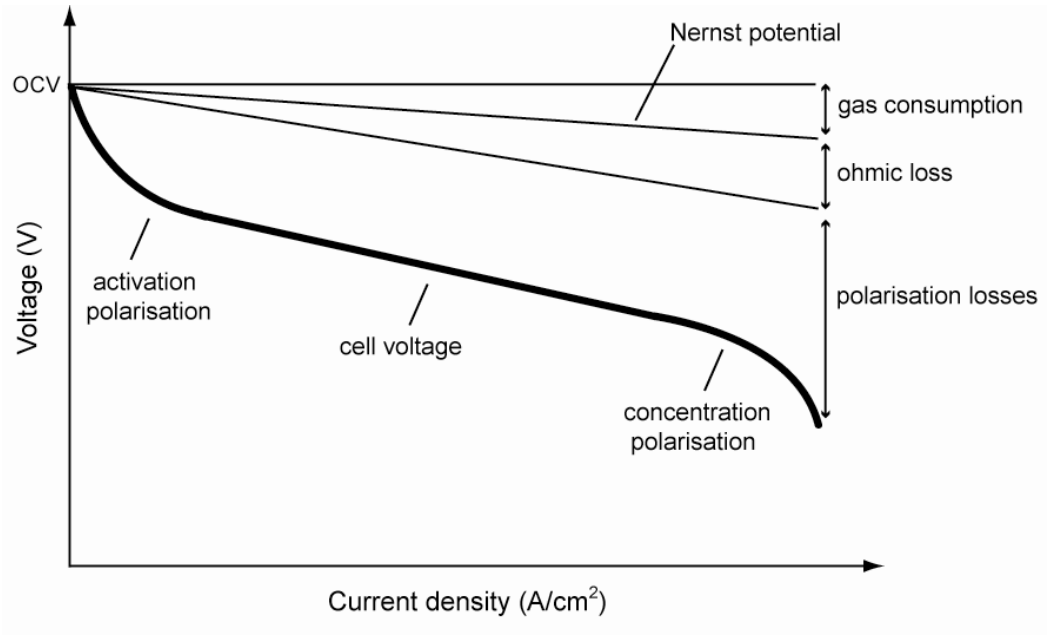


**Figure 1.4 Schematic plot of voltage versus current density showing the different types of polarisation.**

Ohmic polarisation is caused by electrical losses in the cell and it can be described by Ohm's law. At a given current density j the ohmic loss can be expressed as:

$$\eta_{ohm} = (\rho_e l_e + \rho_c l_c + \rho_a l_a + R_{contact})j$$

where ρ is the resistivity and l the thickness. $R_{contact}$ is any possible contact resistance.

As it was said before in most SOFCs the main contribution to $\eta_{ohm}$ is from the electrolyte due to the high ionic resistivity of YSZ compared to the electronic resitivities of anode and cathode.

Concentration polarisation is due to mass transport limitations during cell operations. For simplicity we are considering a SOFC working only with $H_2$ as a fuel. $H_{2\ (g)}$ is transported through the porous anode to the anode/electrolyte interface where it reacts with $O^{2-}$ transported through the electrolyte. Then $H_2O$ is formed and electrons are released and transported to the cathode via the

external circuit. The water has to be transported away through the anode. All these physical 'resistances' to the transport of gaseous species through the anode at a given current density produce an electrical voltage loss, known as anodic concentration polarisation. This polarisation is a function of several parameters as:

$$\eta^{a}_{conc} = f(D_{H2\text{-}H2O}, \text{microstructure, partial pressures, current density})$$

where $D_{H2\text{-}H2O}$ is the binary $H_2$-$H_2O$ diffusivity.

There is a similar situation for the cathode. There $O_2$ and $N_2$ have to be transported to the cathode/electrolyte interface. The polarisation loss is known as cathodic concentration polarisation and is a function of:

$$\eta^{c}_{conc} = f(D_{O2\text{-}N2}, \text{microstructure, partial pressures, current density})$$

where $D_{O2\text{-}N2}$ is the binary $O_2$-$N_2$ diffusivity.

The concentration polarisation increases with increasing current density but not linearly. Usually the anodic concentration polarisation is much lower than the cathodic concentration polarisation. It is due to the higher binary diffusivity of $H_2$-$H_2O$ and the higher values of the partial pressure of hydrogen in the fuel.

Activation polarisation is related to the kinetics of the electrochemical redox (or charge-transfer) reactions taking place at the electrode/electrolyte interfaces of anode and cathode. The triple-phase-boundary (TPB) in the composites is the active site for electrode reactions. For both, anode and cathode, the activation polarisation is a function of several parameters:

$$\eta_{act} = f(\text{material properties, microstructure, T, atmosphere, current density})$$

The relationship between the activation polarisation and the current density is usually nonlinear, except at very low current densities. The activation polarisation follows a semi-empirical equation, called the Tafel equation:

$$\eta_{act} = a + b \ln j \qquad [1.4]$$

where a and b are constants.

### 1.3.4. SOFC components[18]

#### 1.3.4.1. Electrolyte

SOFCs are mostly based on the concept of an oxygen ion conducting electrolyte through which the oxide ions migrate from the cathode side to the anode side where they react with the fuel to generate an electrical voltage, water and heat (if hydrogen is the fuel).

According to this the solid electrolyte must present some characteristics:

- High ionic conductivity
- Negligible electronic conductivity
- Being stable in oxidising and reducing conditions
- Chemically inert towards the other cell components
- Thermal expansion similar to the other cell components
- Must be completely non-porous to prevent mixing of the fuel and oxygen

Currently most of the SOFCs use an yttria-stabilised zirconia (YSZ) electrolyte because it satisfies all these conditions and furthermore is abundant, low in cost and easy to fabricate. Typically the level of yttria ($Y_2O_3$) present in YSZ is around 8 mol %. YSZ possesses the fluorite structure.

Conventional YSZ based SOFCs generally require high operating temperatures. Reduction of operation temperature is very important in SOFC commercialization in the aspect of cost reduction and long-term durability. The operating temperature is mainly governed by the thickness of the electrolyte layer and the nature of the electrolyte, i.e. its ionic conductivity. So, there are two possible approaches to lowering the temperature: reduce the thickness of the YSZ layer or the search of alternative materials with higher ionic conductivity.

Scandia stabilized zirconia (ScSZ), gadolinia doped ceria (CGO) and strontium and magnesium doped lanthanum gallate (LSGM) are so far the most important potential candidates for alternative oxygen ion conducting electrolytes.

ScSZ has much higher electrical conductivity than YSZ[19, 20] but it shows aging effects on long term exposure at high temperatures.[21, 22] However Arachi *et al* have reported[23] that $ZrO_2$ with 11 mol % $Sc_2O_3$ (11ScSZ) does not present aging effects. On the other hand ScSZ shows good mechanical properties and it is a potential electrolyte candidate for intermediate temperature solid oxide fuel cells (IT-SOFCs).

At high temperatures CGO presents a purely ionic conductivity[24, 25] at high oxygen partial pressure. However at lower $pO_2$ (anode conditions) due to $Ce^{4+}$ going to $Ce^{3+}$ it becomes partially reduced. This leads to electronic conductivity which means lower efficiency of the SOFC. Around 500-600°C the electronic conductivity is negligible and CGO has been reported[26-30] as a potential electrolyte for IT-SOFCs.

Ishihara *et al.* were the first to report the perovskite-structure doped-lanthanum gallates[31-34] as a potential electrolyte for SOFCs. In particular, $LaGaO_3$ where the A-site is doped with Strontium and the B-site with Magnesium and Cobalt ($La_{0.8}Sr_{0.2}Ga_{0.8}Mg_{0.2-x}Co_xO_{3-\delta}$: LSGM) is very interesting from the viewpoint of decreasing the operating temperature.[35-39] The ionic conductivity in LSGM at 650°C is comparable to that of YSZ at 1000°C. Furthermore, the performance of LSGM as an electrolyte on a SOFC at 650°C is also comparable to that of YSZ at 1000°C. However there are some concerns over the long term durability of SOFCs with LSGM electrolytes and further research is required.[37]

As already mentioned, there also exists the possibility of SOFCs operating with a proton conductor electrolyte. Iwahara *et al*. reported[40] oxides based on $BaCeO_3$ showing appreciable proton conduction at high temperature. However ionic conductivity at high temperatures in doped $BaCeO_3$ is lower than in YSZ

and furthermore the chemical stability, especially in $CO_2$, is poor. On the other hand, proton conductors are promising candidates as electrolytes for low temperature SOFCs because of their low activation energy for proton conduction. $BaCeO_3$ doped with different elements (Yttrium, Samarium ) has been reported in the literature showing promising performances under fuel cell operation at low temperatures.[41-43]

It is also interesting that $BaCeO_3$ and $BaZrO_3$ easily form solid solutions. So it is possible to replace a desired fraction of Ce in $BaCeO_3$ with Zr creating a solid solution that exhibits good proton conductivity as well as sufficient chemical and thermal stability under fuel cell operation.[44-48]

#### 1.3.4.2. Cathode

The cathode (air electrode) operates in an oxidizing environment and it involves the reduction of $O_2$.

$$\frac{1}{2}O_2(g) + 2e^- \rightarrow O^{2-}(g)$$

The cathode must present some characteristics:

- High ionic and electronic conductivity
- Being stable in oxidising conditions
- High catalytic activity for oxygen reduction
- Chemically inert towards the other cell components
- Thermal expansion similar to the electrolyte and interconnects
- Sufficient porosity to facilitate transport of oxygen to the reaction sites

Strontium-doped lanthanum manganite (LSM) is the most used cathode material for YSZ based SOFCs. $LaMnO_3$ is a perovskite material with intrinsic p-type conductivity as a consequence of the formation of anion vacancies. Therefore the conductivity can be improved using a lower valence ion as a dopant for either the A or B sites.

However, doped-$LaMnO_3$ reacts with YSZ at temperatures above 1200°C forming by-products such as $La_2Zr_2O_7$ that are insulators. This provokes a reduction in the performance of the fuel cell. [49-51]

Doped lanthanum cobaltite has also been studied as cathode material for SOFCs. $LaCoO_3$ presents a perovskite structure and the same p-type conductivity showed by $LaMnO_3$. Good performances have been found when doping the A-site with Sr and the B-site with Fe (LSCF).[49] However at high temperatures doped-$LaMnO_3$ shows more reactivity to zirconia than $LaMnO_3$.[52] The high electrical conductivity of LSCF makes it the most commonly used cathode for IT-SOFCs especially with CGO electrolyte.[53-58]

#### 1.3.4.3. Anode

The role of the anode in a SOFC is to provide the sites for the fuel gas to react with the oxide ions delivered by the electrolyte.

$$O^{2-}(g) + H_2(g) \rightarrow H_2O(g) + 2e^-$$

The anode must present some characteristics:

- High ionic and electronic conductivity
- Being stable in reducing conditions
- High catalytic activity for fuel oxidation
- Chemically inert towards the other cell components
- Thermal expansion similar to the electrolyte and interconnects
- Sufficient porosity to facilitate transport of the products of fuel oxidation

The Ni-YSZ cermet is the state of the art anode material because it satisfies most of the requirements[59]. The reducing conditions present on the fuel side permit the use of a metal such as nickel as the fuel electrode.[60] This is mainly due to the excellent catalytic properties of nickel for breaking hydrogen bonds, good current collection and fairly low cost.[37]

However this cermet anode also presents several drawbacks:

- Long term degradation due to agglomeration of Ni particles at high operating temperatures.[61]
- Sulphur poisoning: Impurities in the fuel stream, especially sulphur, inhibit the anode functionality. Strong reversible poisoning of the Ni/YSZ anode occurred at feed concentrations of 1 ppm $H_2S$ in $H_2$ at 1000°C and as low at 50 ppb $H_2S$ in $H_2$ at 700°C.[62] It is clear that even at these low sulphur concentrations, desulphurization of the fuel gas is needed.
- Oxidation-reduction intolerance: Nickel oxidizes rapidly, and expands more than 30 vol % under re-oxidation.[63] Because of the large volume change during reduction/oxidation, the structure of the anode and its mechanical strength are severely affected and the Ni/YSZ anode heavily degrades during redox cycles.[64]
- Thermal expansion mismatch: The thermal expansion coefficient of the Ni/YSZ anode is generally higher than the electrolyte and other cell components.[65] This can lead to mechanical and dimensional stability problems during e.g. thermal cycling of the fuel cell.
- Hydrocarbon based fuels: It is widely agreed that direct feeding of dry hydrocarbons into the fuel cell must be avoided when using a Ni-based anode. Ni is an efficient catalyst for hydrocarbon cracking, resulting in carbon deposition on the electrode.[66]
- Limitation of the anode reaction to the triple phase boundaries (TPB).[67, 68]

The search of alternative materials to the Ni/YSZ cermets as efficient anodes for SOFCs is one of the main research trends in solid state electrochemistry nowadays. High mixed conductivity, stability under operating conditions, catalytic activity promoting the oxidation of the fuel (preferably methane) or compatibility with the electrolyte (typically YSZ or ceria-based oxides) are some of the properties targeted. There exists a variety of open research lines ranging

from the improvement of the cermet performance by optimising their microstructure or composition[69, 70], to the use of alternative systems such as those based on ceria cermets proposed by Gorte *et al* [71, 72] or perovskites.[73-81]

Some of the perovskite-based anode materials already offer rather competitive performances in hydrogen and methane as reported for several phases in the $(La,Sr)(Cr,Mn)O_3$ system.[73, 74, 76] There exists, however, some concern regarding moderate electronic conductivity under fuel conditions, limiting electrode support design concepts. $(La,Sr)TiO_{3+\delta}$ phases have been considered as good fuel electrode candidates due to their stability under reducing conditions and also because of their resistance to carbon build-up and sulphur poisoning, although their performance under methane was far from competitive in comparison with other state-of-the-art anode materials.[77-79] Nevertheless, there are some reports in the literature regarding titanate-based anodes showing very promising performances, especially using $CeO_2$ composites[79] or partially substituting Ti by other cations such as Sc.[80] The partial substitution of Ti by lower valence cations of similar ionic radii seems to improve the properties of these phases as it has been reported recently for Ruiz-Morales *et al.*[81]

#### 1.3.4.4. Interconnects

The main functions of the SOFC interconnects are to connect the anode and the cathode supporting a flow of electrons necessary to carry out the reaction in the cell and the gas separation within the cell stack. An interconnect must present some characteristics:

- High electronic conductivity with low ionic conductivity
- Being stable in both fuel and air
- Thermal expansion similar to the electrolyte and electrodes
- Chemically inert towards the other cell components
- High mechanical strength

- High thermal conductivity
- Dense to avoid gas leaks

The first three requirements are crucial and for operation at temperatures above 800°C only doped lanthanum chromites ($LaCrO_3$) fit those conditions. $LaCrO_3$ has a perovskite structure and is a p-type conductor. In particular, compositions from the system $(La,Sr,Ca)(Cr,Mg)O_3$ are the leading ceramic interconnects materials. However, they present some problems due to cost and Cr-volatilisation.[52] The use of certain ferritic stainless steel materials as interconnects for IT-SOFCs could be an interesting possibility.[37, 82-84]

### 1.3.4.5. SOFC designs

Individual fuel cells must be combined to produce the voltage level and output power suitable for commercial use. Although many individual designs of SOFCs have been conceived the two most common are the planar and the tubular.

In a planar design the cell components are configured as flat plates which are connected in electrical series. [52] In Figure 1.5 a typical configuration is shown. A single cell consists of a porous cathode, a dense electrolyte, a porous anode and a dense interconnect which are stacked alternately.

The cells are fabricated by low-cost conventional ceramic processing techniques such as tape casting, slurry sintering, screen printing, or by plasma spraying.

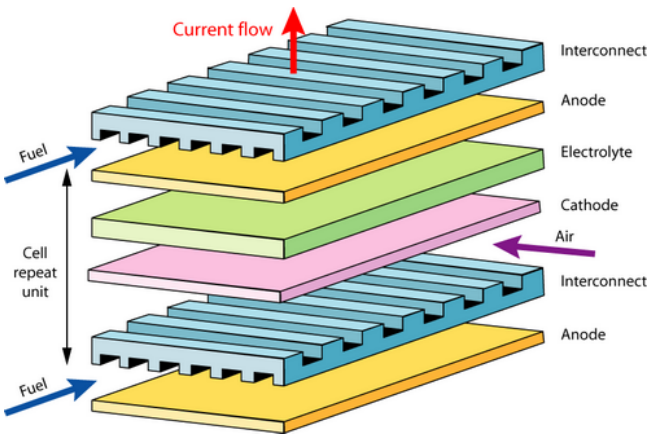


**Figure 1.5 Planar solid oxide fuel cell design.**

Planar cells can achieve very high power densities, have flexibility in the shape and they are easy-manufacturing. On the other hand it is difficult to seal the cell, there is relatively high contact resistance between cells and it is necessary to have mechanical strength because the cell at the bottom of the stack has to support the weight of the stacked cells.

In the tubular cells, as illustrated by the Siemens Westinghouse[85] design shown in Figure 1.6, the cell is built up in layers on the air electrode (cathode) with an axial interconnection that makes the cathode accessible and allows cells to be connected together in series.

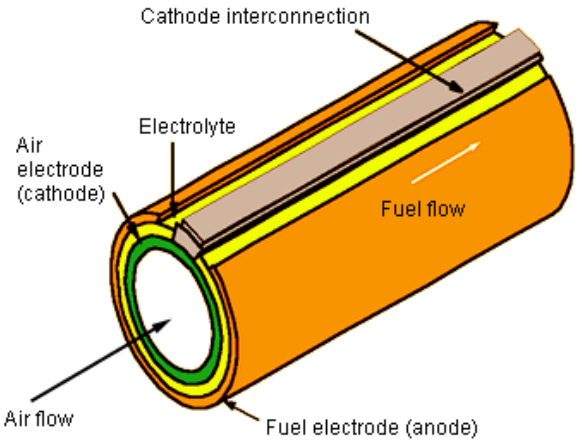


**Figure 1.6 Siemens Cylindrical-tube SOFC Technology[85]**

Tubular cells have a higher mechanical strength than planar cells and can be configured to eliminate or reduce the need for high-temperature seals. However they present lower power densities making them suitable only for stationary power generation and not very attractive for transportation applications.[86] Furthermore, tubular cells usually require many processing steps, often involving expensive deposition equipment.

SOFCroll[87] is a new tubular design developed for St Andrews Fuel Cells based at the University of St Andrews, Figure 1.7.

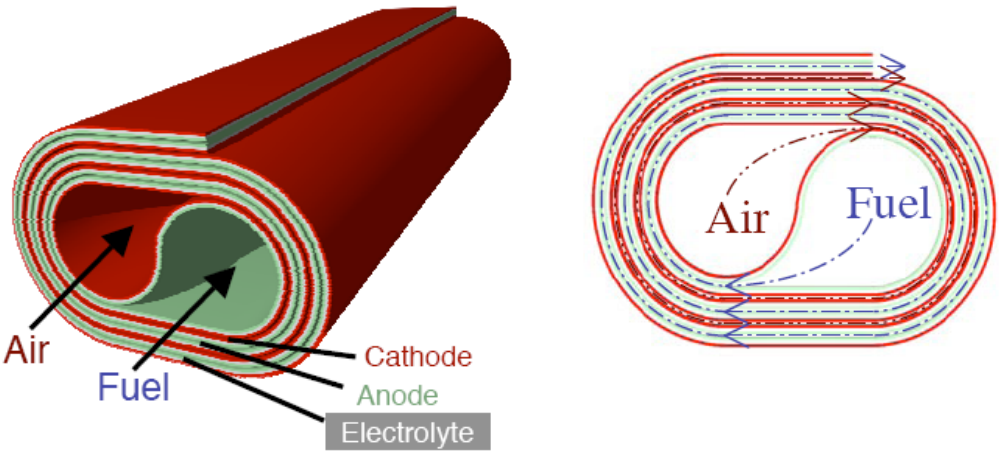


**Figure 1.7 SOFCroll design developed for St Andrews Fuel Cells.**

The SOFCroll design uses a double spiral, which gives both separation of the gases and a tubular form which gives the cell strength. This geometry removes mass and components from the fuel cell and also simplifies the manufacturing process reducing the cost. The components are made by tape casting which is a cheap, standard technique to form flexible sheets of ceramic material. These flexible sheets can then be processed to form the monolithic structure, which is then fired all at once. The two gases (fuel and air) are inserted into the centre holes of the tube and then are forced through the porous electrodes around the spiral. This design makes also the cell suitable for portable power applications.[87]

## 1.4. Perovskites

Perovskite structures have long been studied because of their interesting magnetic, dielectric, optical and conducting properties. Ideal perovskites have the general formula $ABO_3$, where the A-site cations are typically larger than the B-site cations and similar in size to the oxygen anions. The A cations occupy the larger spaces in the 12-fold oxygen coordinated holes; the B cations occupy the much smaller octahedral holes (sixfold coordination), Figure 1.8. Full or partial substitution of the A or B cations with cations of different valence is possible.

When the overall valence of the A-site and B-site cations ($n$ + $m$) adds up to less than 6, the missing charge is made up by introducing vacancies at the oxygen lattice sites.[75] There are many $ABO_3$ compounds for which the ideal cubic structure is distorted to a lower symmetry.

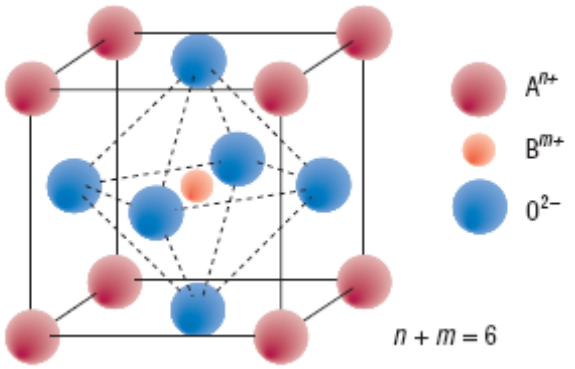


**Figure 1.8 Unit cell of the $ABO_3$ perovskite structure.[75]**

The Goldschmidt tolerance factor (t), which is effectively a ratio between the sizes of the A and B-site cations in $ABO_3$ perovskites, is widely used in solid state chemistry to help predict the stability and structure of perovskite systems.[88]

$$t = \frac{(r_A + r_O)}{\sqrt{2}(r_B + r_O)} \qquad [1.5]$$

where $r_A$, $r_B$ and $r_O$ are the ionic radii of A, B and oxide ion respectively. For ideal structures t is unity, although diverse perovskites structures of lower symmetry can exist for values of t greater than 0.8.

The value of t is not an unambiguous guide to structure type, and is certainly not an indicator of the space group that a particular perovskite will adopt at room temperature and atmospheric pressure. This is because factors other than ion size, e.g. degree of covalency, metal-metal interactions, Jahn-Teller and lone pair effects, play a role in determining the space group or structure adopted. Non-stoichiometry in perovskites is also an extensively investigated topic. Changes in the stoichiometry may affect both cations and oxygen and Figure 1.9 shows several non-stoichiometric families of compounds.

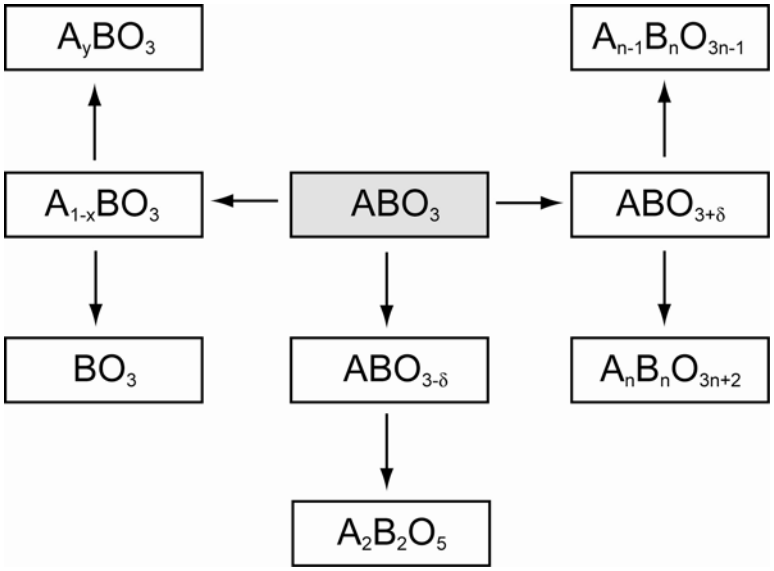


**Figure 1.9 Schematic diagram of several non-stoichiometric perovskites.[9]**

For the $A_nB_nO_{3n+2}$ series, an exhaustive review has been published by Lichtenberg *et al.*[89], where studies from several research groups during the last three decades were presented.

Oxygen over-stoichiometry is not an intuitive concept in perovskites, because in a cubic close packed arrangement there is no space for interstitial elements, it is often addressed as cation deficiency rather than excess oxygen.

As said before, although the ideal perovskite structure is cubic, there are several structural deviations for simple and ordered perovskites. In fact it is more difficult to find a cubic perovskite than a distorted one. The structural distortions are interesting because normally they provoke important effects on the magnetic and electrical properties of the perovskite compounds. A distortion from the ideal perovskite structure can be attributed to one of three mechanisms: distortion of the octahedra, cation displacements within the octahedra or tilting of the octahedra. The first two mechanisms are driving for electronic instabilities of the metal ions within the octahedra. The third and most common distortion mechanism can be realized by tilting $BO_6$ octahedra while maintaining their

sharing corners connectivity.[90] The standard notation for describing octahedra tilting was introduced by Glazer.[91]

### 1.4.1. The perovskite series $A_nB_nO_{3n+2}$

There is a general agreement in describing the structure of $A_nB_nO_{3n+2}$ phases as {110} perovskite slabs containing n-layers joined by crystallographic shearing along the $[100]_p$. $La_2Ti_2O_7$ constitutes one example of these phases and its structure is derived from perovskite blocks containing 4 layers, with adjacent slabs offset from one another by ½$[100]_p$. The connectivity between octahedra sharing corners is broken at the crystallographic shears, where the oxygens beyond the $ABO_3$ stoichiometry are situated. The octahedra are strongly distorted and tilted as reported elsewhere[92-94], and La is shifted from the A site of the hypothetical perovskite towards the crystallographic shears at the end of the blocks, which is the cause of the broken connectivity at these specific locations. Obviously, as one moves towards higher members of the $A_nB_nO_{3n+2}$ series the perovskite blocks become larger with increasing n, which is reflected in the gradual increase of the *c*-axis. Therefore the $A_nB_nO_{3n+2}$ series differ from the rest of the layered families because it is derived entirely from the primitive $ABO_3$ rather than intergrowths with other structures.

In figure 1.10 the oxygen framework is presented alone to highlight the oxygen rich planes that join consecutive blocks.

The unit cell of $La_2Ti_2O_7$ is monoclinic with a=7.81 Å, b=5.56 Å, c=13.01 Å and β=98.66 (space group $P2_1$) and it was first reported simultaneously by Gasperin and Ishizawa *et al*.[95, 96] The relation with perovskite is still clear and thus $a=2a_p$, $b=2\sqrt{2}a_p$ and $c=2\sqrt{2}a_p+\alpha$. The parameter α is the distance between consecutive blocks and it would reflect the length of the crystallographic shears, which in the present case is around 2 Å. Equivalent structures have been found for other phases such as $Ca_2Nb_2O_7$[97], $Nd_2Ti_2O_7$[98] or $Sr_2Nb_2O_7$[96, 99], differing in some

cases with the *a*-axis not being doubled and occasionally the unit cells are orthorhombic rather than monoclinic.

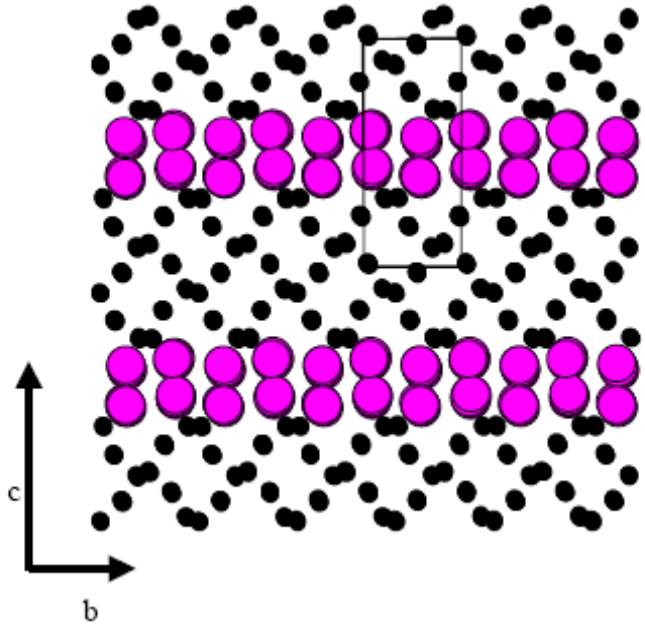


**Figure 1.10. Oxygen framework in $La_2Ti_2O_7$. The oxygen ions in the crystallographic shears that join two consecutive blocks are in purple.**

The n=5 member has also been subject of a number of various systems investigations especially in niobates and titanates, such as $Ca_5Nb_5O_{17}$[89], $Sr_5Nb_5O_{17}$[100], $La_5Ti_5O_{17}$[97], $Ca_5Nb_4TiO_{17}$[101] or $La_4SrTi_5O_{17}$[102]. The structure has been described as derived from perovskite blocks containing 5-layers each and joined by shearing as well. In most of the cases, the c-axis appeared to be doubled in comparison to that of the n=4 member due to slight canting between consecutive blocks. Compounds with n=5 structural-type are especially interesting because of their high conductivity which arises when there is mixed valence of the B-cations, i.e. Ti III/IV and Nb IV/V. Indeed, quasi-1D metallic behaviour has been reported in several of these niobates and titanates at room temperature.[89]

For the n=6 member, there are investigations on $Nd_4Ca_2Ti_6O_{20}$ and $La_4Ca_2Ti_6O_{20}$ reported by Nanot *et al*.[103, 104] Their structure can be described as derived from 6-layers perovskite blocks joined by shearing, although the samples studied seemed to be a mixture of phases.

All the mentioned investigations share a common feature: compounds with n > 5 could not be obtained as a single or, even a major phase, although one of the models predicts larger perovskite blocks with advancing towards until the n=∞ member, which is a cubic perovskite. Figure 1.11 presents a schematic structural model for the $A_nB_nO_{3n+2}$ series.

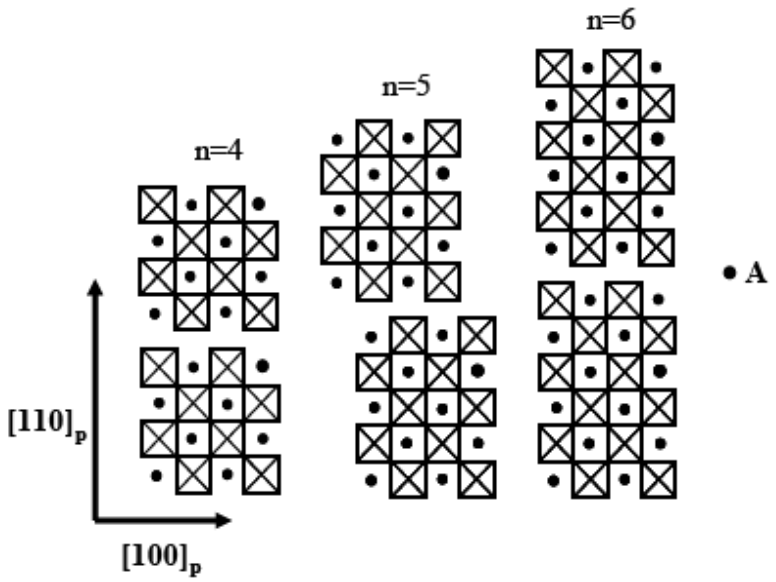


**Figure 1.11 Schematic models for the $A_nB_nO_{3n+2}$ series.**[89]

### 1.4.2. The (La,Sr)$TiO_{3+\delta}$ series

The substitution of $Sr^{2+}$ by $La^{3+}$ in the A-site of $SrTiO_3$ under oxidising conditions represents an intriguing case because charge neutrality dictates the presence of additional oxygen beyond the $ABO_3$ stoichiometry. That is a difficult situation to imagine considering that in a ccp arrangement there is no space for interstitial elements; unless cation vacancies are introduced into the pseudocubic perovskite structure. During the last two decades numerous works have been published on La substituting Sr in $SrTiO_3$. Some of those investigations focused

on A-site deficient perovskites to compensate the different charge of the cations involved. Thus, 2 $La^{3+}$ would substitute 3 $Sr^{2+}$ in the lattice creating one cation vacancy and giving rise to the $La_xSr_{1-3x/2}TiO_3$ system. La contents up to x=0.4 yield simple cubic perovskite unit cells. For higher La contents, vacancies seem to become ordered yielding lower symmetry unit cells as reported in investigations carried out by Battle *et al*.[105] Investigations on the $La_{1-x}Sr_xTiO_3$ system have been also published, i.e. without cation deficiency. The surplus of positive charge caused by $La^{3+}$ substituting $Sr^{2+}$ is counterbalanced by Ti as $Ti^{3+}$ under reducing conditions and thus maintain the electroneutrality of the crystal. These phases are usually achieved by using precursors containing $Ti^{3+}$ and operating always in reducing conditions. For x>0.80 the unit cell remained as cubic, although at higher La contents the compounds crystallise in the orthorhombic space groups Ibmm and Pbnm (x<0.30), which is consistent with the unit cell of the end members of the system. $SrTiO_3$ has a cubic unit cell a=3.9059Å, space group Pm-3m, whilst $LaTiO_3$ has an orthorhombic unit cell with parameters a=5.629 Å, 5.612 Å, c=7.915 Å, with space group Pbnm.[106] When the conditions are oxidising, there exists some controversy although most of the studies conclude that the excess of positive charge is compensated by the formation of vacancies on the A-site, preferentially as Sr vacancies[107-109]. This would lead to the formation of compounds with structure analogous to the Ruddlesden-Popper $Sr_{n+1}Ti_nO_{3n+1}$ series.[110] In other words, Sr vacancies are accommodated by the creation of SrO layers that regularly intergrow with perovskite layers. This can be expressed using Kroger-Vink notation as:

$$3Sr_{Sr}^{x} + 2La_2O_3 \leftrightarrow 2La_{Sr}^{\bullet} + V_{Sr}^{''} + 3SrO$$

Furthermore, Bowden *et al*.[102] attributed the presence of excess oxygen to the creation of planar defects similar to the crystallographic shears observed in $La_2Ti_2O_7$. These were observed distributed randomly within a perovskite matrix.

### 1.4.2.1 The $La_4Sr_{n-4}Ti_nO_{3n+2}$ series[9, 77, 80, 111]

The lower members of the $La_4Sr_{n-4}Ti_nO_{3n+2}$ series, n<7, are layered phases, having oxygen rich planes in the form of crystallographic shears joining consecutive blocks. These planes become more sporadic with increasing n (that is, decreasing the oxygen content) until they are no longer crystallographic features, rendering local oxygen-rich defects randomly distributed within a perovskite framework, n>11. Substitution of $Ti^{4+}$ by $Nb^{5+}$ or $Sc^{3+}$ demonstrates[80] that the oxygen excess parameter (δ) critically determines whether defects are ordered or disordered, with δ=0.167 being a critical parameter, Figure 1.12.

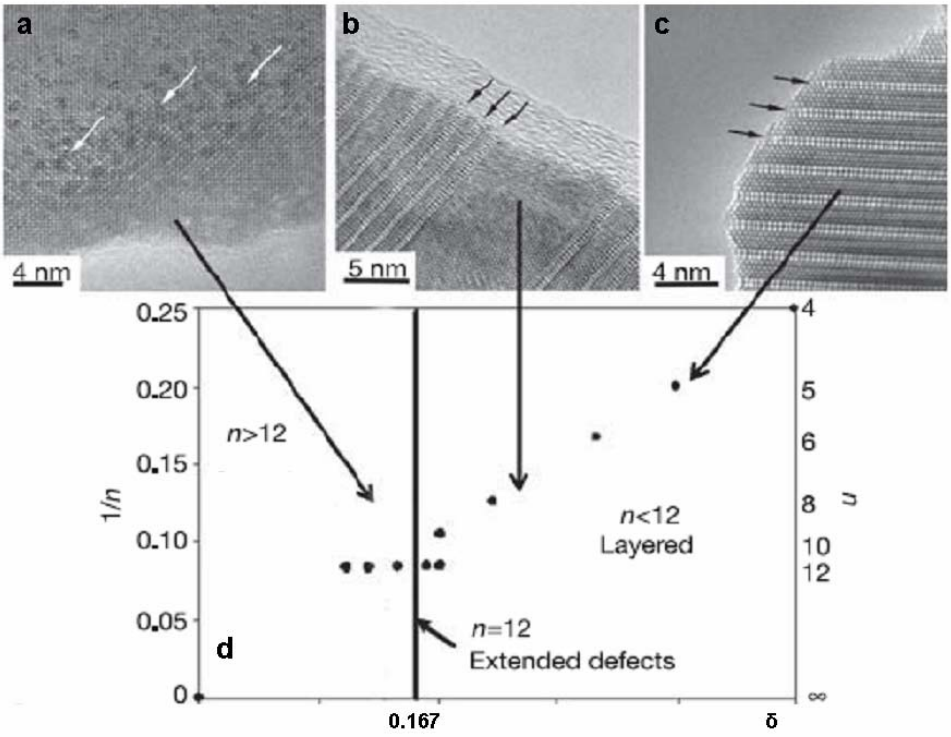


**Figure 1.12. Relation between microstructure and composition of the series '$La_4Sr_{n-4}Ti_nO3_{n+2}$'. (a)–(c), HRTEM images of samples varying from disordered extended defects (a, n=12) through random layers of extended defects (b, n=8) to ordered extended planar oxygen excess defects (c, n=5). (d) The location of these phases on the composition map, with 1/n plotted against oxygen excess δ in perovskite unit $ABO_{3+\delta}$. Adapted from Ruiz-Morales and *al*.[81]**

$La_4Sr_8Ti_{12}O_{38}$ is the n=12 member and the first cubic phase found in the perovskite-based oxygen excess $La_4Sr_{n-4}Ti_nO_{3n+2}$ series. Such layered perovskites are known to be able to accommodate extra oxygen beyond the parental $ABO_3$ perovskite in crystallographic shears. The general structure of the members of this series can therefore be described in terms of blocks containing n-{110} perovskite layers joined by crystallographic oxygen shears. Consecutive blocks are shifted by ½ {001}.[89, 112] The structure evolves with increasing *n*. First, the perovskite blocks become more extensive and the oxygen-rich layers move further apart; then, the spacing between these layers increases further and their repetition becomes more sporadic. Second, the layered structure is lost for compositions with n>11, rendering XRD cubic phases. In these structures, oxygen overstoichiometry is accommodated within the perovskite framework in randomly distributed short-range linear defects. These defects become more dilute as the ideal perovskite, *i.e.*, n =∞, is approached.

The electrical properties of $La_4Sr_8Ti_{12}O_{38}$ have revealed[77] the potential of this mixed oxide as an anode for fuel cells. The total conductivity revealed a strong dependence on oxygen stoichiometry, i.e. the amount of $Ti^{3+}$, showing the typical behaviour of an n-type conductor. A total conductivity of 60 $Scm^{-1}$ at 900°C, mainly electronic, was found for the reduced phases measured under 5% $H_2$/Ar atmospheres, revealing metallic behaviour. A metal-insulator transition was observed when measuring in wet 5% $H_2$/Ar, enhancing the effect of oxygen stoichiometry in the band structure of this material

An anode polarisation resistance of 2.97 $\Omega cm^2$ was achieved in wet $H_2$ at 900°C. Accordingly, the maximum current and power densities were 321 mA $cm^{-2}$ and 76 mW $cm^{-2}$, respectively, in wet $H_2$ at 900°C. However the performance in wet $CH_4$ was not good compared to that in wet $H_2$, *i.e.* a value of anode polarisation resistance of 8.93 $\Omega cm^2$ was obtained.

## 1.5. Aims of the thesis

The aim of this project is the search of novel anode materials for SOFCs under hydrogen fuel or preferably methane. As it has been said before (La,Sr)$TiO_{3+\delta}$ phases have been considered as good fuel electrode candidates due to their stability under reducing conditions and also because of their resistance to carbon build-up and sulphur poisoning, although their performance under methane was far from competitive in comparison with other state-of-the-art anode materials.[77-79] The substitution of $Ti^{4+}$ by $Mn^{3+}$ in the B-site would promote the removal of some oxygen in the structure to maintain the electroneutrality. Assuming that Mn was likely to be $Mn^{+3}$, two different approaches to solve this particular problem were considered. In the first, the La/Sr ratio was maintained giving rise to the $La_4Sr_8Ti_{12-n}Mn_nO_{38-n/2}$ series, whilst in the latter the oxygen overstoichiometry was fixed by changing the La/Sr ratio to compensate the Ti/Mn, i.e. giving rise to the $La_{4+n}Sr_{8-n}Ti_{12-n}Mn_nO_{38}$ series. Therefore if Mn remains in the 3+ oxidation state of the starting material, the resulting phases will all lie within the cubic domain, Figure 1.12. Alternatively, if Mn was in the +4 oxidation state, phases in the regime attempting to compensate by varying the $La_{4+n}Sr_{8-n}Ti_{12-n}Mn_nO_{38}$ La/Sr ratio, *i.e.* $La_{4+n}Sr_{8-n}Ti_{12-n}Mn_nO_{38+\delta}$ will move into the layered domain, considering that the oxygen overstoichiometry (δ) per $ABO_{3+\delta}$ unit cell will be bigger than 0.167. The goal of this project is to decrease the anode polarisation resistance under $H_2$ and especially under methane obtained for $La_4Sr_8Ti_{12}O_{38}$. For that, values of $R_p$ in $H_2$ less than 2.97 $\Omega cm^2$ at 900°C and 8.93 $\Omega cm^2$ in methane at the same temperature would be a starting point. Obviously the value in methane should be improved considerably. Another important issue is to corroborate than no carbon deposition occurs at fuel cell operation conditions. Through this work we can see the structural effects this substitution provokes as well as the electrochemical behaviour and fuel cell performances of these new materials.

## 1.6. References


[1] 'UK Energy in Brief ', The Department for Trade and Industry, 2006.

[2] J. T. S. Irvine, *Journal of Power Sources*, 2004, **136**, 203.

[3] M. M. González-Cuenca, 'Novel Anode Materials for Solid Oxide Fuel Cells', PhD thesis, Twente, 2002.

[4] www.fz-juelich.de.

[5] W. R. Grove, *Phil. Mag.*, 1839, **14**, 127.

[6] L. Mond and C. Langer, *Proc. R. Soc. London*, 1889, **46**, 296.

[7] W. Nernst, *Z. f. Elektrochemie*, 1899, **4**, 41.

[8] 'Fuel Cell Handbook', U.S. Department of Energy, 2000.

[9] J. Canales-Vazquez, 'Studies on oxygen excess perovskite-based titanates for SOFC fuel electrodes', PhD thesis, St Andrews, 2003.

[10] G. Hoogers, 'Fuel Cell Technology Handbook', CRC Press, 2003.

[11] www.bmwworld.com.

[12] www.toyota.com.

[13] www.daimlerchrysler.com.

[14] www.ballard.com.

[15] S. C. Singhal and K. Kendal, in 'High Temperature Solid Oxide Fuel Cells: Fundamentals, Design and Applications', Oxford, 2003.

[16] S. McIntosh, H. He, S.-I. Lee, O. Costa-Nunes, V. Krishnan, J. M. Vohs, and R. J. Gorte, *J. Electrochem. Soc.*, 2004, **151**, A604.

[17] S. McIntosh and R. J. Gorte, *Chem. Rev.*, 2004, **104**, 4845.

[18] R. M. Ormerod, *Chem. Soc. Rev.*, 2003, **32**, 17.

[19] Y. Mizutani, M. Tamura, M. Kawai, and O. Yamamoto, *Solid State Ionics*, 1994, **72**, 271.

[20] O. Yamamoto, Y. Arati, Y. Takeda, N. Imanishi, Y. Mizutani, M. Kawai, and Y. Nakamura, *Solid State Ionics*, 1995, **79**, 137.

[21] K. Nomura, Y. Mizutani, M. Kawai, Y. Nakamura, and O. Yamamoto, *Solid State Ionics*, 2000, **132**, 235–239.

[22] O. Yamamoto, Y. Arachi, H. Sakai, Y. Takeda, N. Imanishi, Y. Mizutani, M. Kawai, and Y. Nakamura, *Ionics*, 1998, **4**, 403.

[23] Y. Arachi, T. Asai, O. Yamamoto, Y. Takeda, N. Imanishi, K. Kawate, and C. Tamakoshib, *J. Electrochem. Soc.*, 2001, **148**, A520.

[24] H. Inaba and H. Tagawa, *Solid State Ionics*, 1996, **83**, 1.

[25] M. Mogensen, N. M. Sammes, and G. A. Tompsett, *Solid State Ionics*, 2000, **129**, 63–94.

[26] B. C. H. Steele, *Solid State Ionics*, 2000, **129**, 95–110.

[27] N. Oishi, A. Atkinson, N. Brandon, J. A. Kilner, and B. C. H. Steele, *Journal of the American Ceramic Society*, 2005, **88**, 1394.

[28] R. T. Leah, N. P. Brandon, and P. Aguiar, *Journal of Power Sources* 2005, **145**, 336.

[29] I. V. Yentekakis, *Journal of Power Sources*, 2006, **160**, 422.

[30] A. O. Stoermer, J. L. M. Rupp, and L. J. Gauckler, *Solid State Ionics*, 2006, **177**, 2075.

[31] T. Ishihara, H. Matsuda, and Y. Takita, *J. Am. Chem. Soc.*, 1994, **116**, 3801.

[32] T. Ishihara, Y. Hiei, and Y. Takita, *Solid State Ionics*, 1995, **79**, 371.

[33] T. Ishihara, H. Matsuda, and Y. Takita, *Solid State Ionics*, 1995, **79**, 147.

[34] T. Ishihara, H. Matsuda, M. Azmi Bin Bustam, and Y. Takita, *Solid State Ionics*, 1996, **86-88**, 197.

[35] T. Ishihara, H. Furutani, M. Honda, T. Yamada, T. Shibayama, T. Akbay, N. Sakai, H. Yokokawa, and Y. Takita, *Chem. Mater.* , 1999, **11**, 2081.

[36] T. Ishihara, H. Furutani, T. Yamada, and Y. Takita, *Ionics*, 1997, **3**, 209.

[37] B. C. H. Steele and A. Heinzel, *Nature*, 2001, **414**, 345.

[38] T. Yamada, N. Chitose, J. Akikusa, N. Murakami, T. Akbay, T. Miyazawa, K. Adachi, A. Hasegawa, M. Yamada, K. Hoshino, K. Hosoi, N. Komada, H. Yoshida, M. Kawano, T. Sasaki, T. Inagaki, K. Miura, T. Ishihara, and Y. Takitad, *J. Electrochem. Soc.*, 2004, **151**, A1712.

[39] T. Yamada, Y. Hiei, T. Akbay, T. Ishihara, and Y. Takita, *Solid State Ionics*, 1998, **113-115**, 253.

[40] H. Iwahara, H. Uchida, K. Ono, and K. Ogaki, *J. Electrochem. Soc.* , 1988, **135**, 529.

[41] T. H. Lee, S. E. Dorris, and U. Balachandran, *Solid State Ionics*, 2005, **176** 1479.

[42] P. Ranran, W. Yan, Y. Lizhai, and M. Zongqiang, *Solid State Ionics*, 2006, **177**, 389.

[43] M. Asamoto, H. Shirai, H. Yamaura, and H. Yahiro, *Journal of the European Ceramic Society*, 2007, **27** 4229.

[44] K. H. Ryu and S. M. Haile, *Solid State Ionics*, 1999, **125**, 355–367.

[45] K. Katahira, Y. Kohchi, T. Shimura, and H. Iwahara, *Solid State Ionics*, 2000, **138**, 91–98.

[46] C. Zuo, T. H. Lee, S.-J. Song, L. Chen, S. E. Dorris, U. Balachandran, and M. Liu, *Electrochem. Solid-State Lett.*, 2005, **8**, J35.

[47] C. Zuo, S. Zha, M. Liu, M. Hatano, and M. Uchiyama, *Adv. Mater.*, 2005, **18**, 3318–3320.

[48] C. Zuo, T. H. Lee, S. E. Dorris, B. U., and M. Liu, *Journal of Power Sources*, 2006, **159**, 1291.

[49] O. Yamamoto, Y. Takeda, R. Kanno, and M. Noda, *Solid State Ionics*, 1988, **22**, 241.

[50] H. Yokokawa, N. Sakai, T. Kawada, and M. Dokiya, *J. Electrochem. Soc.*, 1991, **138**, 2719.

[51] H. Taimatsu, K. Wada, H. Kaneko, and H. Yamamura, *J. Am. Ceram. Soc.*, 1992, **75**, 401.

[52] N. Q. Minh, *J. Am. Ceram. Soc.*, 1993, **76**, 563.

[53] J. M. Bae and B. C. H. Steele, *Solid State Ionics*, 1998, **106**, 247–253.

[54] B. C. H. Steele and J. M. Bae, *Solid State Ionics*, 1988, **106** 255–261.

[55] D. Stoever, H. P. Buchkremer, A. Mai, N. H. Menzler, and M. Zahid, *Materials Science Forum*, 2007, **539-543**, 1367.

[56] A. Esquirol, N. P. Brandon, J. A. Kilner, and M. Mogensen, *J. Electrochem. Soc.*, 2004, **151**, A1847.

[57] W. H. Kim, H. S. Song, J. Moon, and H.-W. Lee, *Solid State Ionics*, 2006, **177** 3211.

[58] Y. Liu, S. Hashimoto, H. Nishino, K. Takei, and M. Mori, *Journal of Power Sources*, 2007, **164** 56.

[59] H. S. Spacil, in 'Electrical device including nickel-containing stabilized zirconia electrode ', US Patent 3 1970.

[60] N. Q. Minh, *ChemTech*, 1991, **21**, 120.

[61] B. C. H. Steele, *Solid State Ionics*, 1996, **86-88**, 1223.

[62] X. J. Chen, Q. L. Sin, S. H. Chan, N. P. Brandon, and K. A. Khor, *Electrochem. Commun.*, 2007, **9**, 767.

[63] J. Qiao, K. Sun, N. Zhang, B. Sun, J. Kong, and D. Zhou, *J. Power Sources*, 2007, **169**, 253.

[64] H. Kurokawa, T. Z. Sholklapper, C. P. Jacobson, L. C. De Jonghe, and S. J. Visco, *Electrochem. Solid-State Lett.*, 2007, **10**, B135.

[65] H. P. He, J. M. Vohs, and R. J. Gorte, *J. Electrochem. Soc.*, 2003, **150**, A1470.

[66] B. C. H. Steele, I. Kelly, H. Middleton, and R. Rudkin, *Solid State Ionics*, 1988, **28–30**, 1547–1552.

[67] H. Koide, Y. Someya, T. Yoshida, and T. Maruyama, *Solid State Ionics*, 2000, **132**, 253.

[68] A. Bieberle, L. P. Meier, and L. J. Gauckler, *J. Electrochem. Soc.*, 2001, **148**, A646.

[69] J. Liu and S. A. Barnett, *Solid State Ionics* 2003, **158**, 11 – 16.

[70] A. Weber, B. Sauer, A. C. Muller, D. Herbstritt, and E. Ivers-Tiffee, *Solid State Ionics*, 2002, **152-153** 543.

[71] S. Park, J. M. Vohs, and R. J. Gorte, *Nature*, 2000, **404** 265.

[72] R. J. Gorte, J. M. Vohs, and S. McIntosh, *Solid State Ionics*, 2004, **175** 1.

[73] J. Liu, B. D. Madsen, Z. Ji, and S. A. Barnett, *Electrochem. Solid-State Lett.*, 2002, **5**, A122.

[74] S. Tao and J. T. S. Irvine, *Nature Mater.*, 2003, **2**, 320.

[75] B. A. Boukamp, *Nature Mater.*, 2003, **2**, 294.

[76] S. W. Tao and J. T. S. Irvine, *Chemistry of Materials*, 2004, **16**, 4116.

[77] J. Canales-Vazquez, S. W. Tao, and J. T. S. Irvine, *Solid State Ionics*, 2003, **159**, 159.

[78] O. A. Marina, N. L. Canfield, and J. W. Stevenson, *Solid State Ionics*, 2002, **149**, 21.

[79] O. A. Marina and R. L. Pederson, Proceedings of the 5$^{th}$ European Solid Oxide Fuel Cell Forum, Lucerne, Switzerland, 2002.

[80] J. Canales-Vazquez, J. C. Ruiz-Morales, J. T. S. Irvine, and W. Z. Zhou, *Journal of the Electrochemical Society*, 2005, **152**, A1458.

[81] J. C. Ruiz-Morales, J. Canales-Vazquez, C. Savaniu, David Marrero-Lopez, W. Zhou, and J. T. S. Irvine, *Nature*, 2006, **439**, 568.

[82] N. Sakai, T. Horita, K. Yamaji, Y. P. Xiong, H. Kishimoto, M. E. Brito, and H. Yokokawa, *Solid State Ionics*, 2006, **177** 1933.

[83] Z. Yang, G. G. Xia, G. D. Maupin, and J. W. Stevenson, *J. Electrochem. Soc.*, 2006, **153**, A1852.

[84] K. Ogasawara, H. Kameda, Y. Matsuzaki, T. Sakurai, T. Uehara, A. Toji, N. Sakai, K. Yamaji, T. Horita, and H. Yokokawa, *J. Electrochem. Soc.*, 2007, **154**, B657.

[85] www.powergeneration.siemens.com.

[86] S. C. Singhal, *Solid State Ionics*, 2002, **152–153**, 405.

[87] *St Andrews Fuel Cells, St Andrews, Fife KY16 9ST, Scotland, UK*.

[88] V. M. Goldschmidt, T. Barth, G. Lunde, and W. Zachariasen, *Mat.-Nat. Kl.*, 1926, **2**, 117.

[89] F. Lichtenberg, A. Herrnberger, K. Wiedenmann, and J. Mannhart, *Prog. in Solid State Chem.*, 2001, **29**, 1.

[90] A. K. Azad, 'Synthesis, Structure and Magnetic properties of $A_2MnBO_6$ and $A_2FeBO_6$', PhD thesis, Goteborg, 2004.

[91] A. M. Glazer, *Acta Crystallographica*, 1972, **B28**, 3384.

[92] C. H. Hervoches, J. T. S. Irvine, and P. Lightfoot, *Phys. Rev. B*, 2001, **64**, 100102.

[93] A. M. Kusainova, S. Yu Stefanovich, J. T. S. Irvine, and P. Lightfoot, *Mater. Chem.*, 2002, **12**, 3413.

[94] A. Snedden, C. H. Hervoches, and P. Lightfoot, *Phys. Rev. B*, 2003, **67**, 092102.

[95] M. Gasperin, *Acta Crystallographica*, 1975, **B31**, 2129.

[96] N. Ishizawa, F. Narumo, T. Kawamura, and M. Kimura, *Acta Crystallographica*, 1975, **B31**, 1912.

[97] T. Williams, H. W. Schmalle, A. Reller, F. Lichtenberg, D. Widmer, and J. G. Bednorz, *J. Solid State Chem.*, 1991, **93**, 534.

[98] J. Sloan, 'Ph. D thesis', Cardiff, 1995.

[99] I. Levin, L. A. Bendersky, T. A. Vanderah, R. S. Roth, and O. M. Stafsudd, *Materials Research Bulletin*, 1998, **33[3]**, 501.

[100] H. W. Schmalle, T. Williams, A. Reller, F. Lichtenberg, D. Widmer, and J. G. Bednorz, *Acta Cryst. C*, 1995, **51**, 1243.

[101] M. Nanot, F. Queyroux, and J. C. Gilles, *J. Solid State Chem.*, 1979, **28**, 137.

[102] M. E. Bowden, D. A. Jefferson, and I. W. M. Brown, *J. Solid State Chem.*, 1995, **117**, 88.

[103] M. Nanot, F. Queyroux, J. C. Gilles, and R. Portier, *J. Solid State Chem.*, 1981, **38**, 74.

[104] M. Nanot, F. Queyroux, J. C. Gilles, and J. J. Capponi, *J. Solid State Chem.*, 1986, **61**, 315.

[105] P. D. Battle, J. E. Bennet, J. Sloan, R. J. D. Tilley, and J. F. Vente, *J. Solid State Chem.*, 2000, **149**, 360.

[106] J. E. Sustrom, S. M. Kauzlarich, and P. Klavins, *Chemistry of Materials*, 1992, **4**, 346.

[107] N. G. Eror and U. Balachandran, *J. Solid State Chemistry*, 1981, **40**, 85.

[108] U. Balachandran and N. G. Eror, *J. Electrochem. Soc.*, 1982, **129**, 1021.

[109] R. Moos, T. Bischoff, W. Menesklou, and K. H. Härdtl, *J. Mater. Sci.*, 1997, **32**, 4247.

[110] R. J. D. Tilley, *J. Solid State Chem.*, 1977, **21**, 293.

[111] J. Canales-Vazquez, M. J. Smith, J. T. S. Irvine, and W. Z. Zhou, *Advanced Functional Materials*, 2005, **15**, 1000.

[112] J. S. Canales-Vazquez, J. T. S. Irvine, and W. Z. Zhou, *Journal of Solid State Chemistry*, 2004, **177**, 2039.

# 2

# Experimental techniques

## 2.1. Introduction

In this chapter, an outline of the techniques most frequently used during the course of this work is presented. First, some comments are given on the preparation of samples and then a summary of XRD, neutron diffraction, TGA, ac impedance spectroscopy, four terminal measurements and fuel cell tests. Some additional techniques such as magnetic studies, SEM and TEM were also used, although not on a regular basis. In relation to these, some comments are added to facilitate the comprehension in the corresponding sections.

## 2.2. Experimental

### 2.2.1. Synthesis preparation

The preparation of samples in the present work was always carried out by traditional solid state reaction, which consists in mixing and grinding the stoichiometric amounts of the appropriate oxides (excepting Sr that was used as carbonate) in acetone. After drying, the mixture was calcined typically at 1000ºC for 6-12 hours to decompose the carbonates. Then it was ground and pressed uniaxially at 1.5-2.0 tons for 1 minute. The resulting pellets were fired at 1350-1400ºC for 48 hours and then ground, pressed and fired at the same temperature for further 48 hours yielding generally grey pellets. Reduced phases were obtained by further firing at 1000ºC for 48 hours in flowing dry 5%$H_2$/Ar. Dense samples were obtained by ball milling in Zirconia containers for 20-30 minutes between every step of the mentioned above.

### 2.2.2. X-ray diffraction (XRD)[1-3]

X-rays were discovered in 1895 by the German physicist Wilhelm C. Röntgen and were so named because their nature was unknown at the time. It was not until 1912 that Laue and co-workers[4] observed the diffraction of x-rays. They suggested that a crystal could be similarly regarded as a 3-dimensional diffraction grating for electromagnetic waves of a wavelength comparable to the atomic spacing (~ 1Å ). A year later W. L. Bragg[5] presented a simple explanation of the diffracted beam from a crystal. Suppose that the incident waves are reflected specularly from parallel planes of atoms in the crystal, with each plane reflecting only a very small fraction of the radiation. In specular (mirrorlike) reflection the angle of incidence is equal to the angle of reflection. The diffracted beams are found when the reflections from parallel planes of atoms interfere constructively, as in Figure 2.1. We treat as elastic scattering, in which the energy of the x-ray is not changed on reflection.

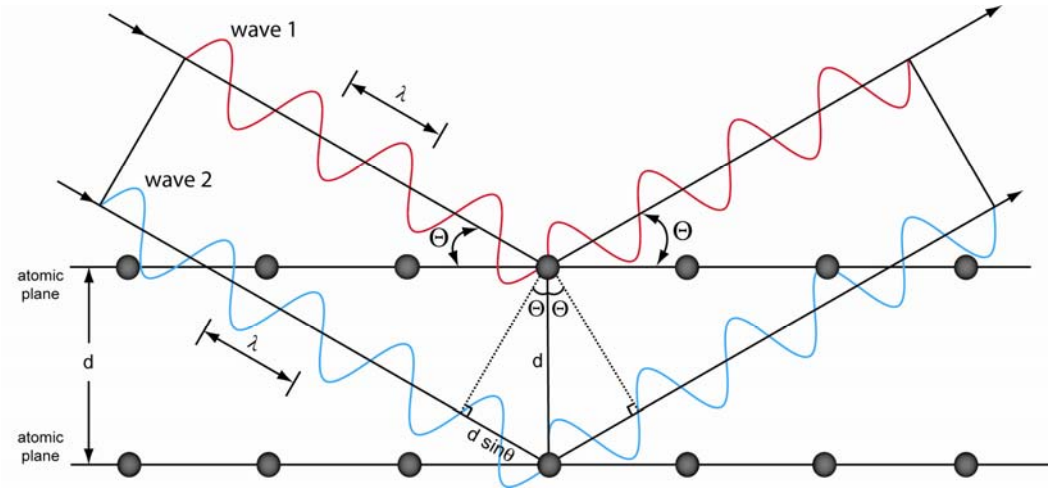


**Figure 2.1 Schematic diagram illustrating Bragg's law for diffraction phenomena.**

Consider parallel lattice planes spaced d apart. The radiation is incident in the plane of the paper. The path difference for rays reflected from adjacent planes is $2d\sin\Theta$, where $\Theta$ is measured from the plane. Constructive interference of the

radiation from successive planes occurs when the path difference is an integral number of wavelengths $\lambda$, so that:

$$2d\sin\Theta = n\lambda \qquad [2.1]$$

Equation 2.1 is the Bragg's law. It states the essential condition which must be met if diffraction is to occur. Here $n$ is called the order of reflection and is equal to the number of wavelengths in the path difference between rays scattered by adjacent planes.

Bragg's law is a consequence of the periodicity of the lattice. Bragg reflection can occur only for wavelength $\lambda \leq 2d$.

When this law is satisfied, the diffracted beams 1 and 2 are in phase (see figure 2.1) and constructively interfere. When the law is not satisfied, the beams are out of phase and destructively interfere. Thus, by keeping $\lambda$ constant and varying $2\Theta$ (the angle between diffracted beams), a graphic of constructive interference can be plotted against angle. This is a diffraction pattern, and the Bragg's law allows us to directly relate the intensity peaks with the interatomic spacing d, giving valuable information about the structure of the crystal.

Data were collected with a Stoe StadiP Transmission X-ray diffractometer, using CuK$\alpha_1$ radiation. The measurement range was from 10º to 70º.

### 2.2.3. Neutron diffraction[6, 7]

The wave-like properties of the neutron were first demonstrated, by means of diffraction, by Mitchell and Powers [8] in 1936 . Thus, neutron diffraction experiments can be used to investigate crystal structures in a manner analogous to X-ray diffraction.

In X-ray or electron diffraction experiments the radiation is scattered by the electrons surrounding the nuclei and an electron density map is obtained, from which the positions of the nuclei can be deduced. Neutrons, however, are

scattered by the nuclei themselves, and thus as neutron diffraction experiment gives a direct measurement of nuclear positions.

Neutron diffraction uses neutrons of wavelengths 1-2 Å, similar to those used for X-rays in XRD, to determine atomic structure in crystalline phases in an essentially similar manner. There are several differences that make the techniques somewhat complementary. Because neutrons are diffracted by the nucleus, whereas X-ray diffraction is an electron density effect, the neutron probing depth is about $10^4$ greater than X-ray. Thus neutron diffraction is an entirely bulk method, which can be used under ambient pressures, and to analyze the interiors of very large samples, or contained samples by passing the neutron flux through the containment walls. Along with this capability, however, goes the difficulty of neutron shielding and safety. Where X-ray scattering cross sections increase with the electron density of the atom, neutron scattering varies erratically across the periodic table and is approximately equal for many atoms. As a result, neutron diffraction “sees” light elements, such as oxygen atoms in oxide superconductors, much more effectively than X-ray diffraction.

A further important difference between neutron and X-ray diffraction is the sensitivity to magnetic structure. The magnetic moments of neutrons interact with the magnetic moments of target atoms, whereas this interaction is much weaker (~$10^{-6}$) for X-rays. The interaction strength is proportional to the magnetic moments of the atoms in the material, and depends on their orientation relative to the neutron moment. These features make neutron diffraction the best technique for probing the spatial arrangement of magnetic moments in magnetic materials.

There are two different ways for the generation of neutrons for diffraction work. The first of these uses a nuclear reactor to source of neutrons, by means of fission. These neutrons are produced continuously and they present a broad range of wavelengths. Selection of wavelengths for diffraction is then achieved

by Bragg scattering from a crystal monochromator. The sample for analysis is mounted in a vanadium can and the diffraction pattern is collected over a range of $2\Theta$, in a similar way to an XRD pattern.

The second method of neutron generation is by spallation. In this technique, neutrons are generated by bombarding a uranium or tantalum target with high energy protons. These protons are released from a synchrotron in pulses and then the neutrons are similarly generated in pulses. These pulses then pass through a chopper in order to remove undesirable wavelengths and to give a zero point in the time of flight (TOF) of the neutrons. The pulses are then diffracted by the sample and the neutron TOF counted using a static detector of known angle to the sample and neutron beam. Because the TOF is proportional to the wavelength of the neutron, and the distance from chopper to detector is known, the detected neutrons can be then processed to give a diffraction pattern. The TOF of neutrons can be converted into d-spacing using the following relationship:

$$d = \frac{ht}{2m_n l \sin\Theta} \qquad [2.2]$$

Where $d$ is the interplanar d-spacing, $h$ is Planck's constant, $t$ is the TOF, $m_n$ is the mass of the neutron, $l$ is the distance between chopper and detector and $\Theta$ is the angle between the beam and the detector.

Neutron diffraction data for this work have been obtained using both techniques. TOF data were collected on the Polaris and HRPD instruments at the ISIS facilities, Rutherford Appleton Laboratories in Oxford, UK. Constant wavelength diffraction data has been obtained using the D2B instrument at Institut Laue Langevin (ILL) in Grenoble, France.

### 2.2.3.1. Powder pattern analysis. The Rietveld method

In Rietveld analysis[9], a model is fitted to the entire diffraction pattern by means of curve fitting and least squares method, rather than by fitting the intensity maxima. By taking this approach, the intensity of each data point is taken into account in the calculation, and so diffraction optics, instrument geometry, and even second phases can be factored into a refinement in order to more accurately characterise a sample. Several pieces of software, capable of processing both x-ray and neutron (constant wavelength and TOF) diffraction data are available. In this work the GSAS[10] package was used.

As well as providing a visual measure of the quality of the refined model in the form of a difference curve, the Rietveld software also provides a quantitative measure of the closeness of fit in terms of R factors, or residual factors. There are four commonly used R factors:

1. Profile R factor, $R_p$
2. Weighted R factor, $R_{wp}$
3. Intensity or Bragg R factor, $R_I$
4. Expected R factor, $R_E$

These are defined as follows:

$$R_p = \frac{\sum_i | I_i(obs) - I_i(cal) |}{\sum_i I_i(obs)}$$

$$R_{wp} = \left[ \frac{\sum_i | I_i(obs) - I_i(cal) |^2}{\sum_i W_i I_i^2(obs)} \right]^{\frac{1}{2}}$$

$$R_I = \sum_k | I_k(obs) - \frac{1}{c} I_k(calc) | \sum_k I_k(obs)$$

$$R_E = \left[ \frac{N - P + C}{\sum_i W_i I_i^2(obs)} \right]^{\frac{1}{2}}$$

Where: I is the peak intensity

W is a weighting factor

C is the number of constrains

N is the number of observations

P is the number of variables

Another guide to the quality of a refinement is $\chi^2$, which is calculated using the following relationship:

$$\chi^2 = \left[\frac{R_{wp}}{R_E}\right]^{\frac{1}{2}}$$

For an ideal refinement then, the weighted and expected R factors should be identical, and hence a value of 1 obtained for $\chi^2$. However, a number of things can affect the value of $\chi^2$, and hence the value should not be used solely on its on as a guide to the quality of a refinement. It is also important to examine the observed and calculated profiles at each stage of refinement in order to assess the progress and future strategy of the refinement. The R factors obtained during the course of a refinement are the best guide to the quality of the fitted profile. The use of specialist equipment such as a furnace or cryostat can also contribute to the background of the collected profile, and hence influence the expected R factors.

### 2.2.4. Thermogravimetric analysis (TGA)[11]

TGA involves registering the difference in mass when thermally treating a sample in various atmospheric conditions. Mass changes can be used to monitor processes such as oxidation-reduction, loss-uptake of water or loss-uptake of $CO_2$.

The instrumentation consists of an ultra-sensitive balance with a sample pan inside a furnace whose temperature can be accurately controlled. Inside the

furnace the sample can be studied under different atmospheric conditions, i.e. flowing wet or dry air, Ar or 5% $H_2$/Ar. Wet conditions are achieved by making the gases flow through a pipe containing soaked cotton wool. The experiment typically consists of heating a sample up to 800-900ºC at a fixed rate of 5-10K/min. Then the temperature is held for 6 hours to finally cool down to room temperature.

The balance used in this work was a Rheotherm TG 1000M Thermogravimetric analyser with Rheometric Scientific Plus V v.5.44 Software.

### 2.2.5. Magnetic measurements[12, 13]

All materials can be classified in terms of their magnetic behaviour falling into one of five categories depending on their bulk magnetic susceptibility. The two most common types of magnetism are diamagnetism and paramagnetism, which account for the magnetic properties of most of the periodic table of elements at room temperature. These elements are usually referred to as non-magnetic, whereas those which are referred to as magnetic are actually classified as ferromagnetic. The only other type of magnetism observed in pure elements at room temperature is antiferromagnetism. Finally, magnetic materials can also be classified as ferrimagnetic although this is not observed in any pure element but can only be found in compounds, such as the mixed oxides, known as ferrites, from which ferrimagnetism derives its name. The magnetic susceptibility value falls into a particular range for each type of material.

#### 2.2.5.1. Diamagnetism

In a diamagnetic material the atoms have no net magnetic moment when there is no applied field. Under the influence of an applied field ($\vec{H}$) the spinning electrons produce a magnetization ($\vec{M}$) in the opposite direction to that of the applied field. All materials have a diamagnetic effect; however, it is often the

case that the diamagnetic effect is masked by the larger paramagnetic or ferromagnetic term. The value of susceptibility is independent of temperature

**2.2.5.2. Paramagnetism**

There are several theories of paramagnetism, which are valid for specific types of material. The Langevin model, which is valid for materials with non-interacting localised electrons, states that each atom has a magnetic moment which is randomly oriented as a result of thermal agitation. The application of a magnetic field creates a slight alignment of these moments and hence a low magnetisation in the same direction as the applied field. As the temperature increases, then the thermal agitation will increase and it will become harder to align the atomic magnetic moments and hence the susceptibility will decrease. This behaviour is known as the Curie law and is shown below in equation 2.3, where C is a material constant called the Curie constant.

$$\chi = \frac{M}{H} = \frac{C}{T} \qquad [2.3]$$

Materials which obey this law are materials in which the magnetic moments are localised at the atomic or ionic sites and where there is no interaction between neighbouring magnetic moments.

In fact the Curie law is a special case of the more general Curie-Weiss law, equation 2.4, which incorporates a temperature constant ($\Theta$) and derives from Weiss theory, proposed for ferromagnetic materials, that incorporates the interaction between magnetic moments.

$$\chi = \frac{C}{T + \Theta} \qquad [2.4]$$

In this equation $\Theta$ can either be positive, negative or zero. Clearly when $\Theta = 0$ then the Curie-Weiss law equates to the Curie law. When $\Theta$ is non-zero then there is an interaction between neighbouring magnetic moments and the material is only paramagnetic above a certain transition temperature. If $\Theta$ is

positive then the material is ferromagnetic below the transition temperature and the value of $\Theta$ corresponds to the transition temperature (Curie temperature, $T_C$). If $\Theta$ is negative then the material is antiferromagnetic below the transition temperature (Néel temperature, $T_N$), however the value of $\Theta$ does not relate to $T_N$. It is important to note that this equation is only valid when the material is in a paramagnetic state. It is also not valid for many metals as the electrons contributing to the magnetic moment are not localised. However, the law does apply to some metals, e.g. the rare-earths, where the 4f electrons, that create the magnetic moment, are closely bound.

The Pauli model of paramagnetism is valid for materials where the electrons are free and interact to form a conduction band; this is valid for most paramagnetic metals. In this model the conduction electrons are considered essentially to be free and under an applied field an imbalance between electrons with opposite spin is set up leading to a low magnetisation in the same direction as the applied field. The susceptibility is independent of temperature, although the electronic band structure may be affected, which will then have an effect on the susceptibility.

#### 2.2.5.3. Ferromagnetism

Ferromagnetism is only possible when atoms are arranged in a lattice and the atomic magnetic moments can interact to align parallel to each other. This effect is explained in classical theory by the presence of a molecular field within the ferromagnetic material, which was first postulated by Weiss in 1907. This field is sufficient to magnetise the material to saturation. In quantum mechanics, the Heisenberg model of ferromagnetism describes the parallel alignment of magnetic moments in terms of an exchange interaction between neighbouring moments.

Weiss postulated the presence of magnetic domains within the material, which are regions where the atomic magnetic moments are aligned. The movement of

these domains determines how the material responds to a magnetic field and as a consequence the susceptible is a function of applied magnetic field. Therefore, ferromagnetic materials are usually compared in terms of saturation magnetisation (magnetisation when all domains are aligned) rather than susceptibility.

In the periodic table of elements only Fe, Co and Ni are ferromagnetic at and above room temperature. As ferromagnetic materials are heated then the thermal agitation of the atoms means that the degree of alignment of the atomic magnetic moments decreases and hence the saturation magnetisation also decreases. Eventually the thermal agitation becomes so great that the material becomes paramagnetic; the temperature of this transition is the Curie temperature, $T_C$ (Fe: $T_C$ = 770°C, Co: $T_C$ = 1131°C and Ni: $T_C$ = 358°C). Above $T_C$ then the susceptibility varies according to the Curie-Weiss law.

#### 2.2.5.4. Antiferromagnetism

In the periodic table the only element exhibiting antiferromagnetism at room temperature is chromium. Antiferromagnetic materials are very similar to ferromagnetic materials but the exchange interaction between neighbouring atoms leads to the anti-parallel alignment of the atomic magnetic moments. Therefore, the magnetic field cancels out and the material appears to behave in the same way as a paramagnetic material. Like ferromagnetic materials these materials become paramagnetic above a transition temperature, known as the Néel temperature, $T_N$. (Cr: $T_N$ = 37ºC).

#### 2.2.5.5. Ferrimagnetism

Ferrimagnetism is only observed in compounds, which have more complex crystal structures than pure elements. Within these materials the exchange interactions lead to parallel alignment of atoms in some of the crystal sites and anti-parallel alignment of others. The material breaks down into magnetic domains, just like a ferromagnetic material and the magnetic behaviour is also

very similar, although ferrimagnetic materials usually have lower saturation magnetisations. For example in barium ferrite ($BaO.6Fe_2O_3$) the unit cell contains 64 ions of which the barium and oxygen ions have no magnetic moment, 16 $Fe^{3+}$ ions have moments aligned parallel and 8 $Fe^{3+}$ aligned anti-parallel giving a net magnetisation parallel to the applied field, but with a relatively low magnitude as only 1/8 of the ions contribute to the magnetisation of the material.

### 2.2.5.6. Measurements

Magnetisation as a function of temperature has been measured in a Superconducting Quantum Interference Device (SQUID) magnetometer at the Department of Physics at St Andrews University. Magnetisation versus temperature curves were measured between 5K and 200K in zero-field-cooled (ZFC) mode with applied fields (H) up to 100 Oe. For measurements in magnetic field, a Helium-cooled superconducting 5T magnet has been used. In the cryostat, illustrated in Figure 2.2, the sample is positioned in the centre of the superconduction solenoid.

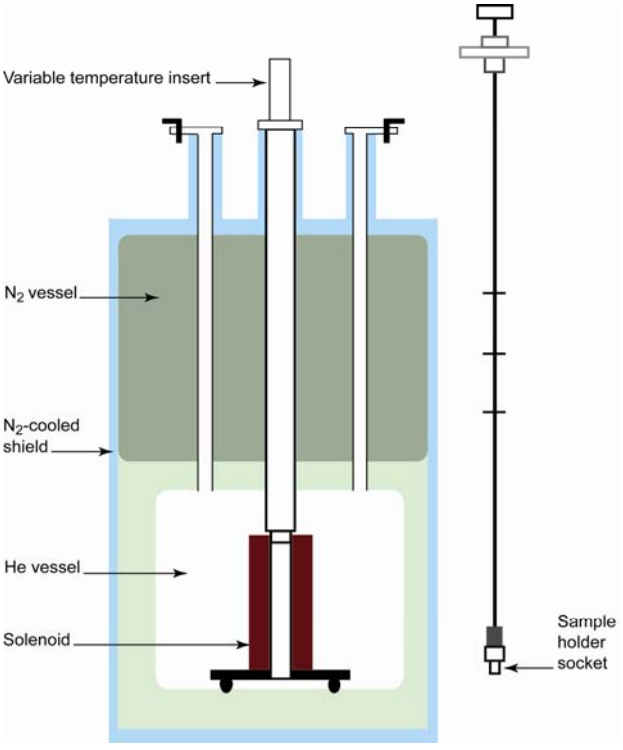


**Figure 2.2 Schematic diagram of a liquid Helium cryostat**

### 2.2.6. Scanning electron microscopy (SEM)[6]

SEM complements optical microscopy for studying the texture, topography and surface features of powders or solid pieces; features up to tens of micrometres in size can be seen and, because of the depth of focus of SEM instruments, the resulting pictures have a definitive three-dimensional quality.

SEM covers the magnification range between the lower resolution limit of optical microscopy (~ 1 μm) to and the upper practical working limit of transmission electron microscopy (TEM) (~ 0.2 nm).

In the SEM, a source of electrons is focused (in vacuum) into a fine probe that is rastered over the surface of the specimen. As the electrons penetrate the surface, a number of interactions occur that can result in the emission of electrons or photons from (or through) the surface. A reasonable fraction of the electrons emitted can be collected by appropriate detectors, and the output can be used to modulate the brightness of a cathode ray tube (CRT) whose x and y inputs are driven in synchronism with the x-y voltages rastering the electron beam. In this way an image is produced on the CRT; every point that the beam strikes on the sample is mapped directly onto a corresponding point on the screen.

The principle images produced in the SEM are of three types: secondary electron images, backscattered electron images, and elemental X-ray maps. Secondary and backscattered electrons are conventionally separated according to their energies. They are produced by different mechanisms. When a high-energy primary electron interacts with an atom, it undergoes either inelastic scattering with atomic electrons or elastic scattering with the atomic nucleus. In an inelastic collision with an electron, some amount of energy is transferred to the other electron. If the energy transfer is very small, the emitted electron will probably not have enough energy to exit the surface. If the energy transferred exceeds the work function of the material, the emitted electron can exit the solid.

When the energy of the emitted electron is less than about 50 eV**,** by convention it is referred to as a secondary electron, or simply a secondary. Most of the emitted secondary electrons are produced within the first few nm of the surface. Secondaries produced much deeper in the material suffer additional inelastic collisions, which lower their energy and trap them in the interior of the solid. Higher energy electrons are primary electrons that have been scattered without loss of kinetic energy (i.e., elastically) by the nucleus of an atom, although these collisions may occur after the primary electron has already lost some of its energy to inelastic scattering.

Backscattered electrons are considered to be the electrons that exit the specimen with an energy greater then 50 eV, including Auger electrons. The higher the atomic number of a material, the more likely it is that backscattering will occur.

An additional electron interaction of major importance in the SEM occurs when the primary electron collides with and ejects a core electron from an atom in the solid. The excited atom will decay to its ground state by emitting either a characteristic X-ray photon or an Auger electron.

The use of the SEM requires very little in regard to sample preparation, provided that the specimen is vacuum compatible. If the sample is conducting, the major limitation is whether it will fit onto the stage. If the sample is an insulator there are still methods by which it can be studied in the instrument. The simplest approach is to coat it with a thin (10 nm) conducting film of gold or some other metal. In following this approach, care must be taken to avoid distortions that could be produced by non uniform coatings or by agglomeration of the coating material.

A Jeol JSM 5600 SEM with a resolution of 3.5nm and magnification up to 300,000 x has been used in the course of this work.

### 2.2.7. Transmission electron microscopy (TEM)[6]

The principle of a TEM experiment can be described as follows: the electron gun (typically made of $LaB_6$) generates an electron beam that is focused by the condenser lenses. After that, the beam interacts with the specimen and passes through it. The transmitted and diffracted electrons are then recombined and focused by the objective lens to form a diffraction pattern and an intermediate image at the backfocal plane. The beams then diverge and are focused by the projector lens to form the final image. Whether an electron diffraction pattern and an image is achieved is determined by choosing images from the backfocal plane or the image plane. Resolution down to less than 2Å can be achieved.

TEM offers two methods of specimen observation, diffraction mode and image mode. In diffraction mode, an electron diffraction pattern is obtained on the fluorescent screen, originating from the sample area illuminated by the electron beam. The diffraction pattern is entirely equivalent to an X-ray diffraction pattern: a single crystal will produce a spot pattern on the screen and a polycrystal will produce a powder or ring pattern. In image mode, the post-specimen lenses are set to examine the information in the transmitted signal at the image plane of the objective lens. Here, the scattered electron waves finally recombine, forming an image with recognizable details related to the sample microstructure (or atomic structure).

A JEOL JEM 2011 HRTEM has been used in the course of this work. Its technical data are listed below:

Resolution: 0.18 nm.

Accelerating Voltage: 80, 100, 120, 160, 200 kV.

Magnification: up to 1,200,000 x.

Specimen grid: up to 3 mm in diameter.

### 2.2.8. AC Impedance[14-17]

AC Impedance spectroscopy is a suitable technique to investigate and characterise the electrical properties of ceramic materials because it differentiates between different electrochemical responses due to bulk, grain boundary, electrode phenomena, etc.

Electrical resistance is the ability of a circuit element or device to resist the flow of electrical current. Ohm's law (equation 2.5) states that the current *I* flowing in a circuit is proportional to the applied potential difference *V*. The constant of proportionality is defined as the resistance *R*,

$$V = IR \qquad [2.5]$$

While this is a well known relationship, its use is limited to only one circuit element, the ideal resistor.

Real circuits exhibit much more complex behaviour. We have to abandon the simple concept of resistance and use impedance which is a more general circuit parameter. Like resistance, impedance is a measure of the ability of a circuit to resist the flow of electrical current. Unlike resistance, impedance is not limited by the properties of an ideal resistor.

Impedance (Z) is generally defined as the total opposition a device or circuit offers to the flow of an alternating current (AC) at a given frequency, and is represented as a complex quantity which is graphically shown on a vector plane. An impedance vector consists of a real part (resistance, R) and an imaginary part (reactance, X). If X>0, the reactance is said to be inductive. If X=0 then the impedance is purely resistive. If X<0, the reactance is said to be capacitive.

Electrochemical impedance is usually measured by applying an AC potential to an electrochemical cell and measuring the current through the cell.

A monochromatic signal involving the single frequency $\nu \equiv \omega / 2\pi$ is applied to a cell,

$$V(t) = V_0 \sin(\omega t) \qquad [2.6]$$

The resulting steady state current is measured,

$$I(t) = I_0 \sin(\omega t + \phi) \quad [2.7]$$

Here $\phi$ is the phase difference between the voltage and the current; it is zero for purely resistive behaviour, whilst for $\phi = 90^\circ$ the system resembles a pure capacitor. Impedance is defined as the opposition of the system to flow of charge:

$$Z = \frac{V(t)}{I(t)} \quad [2.8]$$

Using Euler's relationship,

$$e^{ix} = \cos x + i \sin x \quad [2.9]$$

it is possible to express the impedance as a complex function. The potential is then described as,

$$V(t) = V_0 e^{i\omega t} \quad [2.10]$$

And the current response as,

$$I(t) = I_0 e^{i(\omega t + \phi)} \quad [2.11]$$

The total impedance Z can be described as the sum of two contributions, real and imaginary impedance:

$$Z(\omega) = \frac{V_0}{I_0} e^{-i\phi} = Z_0(\cos\phi - i\sin\phi) = Z' - iZ'' \quad [2.12]$$

If the real part is plotted on the X axis and the imaginary part on the Y axis of a chart we get a Nyquist plot, Figure 2.3.

For a series connection of impedances we get the following equation:

$$Z_{ser} = \sum_k Z_k \quad [2.13]$$

And for a parallel connection of impedances:

$$\frac{1}{Z_{par}} = \sum_k \frac{1}{Z_k} \quad [2.14]$$

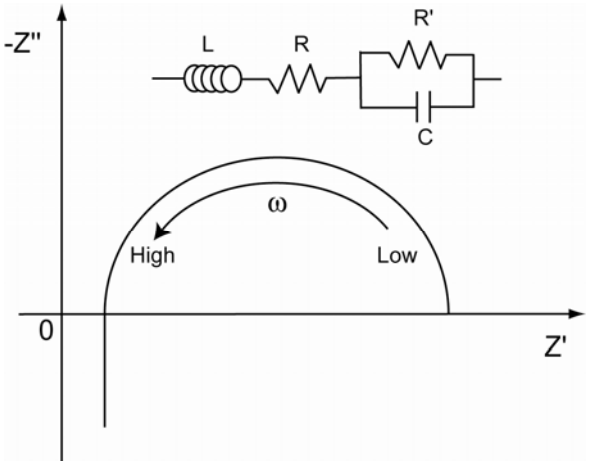


**Figure 2.3 Nyquist plot with equivalent circuit.**

Electrochemistry Impedance Spectroscopy (EIS) is commonly analyzed by fitting it to an electrical circuit model. The elements in that model should have a basis in the physical electrochemistry of the system. In Table 2.1 the impedance of common electrical elements is shown.

| Component | Current vs. Voltage | Impedance |
|---|---|---|
| Resistor | $E = IR$ | $Z = R$ |
| Inductor | $V = LdI/dt$ | $Z = i\omega L$ |
| Capacitor | $I = CdV/dt$ | $Z = 1/i\omega C$ |

**Table 2.1 Impedance of common electrical elements**

When an electrochemical process is described as a RC element; i.e. a resistance and a capacitor in parallel, the impedance can then be expressed as:

$$\frac{1}{Z} = \sum_i \frac{1}{Z_i} = \frac{1}{R} + i\omega C \qquad [2.15]$$

Equation 2.15 can also be expressed as

$$Z = \left[\frac{1}{R} + i\omega C\right]^{-1} = \frac{R}{1+i\omega RC} \times \frac{1-i\omega RC}{1-i\omega RC} = \frac{R}{1+(\omega RC)^2} - \frac{i\omega R^2 C}{1+(\omega RC)^2} \qquad [2.15]$$

In the Nyquist plots there appear as many semicircles in the complex plane as electrochemical (RC) processes occur, being each RC process associated to a time constant ( $\tau$ ),

$$\tau = RC = \frac{1}{2\pi\nu} \qquad [2.16]$$

A Nyquist plot typically exhibits an arc at high frequency (e.g. 1 MHz to 4 kHz), a second arc at intermediate frequencies (e.g. 4 kHz to 25 Hz) and a linear portion at the lower frequencies (e.g. 25Hz to 0.1 Hz). Depending on the capacitance values associated with each of the arcs, these three regimes can correspond to the bulk, grain boundary and electrode response respectively. The magnitude of capacitance associated to a RC process allows discerning between processes occurring in the electrodes, grain boundaries, grain bulk or other processes as listed in table 2.2.

| Capacitance (F) | Phenomenon Responsible |
|---|---|
| $10^{-12}$ | Bulk |
| $10^{-11}$-$10^{-8}$ | Grain boundary |
| $10^{-10}$-$10^{-9}$ | Bulk ferroelectric |
| $10^{-9}$-$10^{-7}$ | Surface layer |
| $10^{-7}$-$10^{-5}$ | Sample-electrode interface |
| $10^{-4}$ | Electrochemical reactions |

**Table 2.2 Capacitance values and their possible interpretation[18].**

Often, the semicircles are not symmetric and show depressions due to deviations from the ideal situation. In these cases, a constant phase element (CPE) is introduced substituting the capacitance. CPE elements can be considered as an illustration of the frequency dispersion of the electrochemical

processes taking place in the sample. The impedance of a CPE can be expressed as:

$$Z_{CPE} = \frac{1}{C(i\omega)^{\alpha}} \qquad [2.18]$$

Where $\alpha$ is called the ionic correlation index and it takes values $0 \leq \alpha \leq 1$. For $\alpha = 1$ we have the ideal capacitor behaviour.

There are some other formalisms related to the impedance, used to study the electrical behaviour of materials such as the modulus function:

$$M=i\omega C_c Z=M'+iM'' \qquad [2.19]$$

In these expressions $C=\varepsilon_0 A_c/l$ is the capacitance of the empty measuring cell of electrode area $A_c$ and electrode separation length l. The quantity $\varepsilon_0$ is the dielectric permittivity of free space, $8.854 \times 10^{-12}$ F/m.

M is a very good complement to the impedance, because whilst the latter picks out the most resistive component, the first highlights the component with smallest capacitance.

M plots are especially helpful when the grain boundary responses are dominant and, sometimes, mask the responses of other electrochemical processes occurring at higher frequencies (bulk) in the impedance plots.

Values of conductivity corresponding to various electrochemical processes can be deduced from the interception of the arcs with the real axis in the Nyquist plots. In addition to the assignment of the RC processes to the different phenomena taking place in the sample, routinely examinations involve studies of the temperature dependence of the conductivity. Conductivity in semiconductors is sometimes explained in terms of the so-called hopping model for transport of species. In the case of semiconductors, it considers that the electrons are localised on individual atoms. They become mobile by 'hopping' to adjacent

atoms if they received sufficient energy, $E_a$ (activation energy). This is a thermally activated process, which can be expressed as:

$$\sigma T = \sigma_0 \exp(-\frac{E_a}{RT}) \qquad [2.20]$$

where $E_a$ is the activation energy and $\sigma_0$ is a factor related with the entropy and number of carries. Plotting log (σT) vs. 1/T straight lines are obtained, being the slope the activation energy for the process. This is called Arrhenius plot.

In the present work AC Impedance data were acquired using a 1260 Solartron impedance analyser typically over the frequency range 0.1 Hz- 1.0 MHz. Measurements were performed on dense pellets coated with organoplatinum paste on each face and fired afterwards at 900ºC for 20 minutes. The samples were mounted in a compression jig with Pt wire electrodes. The measurements were performed in a range of water and oxygen partial pressures (static air, wet and dry 5%$H_2$/Ar, wet and dry $O_2$).

ZView software package was used in this work.

### 2.2.9. Four terminal dc measurements

When the resistance due to the jig design is higher than the resistance of the studied material, the errors in the conductivity measurement from AC impedance spectroscopy become unacceptable large. In this case, four terminal DC measurements can be used to accurately determine the total conductivity, although it is not able to differentiate between conduction processes occurring at the bulk and grain boundaries as in the AC technique.

Four equally spaced Pt strips are adhered to one relatively thin pellet (~1mm) of the sintered sample. A known current is applied to the outer electrodes and the potential difference generated across the inner electrodes is measured, Figure 2.4. By Ohm's law, the relation between the current applied and the voltage

generated is equal to the resistance of the material. The data obtained are correlated to AC impedance data because our set-up is not the standard four-terminal arrangement where current is passed through the opposing faces of a bar and the voltage measured by two well separated electrodes on one length of the bar.

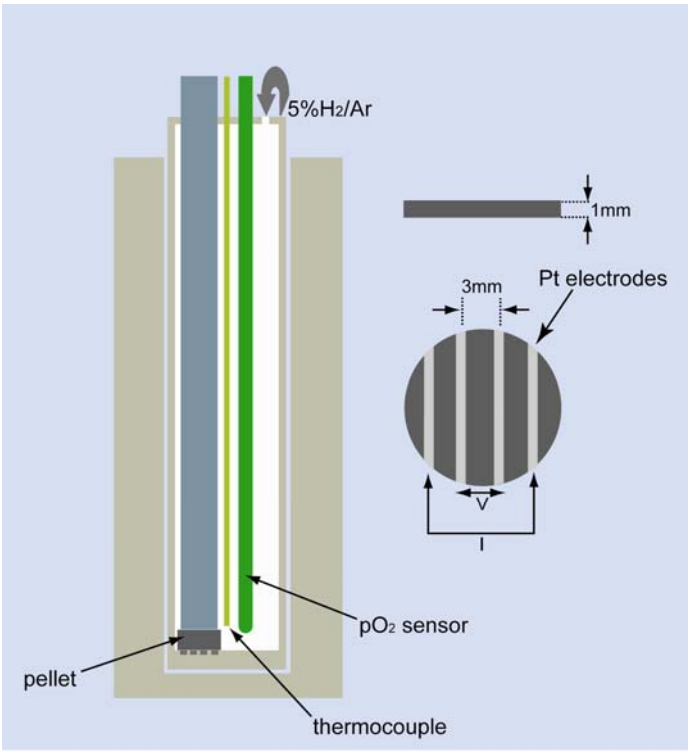


**Figure 2.4 Four terminal dc and $pO_2$ conductivity jig**

Our setup is the four-point collinear probe method and has a correction factor that needs to be applied based on the ratio of pellet thickness to probe separation and also the pellet diameter to probe size.[19] Rather than calculating the correction factor for each pellet it is easier to correct the four terminal conductivity using the accurate AC Impedance data already obtained. Correcting under resistive conditions with 2 terminal AC impedance spectroscopy calibrates the oxidised sample in air and yields a correction factor which can be applied at all conditions of $pO_2$ and temperature.

Unlike the more accurate standard setup, where the current is passed through the whole cross-sectional area and hence the entire volume of the sample, our set-up applies the current to the same surface of the pellet as the measuring electrodes, as is the case for the Van der Pauw method.[20] Such an experimental set-up is susceptible to errors from inhomogeneities due to problems with slow oxidation or reduction kinetics.

The $pO_2$ measurement we are using is essentially a transient technique where the $pO_2$ is always changing, if only slowly, and this difference between the interior and exterior of the pellet can potentially be a source of error.

In our experiments when a constant value of $pO_2$ (log $pO_2$=-20 atm) was reached the sample was kept there for 12-18 hours to achieve full reduction, essentially providing a second stationary measurement point in addition to the calibration point obtained in air. Then the hydrogen supply was stopped and the reoxidation step was recorded. Equilibration with atmosphere depends upon surface exchange and diffusivity. The slope of -1/4 obtained for the measurements is ideal for the expected defect condition:

$$O_x \rightarrow V_O^{\bullet\bullet} + 2e^- + \frac{1}{2}O_2$$

and demonstrates equilibration of the sample with the slowly changing $pO_2$ conditions in the chamber.

The dependence of conductivity upon oxygen partial pressure provides considerable information on the mechanism of conduction. For n-type conduction, conductivity typically decreases with increasing $pO_2$. For p-type conduction conductivity typically increases with increasing $pO_2$ and for ionic conductivity there is no change in conductivity with $pO_2$.

### 2.2.10. Fuel Cell Tests

The anode response was investigated on a 3-electrode setup, Figure 2.5, using 20mm diameter YSZ pellets (2mm thick) as electrolyte, LSM (Praxair) as cathode material and $La_4Sr_8Ti_{12-n}Mn_nO_{38-\delta}$ as anode. The anode was prepared by coating a layer of $La_4Sr_8Ti_{12-n}Mn_nO_{38-\delta}$-based slurry onto the electrolyte pellets. Au mesh was used as current collector. The resulting specimen was fired then at 950ºC for several hours in flowing 5%$H_2$/Ar to achieve full reduction of the anode material.

The impedance of the electrochemical cell was recorded in the range 950-850°C at open circuit voltage (OCV) and at different atmospheres with 20mV as ac signal amplitude in the $1\times10^5$ ~ 0.01Hz frequency domain. Humidified 5%$H_2$ in Ar, 100% $H_2$ and 100% $CH_4$ were used as the fuel at the working electrode, $O_2$ being supplied at the counter electrode. The fuel cell performance was recorded by cyclic-voltammetry at a scan rate of 1mV$s^{-1}$.

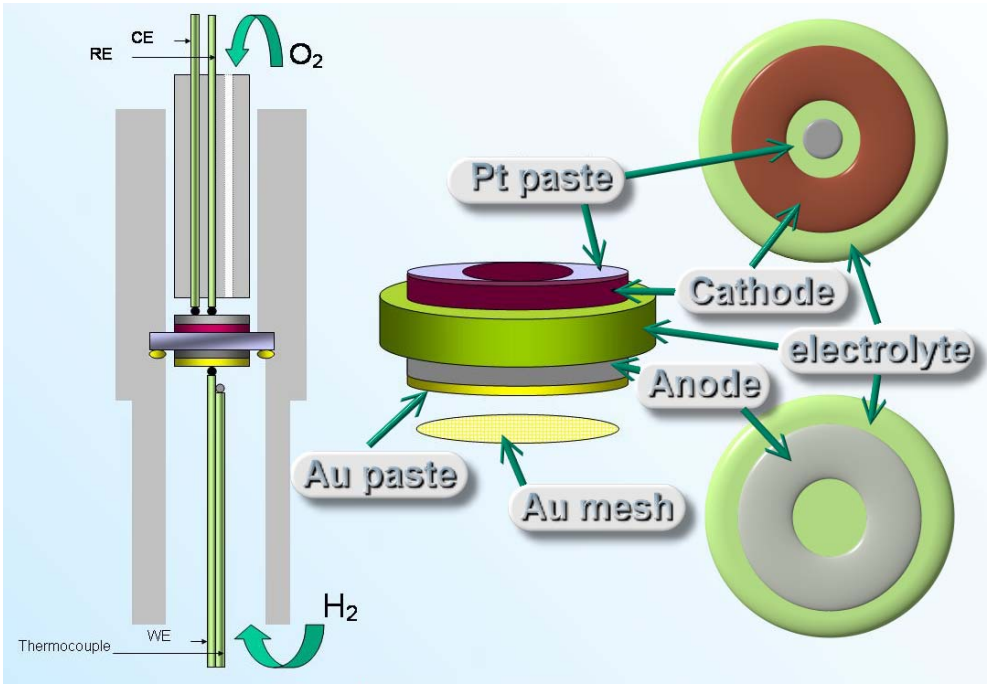


**Figure 2.5 Three-electrode arrangement of the electrochemical cell.**

## 2.3. References


[1] C. Kittel, 'Introduction to Solid State Physics', John Wiley & Sons, 1996.

[2] B. D. Cullity, 'Elements of X-Ray Diffraction', Addison-Wesley, 1967.

[3] A. R. West, 'Basic Solid State Chemistry', John Wiley & Sons Ltd, 2004.

[4] W. Friedrich, P. Knipping, and M. v. Laue, *Sitzungsberichte der Königlich Bayerischen Akademie der Wissenschaften zu München* 1912, 303–22.

[5] W. L. Bragg, *Proc. Camb. Phil. Soc.*, 1913, **17**, 43–58.

[6] C. R. Brundle, J. Charles A. Evans, and S. Wihon, 'Encyclopedia of Materials Characterisation. Surfaces, Interfaces, Thin Films', B-H, 1992.

[7] R. I. Smith, 'Introduction to Neutron Diffraction', ISIS Facility, Rutherford Appleton Laboratory, UK, 2004.

[8] D.P.Mitchell and P.N.Powers, *Physical Review*, 1936, **50**, 486.

[9] J. Rietveld, *Appl. Cryst.*, 1969, **2**, 65.

[10] A. C. Larson and R. B. von Dreele, *GSAS program; Los Alamos National Lab. Rep. No. LA-UR-86748*, 1994.

[11] J. Canales-Vazquez, 'Studies on oxygen excess perovskite-based titanates for SOFC fuel electrodes', PhD thesis, St Andrews, 2003.

[12] www.aacg.bham.ac.uk.

[13] P. V. Pavlov and A. F. Jojlov, 'Física del Estado Sólido', Mir, 1992.

[14] H. Rickert, 'Electrochemical of Solids', Springer-Verlag, 1982.

[15] J. R. Macdonald and E. Barsoukov, 'Impedance Spectroscopy Theory, Experiment and Applications', John Wiley & Sons, 2005.

[16] Gamry-Instruments, in 'Introduction to Electrochemical Impedance Spectroscopy ', 2005.

[17] Agilent-Technologies, in 'Impedance Measurement Handbook', 2003.

[18] J. Irvine, D. Sinclair, and A. West, *Advanced Materials*, 1990, **2**, 132.

[19] 'Low Level Measurements Handbook, Keithley Instruments', 2004.

[20] L. J. Van der Pauw, *Philips Res. Repts.*, 1958, **13**, 1.

# 3

# Structural characterisation

## 3.1. Introduction

$La_4Sr_8Ti_{12}O_{38}$ is the lowest n XRD cubic phase of the $La_4Sr_{n-4}Ti_nO_{3n+2}$ series; lower values of n show extended defects in HRTEM and additional peaks in XRD[1]. The cubic phases have some extra oxygen that is thought to be accommodated in short range linear defects distributed randomly within a perovskite network [1-5]. Such linear defects seem to cause superstructure reflections doubling the $<111>_p$, rendering a face centred cubic unit cell with $a=2a_p$. Previous work has shown that the substitution of Ti by lower valence cations (i.e. Sc or Ga ) does not significantly affect the structure, which remains as XRD cubic ($a\approx3.91$ Å), which is not surprising as such substitution reduces the nominal oxygen excess increasing the destabilisation of any extended oxygen defects. For Mn substitution, there are some questions relating to the oxidation state of Mn in these phases. Assuming that Mn was likely to be $Mn^{+3}$, two different approaches to solve this particular problem were considered. In the first, the La/Sr ratio was maintained giving rise to the $La_4Sr_8Ti_{12-n}Mn_nO_{38-n/2}$ series, whilst in the latter the oxygen overstoichiometry was fixed by changing the La/Sr ratio to compensate the Ti/Mn, i.e. giving rise to the $La_{4+n}Sr_{8-n}Ti_{12-n}Mn_nO_{38}$ series. Therefore if Mn remains in the 3+ oxidation state of the starting material, the resulting phases will all lie within the cubic domain. Alternatively, if Mn was in the +4 oxidation state, phases in the regime attempting to compensate by varying the $La_{4+n}Sr_{8-n}Ti_{12-n}Mn_nO_{38}$ La/Sr ratio, *i.e.* $La_{4+n}Sr_{8-n}Ti_{12-n}Mn_nO_{38+n}$ will move into the layered domain. XRD studies show

that for as prepared samples there is $Mn^{+4}$ at least to some extent, as the phases belonging to the $La_{4+n}Sr_{8-n}Ti_{12-n}Mn_nO_{38}$ series revealed the presence of reflections at $2\theta$ 28-31º, which are characteristic of layered domains. Additionally preliminary TEM studies have corroborated the presence of layered domains in these phases. As such layers appear to have a large negative effect on the electrochemical properties only a few compounds of these series have been characterised.

## 3.2. Studies on the series $La_{4+n}Sr_{8-n}Ti_{12-n}Mn_nO_{38}$

### 3.2.1. Synthesis preparation

Preparation of the samples was carried out using the traditional ceramic route described in section 2.1 at 1350ºC for the samples n=1 and n=2, yielding dark grey pellets. We have doped $La_4Sr_8Ti_{12}O_{38}$ with manganese on the B-site attempting to maintain the content of oxygen constant to obtain the series $La_{4+n}Sr_{8-n}(Ti_{12-n}Mn_n)O_{38}$ in the substitution given in the relation:

$$Sr^{2+} + Ti^{4+} \rightarrow La^{3+} + Mn^{3+} \qquad [3.1]$$

Using Kröger-Vink notation:

$$Sr_{Sr}^{x} + Ti_{Ti}^{x} \rightarrow La_{Sr}^{\bullet} + Mn_{Ti}' \qquad [3.2]$$

We are considering that all the Mn present is in the oxidation state 3+.

### 3.2.2. XRD results

In agreement with literature data[6] the XRD pattern of the $La_4Sr_8Ti_{12}O_{38}$ (n=0) shows a simple cubic perovskite unit cell, space group Pm-3m and a value of a=3.9114(8) Å. The XRD patterns of the $La_{4+n}Sr_{8-n}Ti_{12-n}Mn_nO_{38}$ series (n=1, 2) show some extra peaks when comparing with the sample without manganese, Figure 3.1. The presence of the extra peaks appears to indicate layered domains in the structure of the samples as has been reported before in the

literature[6, 7]. According to literature[7], layered domains provoke a decrease in the conductivity. Due to this only two samples (n=1 and 2) of the series have been characterised.

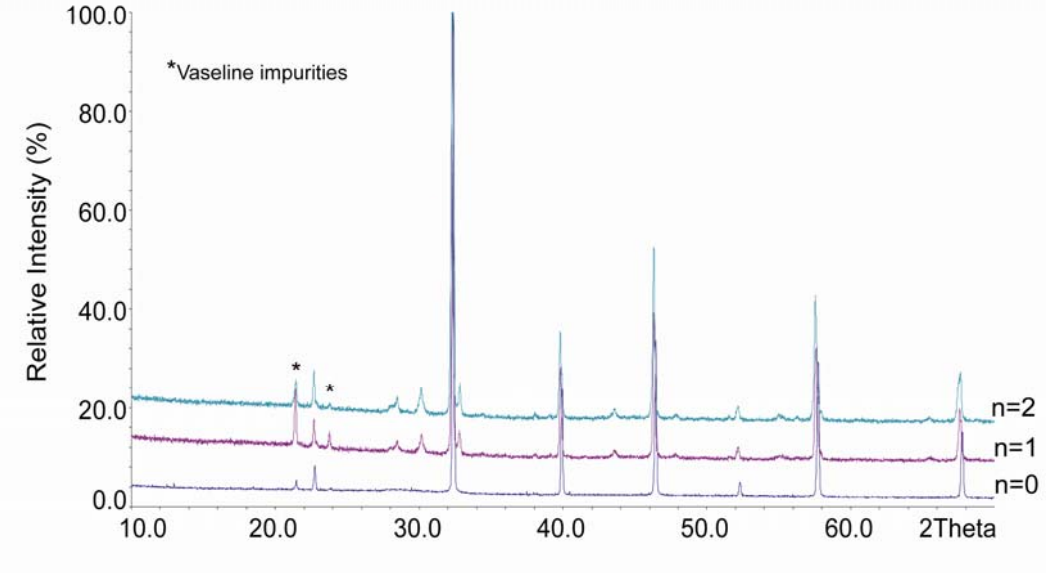


**Figure 3.1 XRD patterns for the series $La_{4+n}Sr_{8-n}Ti_{12-n}Mn_nO_{38}$ where it is possible to observe the presence of reflections at 2θ 28-31º, which are characteristic of layered domains.**

This seems to indicate that at least some Mn exists as $Mn^{4+}$ in the lattice. TGA and TEM studies can give us complementary information about this issue.

### 3.2.3. TGA

TGA experiments were performed during the oxidation at 900ºC in air of a pre-reduced sample as described in section 2.3. From the % of weight regained for each compound it is possible to estimate approximately the amount of oxygen that has been removed during the reduction, Figure 3.2 and Table 3.1. There we can observe that there is a change of about 0.04 oxygen atoms per formula unit for n=0. This result indicates[1] that the oxidized phase for n=0 is essentially $Ti^{+4}$. For n=1 ($La_5Sr_7Ti_{11}Mn_1O_{38}$) and n=2 ($La_6Sr_6Ti_{10}Mn_2O_{38}$) we have found a change

of 0.03 and 0.06 oxygen atoms per formula unit respectively. These values are just a little less than those expected for a change in manganese oxidation state of 1 unit. Nevertheless there is some manganese as $Mn^{+4}$ in the oxidized samples.

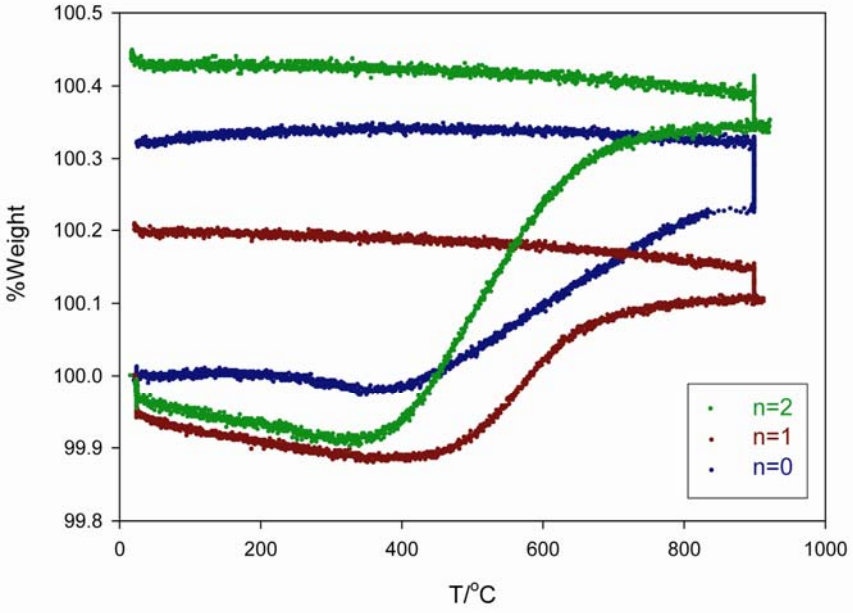


**Figure 3.2 TGA during oxidation of the pre-reduced samples n=0, 1 and 2**

| n | Nominal Oxidised Stoichiometry | $\Delta\delta$ |
|---|---|---|
| 0 | $La_{1/3}Sr_{2/3}TiO_{3.167}$ | -0.04 |
| 1 | $La_{0.42}Sr_{0.58}Ti_{0.92}Mn_{0.08}O_{3.167}$ | -0.03 |
| 2 | $La_{0.5}Sr_{0.5}Ti_{0.83}Mn_{0.17}O_{3.167}$ | -0.06 |

**Table 3.1 Stoichiometry of the oxidised phases and amount of oxygen loss per unit formula.**

### 3.2.4. TEM studies

Some preliminary TEM studies have been performed on n=1. In these studies the main objective was to check if the layered structure expected after the XRD and TGA results is present. Figure 3.3 shows that there is a layered domain in the structure.

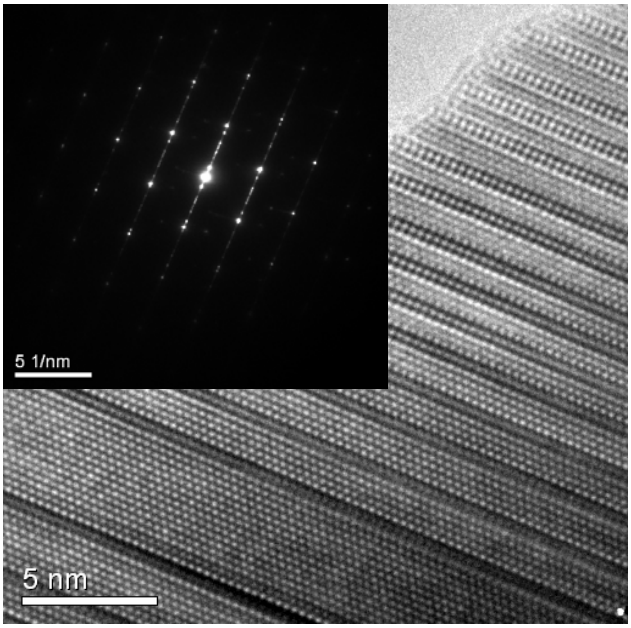


**Figure 3.3 SAED pattern and the corresponding HRTEM image showing the crystallographic shears for $La_5Sr_7Ti_{11}Mn_1O_{38}$ (n=1).**

In Figure 3.4 we can observe HRTEM images showing the presence of layered domains cohabiting with perovskite domains. We can appreciate an irregular intergrowth of layered and cubic domains. Meanwhile in Figure 3.5 we can observe a cubic domain.

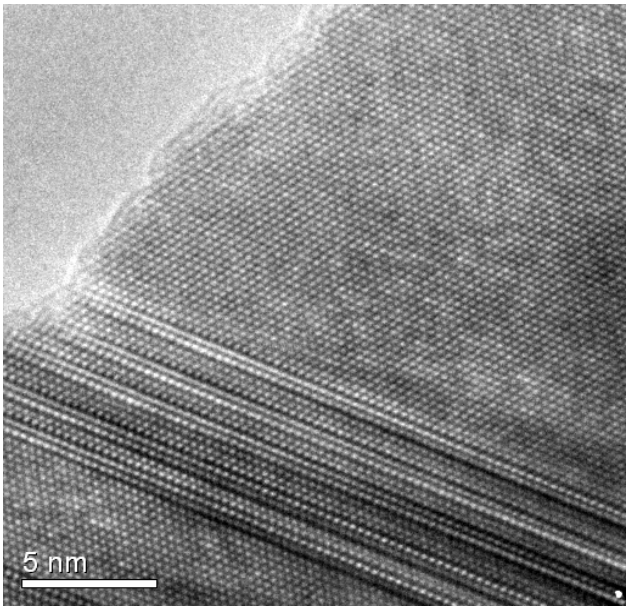


**Figure 3.4 HRTEM image showing the intergrowth of layered and cubic domains**

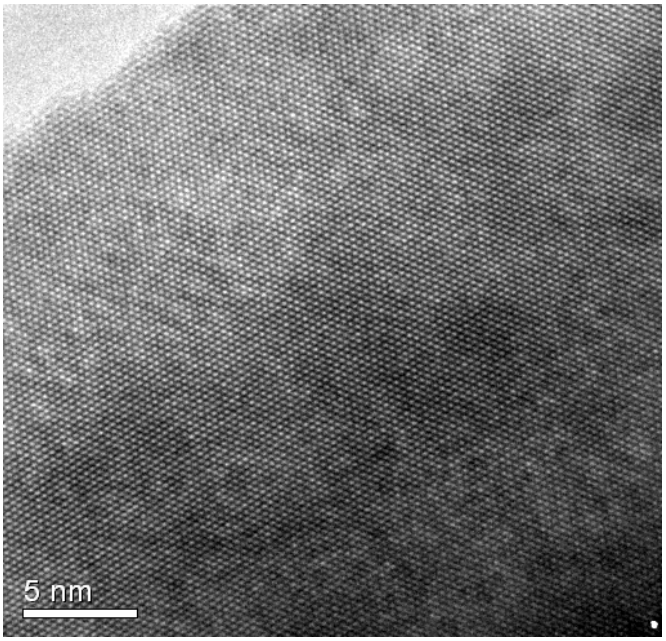


**Figure 3.5 HRTEM image showing a cubic domain for $La_5Sr_7Ti_{11}Mn_1O_{38}$ (n=1).**

## 3.3. Studies on the series $La_4Sr_8Ti_{12-n}Mn_nO_{38-\delta}$

### 3.3.1. Synthesis preparation

Preparation of the samples was carried out using the traditional ceramic route described in section 2.1. The replacement of $Ti^{+4}$ by $Mn^{+3}$ in the B-site would force the removal of oxygen from the structure in order to maintain the electroneutrality in the crystal, thus creating local oxygen vacancies that might favour ionic transport. The ionic radius of $Mn^{+3}$ is 0.645 Å which is similar to the $Ti^{+4}$ ionic radius (0.605 Å).

That leads to the series $La_4Sr_8Ti_{12-n}Mn_nO_{38-\delta}$, where $\delta = n/2$. Thus, the excess oxygen should be reduced gradually with increasing the amount of manganese.

The synthesis was realized at two different temperatures, 1350ºC and 1400ºC, yielding dark grey pellets. It has been observed that synthesis at the higher temperature produces denser and less fragile pellets. So all the structural and electrochemical tests realized in the present work have been done on samples synthesised at 1400ºC.

### 3.3.2. XRD and Neutron Diffraction results

As it was said in section 3.2.2 the XRD pattern for $La_4Sr_8Ti_{12}O_{38}$ (n=0) shows a simple cubic perovskite unit cell, space group Pm-3m and a value of a=3.9114(8) Å, Figure 3.5 and Table 3.2.

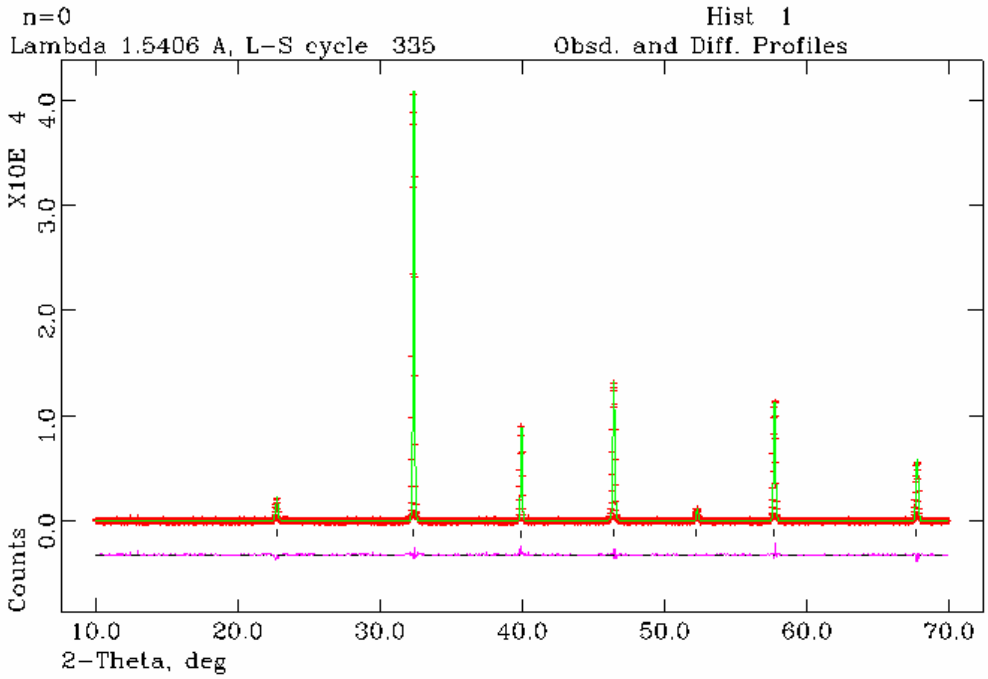


**Figure 3.5 Observed (red), calculated (green) and difference (bottom) XRD pattern for $La_4Sr_8Ti_{12}O_{38}$ (n=0) at room temperature (RT).**

| n=0 | RT |
|---|---|
| a/Å | 3.9114(8) |
| V/Å$^3$ | 59.84(5) |
| Discrepancy factors | |
| $R_{wp}$ (%) | 3.94 |
| $R_p$ (%) | 2.82 |
| $R_F$ (%) | 2.67 |
| $\chi^2$ | 2.137 |

Space group Pm-3m. Atomic positions are 6(a) (0, 0, 0) for La/Sr; 6(b) (1/2, 1/2, 1/2) for Mn/Ti; 18(e) (0, 1/2, 1/2) for O.

**Table 3.2 Refined XRD data for $La_4Sr_8Ti_{12}O_{38}$ (n=0) at room temperature.**

Manganese substitution provokes a splitting in the XRD peaks. This splitting becomes more pronounced as Mn substitution increases (Figures 3.5 and 3.6).

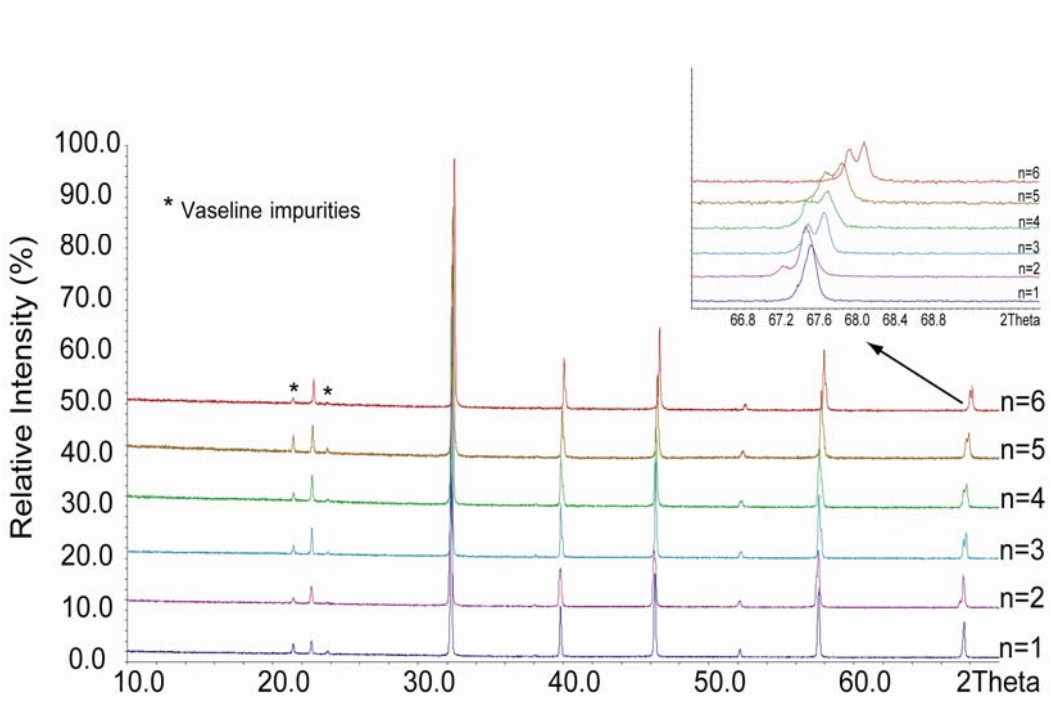


**Figure 3.5 Increased splitting of XRD peaks as degree of Mn substitution in $La_4Sr_8Ti_{12-n}Mn_nO_{38-\delta}$ increases.**

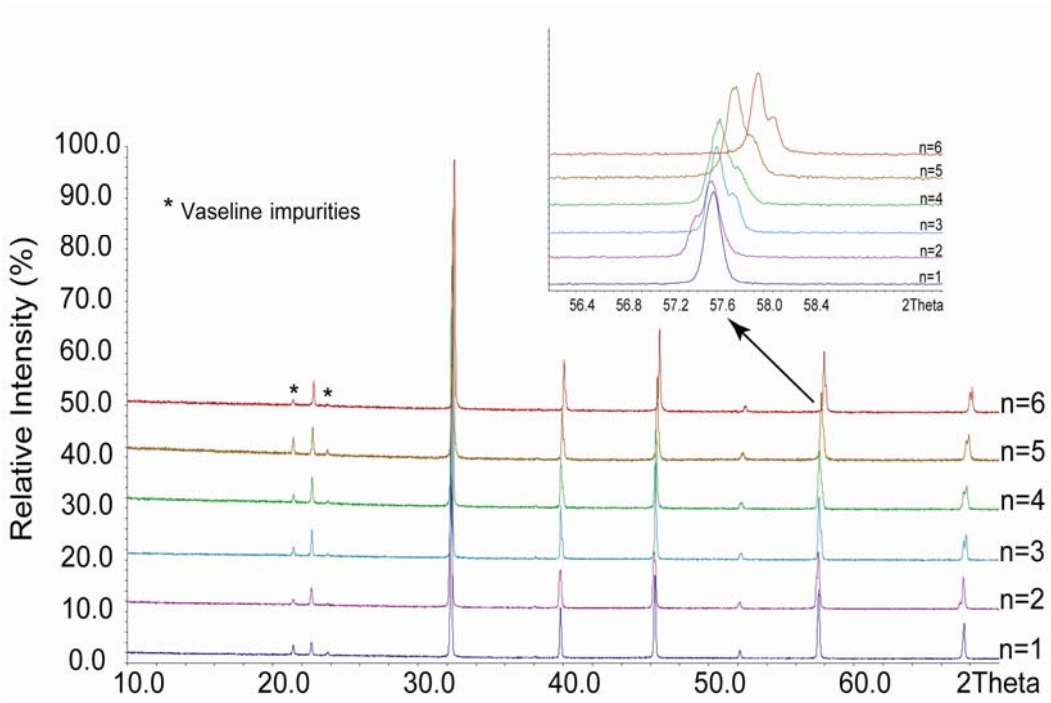


**Figure 3.6 Increased splitting of XRD peaks as degree of Mn substitution in $La_4Sr_8Ti_{12-n}Mn_nO_{38-\delta}$ increases.**

Although these phases still exhibit simple perovskite XRD patterns, they no longer exhibit the simplest cubic form as we will observe in the next sections.

### 3.3.2.1. $La_4Sr_8Ti_{11}MnO_{38-\delta}$ (n=1)

Even at low levels of Mn substitution the combined HRPD and XRD patterns could be better refined as a rhombohedral structure (R−3c), Figures 3.7 and 3.8. Although there is additional oxygen in these compounds we have refined to $ABO_3$ occupations because that oxygen is randomly distributed and not observable in the average structure. The final Rietveld disagreement factors and the refined atomic positions are given in the Table 3.3. Rietveld refinements were carried out using GSAS.[8]

Rhombohedral distortions are common in perovskite manganites and cobaltites and can be ascribed to the R-3c space group as the result of equivalent antiphase octahedra tilting along all the three crystallographic axes, i.e. $a^-a^-a^-$ following Glazier's notation [9].

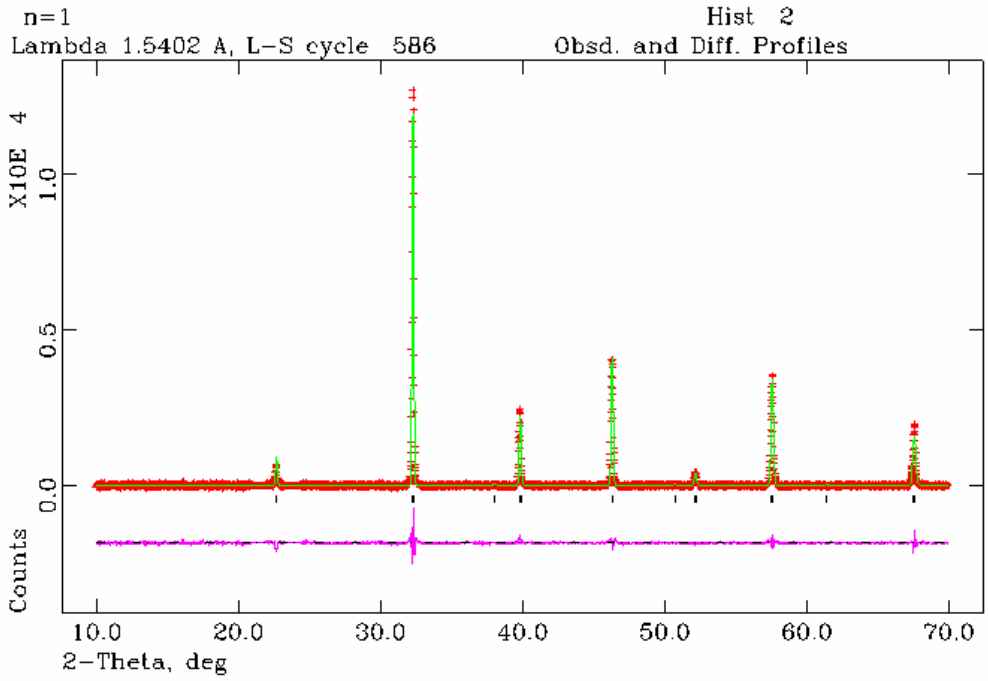


**Figure 3.7 Observed (red), calculated (green) and difference (bottom) XRD pattern for $La_4Sr_8Ti_{11}MnO_{38}$ (n=1) at room temperature.**

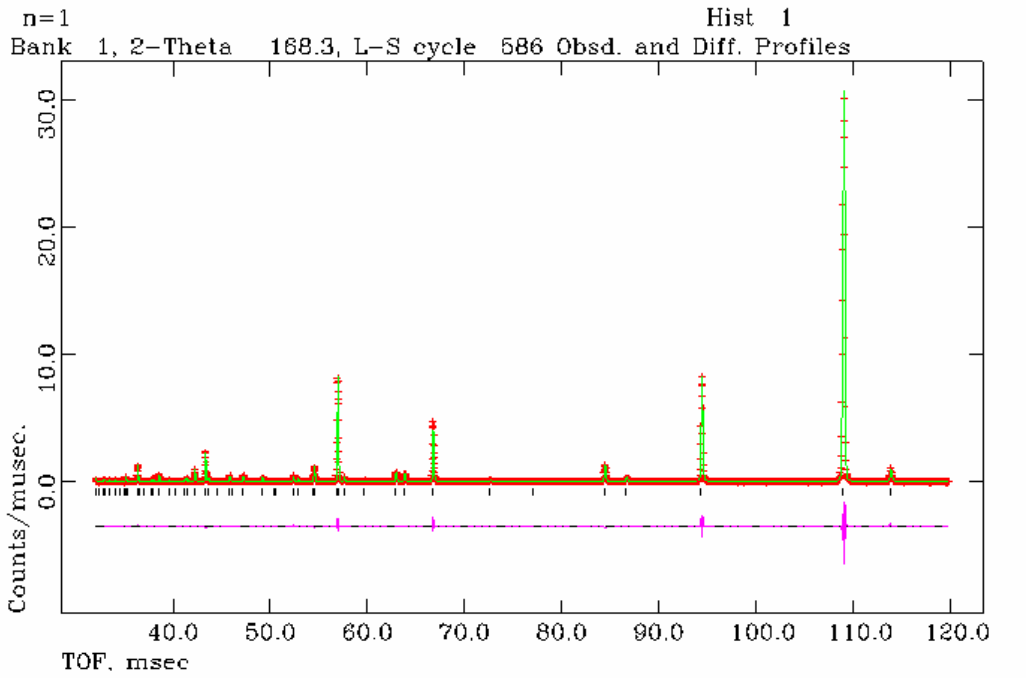


**Figure 3.8 Observed (red), calculated (green) and difference (bottom) HRPD pattern for $La_4Sr_8Ti_{11}MnO_{38}$ (n=1) at room temperature.**

| n=1 | RT |
|---|---|
| a/Å | 5.5458(6) |
| c/Å | 13.5648(1) |
| V/Å$^3$ | 361.31(2) |
| x(O) | 0.4737(1) |
| Discrepancy factors | |
| $R_{wp}^X$ / $R_{wp}^N$ (%) | 5.32/7.41 |
| $R_p^X$ / $R_p^N$ (%) | 4.00/6.29 |
| $R_F^X$ / $R_F^N$ (%) | 2.86/2.23 |
| $\chi^2$ | 2.448 |

Space group R-3c. The atomic positions are 6(a) (0, 0, 1/4) for La/Sr; 6(b) (0, 0, 0) for Mn/Ti; 18(e) (x, 0, 1/4) for O.

**Table 3.3 Refined structural parameters for R-3c $La_4Sr_8Ti_{11}MnO_{38-\delta}$ after Rietveld refinements using combined HRPD and XRD data at room temperature (RT)**

In Figure 3.9 we can observe the XRD patterns for n=1 as prepared and in reducing conditions (after 48 hours in 5%$H_2$/Ar). No colour changes were observed in the reduced samples. There are no significance changes in the structure, Table 3.4, and the reduced phase can be indexed as a rhombohedral structure (R−3c). The volume of the unit cell increases in reducing conditions.

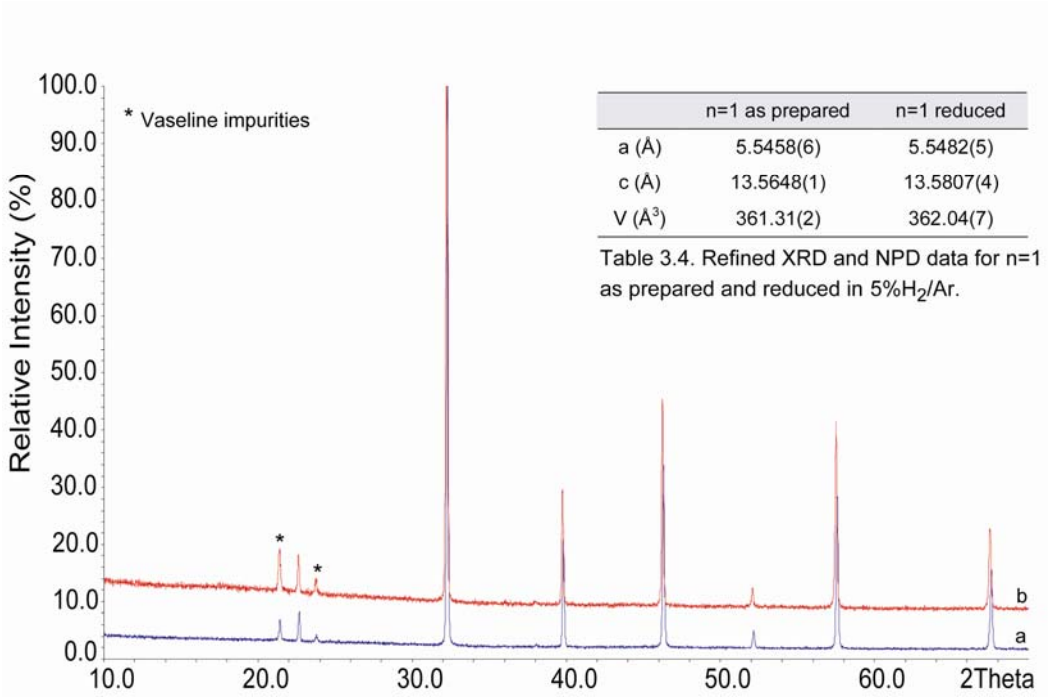


| | n=1 as prepared | n=1 reduced |
|---|---|---|
| a (Å) | 5.5458(6) | 5.5482(5) |
| c (Å) | 13.5648(1) | 13.5807(4) |
| V (Å$^3$) | 361.31(2) | 362.04(7) |

Table 3.4. Refined XRD and NPD data for n=1 as prepared and reduced in 5%$H_2$/Ar.

**Figure 3.9 XRD patterns for $La_4Sr_8Ti_{11}MnO_{38}$ (a) as prepared in oxidising conditions and (b) reduced in 5%$H_2$/Ar at 900$^0$C for 48h. Both phases were indexed as a rhombohedral structure.**

There were some concerns about the stability of the sample with time. To check that we kept an amount of sample n=1 in air at 900$^0$C for 28 days. After this period of time the sample was cooled down to room temperature. No visible changes were observed after this period of time. Figure 3.10 shows the XRD patterns for the sample the same day it was prepared and after 28 days in air at 900$^0$C. The GSAS refinement of these XRD patterns gave exactly the same cell parameters for both samples.

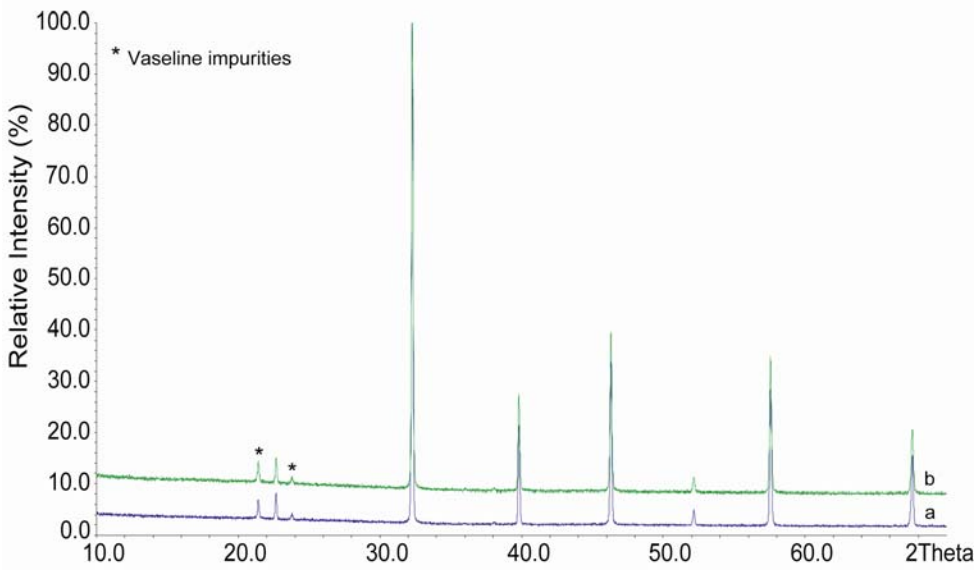


**Figure 3.10 XRD patterns for n=1 (a) as prepared, (b) after 28 days in air at 900$^0$C.**

Conductivity measurements in air and $H_2$ (Chapter 4) suggest a phase transition as the temperature increases. These electrical studies show evidence of metal/insulator transitions. In order to correlate phase transformations with these changes in electrical properties we carried out in situ neutron powder diffraction in air at different temperatures (RT, 100, 300, 500, 700 and 900$^o$C), Figure 3.11.

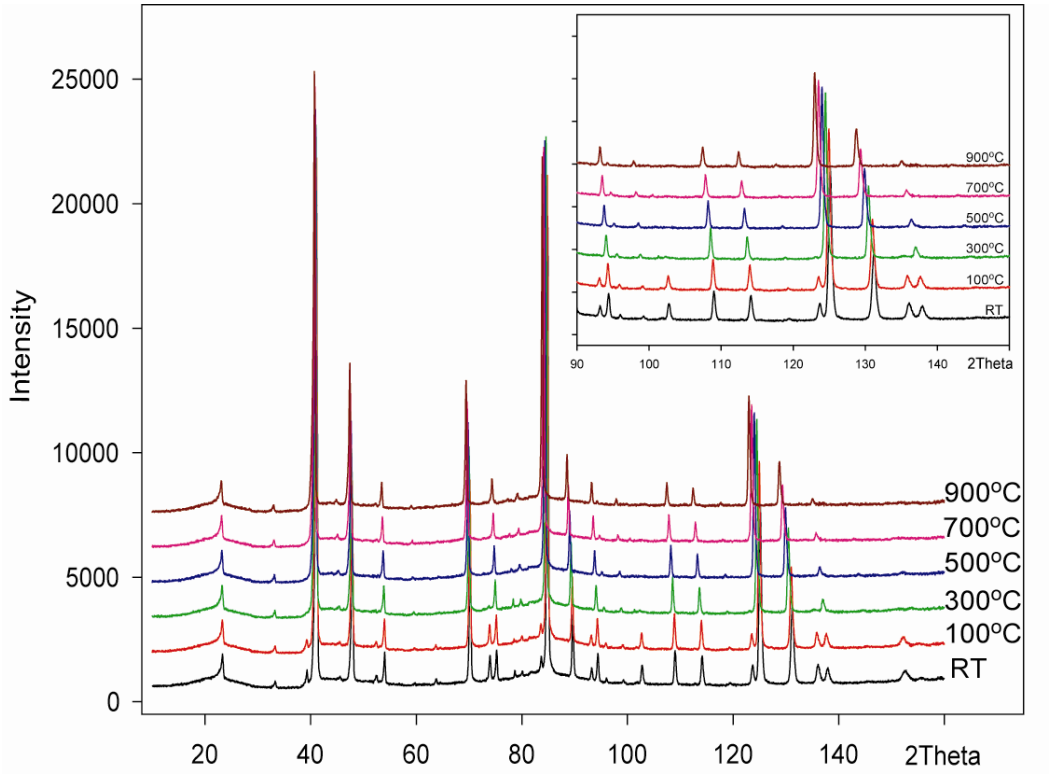


**Figure 3.11 NPD patterns for $La_4Sr_8Ti_{11}MnO_{38-\delta}$ in air at different temperatures.**

Constant wavelength NPD data were collected on the D2B high resolution diffractometer at the Institut Laue Langevin (ILL) in Grenoble, France. The sample was loaded in a quartz tube. The details of the data collections are presented in Figure 3.13 and Table 3.5. The structural data have been obtained from the NPD Rietveld refinements[10] by using the GSAS suite of programs[8].

Figure 3.11 shows the changes in the neutron diffraction pattern corresponding to a change in lattice symmetry as a function of temperature. At room temperature (RT) the structure was refined using the rhombohedral space group R-3c. At 100°C the structure remains in the same symmetry and space group. Only small changes in the refinement parameters are observed.

At 300°C the best fitting was achieved with combined rhombohedral (R-3c) and cubic structures (Pm-3m). The refined fractions for the cubic and rhombohedral phases are 89.5 % and 10.5% respectively. According to the group-subgroup relationships among the perovskite structures, the next possible higher symmetry after R-3c would be Pm-3m.[11]

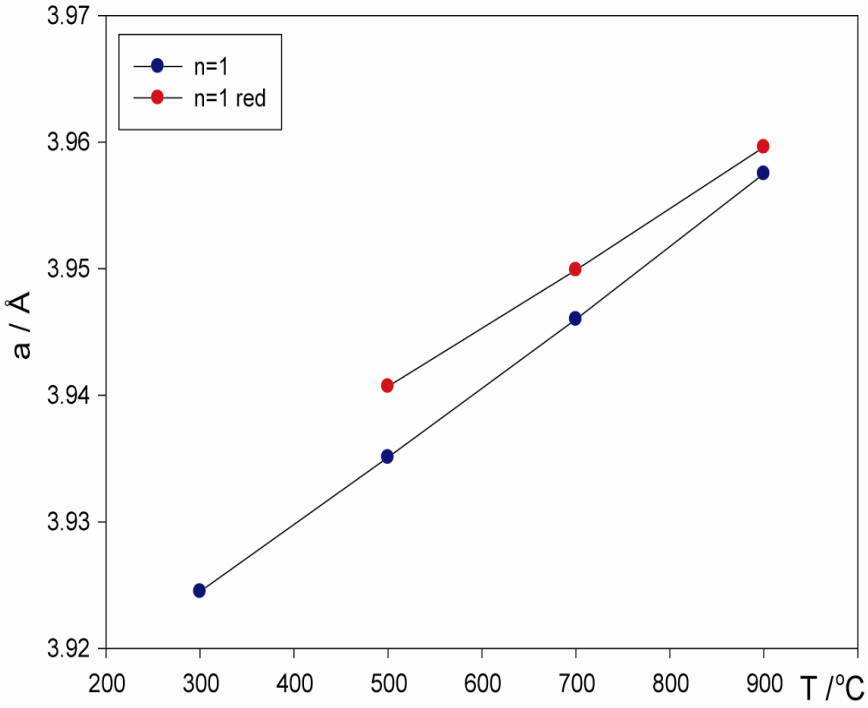


**Figure 3.12 Evolution of the unit cell parameter versus temperature in the cubic phases for n=1 in air and n=1 pre-reduced in 5%$H_2$ in Ar.**

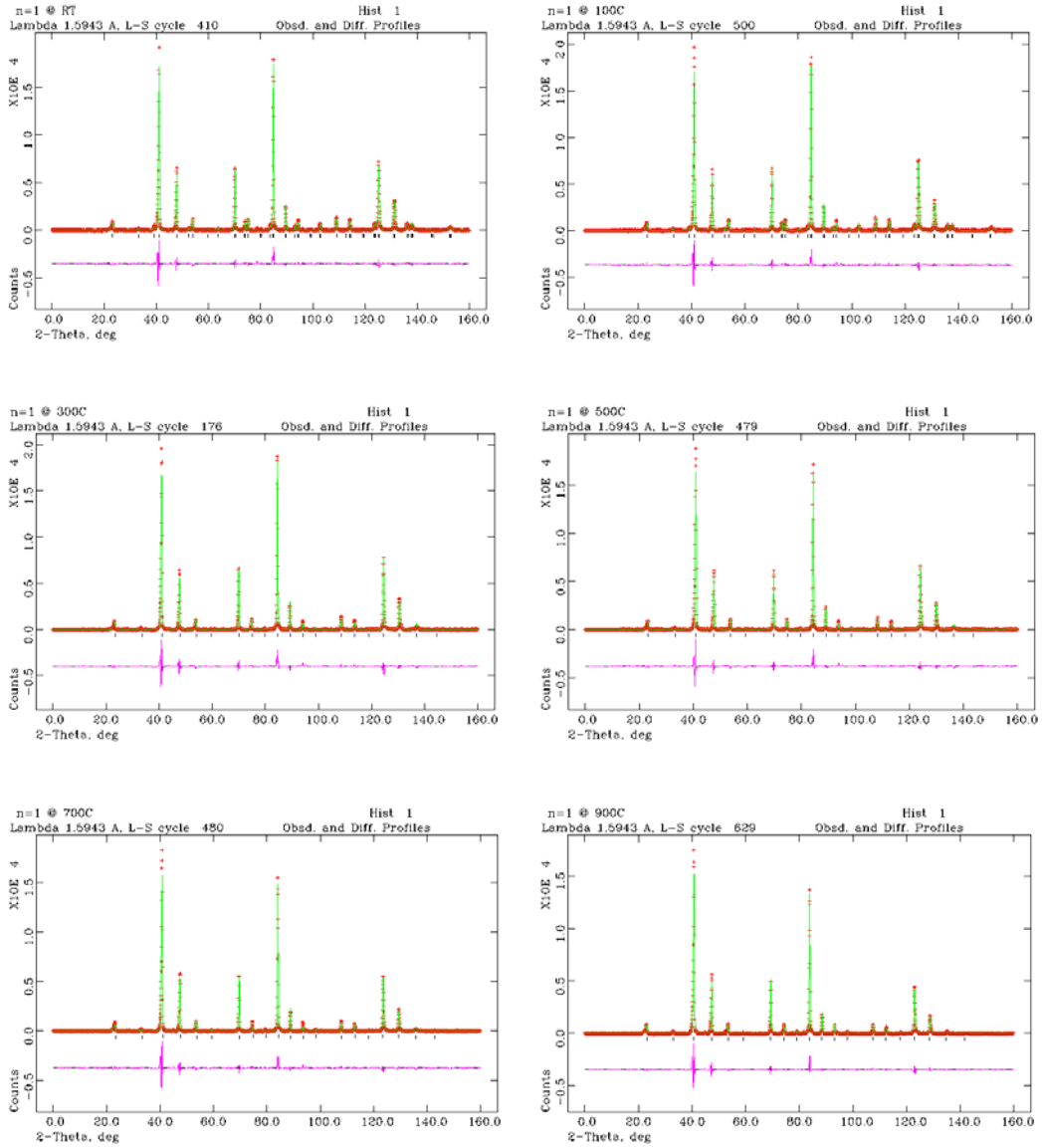


**Figure 3.13 Observed (red), calculated (green) and difference (bottom) neutron powder patterns for $La_4Sr_8Ti_{11}MnO_{38}$ (n=1) in air at different temperatures.**

The unit cell parameter of the cubic unit cell is a=3.9285(8) Å and the volume is 60.62(6) $Å^3$ at 300°C, meanwhile for the rhombohedral phase the parameters obtained are slightly higher that the ones calculated for 100°C.

From 500°C to 900°C the structure remains in the cubic symmetry and space group Pm-3m. The cell parameter increases continuously in the whole temperature range investigated, Figure 3.12. At 900°C the a value of the unit cell is 3.9575(2) Å and the volume is 61.98(3) $Å^3$.

**Table 3.5 Structural parameters extracted from refinement of NPD data for the compound $La_4Sr_8Ti_{11}MnO_{38-\delta}$ (n=1) in air at different temperatures**

| | n=1 in air | | | | | | |
|---|---|---|---|---|---|---|---|
| | RT | 100°C | 300°C | | 500°C | 700°C | 900°C |
| **Crystal system** | Rhombohedral | Rhombohedral | Rhombohedral | Cubic | Cubic | Cubic | Cubic |
| **Space group** | R-3c | R-3c | R-3c | Pm-3m | Pm-3m | Pm-3m | Pm-3m |
| a (Å) | 5.5383(4) | 5.5423(2) | 5.5556(2) | 3.9245(3) | 3.9351(9) | 3.9460(7) | 3.9575(2) |
| c (Å) | 13.5523(3) | 13.5669(5) | 13.5878(7) | 3.9245(3) | 3.9351(9) | 3.9460(7) | 3.9575(2) |
| Volume ($Å^3$) | 360.00(1) | 360.90(9) | 363.20(2) | 60.44(3) | 60.94(0) | 61.44(6) | 61.98(3) |
| O (x) | 0.4765(1) | 0.4789(4) | 0.4859(1) | 0.5 | 0.5 | 0.5 | 0.5 |
| **Isotropic temperature factors; $U_{iso}$x100/$Å^2$** | | | | | | | |
| La | 0.951(11) | 1.579(12) | 0.208(23) | 1.198(05) | 1.180(96) | 2.007(23) | 3.138(62) |
| Sr | 0.685(51) | 0.763(50) | 0.228(14) | 1.708(71) | 2.715(78) | 2.653(81) | 2.624(83) |
| Ti | 0.483(59) | 0.324(55) | 0.127(27) | 0.261(60) | 0.588(60) | 0.901(68) | 1.165(75) |
| Mn | 0.108(07) | 1.049(70) | 1.148(07) | 1.190(04) | 0.226(68) | 0.423(76) | 1.171(25) |
| O | 1.192(24) | 1.401(25) | 1.523(13) | 1.186(28) | 2.091(28) | 2.613(31) | 3.027(34) |
| **Occupancies** | | | | | | | |
| La | 0.3330 | 0.3330 | 0.3330 | 0.3330 | 0.3330 | 0.3330 | 0.3330 |
| Sr | 0.6670 | 0.6670 | 0.6670 | 0.6670 | 0.6670 | 0.6670 | 0.6670 |
| Ti | 0.9200 | 0.9200 | 0.9200 | 0.9200 | 0.9200 | 0.9200 | 0.9200 |
| Mn | 0,0800 | 0.0800 | 0.0800 | 0.0800 | 0.0800 | 0.0800 | 0.0800 |
| O | 1.00 | 1.00 | 1.00 | 1.00 | 1.00 | 1.00 | 1.00 |
| **R-factors** | | | | | | | |
| $R_{wp}$ (%) | 6.60 | 6.61 | 4.28 | | 6.55 | 6.29 | 5.84 |
| $R_p$ (%) | 4.25 | 4.22 | 3.14 | | 4.13 | 3.86 | 3.48 |
| $R_F$ (%) | 1.92 | 2.04 | 2.31 | | 1.93 | 2.10 | 1.80 |
| $\chi^2$ (%) | 4.544 | 4.539 | 1.901 | | 4.499 | 4.201 | 3.652 |

The same kind of thermal neutron powder diffraction studies have been realized for a pre-reduced sample in 5%$H_2$ in Ar for 48 hours, Figures 3.14 and 3.15. The sample was loaded in a vanadium can.

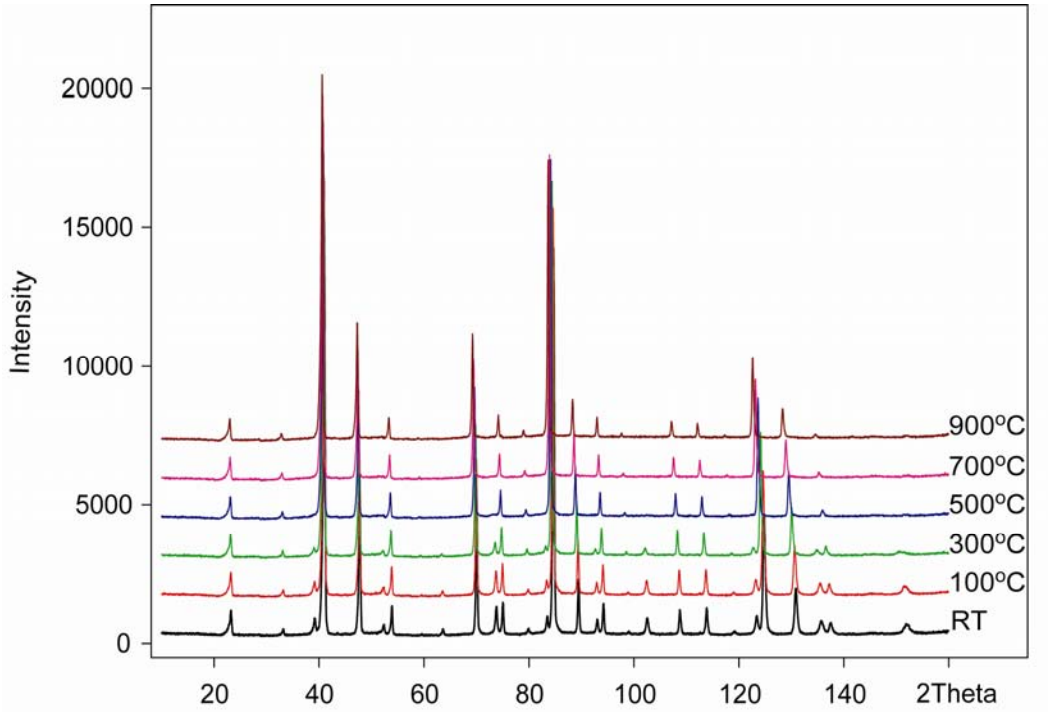


**Figure 3.14 NPD patterns for the reduced n=1 sample at different temperatures.**

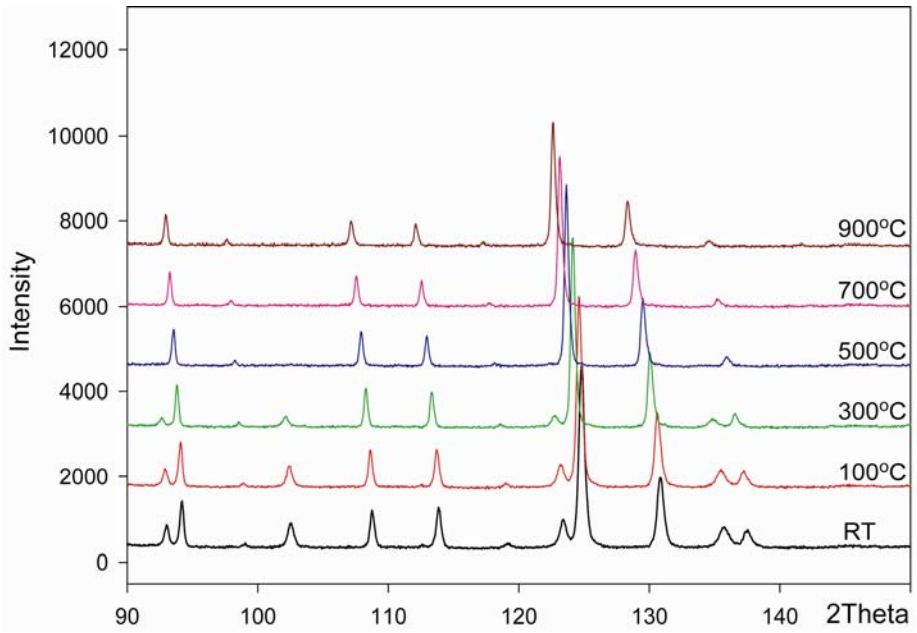


**Figure 3.15 Detail of the NPD patterns for the reduced n=1 sample at different temperatures. At temperatures above 300°C some peaks disappear.**

Figure 3.13 and Figure 3.14 show the changes in the neutron diffraction pattern corresponding to a change in the lattice symmetry as a function of temperature. For the reduced sample that changes occurs at higher temperature i.e., 500°C. A summary of structure parameters, isotropic temperature factors, occupancies and R-factors, obtained at different temperatures are presented in Table 3.6. The cubic cell parameter increases continuously in the whole temperature range investigated, Figure 3.12.

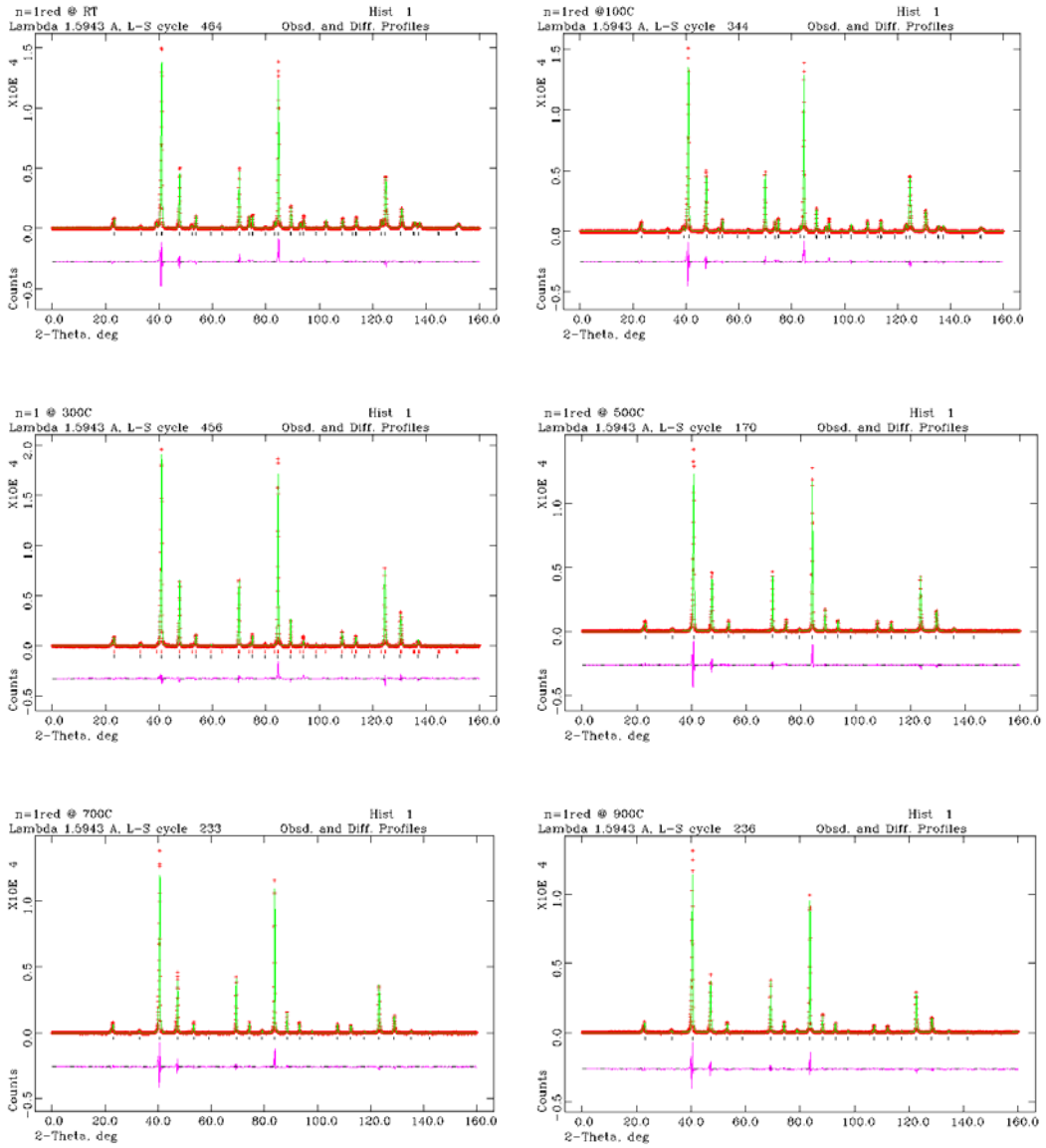


**Figure 3.16 Observed (red), calculated (green) and difference (bottom) NPD patterns for $La_4Sr_8Ti_{11}MnO_{38}$ (n=1) in reducing conditions at different temperatures**

**Table 3.6 Structural parameters extracted from refinement of NPD data for the compound n=1 in reducing conditions at different temperatures**

| | n=1 reduced | | | | | |
|---|---|---|---|---|---|---|
| | RT | 100°C | 300°C | 500°C | 700°C | 900°C |
| **Crystal system** | Rhombohedral | Rhombohedral | Rhombohedral | Cubic | Cubic | Cubic |
| **Space group** | R-3c | R-3c | R-3c | Pm-3m | Pm-3m | Pm-3m |
| a (Å) | 5.5482(4) | 5.5494(7) | 5.5626(9) | 3.9407(9) | 3.9499(5) | 3.9596(9) |
| c (Å) | 13.5807(7) | 13.5839(4) | 13.6094(6) | 3.9407(9) | 3.9499(5) | 3.9596(9) |
| Volume ($Å^3$) | 362.04(8) | 362.30(6) | 364.70(5) | 61.20(1) | 61.62(8) | 62.08(5) |
| O (x) | 0.4711(7) | 0.4736(7) | 0.4808(3) | 0.5 | 0.5 | 0.5 |
| **Isotropic temperature factors; $U_{iso}$x100/$Å^2$** | | | | | | |
| La | 3.116(05) | 2.161(31) | 4.176(09) | 2.187(26) | 3.102(47) | 3.503(59) |
| Sr | 0.696(37) | 1.256(61) | 1.211(60) | 2.435(77) | 2.527(75) | 3.103(86) |
| Ti | 0.609(44) | 0.547(65) | 0.890(71) | 0.860(68) | 1.140(70) | 1.277(74) |
| Mn | 0.287(66) | 0.843(07) | 0.312(76) | 0.793(50) | 1.485(43) | 4.978(61) |
| O | 1.640(20) | 1.937(29) | 2.334(33) | 2.853(33) | 3.177(34) | 3.506(37) |
| **Occupancies** | | | | | | |
| La | 0.3330 | 0.3330 | 0.3330 | 0.3330 | 0.3330 | 0.3330 |
| Sr | 0.6670 | 0.6670 | 0.6670 | 0.6670 | 0.6670 | 0.6670 |
| Ti | 0.9200 | 0.9200 | 0.9200 | 0.9200 | 0.9200 | 0.9200 |
| Mn | 0.0800 | 0.0800 | 0.0800 | 0.0800 | 0.0800 | 0.0800 |
| O | 1.00 | 1.00 | 1.00 | 1.00 | 1.00 | 1.00 |
| **R-factors** | | | | | | |
| $R_{wp}$ (%) | 9.48 | 9.49 | 9.76 | 9.29 | 8.58 | 8.30 |
| $R_p$ (%) | 6.51 | 6.43 | 6.55 | 6.11 | 5.51 | 5.26 |
| $R_F$ (%) | 2.38 | 2.30 | 2.32 | 2.41 | 2.45 | 2.19 |
| $\chi^2$ (%) | 2.502 | 4.818 | 5.018 | 4.525 | 3.899 | 3.640 |

### 3.3.2.2. $La_4Sr_8Ti_{10}Mn_2O_{38-\delta}$ (n=2)

The XDR and NPD patterns can be indexed as a rhombohedral structure, space group R-3c (Figures 3.17 and 3.18). The refined structural parameters after combined XRD and NPD can be observed on Table 3.7.

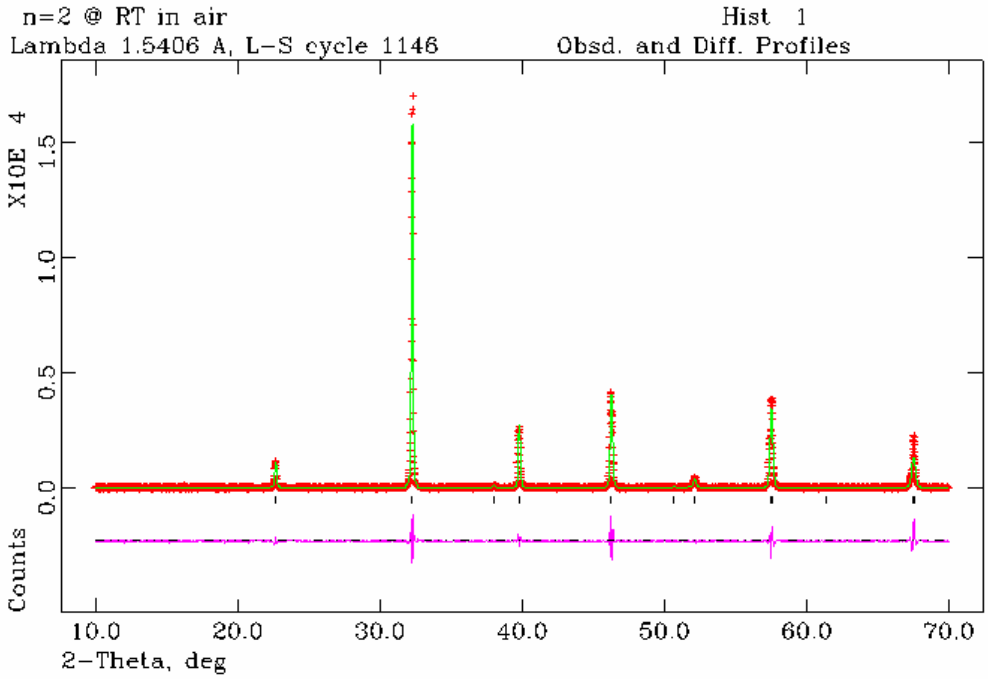


**Figure 3.17 Observed (red), calculated (green) and difference XRD pattern for n=2.**

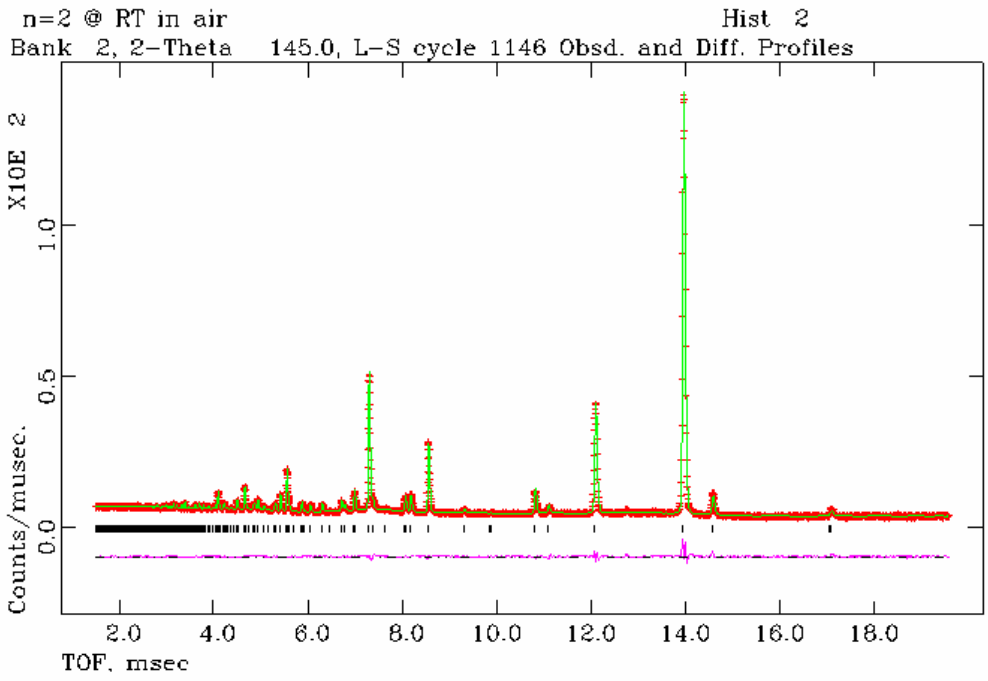


**Figure 3.18 Observed (red), calculated (green) and difference NPD pattern for n=2.**

| n=2 | RT |
|---|---|
| a/Å | 5.5442(2) |
| c/Å | 13.5529(1) |
| V/Å$^3$ | 360.78(2) |
| x(O) | 0.4685(2) |
| Discrepancy factors | |
| $R_{wp}^X$ / $R_{wp}^N$ (%) | 7.03/1.88 |
| $R_p^X$ / $R_p^N$ (%) | 4.77/2.81 |
| $R_F^X$ / $R_F^N$ (%) | 4.47/6.28 |
| $\chi^2$ | 3.906 |

Space group R-3c. The atomic positions are 6(a) (0, 0, 1/4) for La/Sr; 6(b) (0, 0, 0) for Mn/Ti; 18(e) (x, 0, 1/4) for O.

**Table 3.7 Refined structural parameters for R-3c $La_4Sr_8Ti_{10}Mn_2O_{38-\delta}$ (n=2) after Rietveld refinements using combined NPD and XRD data at room temperature.**

In Figure 3.19 we can observe the XRD patterns for n=2 as prepared and in reducing conditions (after 48 hours in 5%$H_2$/Ar). The volume of the unit cell increases in reducing conditions as happened for n=1.

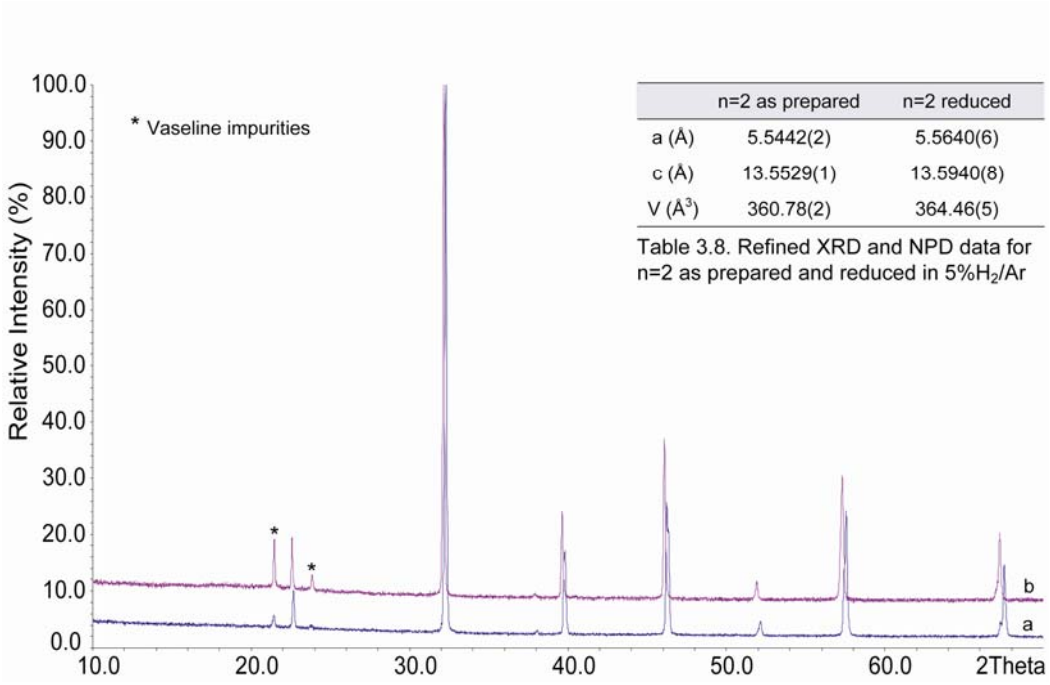


**Figure 3.19 XRD patterns for n=2 (a) as prepared in oxidising conditions and (b) reduced in 5%$H_2$ in Ar for 48 hours.**

As has been said before for n=1, conductivity measurements in air and $H_2$ (Chapter 4) suggest a phase transition as the temperature increases. In order to correlate phase transformations with these changes in electrical properties we carried out in situ time-of-flight neutron diffraction studies on the POLARIS diffractometer at the ISIS facilities, Rutherford Appleton Laboratories, Oxford. The sample was loaded into a quartz tube which was vented to the air (thus allows the furnace to run under high vacuum to prevent damage to the element and heat shields). Figure 3.20 shows the patterns obtained in air at different temperatures.

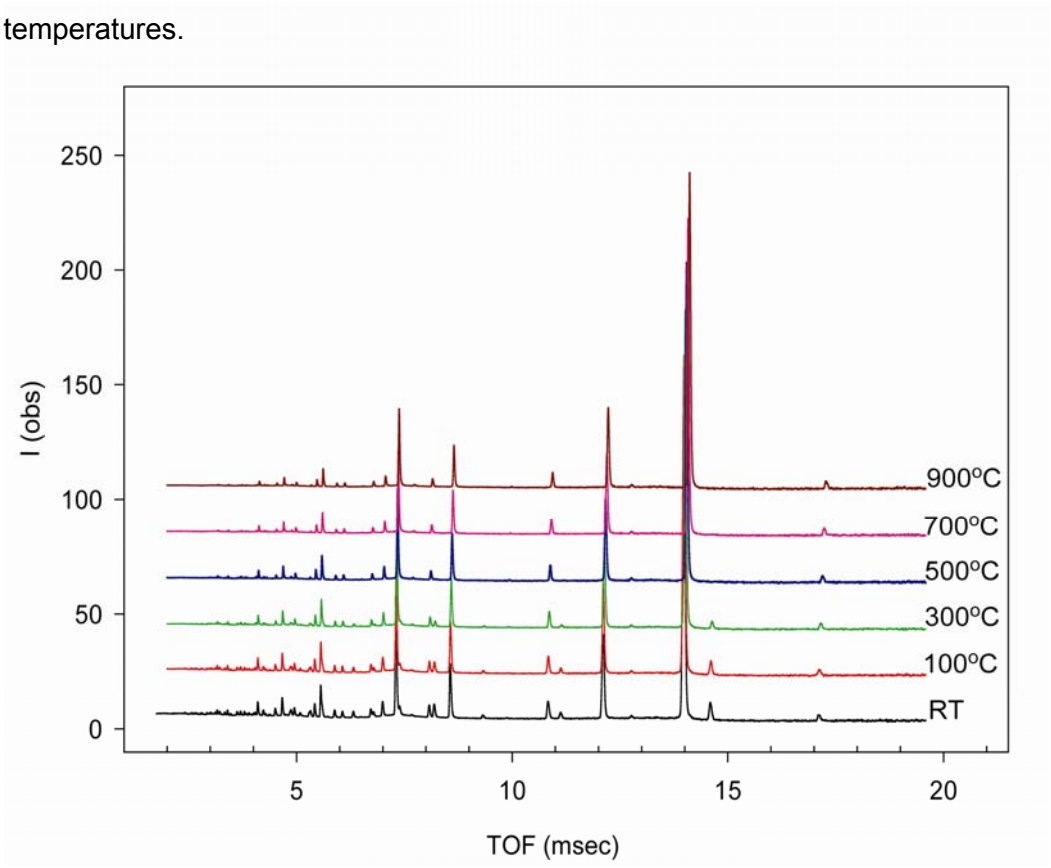


**Figure 3.20 NPD patterns for $La_4Sr_8Ti_{10}Mn_2O_{38-\delta}$ in air at different temperatures.**

The details of the data collections are presented in Figure 3.21 and Table 3.9. From room temperature (RT) to 300°C the structure was refined using the rhombohedral space group R-3c. As temperature increases from room temperature to 300°C the cell parameters increase continuously.

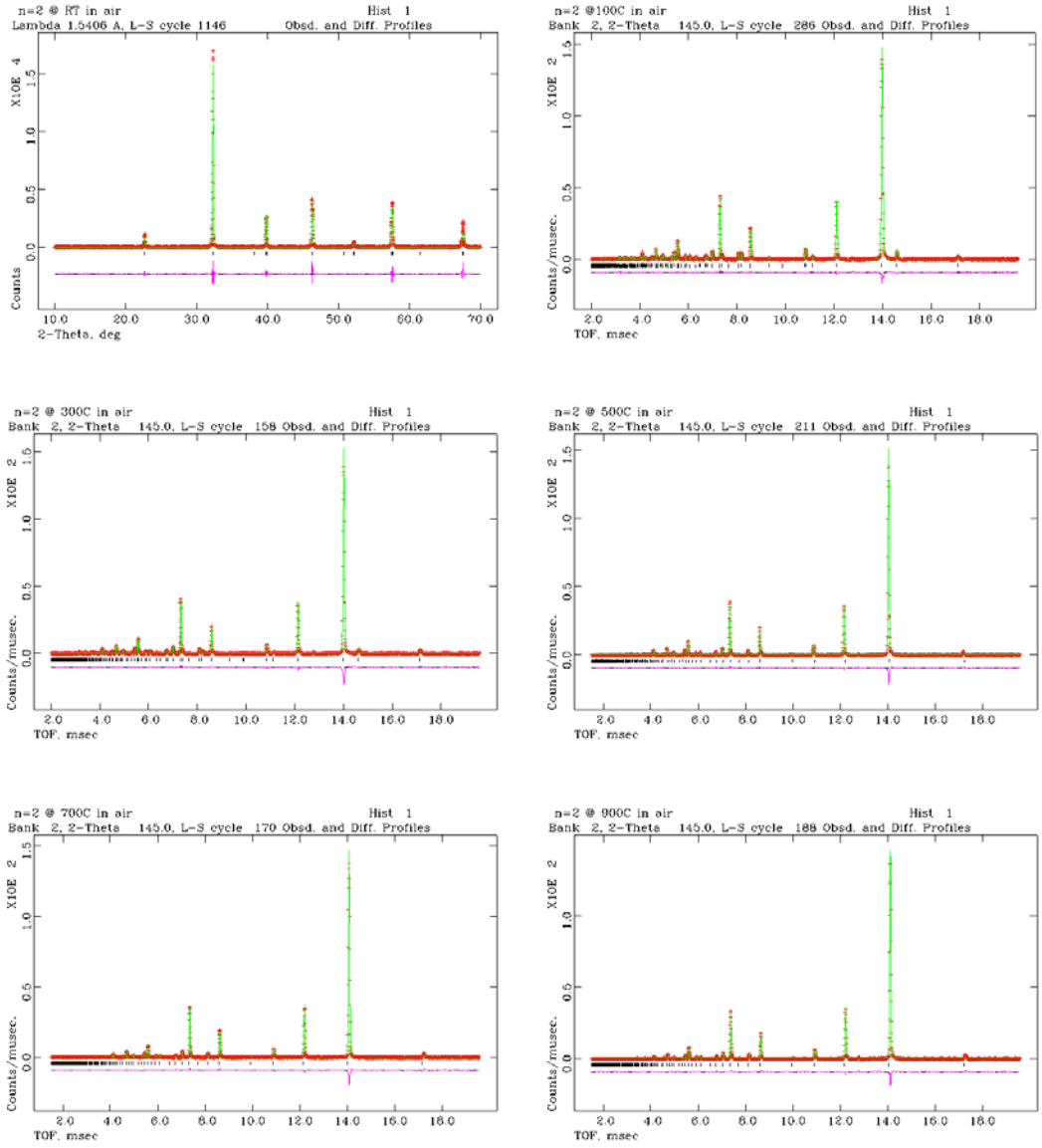


**Figure 3.21 Observed (red), calculated (green) and difference (bottom) neutron powder patterns for $La_4Sr_8Ti_{10}Mn_2O_{38}$ (n=2) in air at different temperatures.**

At 500°C the neutron diffraction pattern could be better refined as a simple cubic structure, space group Pm-3m. The value of the cubic unit cell is a=3.9455(6) Å and the volume is 61.42(1) $Å^3$. At higher temperatures (700°C and 900°C) the structure remains cubic. The R-factors are getting better as temperature increases and chi square is just 1.880 for the highest temperature. These values indicate that a good fitting was achieved. As happened for n=1 the cubic cell parameter increases continuously in the whole temperature range investigated.

**Table 3.9 Structural parameters extracted from refinement of NPD data for the compound $La_4Sr_8Ti_{10}Mn_2O_{37}$ (n=2) in air at different temperatures**

| | n=2 in air | | | | | |
|---|---|---|---|---|---|---|
| | RT | 100°C | 300°C | 500°C | 700°C | 900°C |
| **Crystal system** | Rhombohedral | Rhombohedral | Rhombohedral | Cubic | Cubic | Cubic |
| **Space group** | R-3c | R-3c | R-3c | Pm-3m | Pm-3m | Pm-3m |
| a (Å) | 5.5442(2) | 5.5598(5) | 5.5684(6) | 3.9455(2) | 3.9554(3) | 3.9651(6) |
| c (Å) | 13.5529(1) | 13.5904(5) | 13.6311(1) | 3.9455(2) | 3.9554(3) | 3.965196) |
| Volume ($Å^3$) | 360.78(2) | 363.82(4) | 366.04(2) | 61.42(1) | 61.88(5) | 62.34(2) |
| O (x) | 0.4685(2) | 0.4710(1) | 0.4776(7) | 0.5 | 0.5 | 0.5 |
| **Isotropic temperature factors; $U_{iso}$x100/$Å^2$** | | | | | | |
| La | 0.137(81) | 0.431(21) | 0.788(28) | 0.868(15) | 1.651(36) | 2.083(41) |
| Sr | 0.177(50) | 0.927(35) | 1.173(24) | 1.988(15) | 2.147(28) | 2.523(31) |
| Ti | 0.141(32) | 0.576(06) | 0.635(2) | 0.780(18) | 0.892(22) | 1.064(23) |
| Mn | 0.163(59) | 0.756(72) | 0.703(86) | 2.544(18) | 1.152(99) | 1.778(12) |
| O | 1.110(67) | 1.354(07) | 1.697(09) | 2.490(10) | 2.806(10) | 3.206(11) |
| **Occupancies** | | | | | | |
| La | 0.3330 | 0.3330 | 0.3330 | 0.3330 | 0.3330 | 0.3330 |
| Sr | 0.6670 | 0.6670 | 0.6670 | 0.6670 | 0.6670 | 0.6670 |
| Ti | 0.8333 | 0.8333 | 0.8333 | 0.8333 | 0.8333 | 0.8333 |
| Mn | 0.1667 | 0.1667 | 0.1667 | 0.1667 | 0.1667 | 0.1667 |
| O | 1.00 | 1.00 | 1.00 | 1.00 | 1.00 | 1.00 |
| **R-factors** | | | | | | |
| $R_{wp}$ (%) | 1.88 | 1.57 | 1.59 | 1.35 | 1.18 | 1.08 |
| $R_p$ (%) | 2.81 | 2.70 | 3.16 | 2.54 | 2.41 | 2.29 |
| $R_F$ (%) | 5.12 | 4.13 | 4.33 | 4.71 | 4.65 | 4.59 |
| $\chi^2$ (%) | 3.906 | 3.683 | 3.792 | 2.936 | 2.262 | 1.880 |

For reducing conditions we used at POLARIS an "in situ reaction cell" sample can assembly which is made from stainless steel .It allows gases to be passed through the sample whilst in the beam. The sample can is cylindrical and has an internal diameter of 11 mm. Ideally, it needs to be filled to a depth of about 40 mm with sample which is held in the cell with glass frits and quartz glass wool. Gas enters the sample can at the bottom and exits at the top. Because the sample cell is made from stainless steel there will be intense Bragg reflections present in the diffraction patterns collected. However, the slits cut in this mask to allow the beam in and out are only around 6mm wide, which means that only part of the sample in the reaction cell is illuminated and, thus, the counting times required are increased. Figure 3.21 shows the patterns obtained at different temperatures.

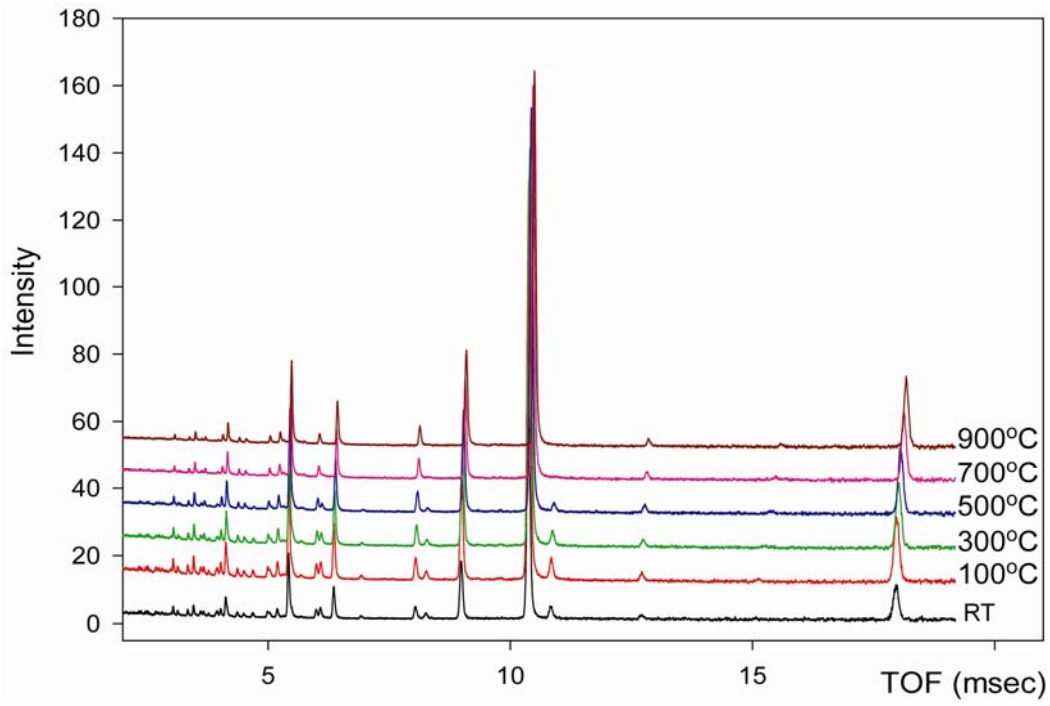


**Figure 3.22 NPD patterns for $La_4Sr_8Ti_{10}Mn_2O_{38-\delta}$ (n=2) in 5%$H_2$ in Ar at different temperatures**

The details of the data collections are presented in Figure 3.23. A summary of structure parameters, isotropic temperature factors, occupancies and R-factors, obtained at different temperatures are presented in Table 3.10.

In reducing conditions from room temperature to 500°C the data may be refined well with the rhombohedral perovskite model. At 700°C and 900°C the best refinement is achieved with the cubic structure. For both, the cubic and rhombohedral structures the cell parameters increase continuously in the whole temperature range investigated.

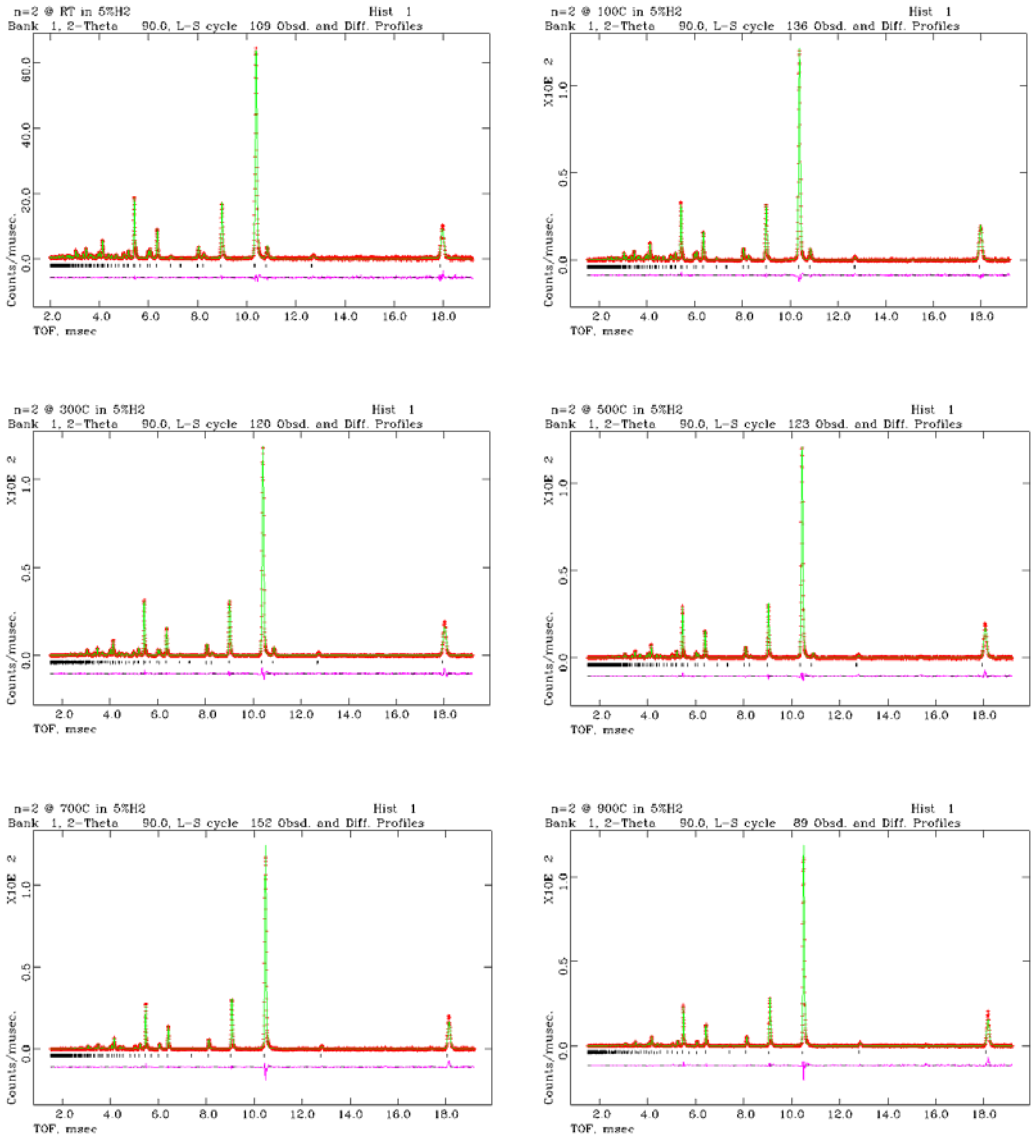


**Figure 3.23 Observed (red), calculated (green) and difference (bottom) neutron powder patterns for $La_4Sr_8Ti_{10}Mn_2O_{37}$ (n=2) in 5%$H_2$ in Ar at different temperatures.**

**Table 3.10 Structural parameters extracted from refinement of NPD data for the compound n=2 in 5%$H_2$ in Ar at different temperatures.**

| | n=2 in 5%$H_2$ in Ar | | | | | |
|---|---|---|---|---|---|---|
| | RT | 100°C | 300°C | 500°C | 700°C | 900°C |
| **Crystal system** | Rhombohedral | Rhombohedral | Rhombohedral | Rhombohedral | Cubic | Cubic |
| **Space group** | R-3c | R-3c | R-3c | R-3c | Pm-3m | Pm-3m |
| a (Å) | 5.5640(6) | 5.5654(3) | 5.5784(6) | 5.5911(3) | 3.9656(6) | 3.9761(3) |
| c (Å) | 13.5940(8) | 13.5984(9) | 13.6389(4) | 13.6720(3) | 3.9656(6) | 3.9761(3) |
| Volume ($Å^3$) | 364.46(5) | 364.77(1) | 367.57(1) | 370.13(8) | 62.36(6) | 62.86(1) |
| O (x) | 0.4642(6) | 0.4658(3) | 0.4705(8) | 0.4774(6) | 0.5 | 0.5 |
| **Isotropic temperature factors; $U_{iso}$x100/$Å^2$** | | | | | | |
| La | 0.820(23) | 0.714(24) | 1.472(64) | 2.806(84) | 0.881(57) | 1.632(71) |
| Sr | 0.588(17) | 0.594(16) | 0.644(27) | 0.804(27) | 2.153(46) | 2.157(46) |
| Ti | 0.443(29) | 0.567(26) | 0.792(34) | 0.956(34) | 0.961(39) | 0.943(41) |
| Mn | 1.013(12) | 0.640(97) | 0.005(02) | 0.315(93) | 0.281(59) | 1.220(21) |
| O | 1.293(07) | 1.287(09) | 1.665(12) | 2.322(13) | 3.242(17) | 3.507(18) |
| **Occupancies** | | | | | | |
| La | 0.3330 | 0.3330 | 0.3330 | 0.3330 | 0.3330 | 0.3330 |
| Sr | 0.6670 | 0.6670 | 0.6670 | 0.6670 | 0.6670 | 0.6670 |
| Ti | 0.8333 | 0.8333 | 0.8333 | 0.8333 | 0.8333 | 0.8333 |
| Mn | 0.1667 | 0.1667 | 0.1667 | 0.1667 | 0.1667 | 0.1667 |
| O | 1.00 | 1.00 | 1.00 | 1.00 | 1.00 | 1.00 |
| **R-factors** | | | | | | |
| $R_{wp}$ (%) | 3.66 | 2.85 | 2.95 | 2.75 | 2.97 | 2.84 |
| $R_p$ (%) | 6.05 | 4.07 | 4.32 | 4.12 | 4.55 | 4.46 |
| $R_F$ (%) | 2.54 | 3.91 | 3.49 | 3.52 | 3.70 | 3.74 |
| $\chi^2$ (%) | 0.8349 | 1.878 | 2.008 | 1.759 | 2.045 | 1.861 |

### 3.3.2.3. $La_4Sr_8Ti_9Mn_3O_{38-\delta}$ (n=3)

The XRD and NPD patterns can be indexed to a rhombohedral structure, space group R-3c, Figure 3.24, Figure 3.25 and Table 3.11.

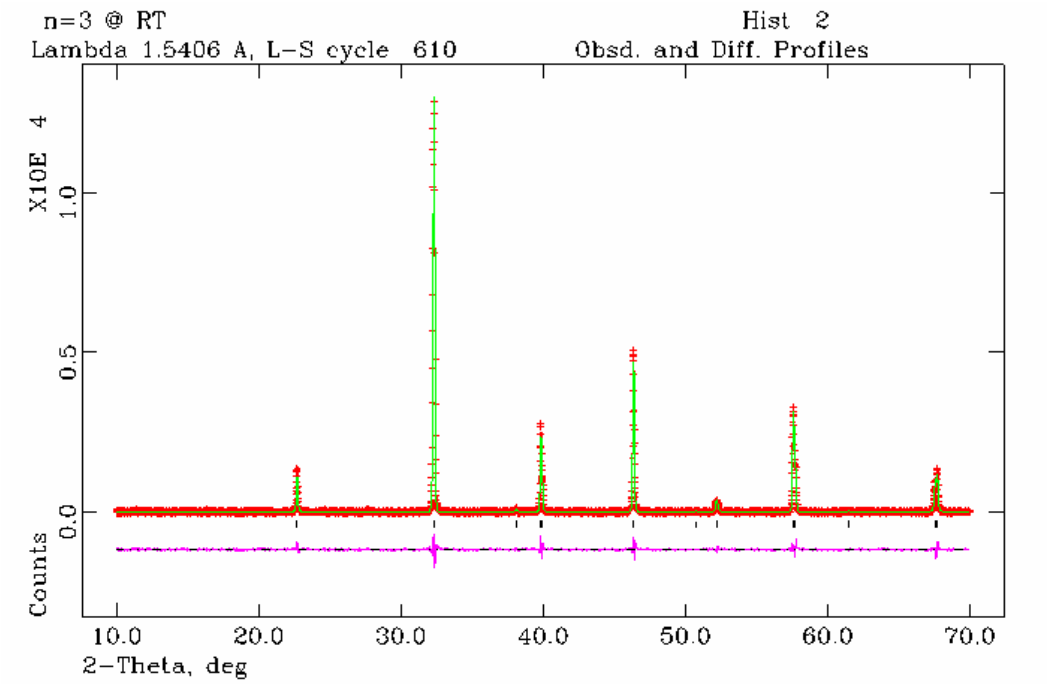


**Figure 3.24 Observed (red), calculated (green) and difference XRD pattern for n=3.**

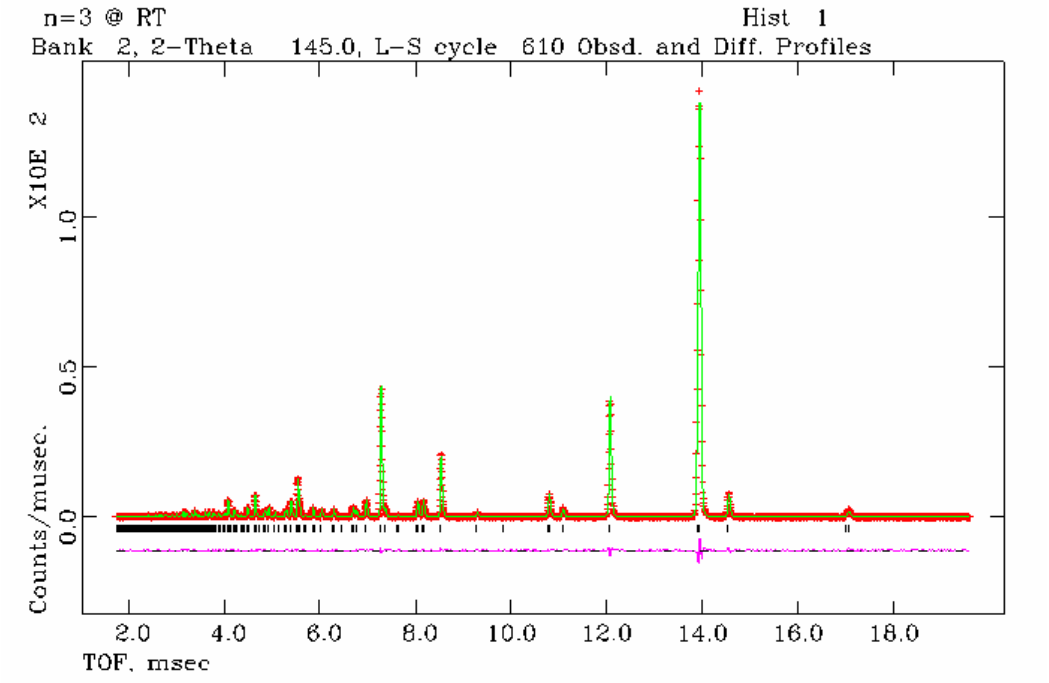


**Figure 3.25 Observed (red), calculated (green) and difference NPD pattern for n=3.**

| n=3 | RT |
|---|---|
| a/Å | 5.5422(2) |
| c/Å | 13.5352(6) |
| V/Å$^3$ | 360.05(2) |
| x(O) | 0.4671(4) |
| Discrepancy factors | |
| $R_{wp}^X$ / $R_{wp}^N$ (%) | 5.85/1.81 |
| $R_p^X$ / $R_p^N$ (%) | 4.37/3.15 |
| $R_F^X$ / $R_F^N$ (%) | 3.77/5.18 |
| $\chi^2$ | 2.267 |

Space group R-3c. The atomic positions are 6(a) (0,0,1/4) for La/Sr; 6(b) (0,0,0) for Mn/Ti; 18(e) (x,0,1/4) for O.

**Table 3.11 Refined structural parameters for R-3c $La_4Sr_8Ti_9Mn_3O_{38-\delta}$ (n=3) after Rietveld refinements using combined NPD and XRD data at room temperature.**

In Figure 3.26 we can observe the XRD patterns for n=3 as prepared and in reducing conditions (after 48 hours in 5%$H_2$/Ar).

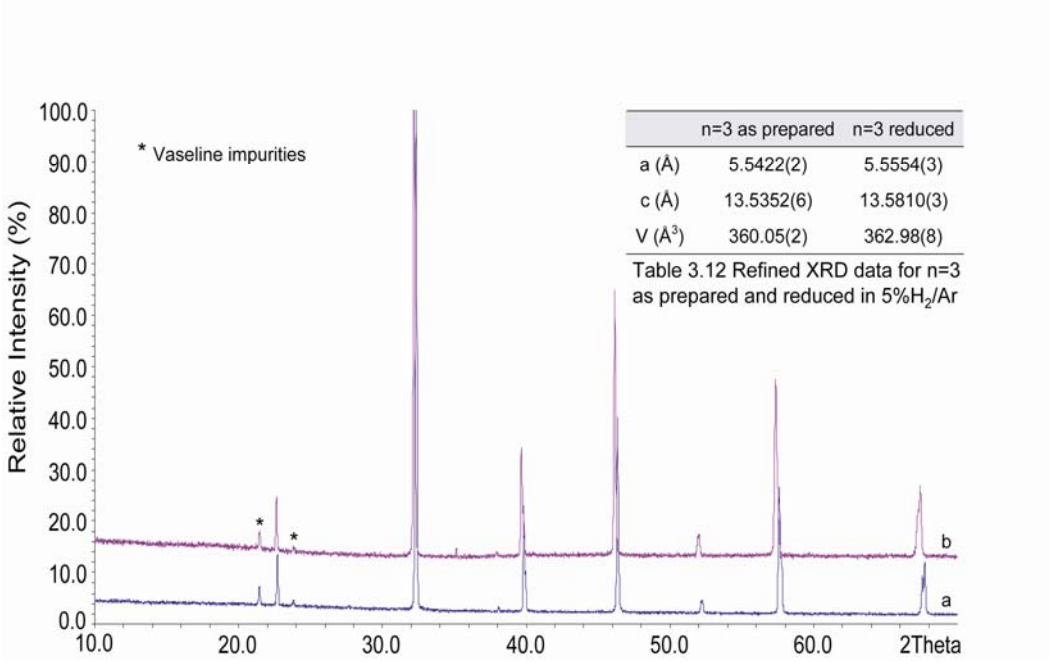


**Figure 3.26 XRD patterns for n=3 (a) as prepared and (b) reduced in 5%$H_2$/Ar.**

### 3.3.2.4. $La_4Sr_8Ti_8Mn_4O_{38-\delta}$ (n=4)

The XRD and NPD patterns can be indexed to a rhombohedral structure, space group R-3c, Figure 3.27, Figure 3.28 and Table 3.13.

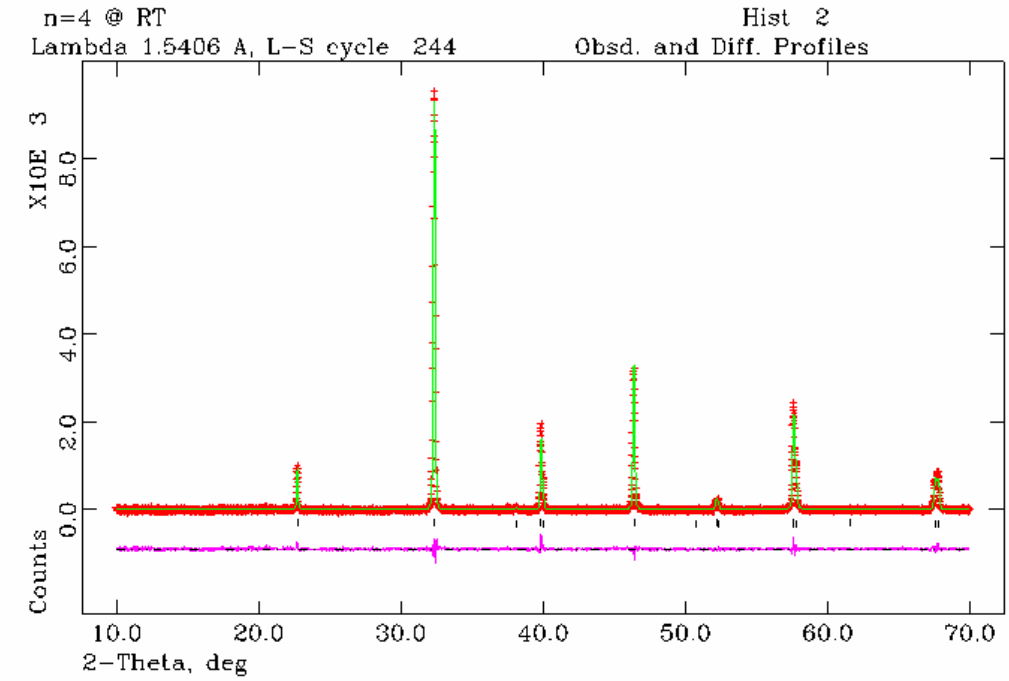


**Figure 3.27 Observed (red), calculated (green) and difference XRD pattern for n=4.**

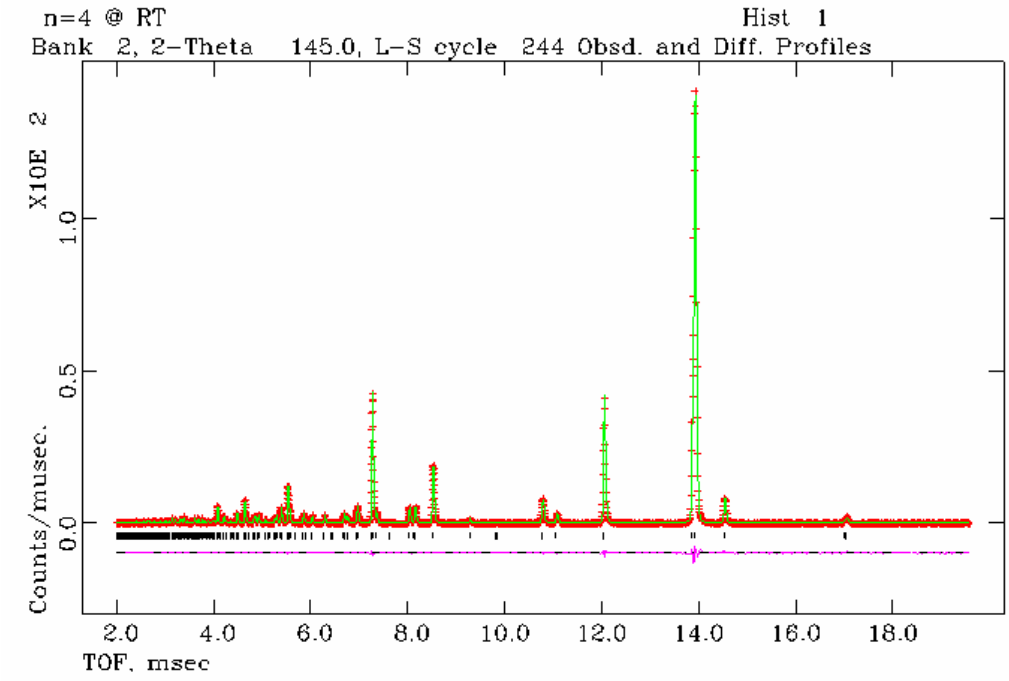


**Figure 3.28 Observed (red), calculated (green) and difference NPD pattern for n=4.**

| n=4 | RT |
|---|---|
| a/Å | 5.5394(8) |
| c/Å | 13.5173(3) |
| V/Å$^3$ | 359.21(9) |
| x(O) | 0.4668(8) |
| Discrepancy factors | |
| $R_{wp}^X$ / $R_{wp}^N$ (%) | 5.11/1.59 |
| $R_p^X$ / $R_p^N$ (%) | 3.97/2.76 |
| $R_F^X$ / $R_F^N$ (%) | 2.45/5.22 |
| $\chi^2$ | 1.578 |

Space group R-3c. The atomic positions are 6(a) (0,0,1/4) for La/Sr; 6(b) (0,0,0) for Mn/Ti; 18(e) (x,0,1/4) for O.

**Table 3.13 Refined structural parameters for R-3c $La_4Sr_8Ti_8Mn_4O_{38-\delta}$ (n=4) after Rietveld refinements using combined NPD and XRD data at room temperature.**

In Figure 3.29 we can observe the XRD patterns for n=4 as prepared and in reducing conditions (after 48 hours in 5%$H_2$/Ar).

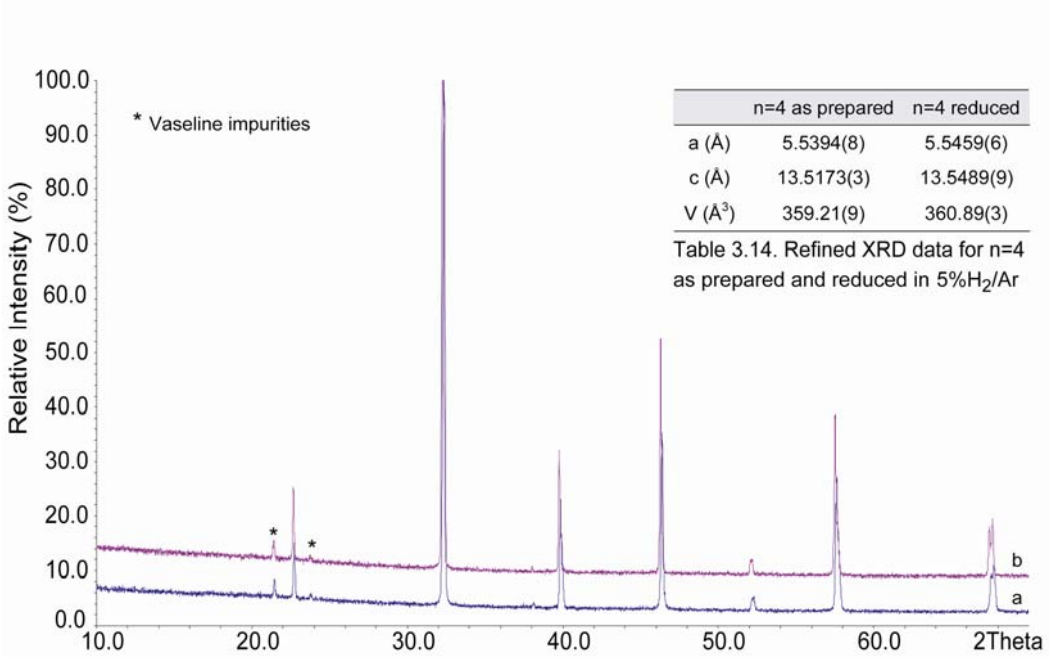


**Figure 3.29 XRD patterns for n=4 (a) as prepared and (b) reduced in 5%$H_2$/Ar.**

### 3.3.2.5. $La_4Sr_8Ti_7Mn_5O_{38-\delta}$ (n=5)

The XRD and NPD patterns can be indexed to a rhombohedral structure, space group R-3c, Figure 3.30, Figure 3.31 and Table 3.15.

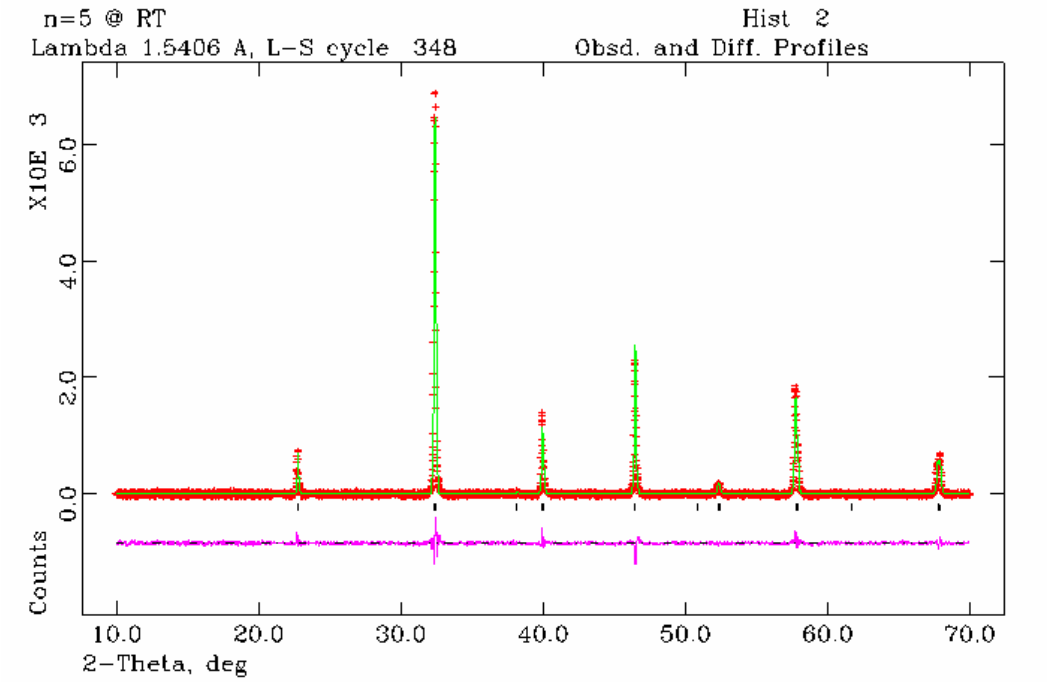


**Figure 3.30 Observed (red), calculated (green) and difference XRD pattern for n=5.**

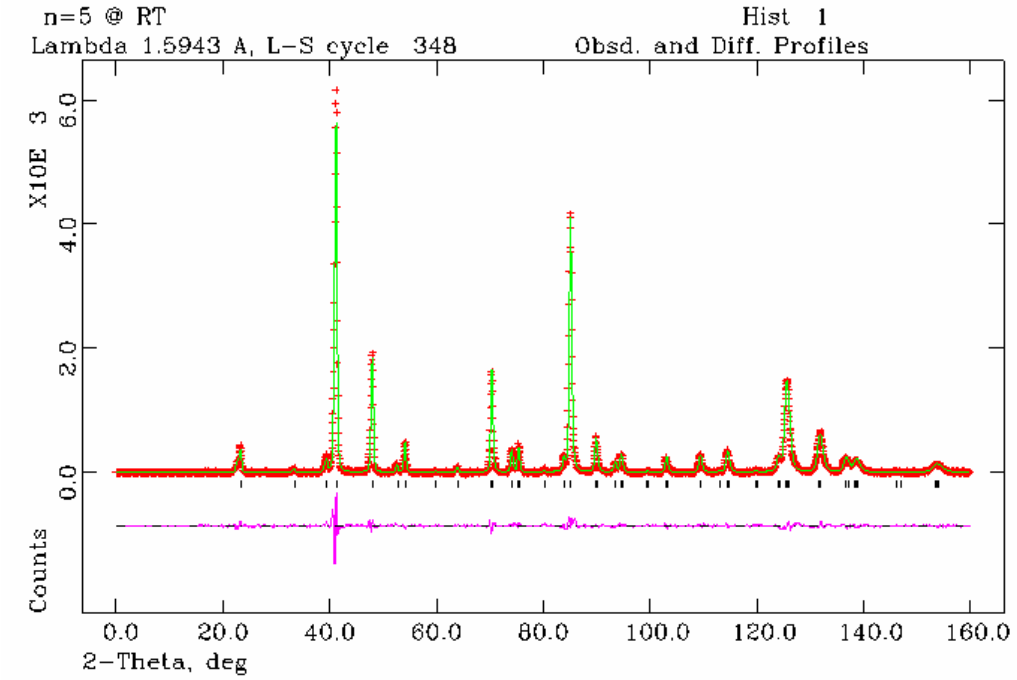


**Figure 3.31 Observed (red), calculated (green) and difference NPD pattern for n=5.**

| n=5 | RT |
|---|---|
| a/Å | 5.5265(7) |
| c/Å | 13.4927(8) |
| V/Å$^3$ | 356.89(9) |
| x(O) | 0.4718(4) |
| Discrepancy factors | |
| $R_{wp}^X$ / $R_{wp}^N$ (%) | 6.40/6.51 |
| $R_p^X$ / $R_p^N$ (%) | 4.94/4.79 |
| $R_F^X$ / $R_F^N$ (%) | 4.28/2.22 |
| $\chi^2$ | 1.336 |

Space group R-3c. The atomic positions are 6(a) (0,0,1/4) for La/Sr; 6(b) (0,0,0) for Mn/Ti; 18(e) (x,0,1/4) for O.

**Table 3.15 Refined structural parameters for R-3c $La_4Sr_8Ti_7Mn_5O_{38-\delta}$ (n=5) after Rietveld refinements using combined NPD and XRD data at room temperature.**

In Figure 3.32 we can observe the XRD patterns for n=5 as prepared and in reducing conditions (after 48 hours in 5%$H_2$/Ar).

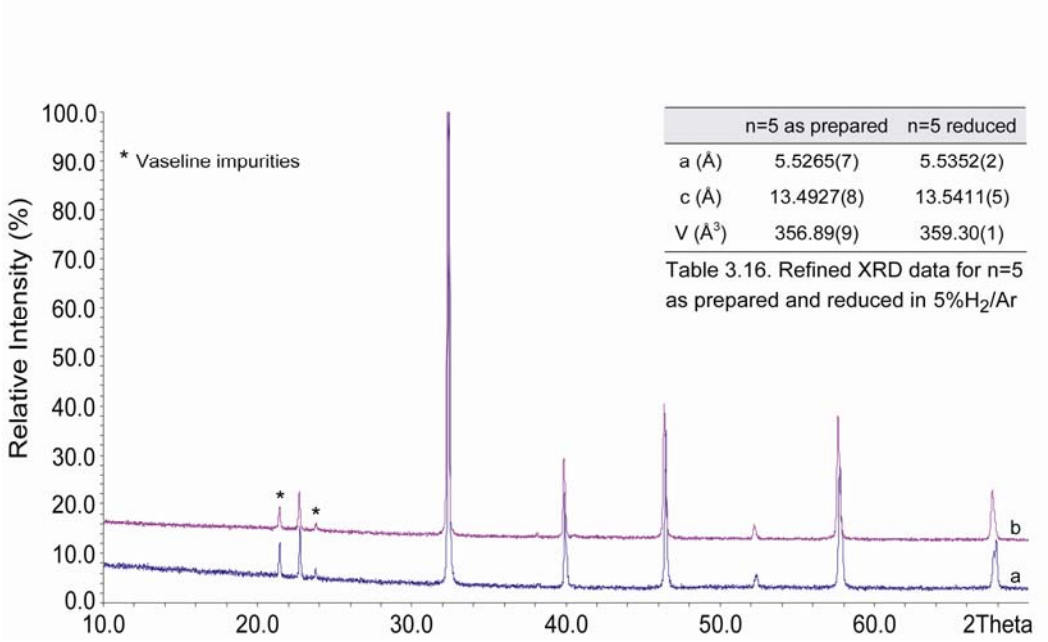


**Figure 3.32 XRD patterns for n=5 (a) as prepared and (b) reduced in 5%$H_2$/Ar.**

### 3.3.2.6. $La_4Sr_8Ti_6Mn_6O_{38-\delta}$ (n=6)

The XRD and NPD patterns can be indexed to a rhombohedral structure, space group R-3c, Figure 3.33, Figure 3.34 and Table 3.17.

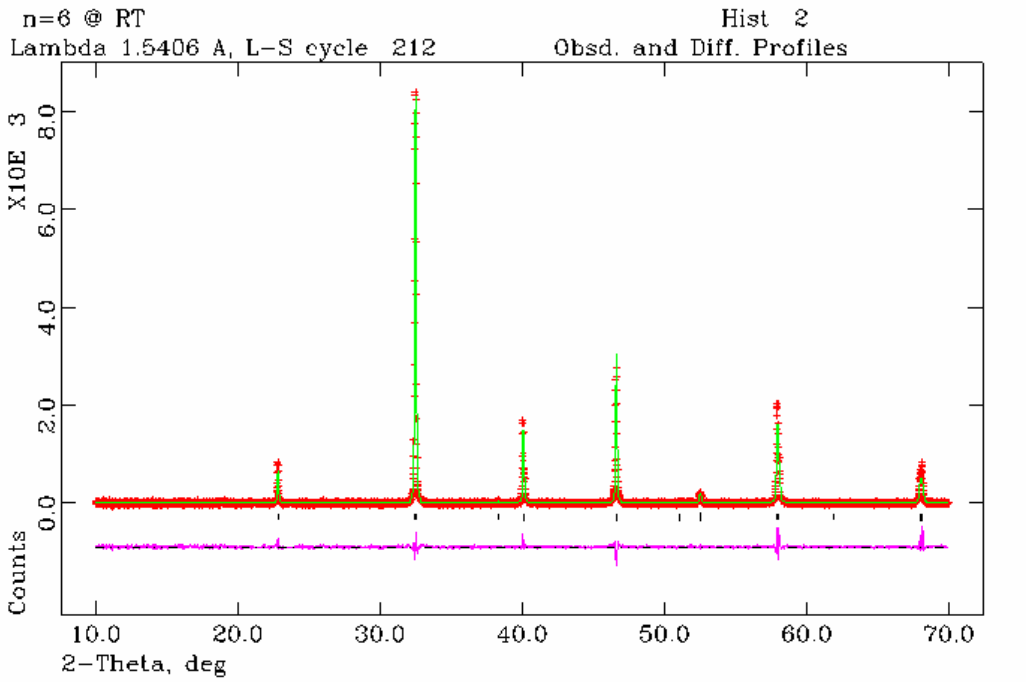


**Figure 3.33 Observed (red), calculated (green) and difference XRD pattern for n=6.**

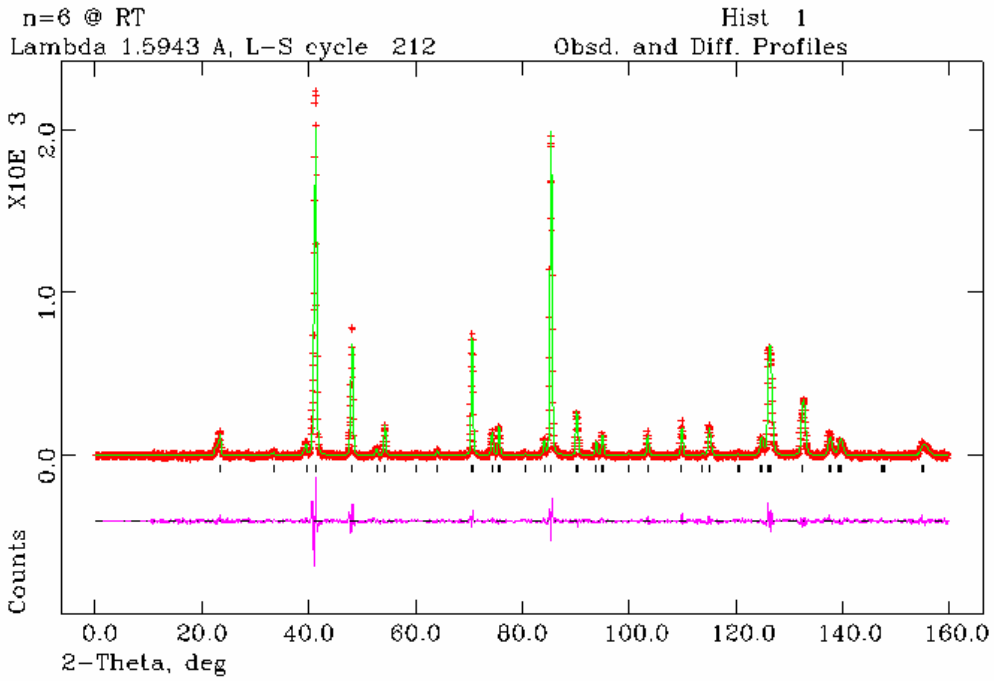


**Figure 3.34 Observed (red), calculated (green) and difference NPD pattern for n=6.**

| n=6 | RT |
|---|---|
| a/Å | 5.5101(7) |
| c/Å | 13.4602(9) |
| V/Å$^3$ | 353.92(8) |
| x(O) | 0.4728(4) |
| Discrepancy factors | |
| $R_{wp}^X$ / $R_{wp}^N$ (%) | 6.39/8.25 |
| $R_p^X$ / $R_p^N$ (%) | 4.72/9.64 |
| $R_F^X$ / $R_F^N$ (%) | 5.40/3.09 |
| $\chi^2$ | 1.255 |

Space group R-3c. The atomic positions are 6(a) (0,0,1/4) for La/Sr; 6(b) (0,0,0) for Mn/Ti; 18(e) (x,0,1/4) for O.

**Table 3.17 Refined structural parameters for R-3c $La_4Sr_8Ti_6Mn_6O_{38-\delta}$ (n=6) after Rietveld refinements using combined NPD and XRD data at room temperature.**

In Figure 3.35 we can observe the XRD patterns for n=6 as prepared and in reducing conditions (after 48 hours in 5%$H_2$/Ar).

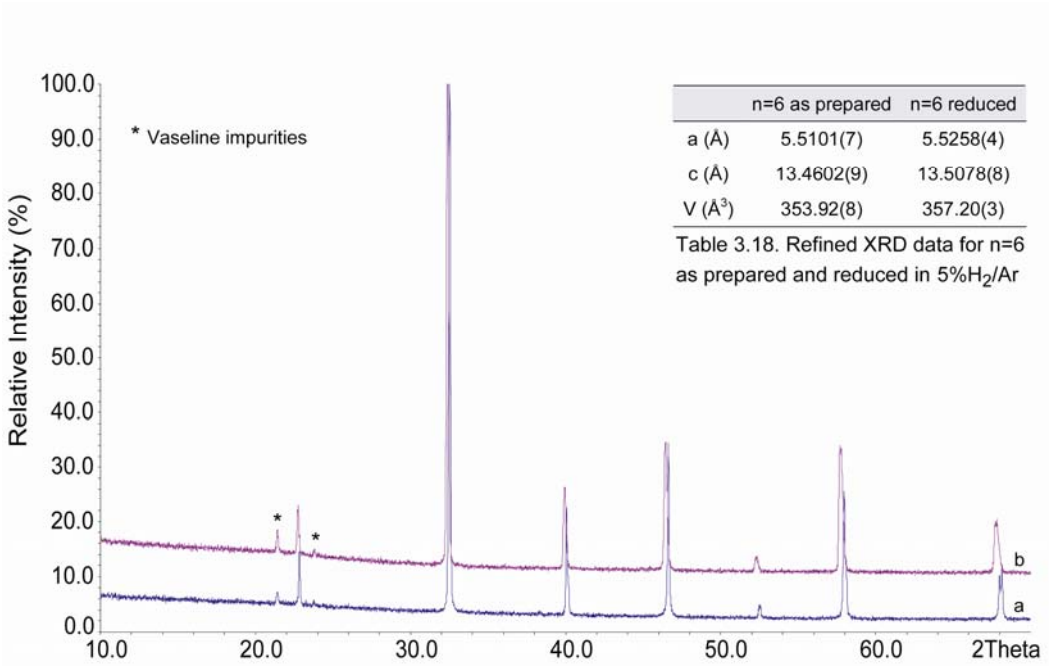


**Figure 3.35 XRD patterns for n=6 (a) as prepared and (b) reduced in 5%$H_2$/Ar.**

### 3.3.2.7. $La_4Sr_8Ti_7Mn_5O_{38-\delta}$ (n=7)

The XRD pattern can be indexed to a rhombohedral structure, space group R-3c, Figure 3.36 and Table 3.19.

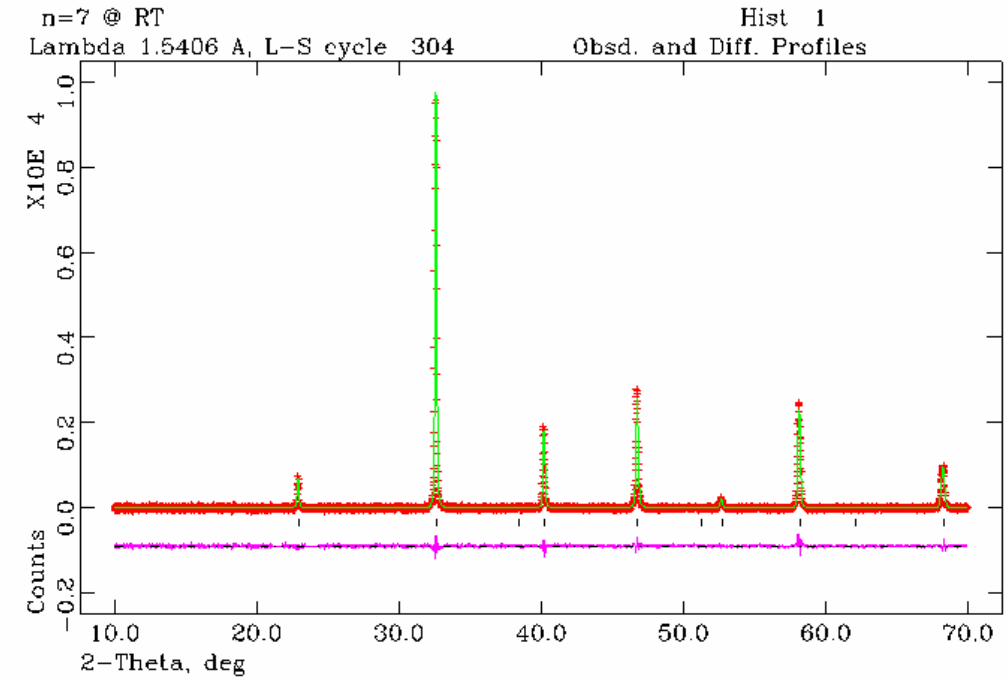


**Figure 3.36 Observed (red), calculated (green) and difference XRD pattern for n=7.**

| n=7 | RT |
|---|---|
| a/Å | 5.4960(8) |
| c/Å | 13.4371(7) |
| V/Å$^3$ | 351.51(2) |
| x(O) | 0.4992(7) |
| Discrepancy factors | |
| $R_{wp}$ (%) | 4.37 |
| $R_p$ (%) | 3.41 |
| $R_F$ (%) | 4.05 |
| $\chi^2$ | 1.145 |

Space group R-3c. The atomic positions are 6(a) (0,0,1/4) for La/Sr; 6(b) (0,0,0) for Mn/Ti; 18(e) (x,0,1/4) for O.

**Table 3.19 Refined structural parameters for R-3c $La_4Sr_8Ti_5Mn_7O_{38-\delta}$ (n=7) after Rietveld refinements using XRD data at room temperature.**

In Figure 3.37 we can observe the XRD patterns for n=7 as prepared and in reducing conditions (after 48 hours in 5%$H_2$/Ar).

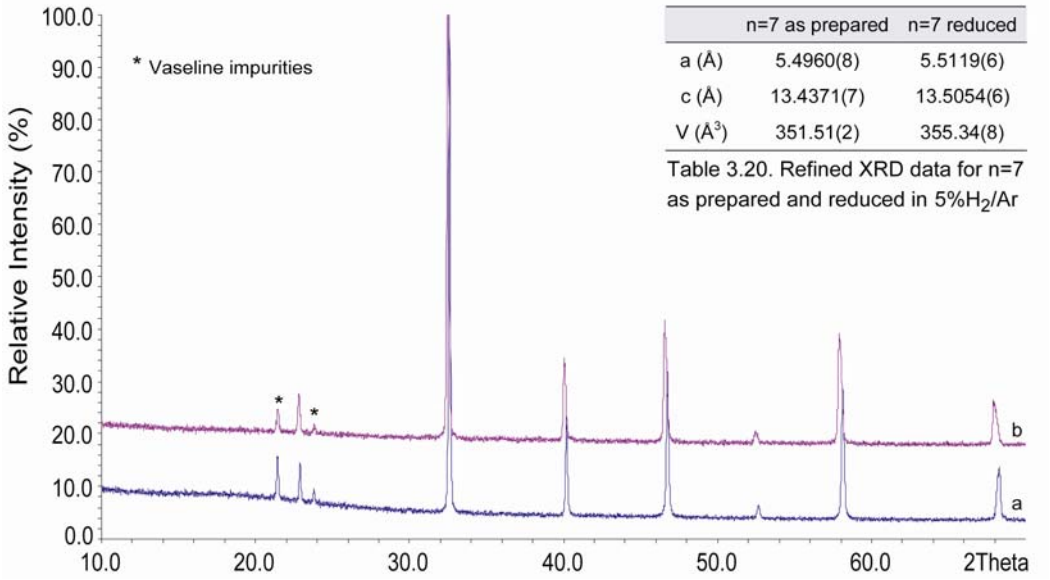


| | n=7 as prepared | n=7 reduced |
|---|---|---|
| a (Å) | 5.4960(8) | 5.5119(6) |
| c (Å) | 13.4371(7) | 13.5054(6) |
| V (Å$^3$) | 351.51(2) | 355.34(8) |

Table 3.20. Refined XRD data for n=7 as prepared and reduced in 5%$H_2$/Ar

**Figure 3.37 XRD patterns for n=7 (a) as prepared and (b) reduced in 5%$H_2$/Ar.**

### 3.3.2.8. $La_4Sr_8Ti_1Mn_{11}O_{38-\delta}$ (n=11)

The XRD and NPD patterns are shown in Figures 3.38 and 3.39 respectively.

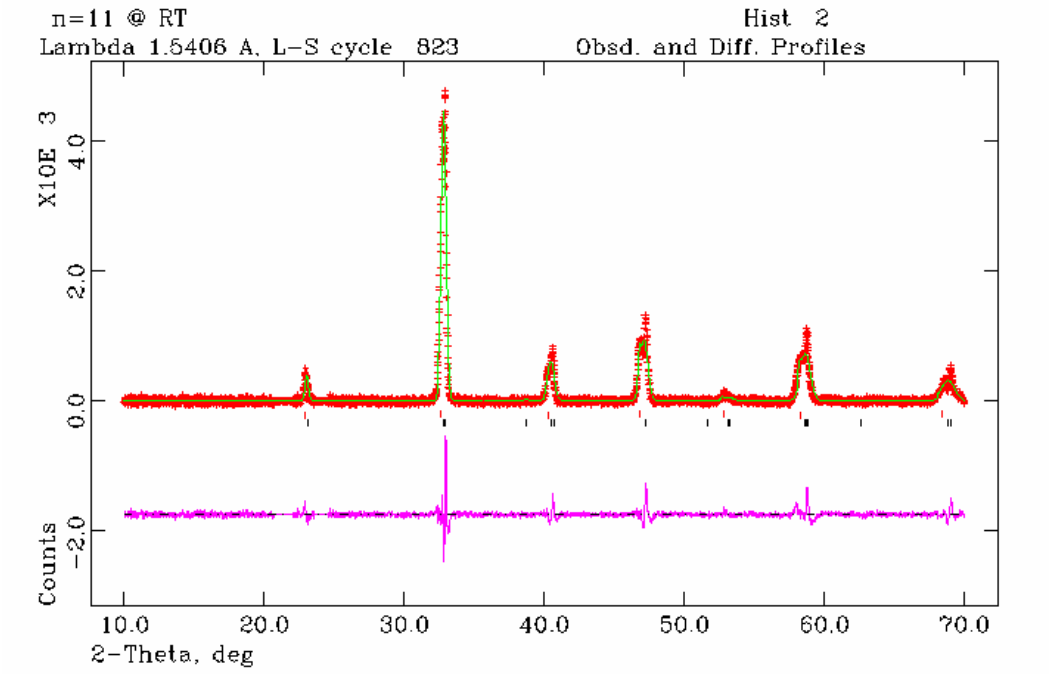


**Figure 3.38 Observed (red), calculated (green) and difference XRD pattern for n=11 refined as two phases, rhombohedral R-3c and cubic Pm-3m.**

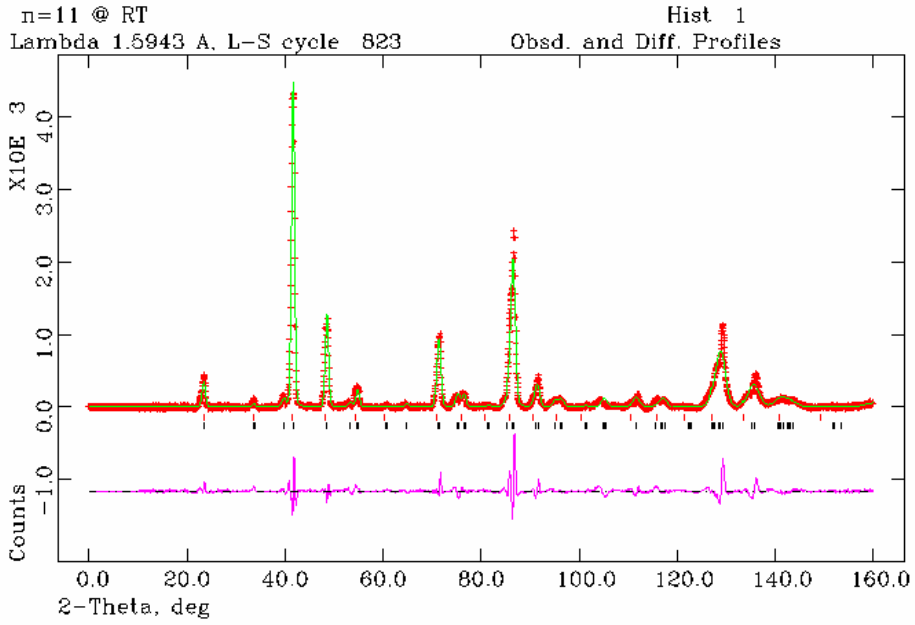


**Figure 3.39 Observed (red), calculated (green) and difference NPD pattern for n=11 refined as two phases, rhombohedral R-3c and cubic Pm-3m.**

Some peaks are very sharp whilst others are not suggesting we have 2 phases. The best fitting was achieved with combined rhombohedral (R-3c) and cubic structures (Pm-3m). The refined fractions for the rhombohedral and cubic phases are 90.5 % and 9.5% respectively. The refinement is not very good but n=11 is out of the scope of this work and not further investigations were done.

| n=11 | R-3c | Pm-3m |
|---|---|---|
| a/Å | 5.4491(7) | 3.8793(7) |
| c/Å | 13.2927(1) | 3.8793(7) |
| V/Å$^3$ | 341.82(8) | 58.38(3) |
| x(O) | 0.4721(2) | |
| Discrepancy factors | | |
| $R_{wp}^X$ / $R_{wp}^N$ (%) | 6.19/11.52 | |
| $R_p^X$ / $R_p^N$ (%) | 8.49/4.19 | |
| $R_F^X$ / $R_F^N$ (%) | 5.34/4.07 | |
| $\chi^2$ | 3.088 | |

R-3c: 6(a) (0,0,1/4) for La/Sr; 6(b) (0,0,0) for Mn/Ti; 18(e) (x,0,1/4) for O.
Pm-3m: 6(a) (0,0,0) for La/Sr; 6(b) (0.5,0.5,0.5) for Mn/Ti; 18(e) (0,0.5,0.5) for O

**Table 3.21 Refined structural parameters for $La_4Sr_8Ti_1Mn_{11}O_{38-\delta}$ (n=11) after Rietveld refinements using combined NPD and XRD data at room temperature.**

Structural characterisation has been done for samples n≤1, i.e., n=0.25, 0.5 and 0.75. In next sections the recorded data are presented.

### 3.3.2.9. $La_4Sr_8Ti_{11.75}Mn_{0.25}O_{38-\delta}$ (n=0.25)

The XRD pattern can be indexed to a cubic structure, space group Pm-3m (Figure 3.40 and Table 3.22).

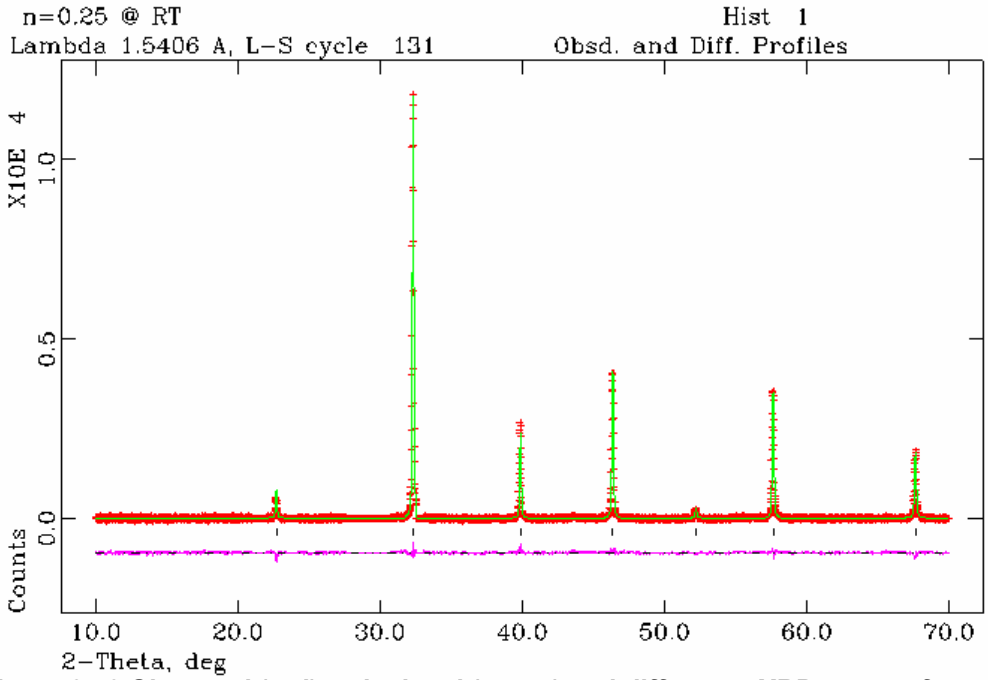


**Figure 3.40 Observed (red), calculated (green) and difference XRD pattern for n=0.5**

| n=0.25 | RT |
|---|---|
| a/Å | 3.9155(4) |
| V/Å$^3$ | 60.01(2) |
| Discrepancy factors | |
| $R_{wp}$ (%) | 5.15 |
| $R_p$ (%) | 3.88 |
| $R_F$ (%) | 3.46 |
| $\chi^2$ | 1.369 |

Space group Pm-3m. The atomic positions are 6(a) (0,0,0) for La/Sr; 6(b) (0.5,0.5,0.5) for Mn/Ti; 18(e) (0,0.5,0.5) for O.

**Table 3.22 Refined structural parameters for Pm-3m $La_4Sr_8Ti_{11.75}Mn_{0.25}O_{38-\delta}$ (n=0.25) after Rietveld refinements using XRD data at room temperature.**

In Figure 3.41 we can observe the XRD patterns for n=0.25 as prepared and in reducing conditions (after 48 hours in 5%$H_2$/Ar).

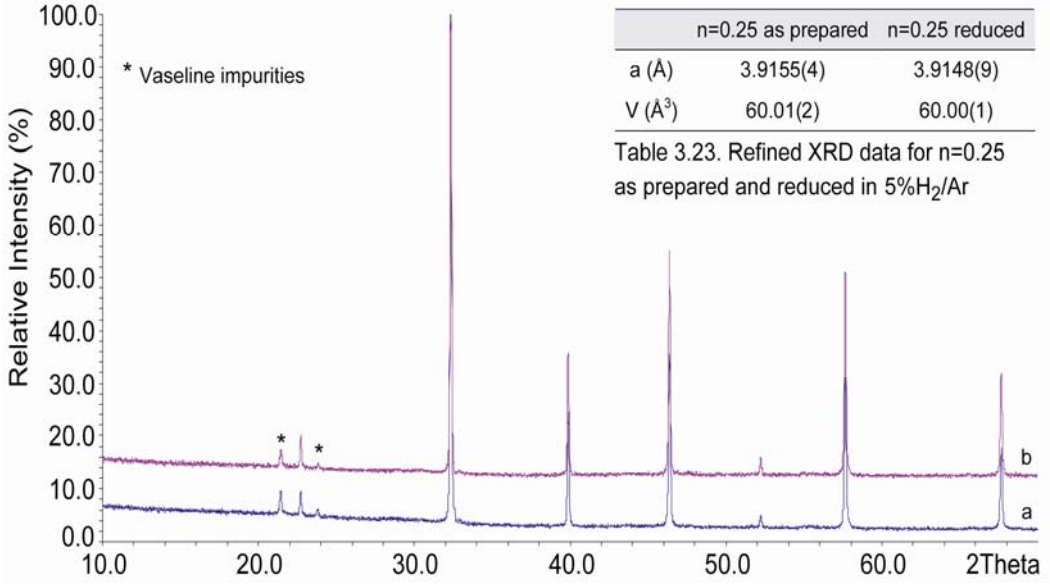


| | n=0.25 as prepared | n=0.25 reduced |
|---|---|---|
| a (Å) | 3.9155(4) | 3.9148(9) |
| V (Å$^3$) | 60.01(2) | 60.00(1) |

Table 3.23. Refined XRD data for n=0.25 as prepared and reduced in 5%$H_2$/Ar

**Figure 3.41 XRD patterns for n=0.25 (a) as prepared and (b) reduced in 5%$H_2$/Ar.**

### 3.3.2.10. $La_4Sr_8Ti_{11.5}Mn_{0.5}O_{38-\delta}$ (n=0.5)

The XRD pattern can be indexed to a cubic structure, space group Pm-3m (Figure 3.42 and Table 3.24).

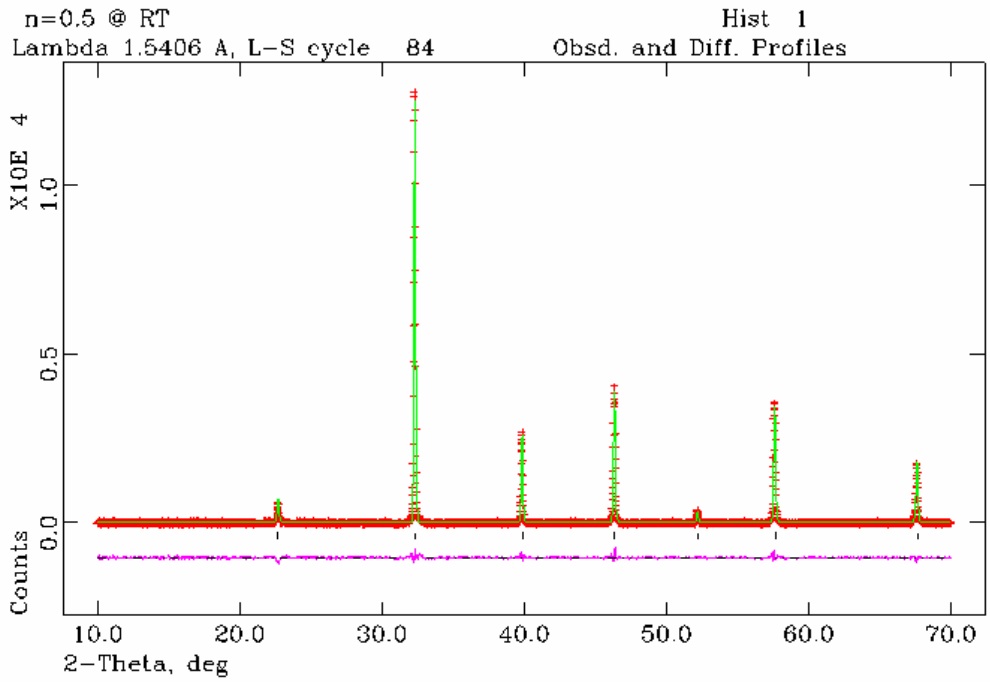


**Figure 3.42 Observed (red), calculated (green) and difference XRD pattern for n=0.5**

| n=0.5 | RT |
|---|---|
| a/Å | 3.9216(2) |
| V/Å$^3$ | 60.31(1) |
| Discrepancy factors | |
| $R_{wp}$ (%) | 5.36 |
| $R_p$ (%) | 3.99 |
| $R_F$ (%) | 2.08 |
| $\chi^2$ | 1.276 |

Space group Pm-3m. The atomic positions are 6(a) (0,0,0) for La/Sr; 6(b) (0.5,0.5,0.5) for Mn/Ti; 18(e) (0,0.5,0.5) for O.

**Table 3.24 Refined structural parameters for Pm-3m $La_4Sr_8Ti_{11.5}Mn_{0.5}O_{38-\delta}$ (n=0.5) after Rietveld refinements using XRD data at room temperature.**

In Figure 3.43 we can observe the XRD patterns for n=0.5 as prepared and in reducing conditions (after 48 hours in 5%$H_2$/Ar).

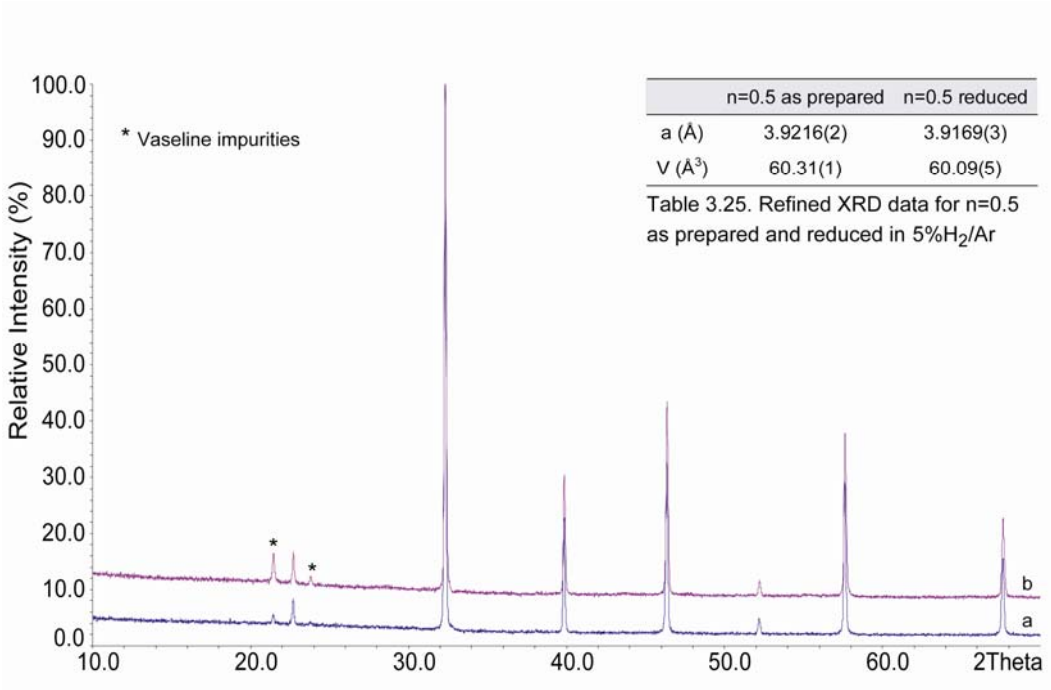


**Figure 3.43 XRD patterns for n=0.5 (a) as prepared and (b) reduced in 5%$H_2$/Ar.**

### 3.3.2.11. $La_4Sr_8Ti_{11.25}Mn_{0.75}O_{38-\delta}$ (n=0.75)

The XRD and NPD patterns can be indexed to a rhombohedral structure, space group R-3c, Figure 3.44, Figure 3.45 and Table 3.26.

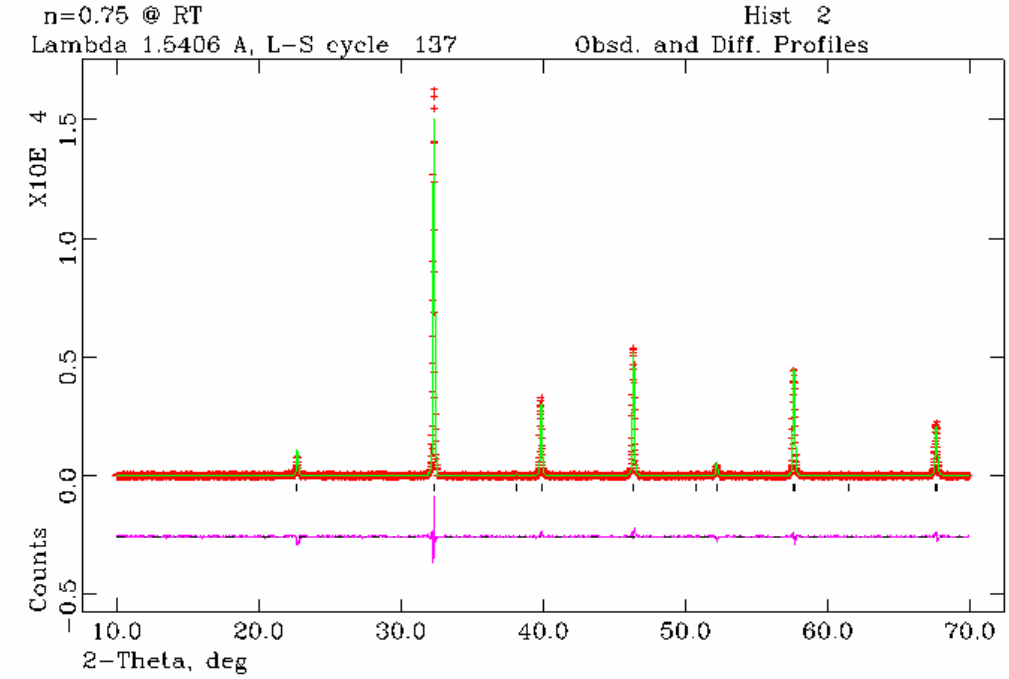


**Figure 3.44 Observed (red), calculated (green) and difference XRD pattern for n=0.75**

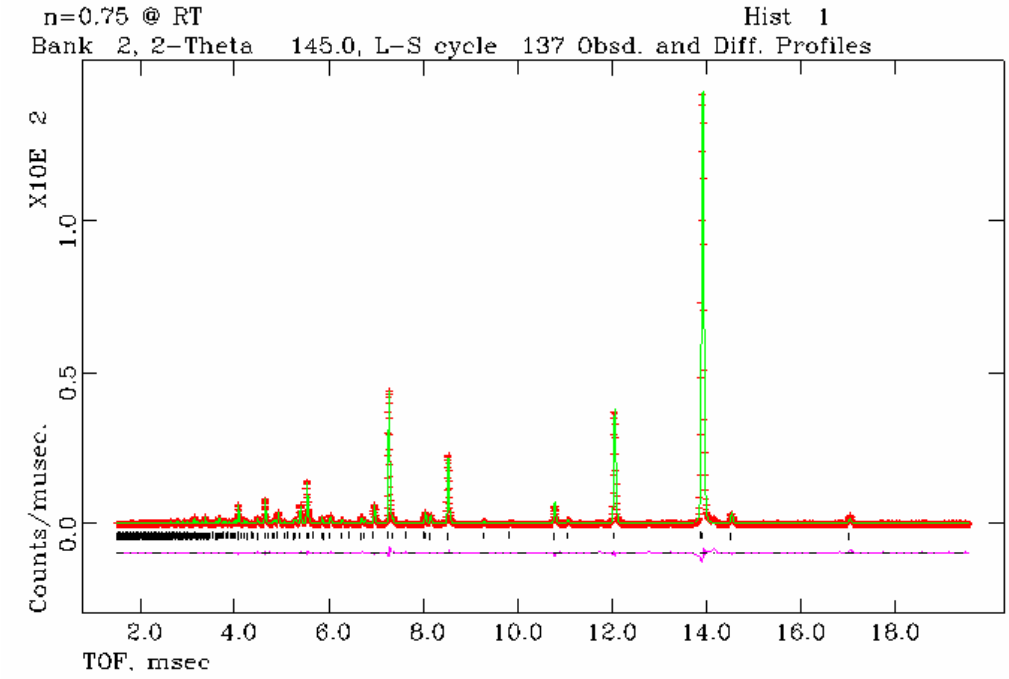


**Figure 3.45 Observed (red), calculated (green) and difference NPD pattern for n=0.75**

| n=0.75 | RT |
|---|---|
| a/Å | 5.5351(9) |
| c/Å | 13.5490(7) |
| V/Å$^3$ | 359.50(7) |
| x(O) | 0.4764(1) |
| Discrepancy factors | |
| $R_{wp}^X$ / $R_{wp}^N$ (%) | 5.27/2.60 |
| $R_p^X$ / $R_p^N$ (%) | 3.98/4.22 |
| $R_F^X$ / $R_F^N$ (%) | 3.47/10.89 |
| $\chi^2$ | 3.570 |

Space group R-3c. The atomic positions are 6(a) (0,0,1/4) for La/Sr; 6(b) (0,0,0) for Mn/Ti; 18(e) (x,0,1/4) for O.

**Table 3.26 Refined structural parameters for R-3c $La_4Sr_8Ti_{11.25}Mn_{0.75}O_{38-\delta}$ (n=0.75) after Rietveld refinements using combined NPD and XRD data at room temperature**

In Figure 3.46 we can observe the XRD patterns for n=0.75 as prepared and in reducing conditions (after 48 hours in 5%$H_2$/Ar).

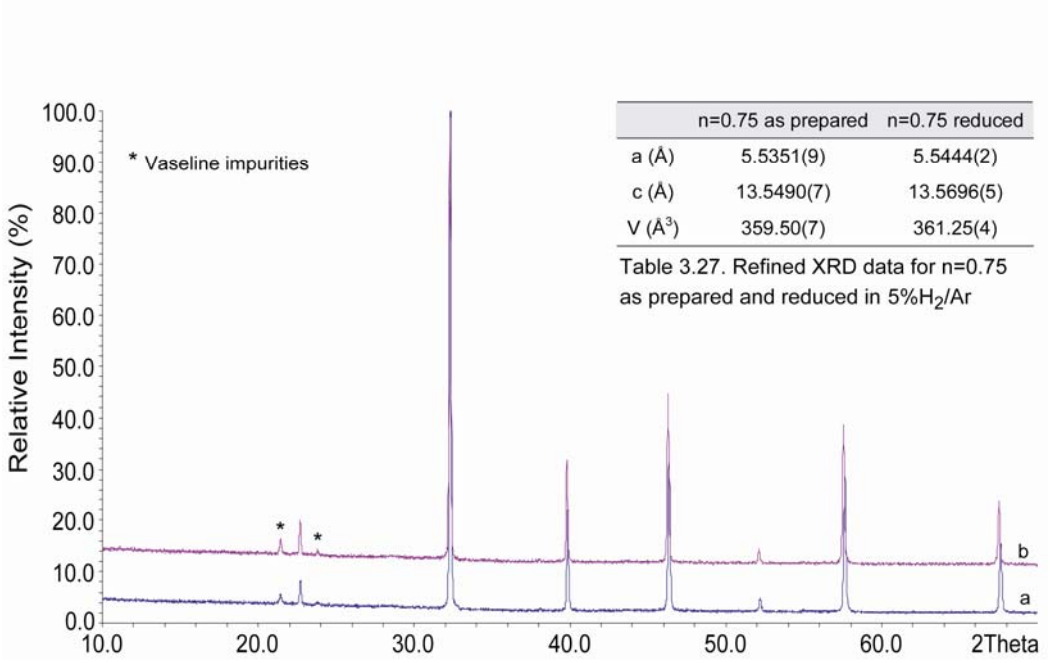


**Figure 3.46 XRD patterns for n=0.75 (a) as prepared and (b) reduced in 5%$H_2$/Ar.**

### 3.3.2.10. Summary

As shown in figure 3.47 and table 3.28, the volume of the unit cell in oxidised conditions gradually decreases with increasing the Mn content following Vegard's law, which indicates a random distribution of Mn in the B-sites. Clearly the rhombohedral distortion may influence how the oxygen excess is accommodated within the perovskite but this must still involve some short range defects. In order to corroborate this some preliminary TGA and TEM studies have been realized; these results are presented in next sections.

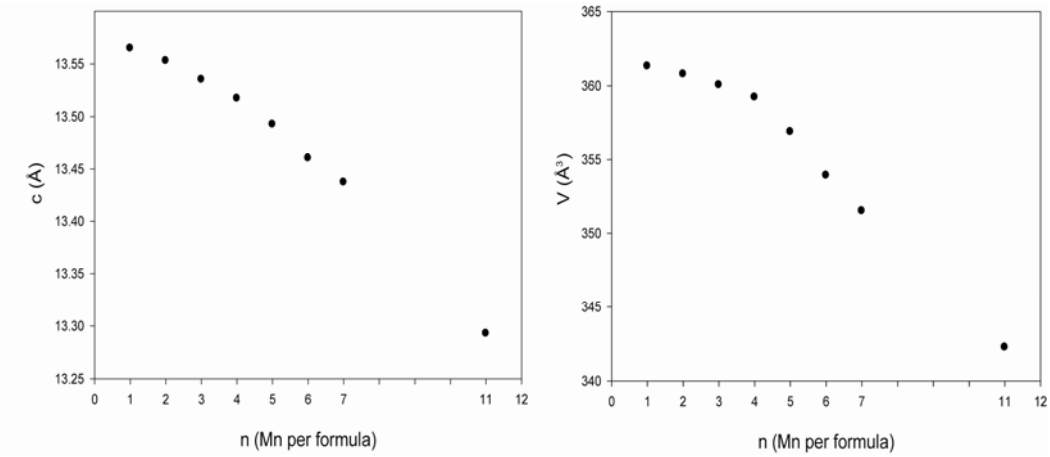


**Figure 3.47 Unit cell parameters as a function of the degree of substitution in the series $La_4Sr_8Ti_{12-n}Mn_nO_{38-\delta}$ as prepared.**

| n | a (Å) | c (Å) | V (Å$^3$) |
|---|---|---|---|
| 1 | 5.5458(6) | 13.5648(1) | 361.31(2) |
| 2 | 5.5442(2) | 13.5529(1) | 360.78(2) |
| 3 | 5.5422(2) | 13.5352(6) | 360.05(2) |
| 4 | 5.5394(8) | 13.5173(3) | 359.21(9) |
| 5 | 5.5265(2) | 13.4927(8) | 356.89(9) |
| 6 | 5.5101(7) | 13.4602(9) | 353.92(8) |
| 7[a] | 5.4960(8) | 13.4371(7) | 351.51(2) |
| 11 | 5.4526(7) | 13.2928(1) | 342.26(8) |

**Table 3.28 Refined structural parameters for R-3c $La_4Sr_8Ti_{12-n}Mn_nO_{38-\delta}$ as prepared after the combined XRD and NPD Rietveld refinements at RT ([a] Only XRD)**

The slope changes at n=4 which would correspond to the nominal perovskite $ABO_3$ with no oxygen excess if $Mn^{+3}$ replaces $Ti^{4+}$.

Table 3.29 shows the evolution of the cell parameters in reducing conditions.

| n | a (Å) | c (Å) | V (Å$^3$) |
|---|---|---|---|
| 1[a] | 5.5482(5) | 13.5807(4) | 362.04(7) |
| 2[a] | 5.5640(6) | 13.5940(8) | 364.46(5) |
| 3 | 5.5554(3) | 13.5810(3) | 362.98(8) |
| 4 | 5.5459(6) | 13.5489(9) | 360.89(3) |
| 5 | 5.5352(2) | 13.5411(5) | 359.30(1) |
| 6 | 5.5258(4) | 13.5078(8) | 357.20(3) |
| 7 | 5.5119(6) | 13.5054(6) | 355.34(8) |

**Table 3.29 Refined structural parameters for $La_4Sr_8Ti_{12-n}Mn_nO_{38-\delta}$ in reducing conditions after the XRD Rietveld refinements at RT ([a] Joint XRD and NPD data)**

Figure 3.48 (a) shows the primitive perovskite cell volumes for the series as prepared in oxidizing conditions. For these samples the primitive volume increases reaching a maximum for n=1 coinciding with the transition phase from cubic to rhombohedral. Then gradually decreases and a change in the slope can be observed at n=4. This correlates with the structure change as n=4 presents the $ABO_3$ perovskite structure.

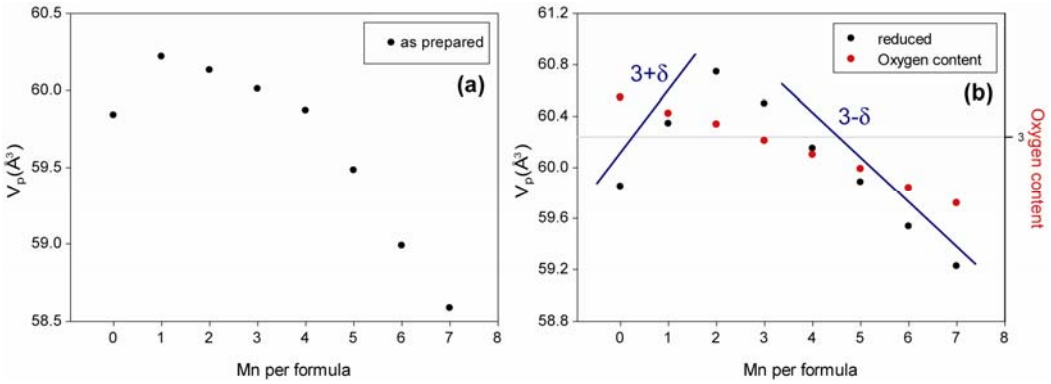


**Figure 3.48 Primitive perovskite cell volumes as a function of the degree of substitution in the series $La_4Sr_8Ti_{12-n}Mn_nO_{38-\delta}$ (a) as prepared and (b) in reducing conditions and correlation with the oxygen content.**

In figure 3.48 (b) the cell volumes for the series in reducing conditions can be observed. For the reduced samples the primitive volume correlates with the cation stoichiometry. The lattice expands as Mn content increases. Once oxygen vacancies appear, at n>3, these dominate causing an overall decrease in lattice volume.

In Figure 3.49 the cell volume increase (calculated as $\Delta V=V_{red}-V_{ox}$) as a function of manganese substitution is shown.

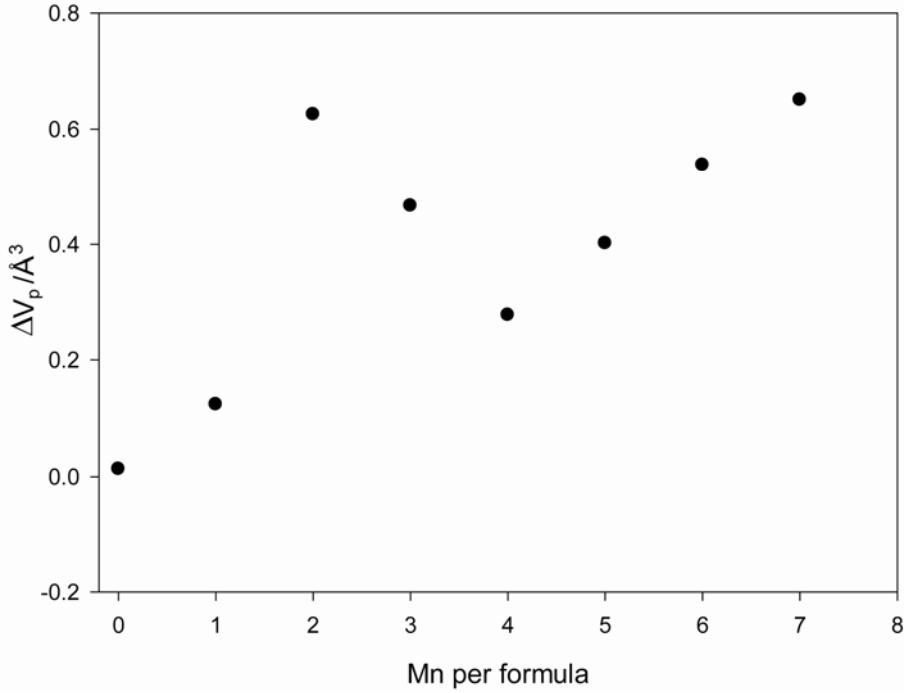


**Figure 3.49 Cell volume increase ($\Delta V=V_{red}-V_{ox}$) in the series $La_4Sr_8Ti_{12-n}Mn_nO_{38-\delta}$ as a function of the degree of manganese substitution.**

Under reducing conditions, substitution of Mn for Ti leads to a lattice expansion. Upon reduction, both Mn and Ti tend to have lower valence states and larger ionic radii, giving rise to larger lattice parameters. The expansion of n=2 and n=3 is larger than the rest of compositions. This anomaly could be due to the difference in positions where the maxima in plots of unit cell volume against Mn content in oxidising and reducing conditions occur as presented in figure 3.48.

### 3.3.3. TGA

TGA experiments were performed during the oxidation at 900ºC in air of a pre-reduced sample as described in section 2.3. From the % of weight regained for each compound it is possible to estimate approximately the amount of oxygen that has been removed during the reduction, Figures 3.50, 3.51 and Table 3.30.

For the cubic phases (n=0, 0.25, 0.5) the amount of oxygen regained is approximately the same. For the rhombohedral phases (n=0.75-7) this increases continuously, Figure 3.52, and it can be seen that the re-oxidation is gradually faster, i.e. higher slopes considering that the same ramp rate was used for each experiment.

Considering that previous work[6] suggested that approximately 10% of Ti is present as $Ti^{+3}$ in the reduced samples it can deduced from the current data that most of the Mn present in the oxidised phases is present as $Mn^{+3}$ although some $Mn^{+4}$ is present (less than 10%). TEM studies should show some crystallographic shears distributed randomly within the perovskite matrix.

| n | Nominal Oxidised Stoichiometry | Reduced | $\Delta\delta$ |
|---|---|---|---|
| 0 | $La_4Sr_8Ti_{12}O_{38}$ | $La_4Sr_8Ti_{12}O_{37.52}$ | 0.48 |
| 0.25 | $La_4Sr_8Ti_{11.75}Mn_{0.25}O_{37.875}$ | $La_4Sr_8Ti_{11.75}Mn_{0.25}O_{37.415}$ | 0.46 |
| 0.50 | $La_4Sr_8Ti_{11.5}Mn_{0.5}O_{37.75}$ | $La_4Sr_8Ti_{11.5}Mn_{0.5}O_{37.23}$ | 0.52 |
| 0.75 | $La_4Sr_8Ti_{11.25}Mn_{0.75}O_{37.625}$ | $La_4Sr_8Ti_{11.25}Mn_{0.75}O_{37.185}$ | 0.44 |
| 1 | $La_4Sr_8Ti_{11}Mn_1O_{37.50}$ | $La_4Sr_8Ti_{11}Mn_1O_{37.05}$ | 0.45 |
| 2 | $La_4Sr_8Ti_{10}Mn_2O_{37}$ | $La_4Sr_8Ti_{10}Mn_2O_{36.4}$ | 0.60 |
| 3 | $La_4Sr_8Ti_9Mn_3O_{36.5}$ | $La_4Sr_8Ti_9Mn_3O_{35.84}$ | 0.66 |
| 4 | $La_4Sr_8Ti_8Mn_4O_{36}$ | $La_4Sr_8Ti_8Mn_4O_{35.3}$ | 0.70 |
| 5 | $La_4Sr_8Ti_7Mn_5O_{35.5}$ | $La_4Sr_8Ti_7Mn_5O_{34.74}$ | 0.76 |
| 6 | $La_4Sr_8Ti_6Mn_6O_{35}$ | $La_4Sr_8Ti_6Mn_6O_{33.99}$ | 1.01 |
| 7 | $La_4Sr_8Ti_5Mn_7O_{34.5}$ | $La_4Sr_8Ti_5Mn_7O_{33.38}$ | 1.12 |

**Table 3.30 Stoichiometry of the reduced and nominal oxidised phases and amount of oxygen loss per formula.**

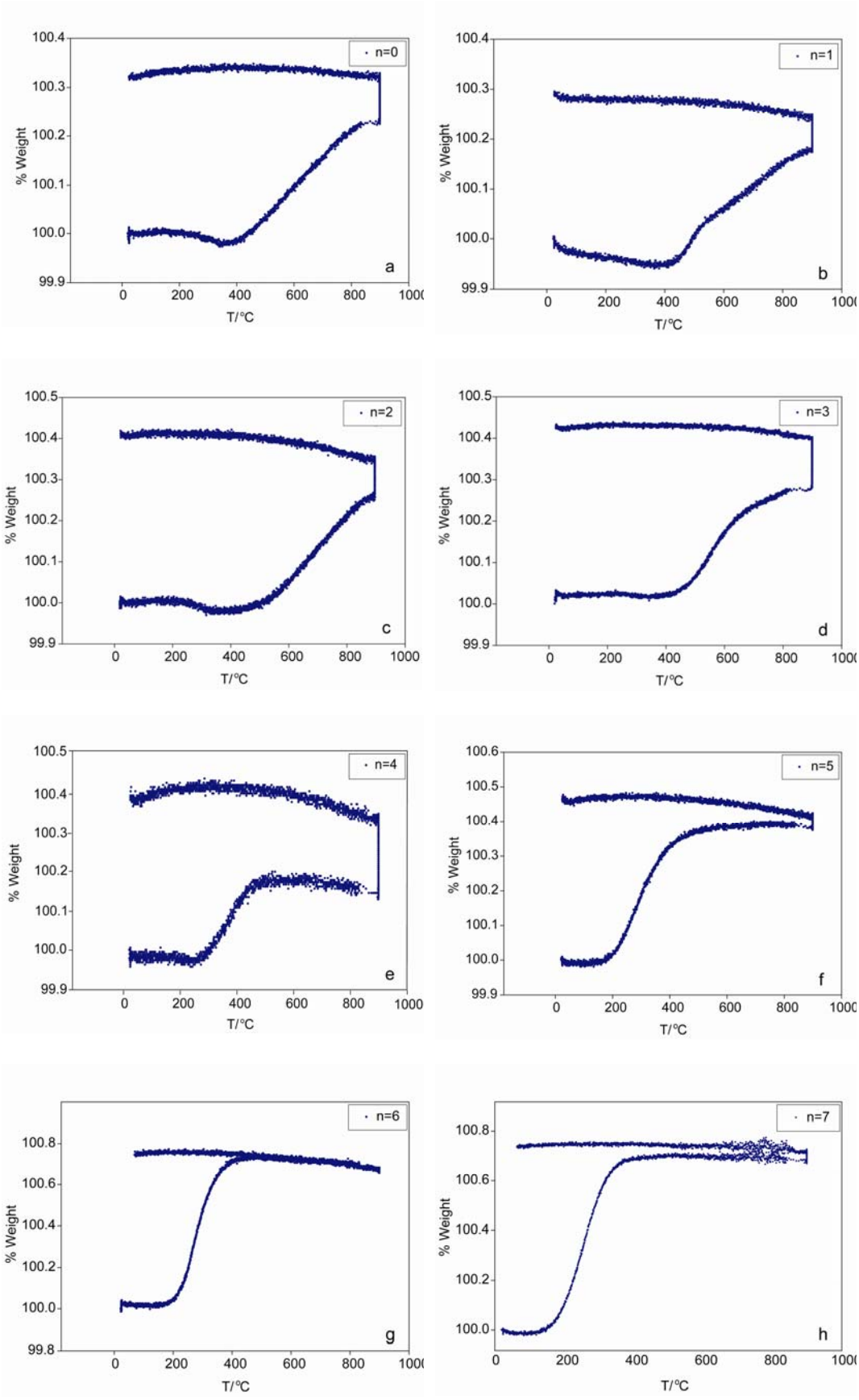


**Figure 3.50 TGA experiment recorded during the oxidation of pre-reduced samples of $La_4Sr_8Ti_{12-n}Mn_nO_{38-\delta}$ from a) n=0 to h) n=7.**

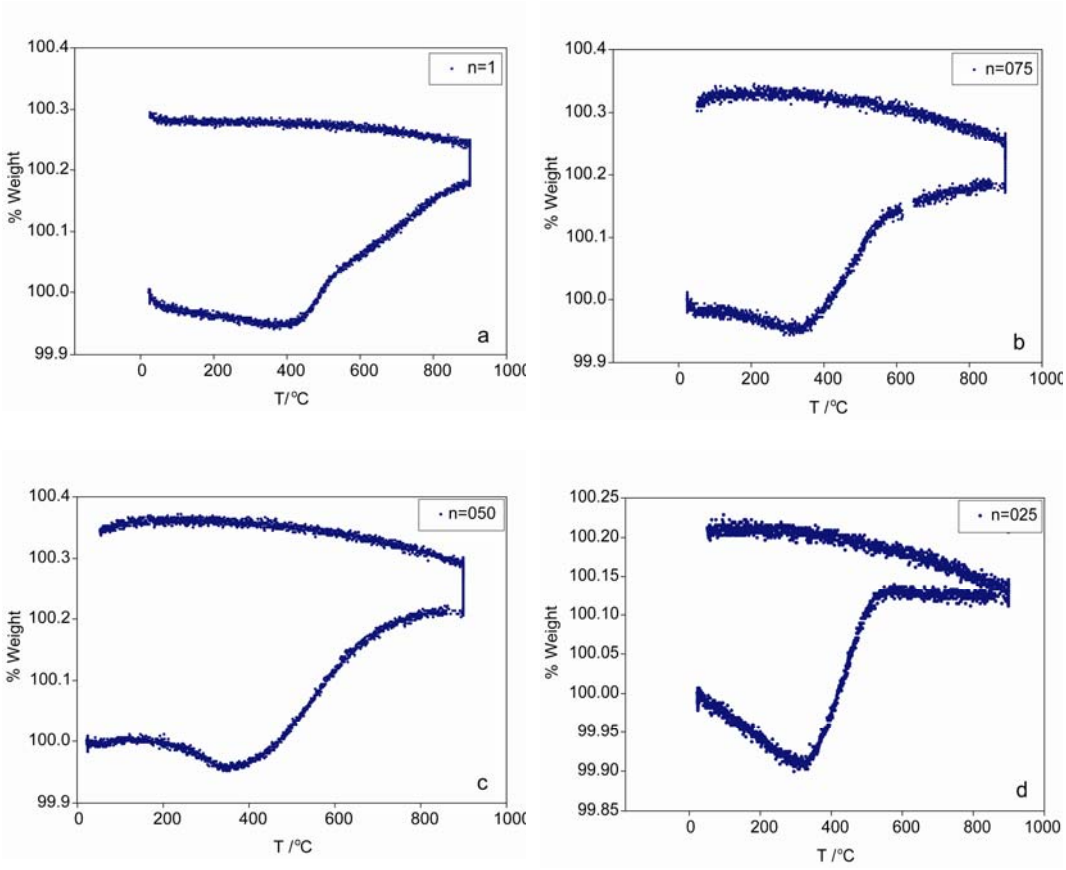


**Figure 3.51 TGA experiment recorded during the oxidation of the pre-reduced samples of $La_4Sr_8Ti_{12-n}Mn_nO_{38-\delta}$ for n≤1.**

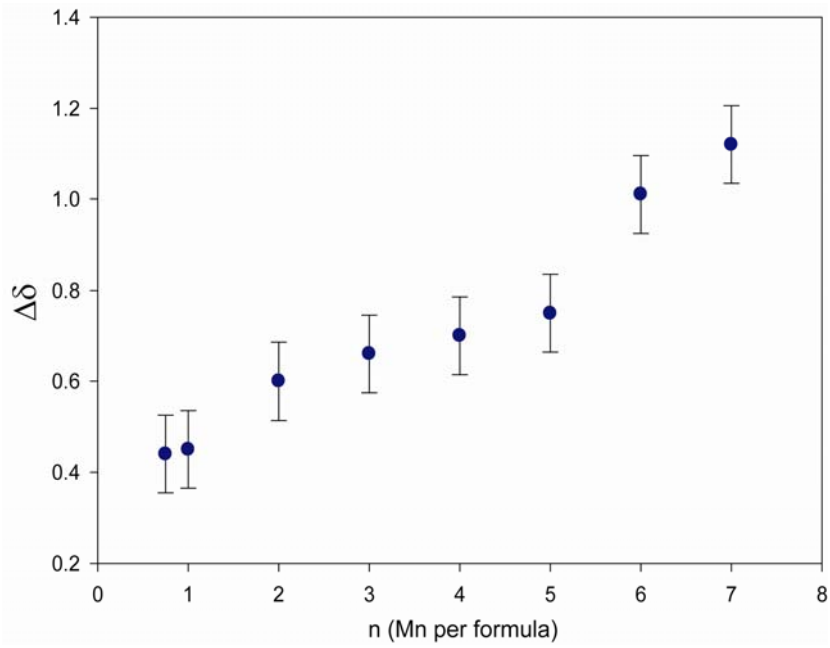


**Figure 3.52 Evolution of delta values of the series $La_4Sr_8Ti_{12-n}Mn_nO_{38-\delta}$ for the rhombohedral phases.**

### 3.3.4. SEM studies

It has been proved that the electrochemical activity of the cermet anode strongly depends on the three-phase boundary (TPB) composed of the sample grains, YSZ and pores. Larger TPB provides larger reacting surface area. Accordingly, the length of triple-phase-boundary plays an important role in overall performance of the cell. The original powder preparation technique can influence the TPB length.

Some SEM micrographs of different samples, Figures 3.53, 3.54 and 3.55, have been recorded on synthesized pellets. There has been observed a good particle size and a good distribution of the pores. Nevertheless, further optimisation of the microstructure is always advisable.

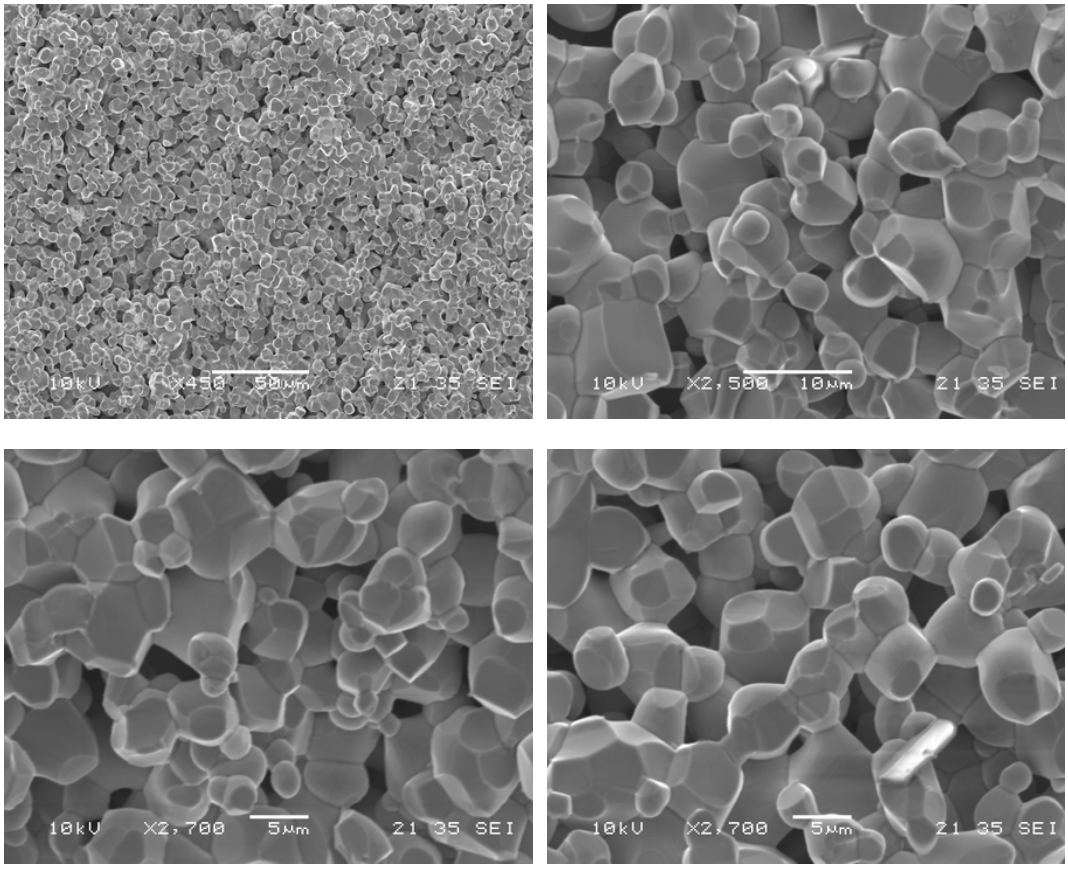


**Figure 3.53 SEM micrographs of the sample $La_4Sr_8Ti_9Mn_3O_{38-\delta}$ (n=3)**

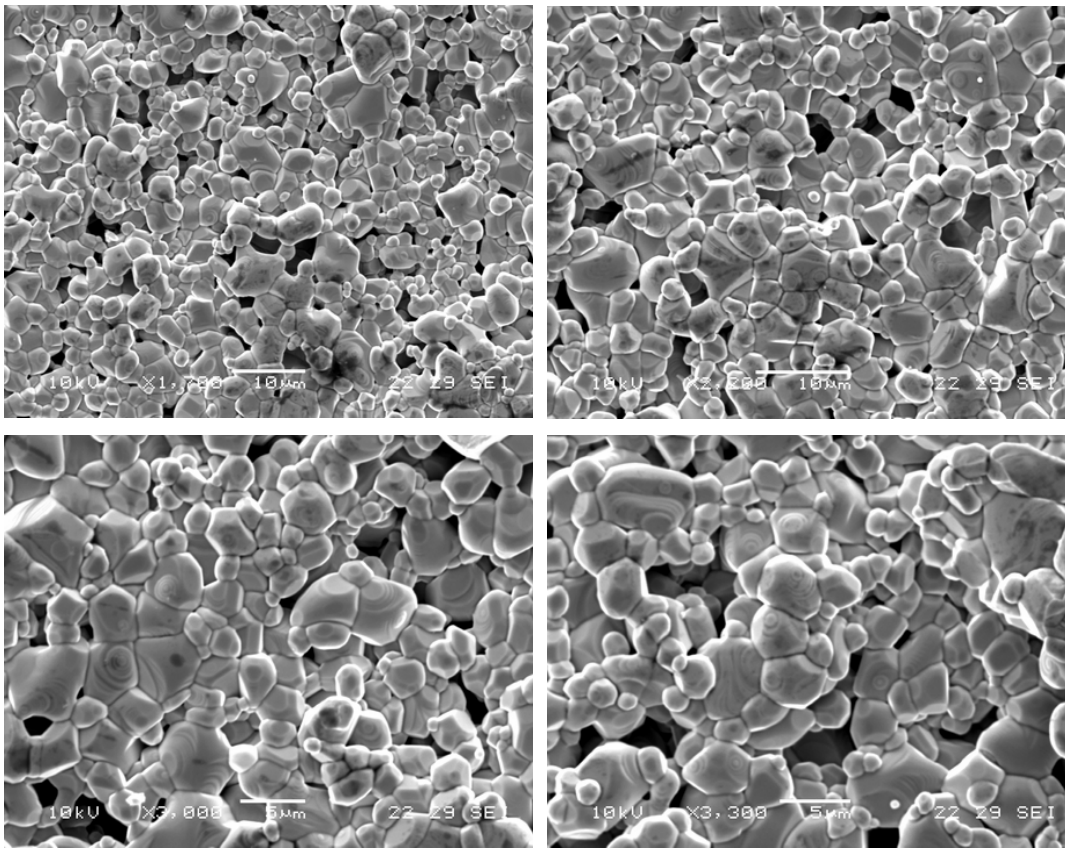


**Figure 3.54 SEM micrographs of the sample $La_4Sr_8Ti_8Mn_4O_{38-\delta}$ (n=4)**

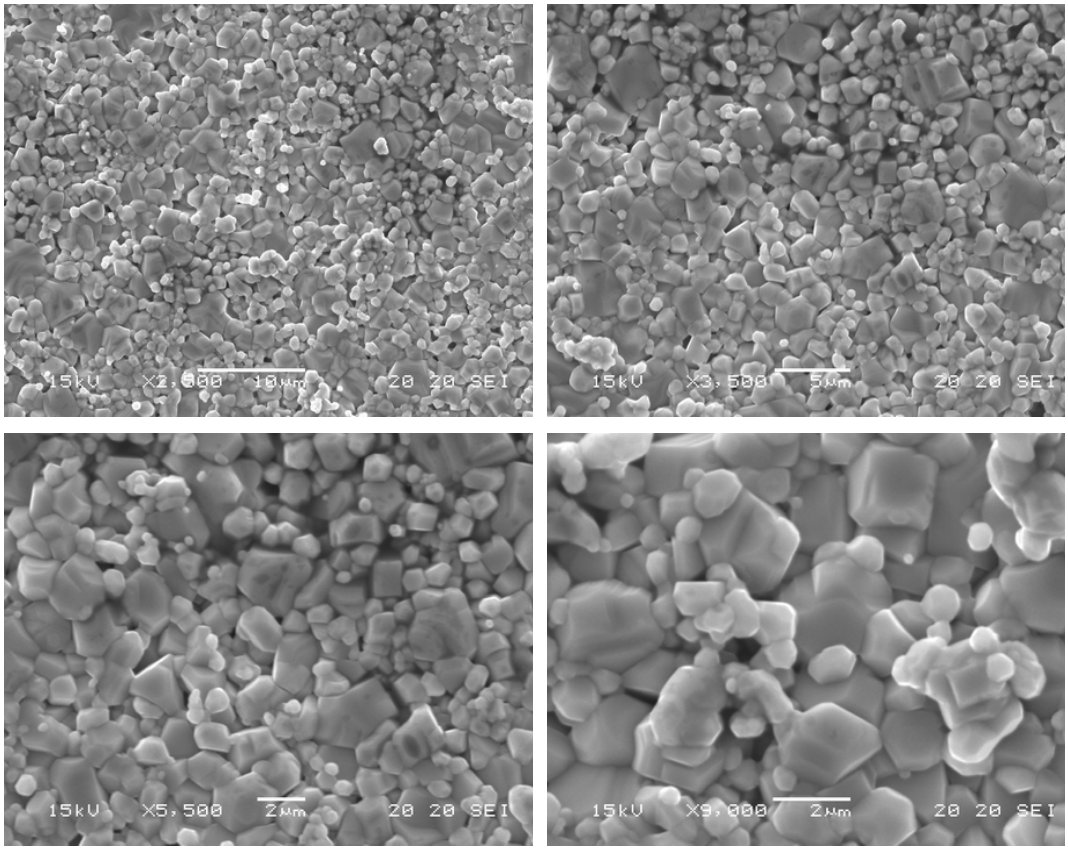


**Figure 3.55 SEM micrographs of the sample $La_4Sr_8Ti_7Mn_5O_{38-\delta}$ (n=5)**

### 3.3.5. TEM studies

Figures 3.56 and 3.57 show some preliminary HRTEM studies that have been done on samples n=2 and n=3.

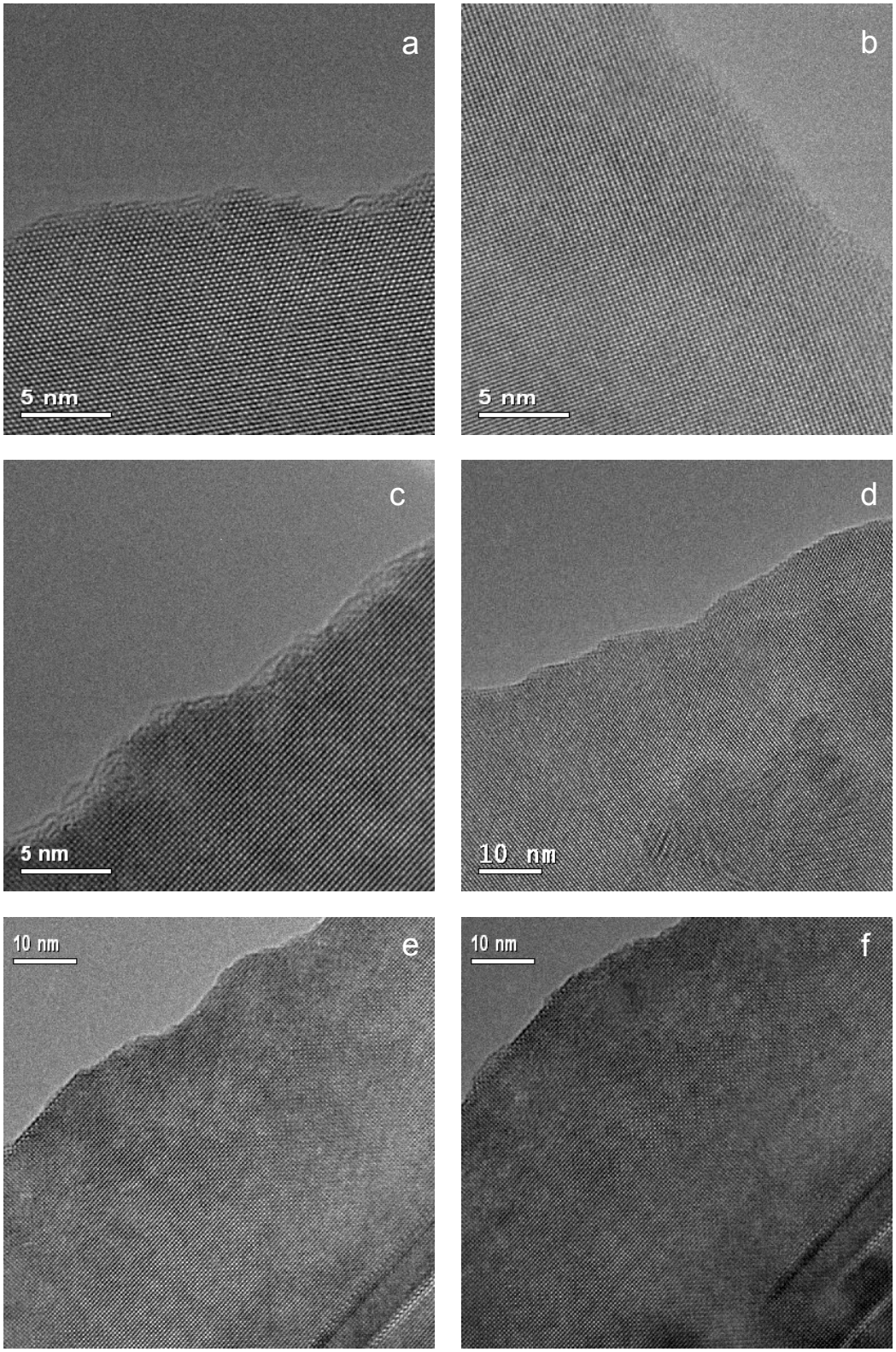


**Figure 3.56 TEM micrographs of the sample n=2 ($La_4Sr_8Ti_{10}Mn_2O_{38-\delta}$)**

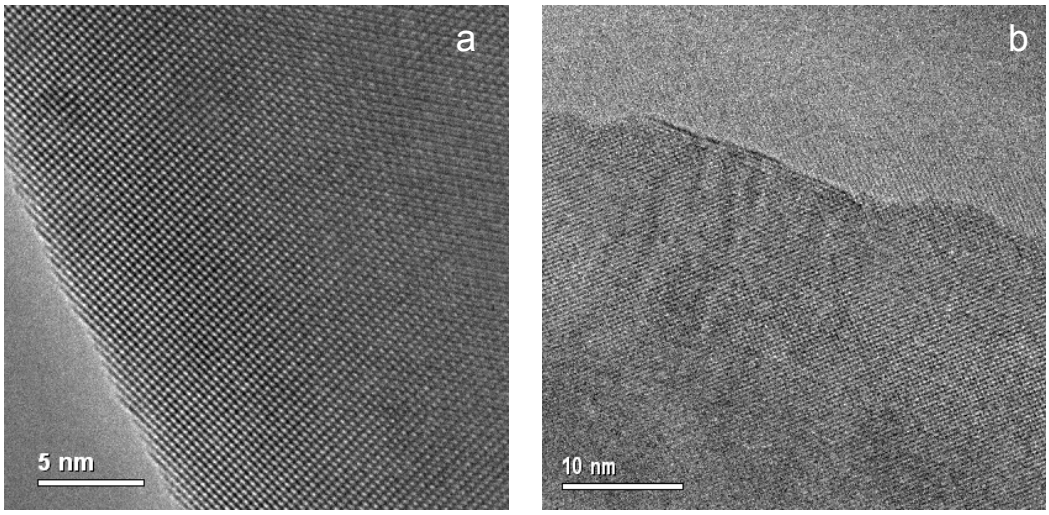


**Figure 3.57 TEM micrographs of the sample n=3 ($La_4Sr_8Ti_9Mn_3O_{38-\delta}$)**

These preliminary investigations have revealed that some crystallographic shears distributed randomly within a perovskite matrix may remain in the structure, Figure 3.56 d, e and f (for n=2) and Figure 3.57 b (for n=3). There we can see the presence of randomly distributed defects embedded within a perovskite framework. That implies that the oxygen overstoichiometry is compatible with rhombohedral distortions in the oxygen sublattice. Indeed, $La_4Sr_{n-4}Ti_nO_{3n+2}$ ($4 \leq n \leq 6$) phases show very distorted $TiO_6$ octahedra and are also able to accommodate the oxygen excess[12].

A model of the defects is shown in Figure 3.58.

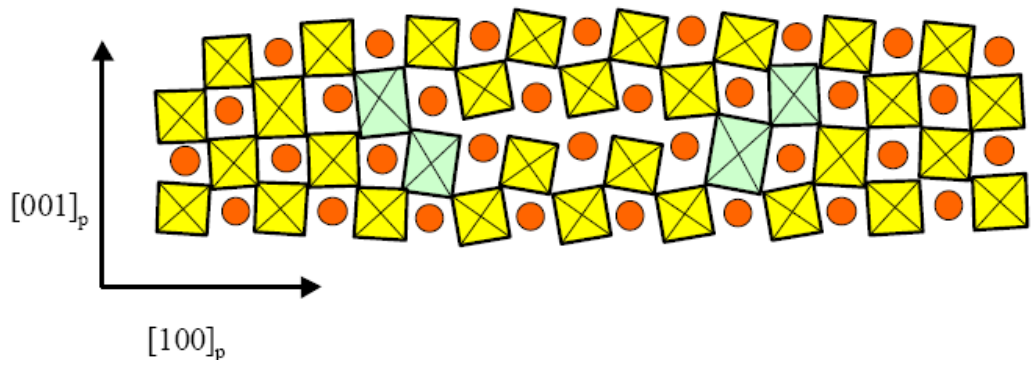


**Figure 3.58 Structural model proposed for the short range shearing (linear defect)**

## 3.4. Conclusions[13]

A new family of perovskite titanates with formulas $La_{4+n}Sr_{8-n}Ti_{12-n}Mn_nO_{38}$ and $La_4Sr_8Ti_{12-n}Mn_nO_{38-\delta}$ have been structural characterized by means of different techniques.

Due to the presence of $Mn^{+4}$ the phases belonging to the $La_{4+n}Sr_{8-n}Ti_{12-n}Mn_nO_{38}$ series present reflections at $2\theta$ 28-31º on the XRD patterns, which are characteristic of layered domains. Additionally preliminary TEM studies have corroborated the presence of these layered domains in the phases. As such layers appear to have a large negative effect over the electrochemical properties only a few compounds of these series have been characterised.

Although the series $La_4Sr_8Ti_{12-n}Mn_nO_{38-\delta}$ still exhibit simple perovskite XRD patterns, they no longer exhibit the simplest cubic form. Even at low levels of Mn substitution (n=0.75) the combined NPD and XRD patterns could be better refined as a rhombohedral structure (R−3c). As Mn substitution increases the rhombohedral splitting becomes more pronounced. Rhombohedral distortions are common in perovskite manganites and cobaltites and can be ascribed to the R−3c space group as the result of equivalent antiphase octahedra tilting along all the three crystallographic axes, i.e., a−a−a− following Glazier's notation[9]. The volume of the unit cell gradually decreases with increasing the Mn content following Vegard's law, which indicates a random distribution of Mn in the B-sites. In reducing conditions the primitive volume correlates with the oxygen content. Clearly the rhombohedral distortion may influence how the oxygen excess is accommodated within the perovskite but this must still involve some short-range defects. Preliminary HRTEM investigations have revealed that some crystallographic shears distributed randomly within a perovskite matrix remain in the structure, which implies that the oxygen overstoichiometry is compatible with rhombohedral distortions in the oxygen sublattice.

Although at room temperature the structures remain rhombohedral it has been showed that at higher temperatures there is a transition phase to a cubic structure. For n=1 both phases cohabit at 300°C in the oxidised sample and at 500°C only the cubic phase remains. In reducing conditions the phase transition temperature is slightly higher. For n=2 the same pattern is observed and the transition phase temperature is slightly higher than for n=1.

TGA studies have showed that the Mn present is mainly as $Mn^{+3}$ although some $Mn^{+4}$ is present.

The microstructure of the synthesized pellets show a good particle size and a good distribution of the pores, which it is an important factor to improve the electrical response.

## 3.5. References

[1] J. Canales-Vazquez, M. J. Smith, J. T. S. Irvine, and W. Z. Zhou, *Advanced Functional Materials*, 2005, **15**, 1000.

[2] J. Canales-Vazquez, S. W. Tao, and J. T. S. Irvine, *Solid State Ionics*, 2003, **159**, 159.

[3] J. Canales-Vazquez, J. C. Ruiz-Morales, J. T. S. Irvine, and W. Z. Zhou, *Journal of the Electrochemical Society*, 2005, **152**, A1458.

[4] O. A. Marina, N. L. Canfield, and J. W. Stevenson, *Solid State Ionics*, 2002, **149**, 21.

[5] O. A. Marina and R. L. Pederson, Proceedings of the 5th European Solid Oxide Fuel Cell Forum, Lucerne, Switzerland, 2002.

[6] J. Canales-Vazquez, 'Studies on oxygen excess perovskite-based titanates for SOFC fuel electrodes', PhD thesis, St Andrews, 2003.

[7] F. Lichtenberg, A. Herrnberger, K. Wiedenmann, and J. Mannhart, *Progress in Solid State Chemistry*, 2001, **29**, 1.

[8] A. C. Larson and R. B. von Dreele, *GSAS program; Los Alamos National Lab. Rep. No. LA-UR-86748*, 1994.

[9] A. M. Glazer, *Acta Crystallographica*, 1972, **B28**, 3384.

[10] H. M. Rietveld, *J. Appl. Crystallogr.*, 1969, **65**.

[11] C. J. Howard and H. T. Stokes, *Acta Crystallographica*, 1998, **B**, 782.

[12] J. S. Canales-Vazquez, J. T. S. Irvine, and W. Z. Zhou, *Journal of Solid State Chemistry*, 2004, **177**, 2039.

[13] A. Ovalle, J. C. Ruiz-Morales, J. Canales-Vazquez, D. Marrero-Lopez, and J. T. S. Irvine, *Solid State Ionics*, 2006, **177**, 1997.

# 4

# Electrical and magnetic characterisation

## 4.1. Introduction

The electrical and magnetic properties of the family of perovskite titanates with formula $La_4Sr_8Ti_{12-n}Mn_nO_{38-\delta}$ have been investigated. As it has been showed in the previous chapter these phases present a rhombohedral (R-3c) unit cell at room temperature but cubic (Pm-3m) above 500°C. In addition they present some local defects where we believe the oxygen overstoichiometry characteristic of these phases is accommodated. The electrical properties have been investigated using ac impedance spectroscopy and four terminal dc measurements. By means of impedance spectroscopy we can separate responses for bulk, grain boundary and electrode processes. These responses are often dependent on the microstructure of the material. Mn substitution appears not to have a large impact on the bulk conductivity of the phases studied, which remains close to the values observed in other related titanates, although the grain boundary contributions are largely improved. Four terminal dc measurements have been done to evaluate the total conductivity when the resistance of the material is lower than the resistance due to the jig design. Magnetic studies have shown that at low values of n the samples present a paramagnetic behaviour but antiferromagnetic at higher values of manganese substitution. From the magnetic studies and conductivity as a function of the $pO_2$ measurements we can determine the oxidation state of manganese and the type of conductivity present in the samples of these series.

## 4.2. AC Impedance spectroscopy

Impedance studies were carried out on the rhombohedral members of the $La_4Sr_8Ti_{12-n}Mn_nO_{38-\delta}$ series, in static air and in dry 5%$H_2$ in Ar.

### 4.2.1. $La_4Sr_8Ti_{11.25}Mn_{0.75}O_{38-\delta}$ (n=0.75)

The AC impedance responses in static air consisted typically of two well-defined arcs, one associated with the grain boundary ($2\times10^{-9}$ $Fcm^{-1}$) and the second with bulk processes ($3\times10^{-11}$ $Fcm^{-1}$). At temperatures above 700 °C, only the grain boundary response was observed as shown in Figure 4.1 (a) and (b).

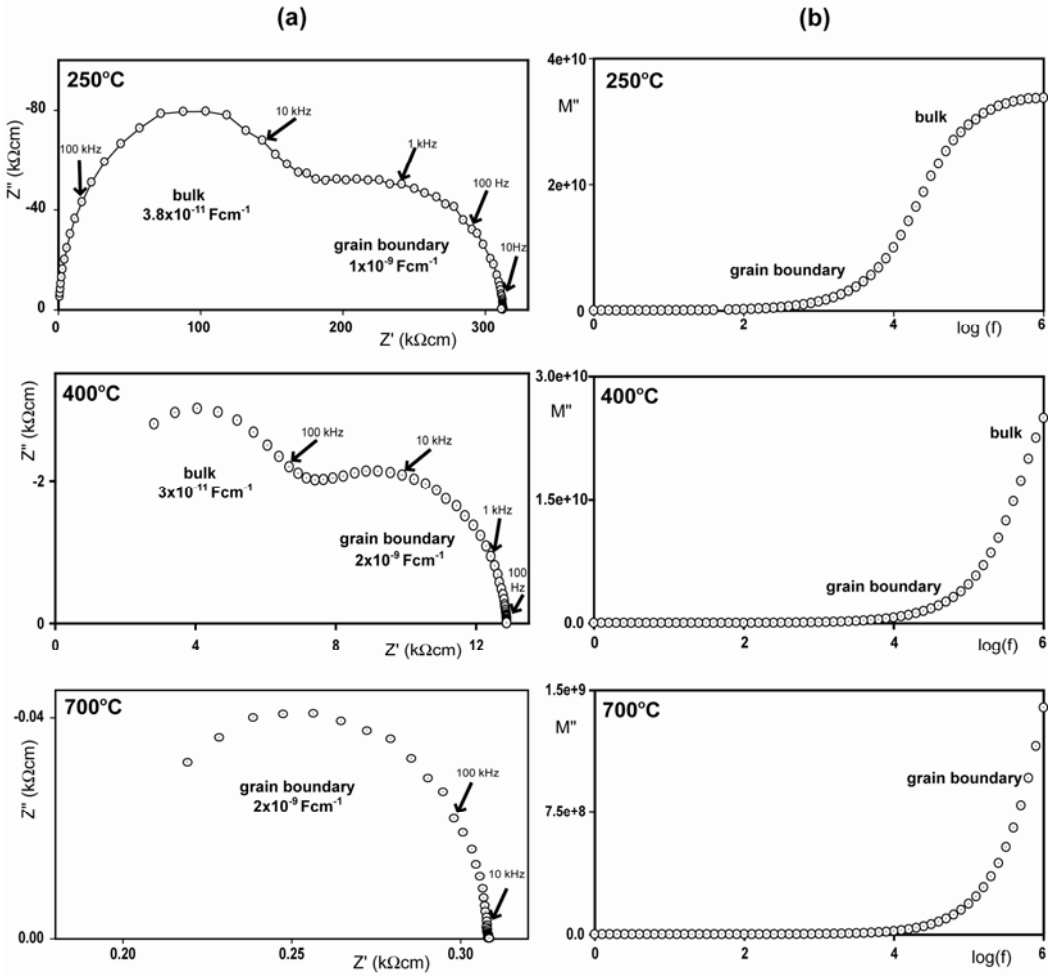


**Figure 4.1 (a) Nyquist plots showing the change with temperature in the bulk and grain boundary contributions of a $La_4Sr_8Ti_{11.25}Mn_{0.75}O_{38-\delta}$ (n=0.75) pellet and (b) the related modulus (M″).**

For the lower temperatures the impedance spectra could be fitted as two R-CPE (i.e., a resistor and a constant phase element in parallel) in series. In Figure 4.2 the equivalent circuits and fitting parameters for T=250°C are showed.

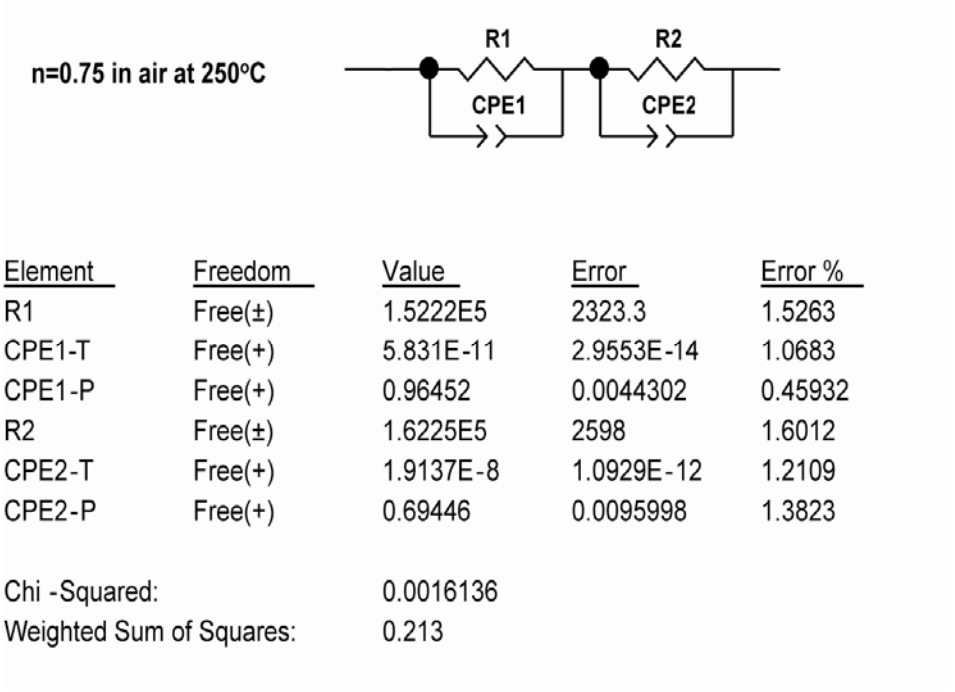


| Element | Freedom | Value | Error | Error % |
|---|---|---|---|---|
| R1 | Free(±) | 1.5222E5 | 2323.3 | 1.5263 |
| CPE1-T | Free(+) | 5.831E-11 | 2.9553E-14 | 1.0683 |
| CPE1-P | Free(+) | 0.96452 | 0.0044302 | 0.45932 |
| R2 | Free(±) | 1.6225E5 | 2598 | 1.6012 |
| CPE2-T | Free(+) | 1.9137E-8 | 1.0929E-12 | 1.2109 |
| CPE2-P | Free(+) | 0.69446 | 0.0095998 | 1.3823 |
| Chi -Squared: | | 0.0016136 | | |
| Weighted Sum of Squares: | | 0.213 | | |

**Figure 4.2 Equivalent circuits (non-linear fitting) for n=0.75 at 250°C. The low CPE2-P indicates a large deviation from the ideal model in the grain boundary.**

The parameter CPE-T obtained using a non-linear fitting method is not the capacitance associated to the process. In this case, the capacitance can be estimated from the definition of the relaxation frequency:

$$RC = \frac{1}{2\pi f} = [R(CPE-T)]^{\frac{1}{n}} \qquad [4.1]$$

Where n is CPE-P in the data fit table.

From equation 4.1 the capacitance can be calculated as:

$$C = R^{\frac{1-n}{n}}(CPE-T)^{\frac{1}{n}} \qquad [4.2]$$

Thus the capacitance associated with the bulk and grain boundary processes are those showed in Figure 4.1.

The Arrhenius plots of this phase corresponding to overall and bulk conductivities are showed in Figure 4.3. The total activation energy is 0.65 eV. The overall conductivity is dominated by the bulk response.

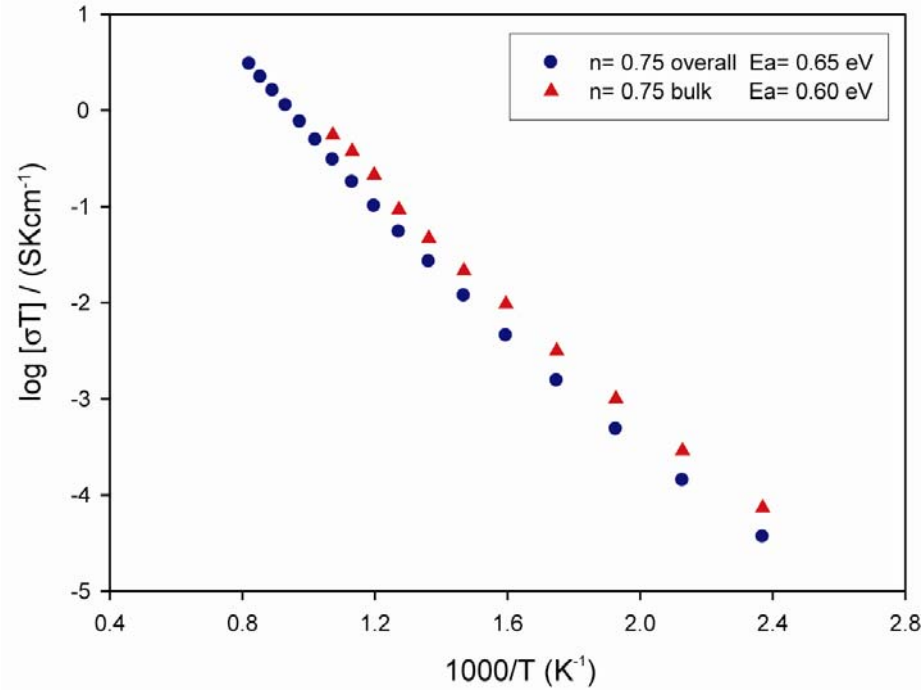


**Figure 4.3 Arrhenius plots of the bulk and overall conductivity corresponding to $La_4Sr_8Ti_{11.25}Mn_{0.75}O_{38-\delta}$ (n=0.75) in air. The total conductivity is limited by the bulk contribution**

Impedance studies under more reducing conditions were limited due to the very high total conductivity of these phases. Four terminal dc measurements were carried out to study the conductivity in 5% $H_2$ in Ar. In this case, as it was said in Chapter 2, it is not possible to differentiate between processes occurring at the bulk, grain boundary, etc.

The total conductivity of the sample improves clearly under reducing conditions as it is showed in Figure 4.4. There is an increase on the total conductivity of two orders of magnitude, i.e. 2mScm$^{-1}$ at 950°C in air and at the same temperature in 5%$H_2$ a value of 0.464 Scm$^{-1}$ was obtained.

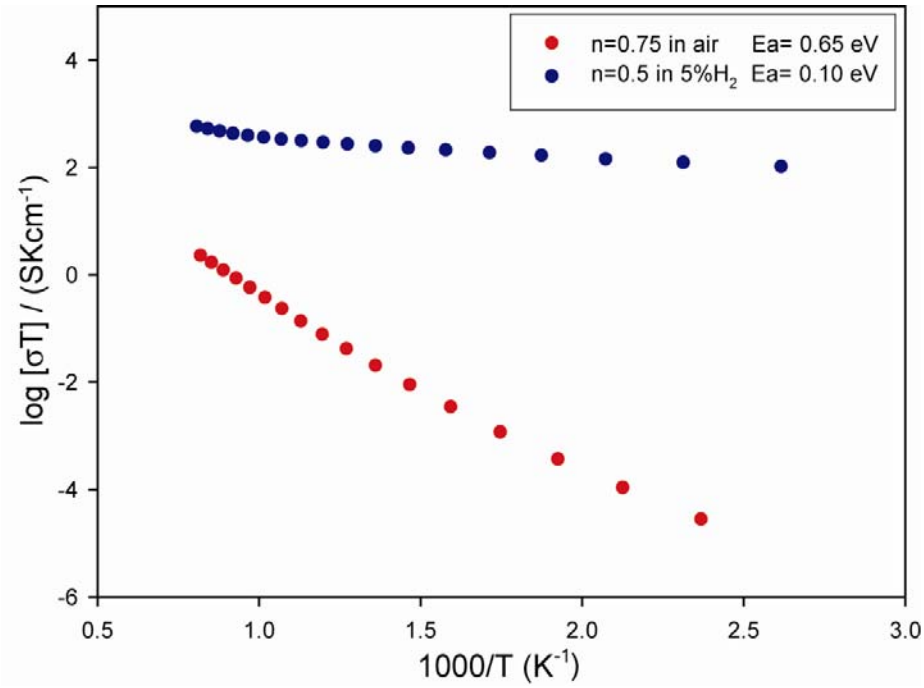


**Figure 4.4 Arrhenius plots of the overall conductivity corresponding to n=0.75 in air and in 5%$H_2$ in Ar. The total conductivity increases two orders of magnitude in reducing conditions.**

### 4.2.2. $La_4Sr_8Ti_{11}Mn_1O_{38-\delta}$ (n=1)

The AC impedance responses in static air consisted typically of two well-defined arcs, one associated with the grain boundary ($3\times10^{-9}$ $Fcm^{-1}$) and the second with bulk processes ($1\times10^{-11}$ $Fcm^{-1}$). At temperatures above 400°C, only the grain boundary response was observed as shown in the Nyquist plots in Figure 4.5 (a) and in the spectroscopy plots of the imaginary contribution of the electric modulus (M"), Figure 4.5 (b). No low-frequency phenomena associated with electrode processes were observed in the range of temperatures studied.

The AC Impedance responses at low temperatures could be fitted as two R-CPE (i.e., a resistor and a constant phase element in parallel) in series, Figure 4.6. At 600°C only one R-CPE in parallel was used. For n=1 the values of CPE-P are closer to 1. This is an indication that where are closer to the ideal model.

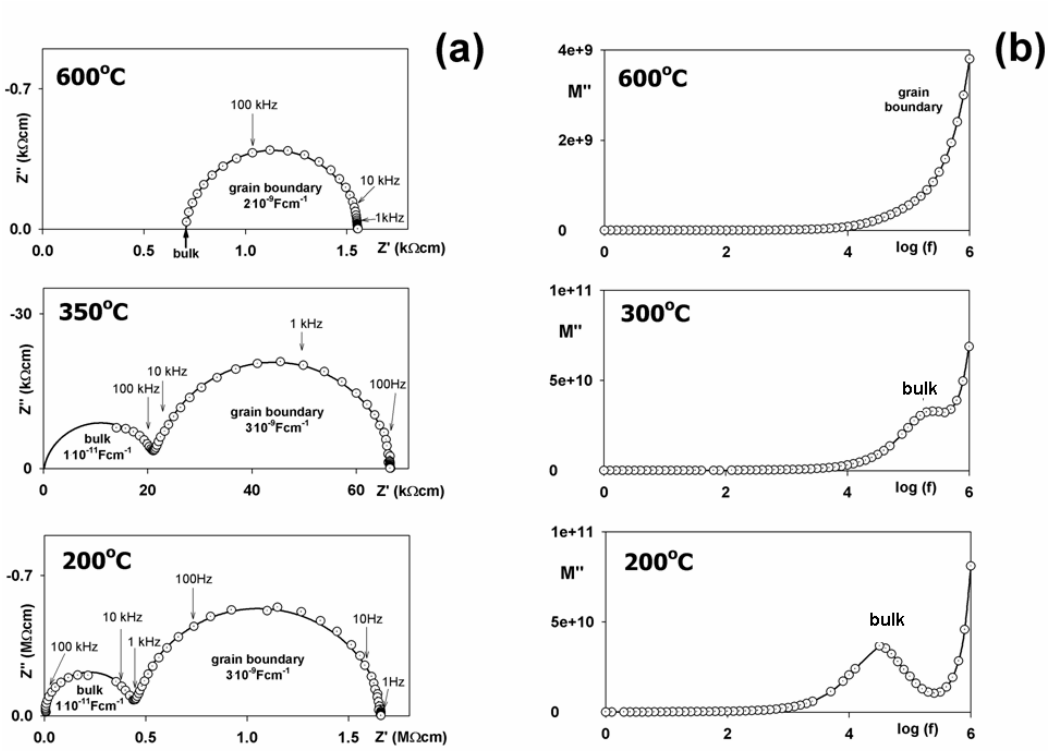


**Figure 4.5 (a) Nyquist plots showing the temperature dependence of the bulk and grain boundary contributions of a $La_4Sr_8Ti_{11}Mn_1O_{38-\delta}$ (n=1) pellet (b) Temperature variation of the related modulus (M″).**

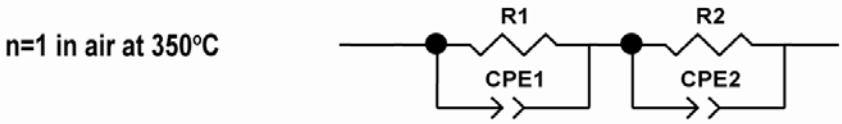


| Element | Freedom | Value | Error | Error % |
|---|---|---|---|---|
| R1 | Free(+) | 18264 | 47.969 | 0.26264 |
| CPE1-T | Free(+) | 1.9129E-11 | 6.1659E-12 | 1.007 |
| CPE1-P | Free(+) | 0.90186 | 0.0074868 | 0.83015 |
| R2 | Free(+) | 39385 | 145.3 | 0.36892 |
| CPE2-T | Free(+) | 5.9149E-9 | 1.495E-10 | 0.8275 |
| CPE2-P | Free(+) | 0.92558 | 0.0027978 | 0.30228 |

| | |
|---|---|
| Chi-Squared: | 8.4233E-5 |
| Weighted Sum of Squares: | 0.005054 |

**Figure 4.6 Equivalent circuits (non-linear fitting) for n=1 at 350°C.**

The Arrhenius plots obtained in static air (Figure 4.7) revealed that the bulk conductivity of the manganese substituted phases is comparable to the non-substituted[1, 2] counterpart, although the grain boundary contribution appears to be diminished. The conductivity was thermally activated with an activation energy of 0.76 eV.

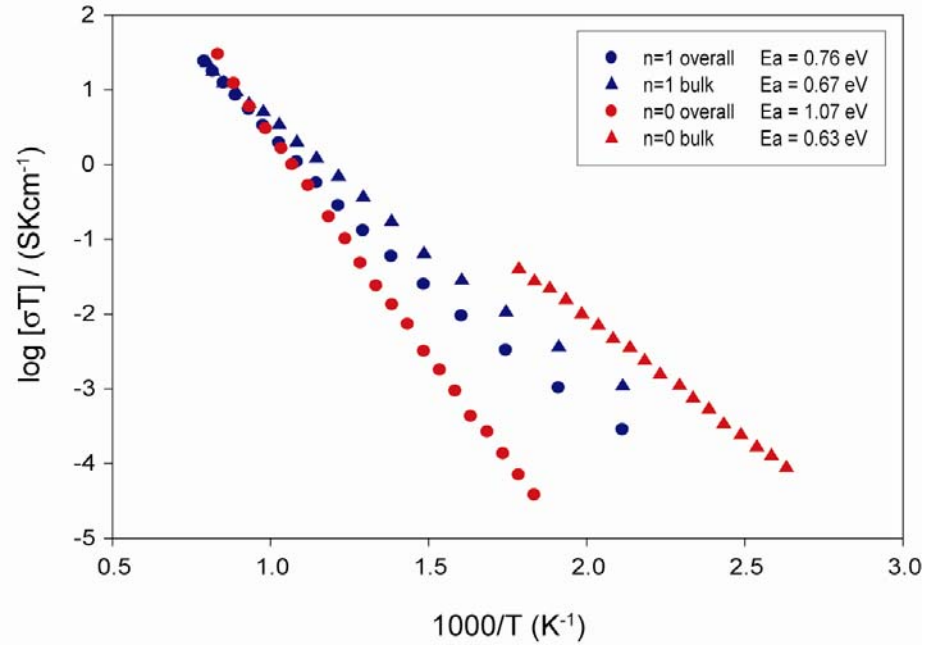


**Figure 4.7 Arrhenius plots corresponding to $La_4Sr_8Ti_{12}O_{38-\delta}$ (n=0) and $La_4Sr_8Ti_{11}Mn_1O_{38-\delta}$ (n=1) in static air. Although the overall conductivity is quite similar for both the non-substituted and the Mn-substituted counterparts, the grain boundary contribution is reduced for the latter.**

Impedance studies under more reducing conditions were limited due to the very high total conductivity of these phases, meaning that no elements could be resolved. Four terminal dc measurements were carried out on the sample under 5%$H_2$ in Ar. Before the data were collected the sample was under reducing conditions for several hours. Figure 4.8 shows the Arrhenius plots for n=1 in both air and reducing conditions. The conductivity increases two orders of magnitude under reducing conditions, i.e. 0.01 $Scm^{-1}$ at 900°C in air and 2.196 $Scm^{-1}$ in 5%$H_2$ in Ar.

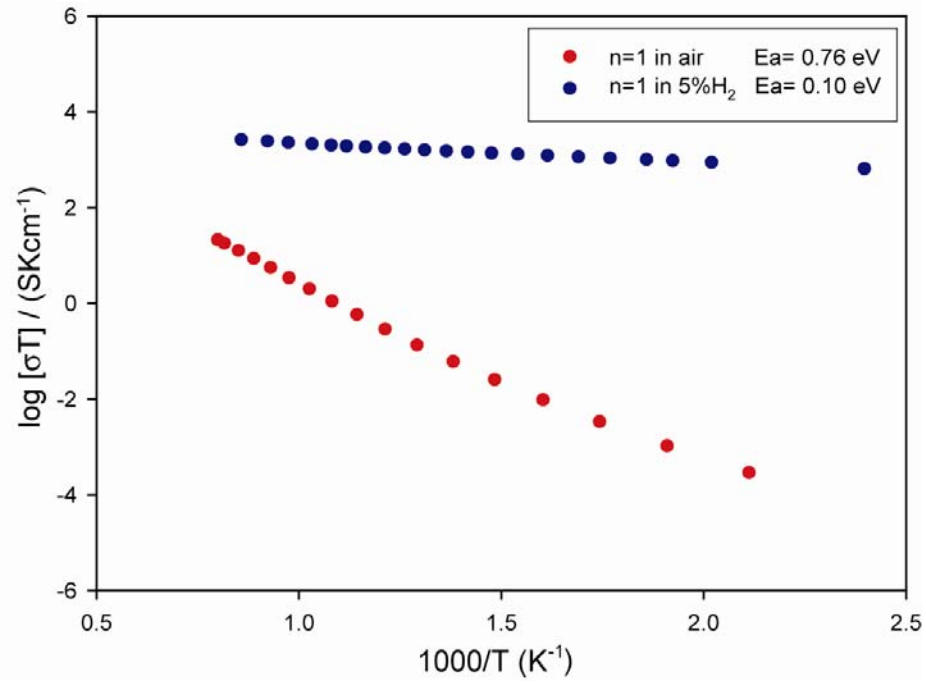


**Figure 4.8 Arrhenius plots corresponding to $La_4Sr_8Ti_{11}Mn_1O_{38-\delta}$ in static air and in 5%$H_2$/Ar. The total conductivity increases considerably in reducing conditions.**

On more careful inspection of the data, it was found that there is a small activation energy change for the conductivity in both air and 5%$H_2$. In Figure 4.9 we can observe that there is a change in the slope of the Arrhenius plot in air around 400°C. Under reducing conditions that change occurs at higher temperature, i.e. 500°C. These values are in agreement with those obtained in Chapter 2 related to a phase change with temperature. There we have seen that there is a transition phase from rhombohedral R-3c to cubic Pm-3m at approximately 350-400°C for the sample n=1 in air and at ~ 500°C in reducing conditions.

Some authors[3, 4] think the changes in the slopes of these materials can be explained by the oxygen exchange between the material and its surrounding atmosphere. We have seen that this behaviour is mainly a consequence of a transition phase related to temperature from rhombohedral to cubic.

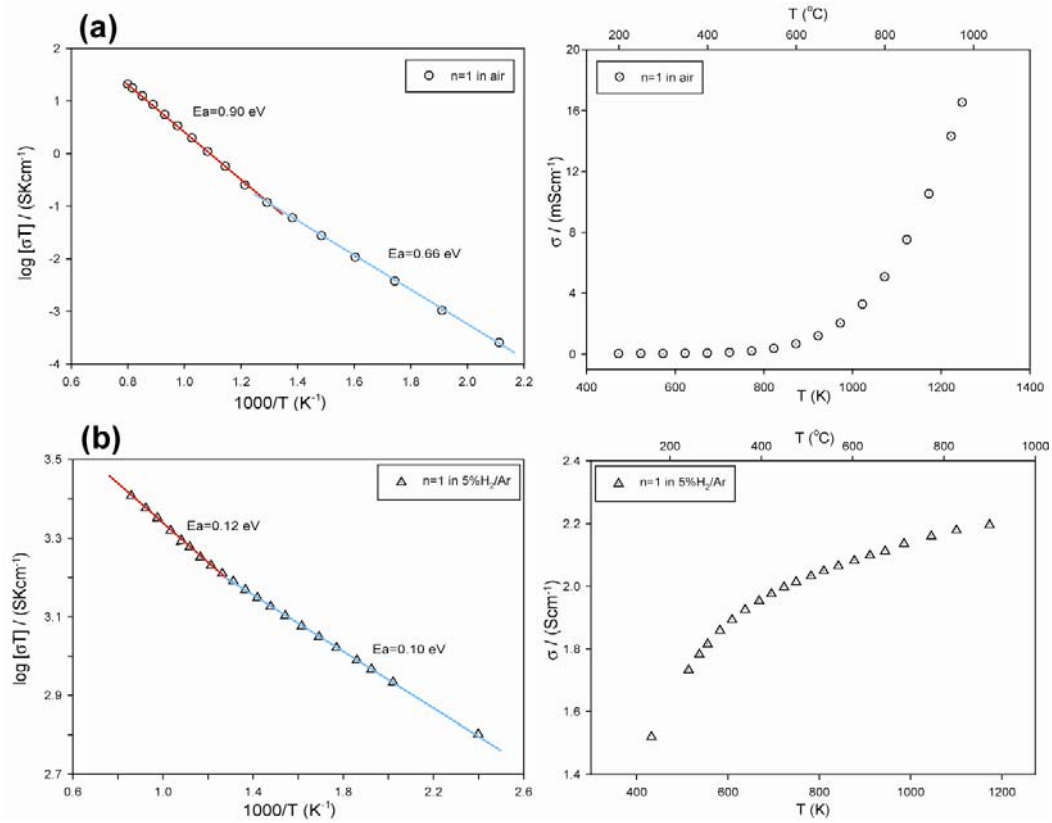


**Figure 4.9 Activation energy change and conductivity as a function of temperature for n=1 (a) in air and (b) under reducing conditions.**

### 4.2.3. $La_4Sr_8Ti_{10}Mn_2O_{38-\delta}$ (n=2)

At temperatures below 300°C the AC impedance responses in static air consisted typically of one well-defined arc associated with the grain boundary as shown in Figure 4.10 (a) and (b). At temperatures above 300°C only the total resistance was observed.

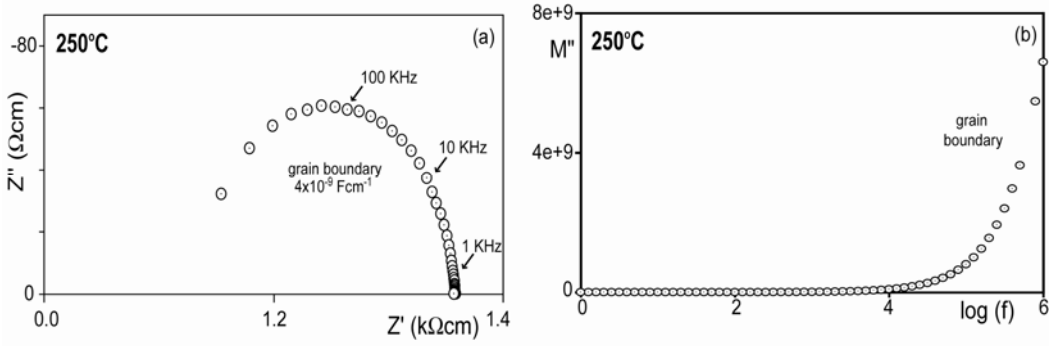


**Figure 4.10 (a) Nyquist plot of a n=2 pellet at 250°C and (b) Variation of the related modulus (M″) at the same temperature.**

The AC Impedance responses at low temperatures could be fitted as one R and one R-CPE in series.

Impedance studies under more reducing conditions were limited due to the high total conductivity of these phases and only the total resistance was observed. Figure 4.11 shows the Arrhenius plots for the sample in static air and in 5%$H_2$ in Ar. Although the total conductivity is still higher in reduced conditions than in static air the gap has diminished. The activation energy (Ea) is slightly higher in the reducing atmosphere.

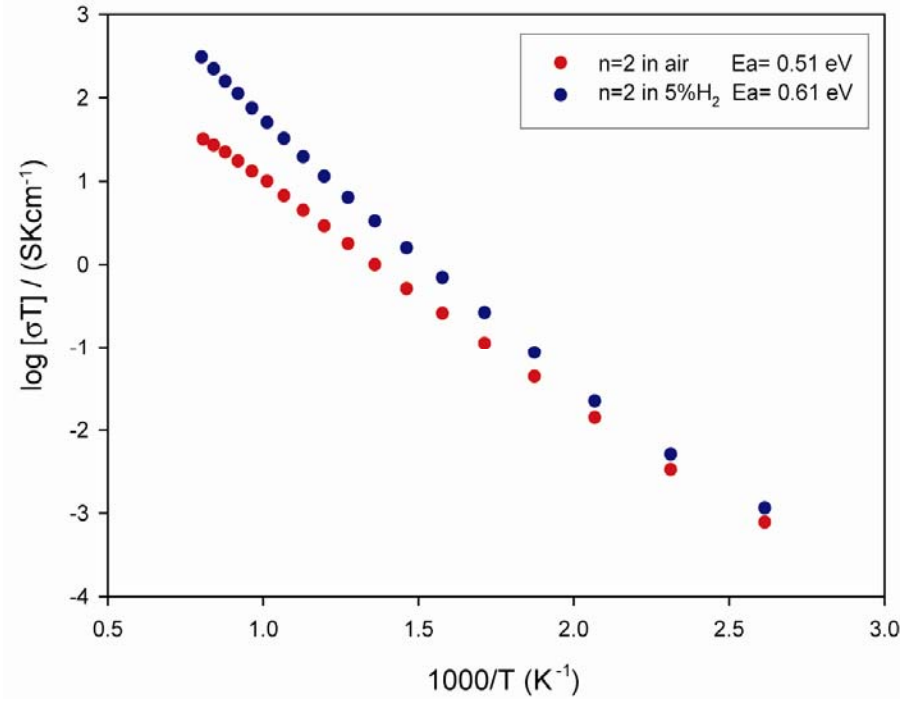


**Figure 4.11 Arrhenius plots corresponding to $La_4Sr_8Ti_{10}Mn_2O_{38-\delta}$ (n=2) in static air and in 5%$H_2$ in Ar. The total conductivity is slightly higher in reducing conditions.**

As it happened for n=1 on more careful inspection of the data, it was found that there is a small activation energy change for the conductivity in both air and 5%$H_2$. In Figure 4.12 we can observe that there is a change in the slope of the Arrhenius plot in air around 500°C. Under reducing conditions that change occurs at higher temperature, ~ 650°C. These values are again in good agreement with those obtained in Chapter 2 related to a phase change with temperature.

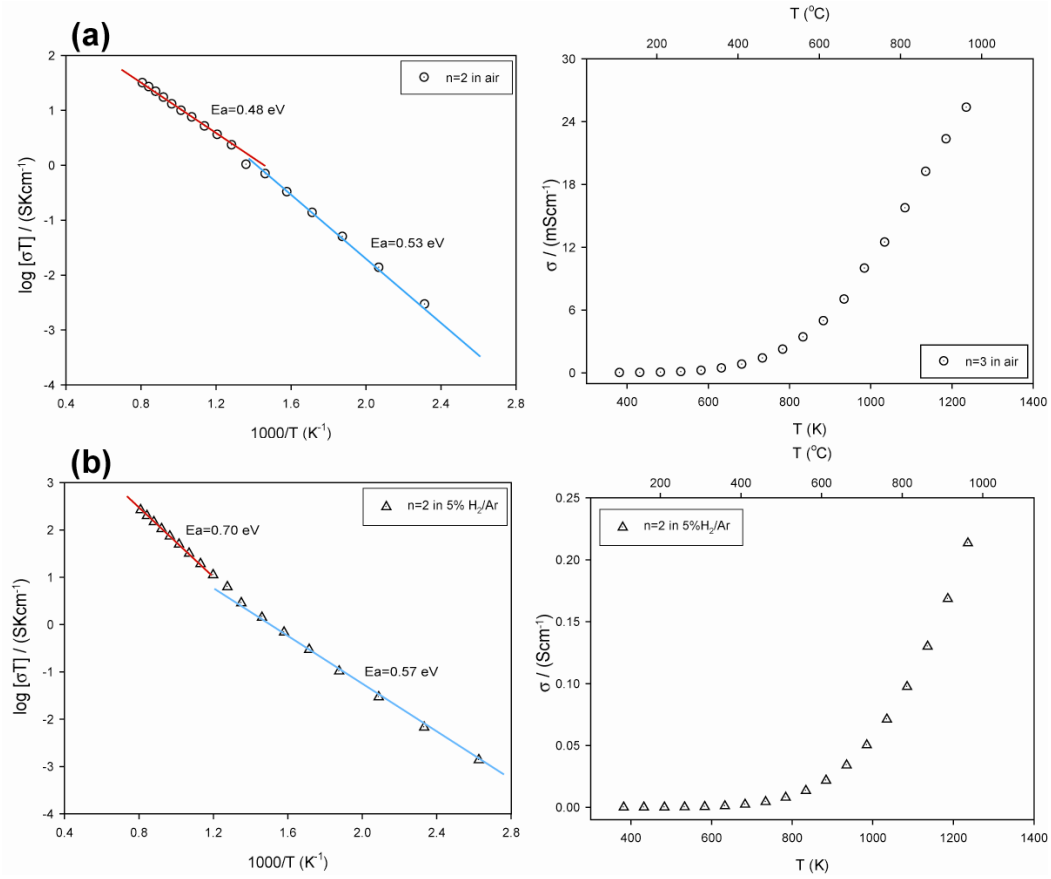


**Figure 4.12 Activation energy change and conductivity as a function of temperature for n=2 (a) in air and (b) under reducing conditions. The change in the slope of the Arrhenius plots is related to a transition phase on the sample.**

### 4.2.4. $La_4Sr_8Ti_9Mn_3O_{38-\delta}$ (n=3) and $La_4Sr_8Ti_8Mn_4O_{38-\delta}$ (n=4)

The impedance studies on n=3 and n=4 were limited in both air and 5%$H_2$, as only the total resistance could be observed at different temperatures. As shown in Figures 4.13 and 4.14 the total conductivity is now higher in air than in reducing conditions. The Arrhenius plots reveal especially for n=3 in 5%$H_2$ two different slopes. A more careful inspection of the data shows that there is a small activation energy change for the conductivity in both samples in both atmospheres. No structural studies with temperature have been realized in these samples but we think that a phase transition is the responsible for this behaviour although a change from grain boundary domination to bulk

domination is also possible. The activation energies calculated are in fact an average activation energy for both bulk and grain boundary.

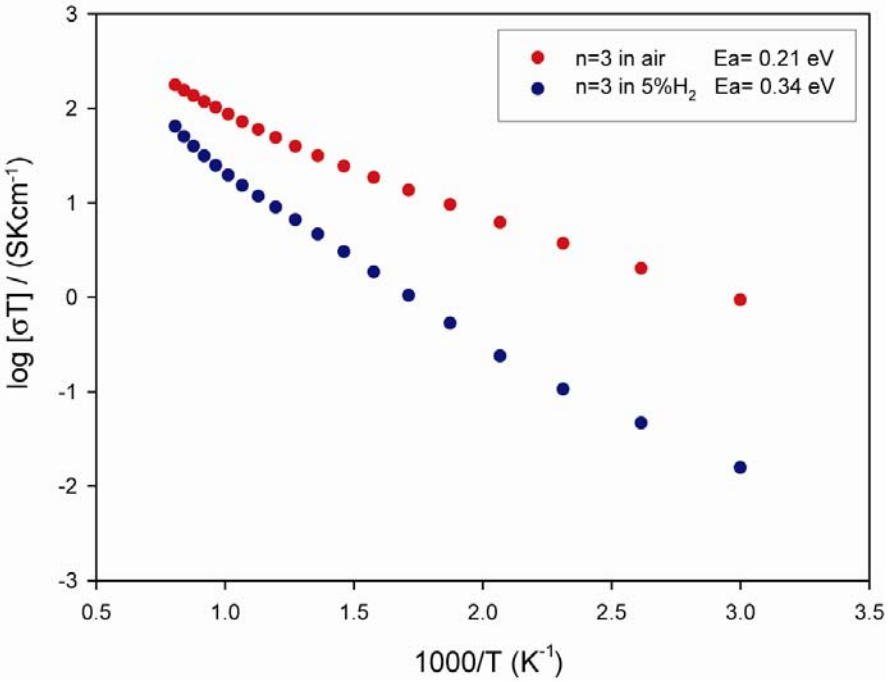


**Figure 4.13 Arrhenius plots corresponding to $La_4Sr_8Ti_9Mn_3O_{38-\delta}$ (n=3) in static air and in 5%$H_2$ in Ar. For the first time in the series the total conductivity is higher in air than in reducing conditions.**

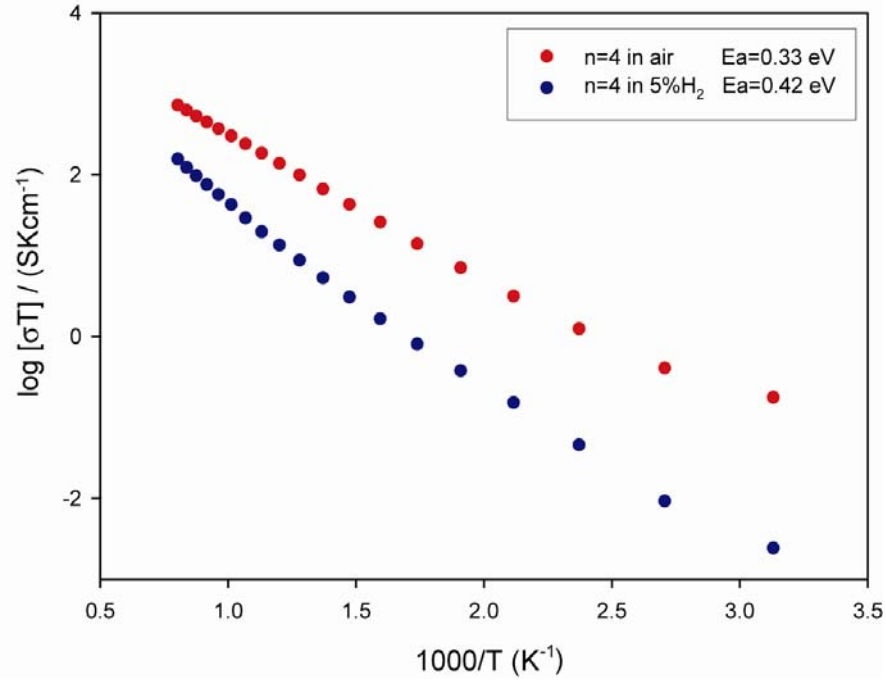


**Figure 4.14 Arrhenius plots corresponding to n=4 in static air and in 5%$H_2$ in Ar. The total conductivity increases one order of magnitude in air conditions.**

### 4.2.5. $La_4Sr_8Ti_7Mn_5O_{38-\delta}$ (n=5)

The impedance studies were limited in air where only the total resistance was observed at different temperatures. Following the tendency seen so far the total conductivity in air increases when increasing the manganese content.

The AC impedance responses in 5%$H_2$ at low temperature consisted typically of two well-defined arcs, one associated with the grain boundary ($1\times10^{-9}$ $Fcm^{-1}$) and the second with bulk processes ($1\times10^{-11}$ $Fcm^{-1}$). At temperatures above 200°C, only the grain boundary response was observed. The geometry corrected Nyquist plots and the corresponding spectroscopic plots of M" and Z" at different temperatures are shown in Figure 4.15 (a) and (b).

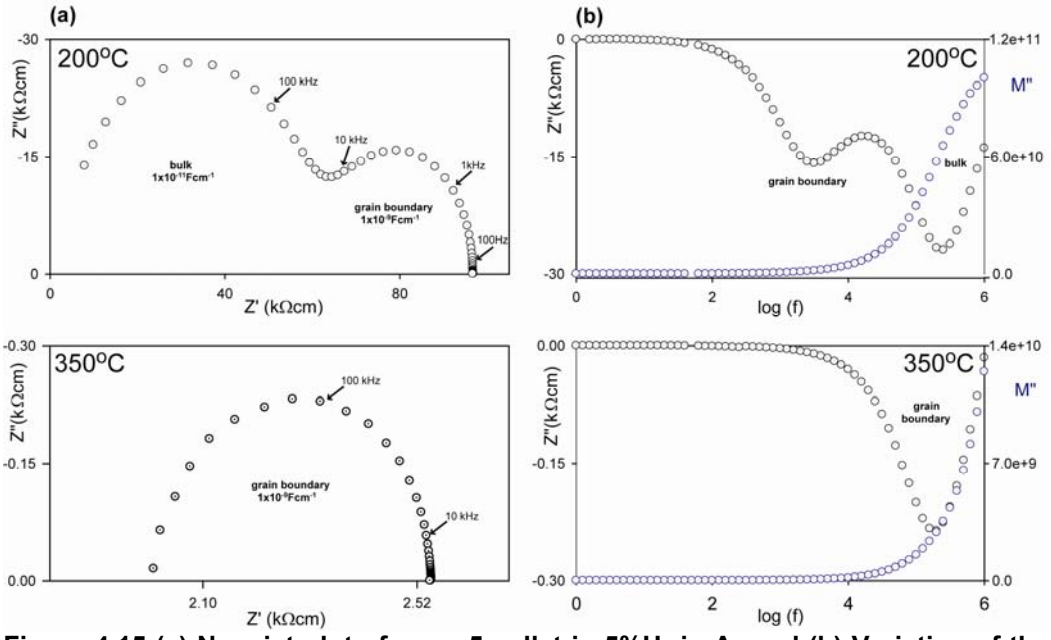


**Figure 4.15 (a) Nyquist plot of an n=5 pellet in 5%$H_2$ in Ar and (b) Variation of the related modulus (M″) and Z''**

The AC Impedance responses at low temperatures could be fitted as two R-CPE (i.e., a resistor and a constant phase element in parallel) in series, Figure 4.16. At 350°C only one R-CPE in parallel was used.

n=5 in 5%$H_2$ in Ar at 200°C

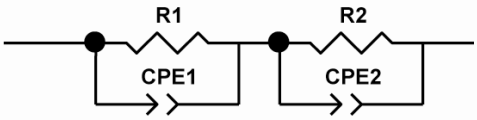


| Element | Freedom | Value | Error | Error % |
|---|---|---|---|---|
| R1 | Free(+) | 63141 | 174.29 | 0.27603 |
| CPE1-T | Free(+) | 5.3697E-11 | 1.7603E-12 | 3.2782 |
| CPE1-P | Free(+) | 0.88266 | 0.0022774 | 0.25802 |
| R2 | Free(+) | 33900 | 208.68 | 0.61558 |
| CPE2-T | Free(+) | 3.7861E-9 | 1.8295E-10 | 4.8321 |
| CPE2-P | Free(+) | 0.90712 | 0.0055547 | 0.61234 |

| | |
|---|---|
| Chi-Squared: | 0.00026676 |
| Weighted Sum of Squares: | 0.025609 |

**Figure 4.16 Equivalent circuits (non-linear fitting) for n=5 at 200°C in 5%$H_2$ in Ar**

Figure 4.17 shows the Arrhenius plots for n=5 in static air and in 5%$H_2$ in Ar. The total conductivity is higher in static air than in 5%$H_2$ with values at 900°C of 0.701 $Scm^{-1}$ and 0.018 $Scm^{-1}$ respectively. The Arrhenius plots obtained show a change in the slopes at high temperature. An average Ea has been calculated.

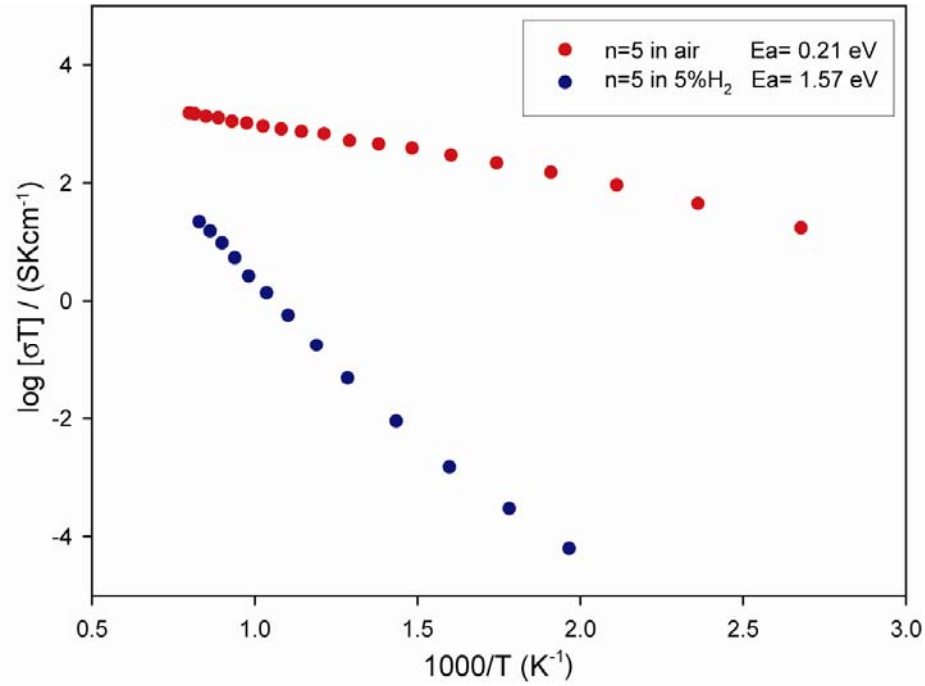


**Figure 4.17 Arrhenius plots corresponding to $La_4Sr_8Ti_7Mn_5O_{38-\delta}$ (n=5) in static air and in 5%$H_2$ in Ar. The total conductivity decreases in reducing conditions.**

### 4.2.6. $La_4Sr_8Ti_6Mn_6O_{38-\delta}$ (n=6)

The impedance studies in air were limited due to the high conductivity of the sample. Four terminal dc measurements were carried out to study the total conductivity of the sample. Under 5%$H_2$ in Ar AC impedance measurements were performed but only the total resistances at different temperatures were recorded. As showed in Figure 4.18 the total conductivity is much higher in air. At 930°C the values of conductivity in air and in 5%$H_2$ were 9.471 $Scm^{-1}$ and 0.030 $Scm^{-1}$ respectively. The activation energy in air is 0.20 eV and no changes in the slope of the Arrhenius plot were observed. Whereas in reduced conditions two clear slopes can be appreciate. At lower temperatures a value of 0.17 eV was found meanwhile when temperature increases the value of Ea increases as far as 0.57 eV.

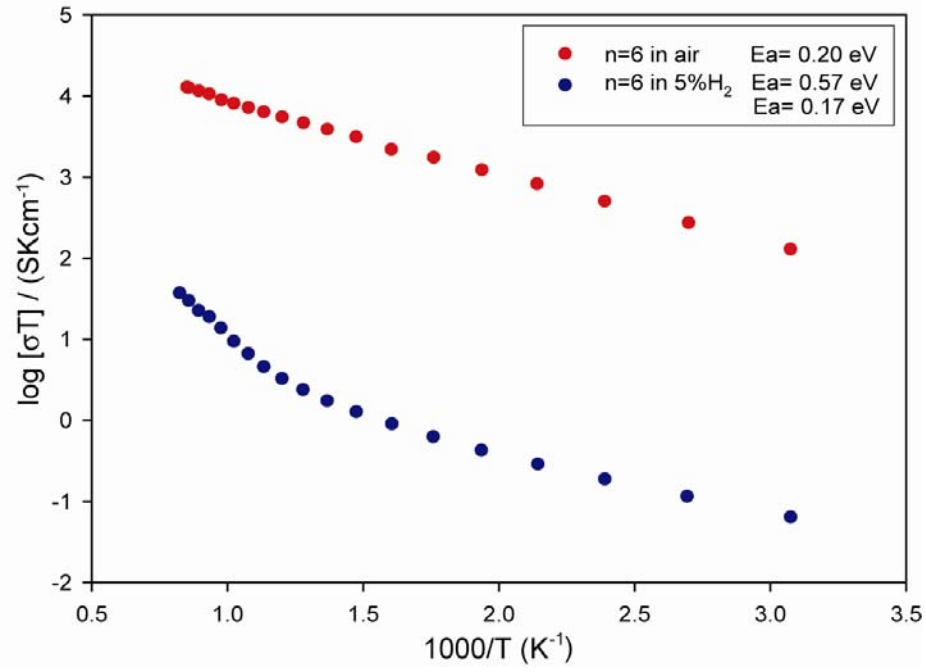


**Figure 4.18 Arrhenius plots corresponding to $La_4Sr_8Ti_6Mn_6O_{38-\delta}$ (n=6) in static air and in 5%$H_2$ in Ar. The conductivity in air was recorded using a 4 terminal setup. The total conductivity increases as far as three orders of magnitude in air conditions.**

### 4.2.7. $La_4Sr_8Ti_5Mn_7O_{38-\delta}$ (n=7)

As it happened for n=6 the impedance studies on n=7 in air were limited due to the high conductivity of the sample. Four terminal dc measurements were carried out to study the total conductivity of the sample. Studies under 5%$H_2$ were carried out using AC impedance but only the total resistance at different temperatures were obtained. Figure 4.19 shows the Arrhenius plots of the sample under both atmospheres. The total conductivity is three orders of magnitude higher in static air than in 5%$H_2$ with values at 950°C of 11.40 $Scm^{-1}$ and 0.031 $Scm^{-1}$ respectively.

No changes in the slope of the Arrhenius plot were observed in air and a value of 20 eV for the activation energy was obtained. For reducing conditions there is a small change in the slope of the Arrhenius plot at the higher temperatures.

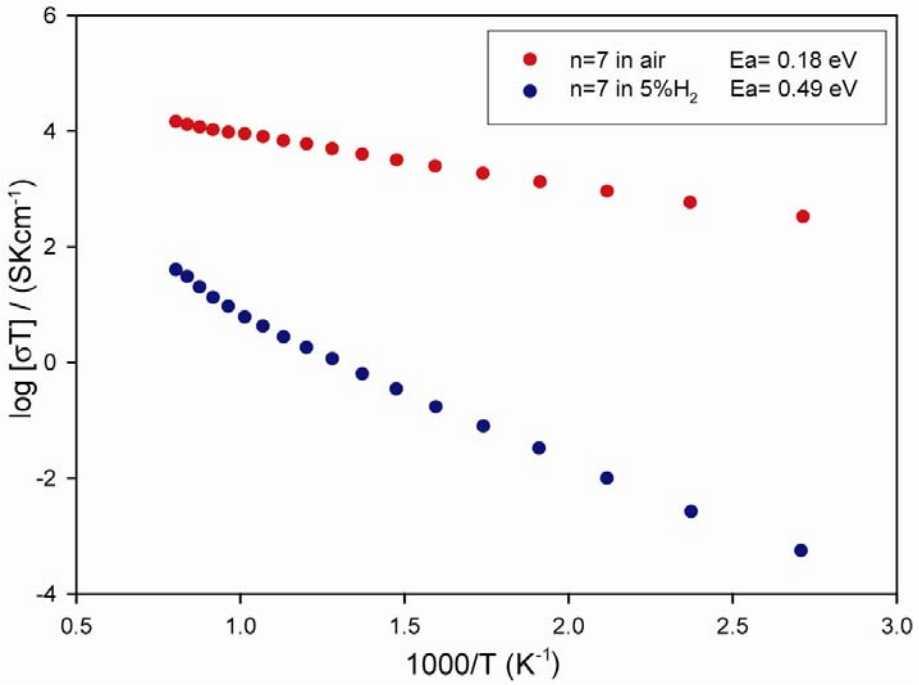


**Figure 4.19 Arrhenius plots corresponding to $La_4Sr_8Ti_5Mn_7O_{38-\delta}$ (n=7) in static air and in 5%$H_2$ in Ar. The total conductivity increases three orders of magnitude in air conditions.**

### 4.2.8. $La_4Sr_8Ti_1Mn_{11}O_{38-\delta}$ (n=11)

The impedance studies in air were limited due to the high conductivity of the sample. Four terminal dc measurements were carried out to study the total conductivity of the sample. Under reducing conditions AC impedance measurements were performed but only the total resistances at different temperatures were recorded. No significant changes in the slope of the Arrhenius plots were observed.

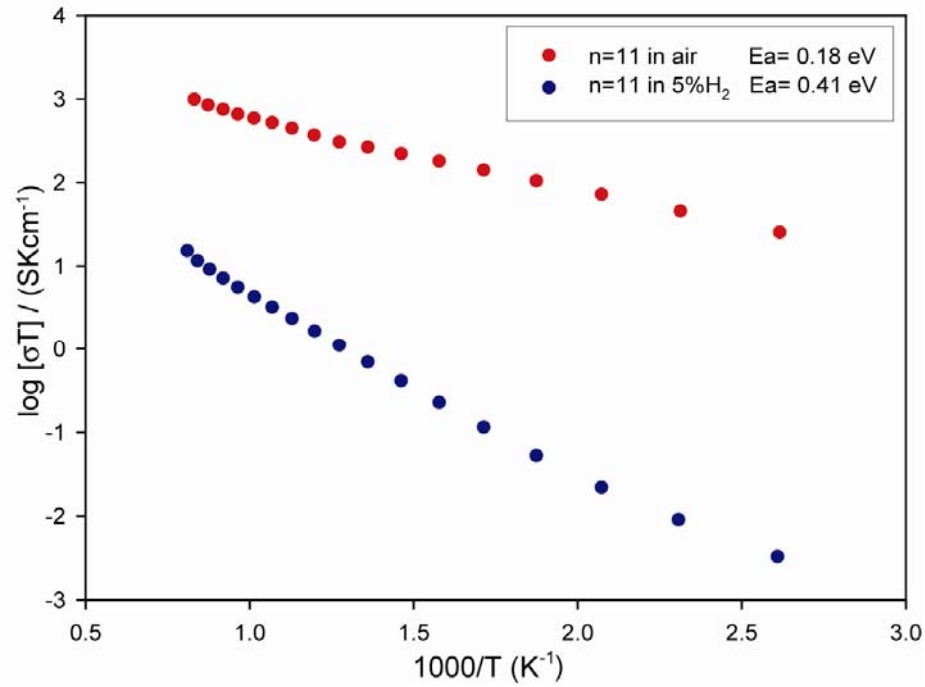


**Figure 4.20 Arrhenius plots corresponding to n=11 in static air and in 5%$H_2$ in Ar.**

### 4.2.9. Summary

Figure 4.21 shows the electrical behaviour of the series $La_4Sr_8Ti_{12-n}Mn_nO_{38-\delta}$ in air and in 5%$H_2$ in Ar. The overall conductivity increases with increasing manganese content in air. However in reducing conditions the overall conductivity decreases with increasing the manganese content. Small changes in the slopes of the Arrhenius plots have been observed. We believe that these changes are associated to a transition phase especially where these changes are clearly associated with the bulk behaviour.

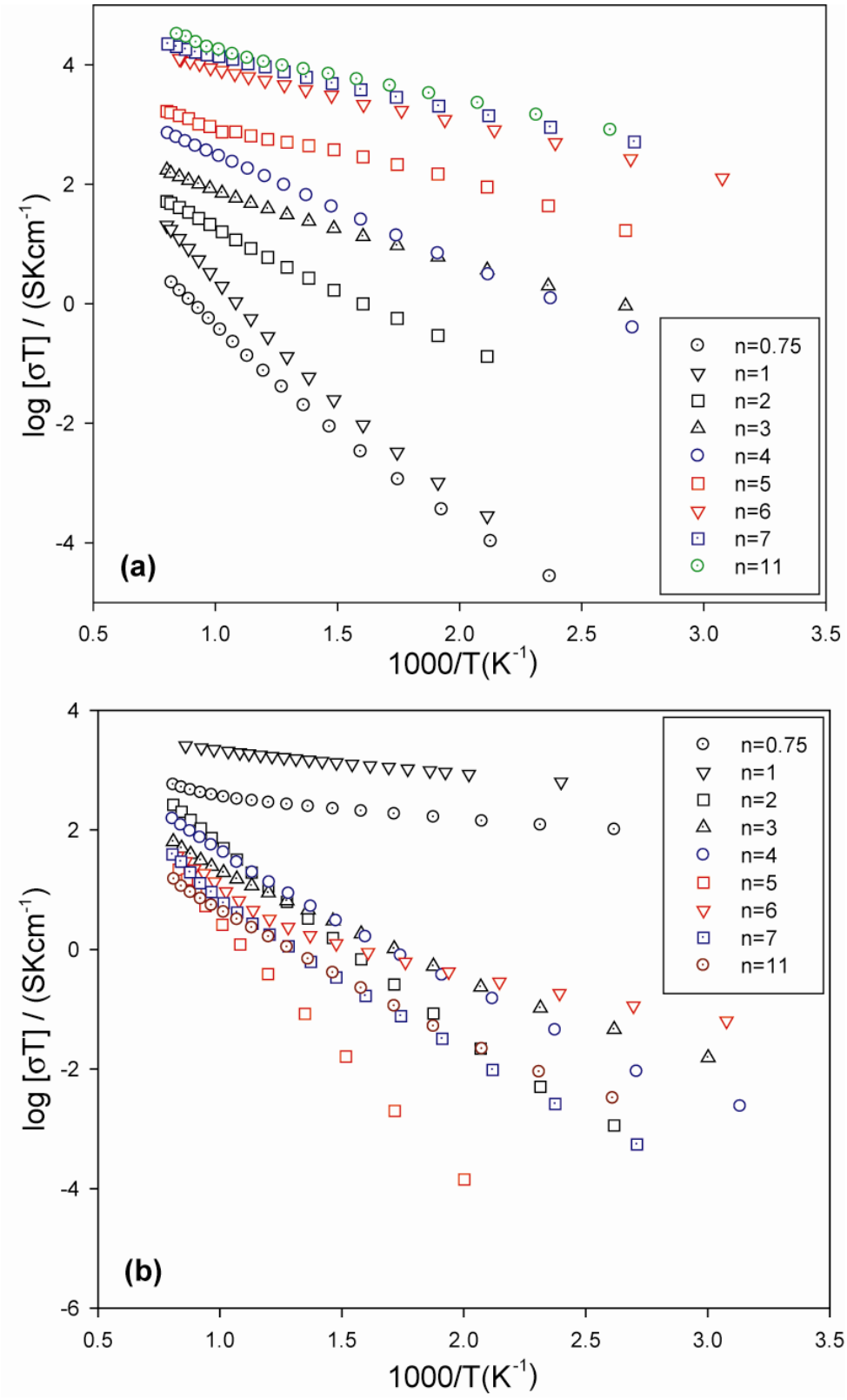


**Figure 4.21 Arrhenius plots corresponding to the $La_4Sr_8Ti_{12-n}Mn_nO_{38-\delta}$ series (a) in static air and (b) in 5%$H_2$ in Ar. The overall conductivity increases with increasing manganese content in air. Under reducing conditions the overall conductivity decreases with increasing manganese content.**

### 4.2.10. $La_4Sr_8Ti_{12-n}Mn_nO_{38-\delta}$ for n<0.75

Studies carried out in our group[5] where the lanthanum strontium titanates were doped in the B-site with Mn (n=0.5) and Ga (n=0.5) have produced excellent results. In order to investigate the effect of doping only with low levels of Mn we have carried out 4 terminal dc measurements of samples n=0.5 and n=0.25. Figure 4.22 shows the data collected and compares the values to those obtained for n=0.75 and n=1.

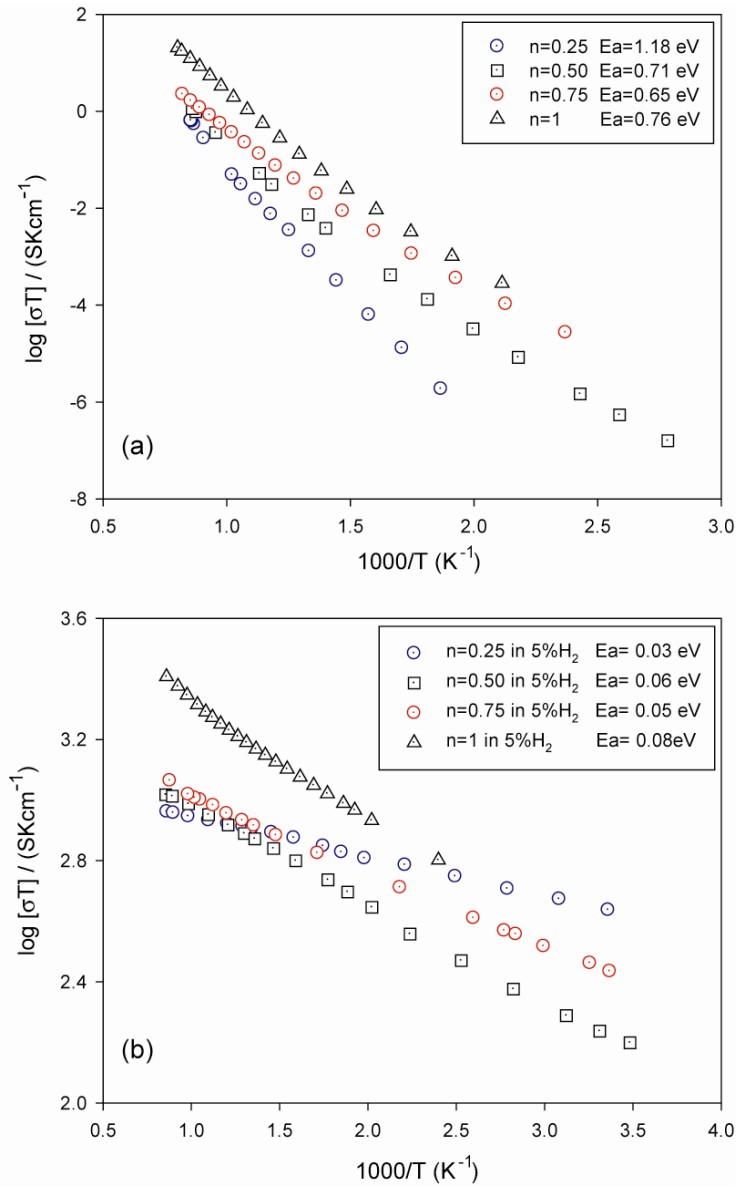


**Figure 4.22 Arrhenius plots corresponding to the $La_4Sr_8Ti_{12-n}Mn_nO_{38-\delta}$ series (n<1) (a) in static air and (b) in 5%$H_2$ in Ar.**

In air the conductivity decreases at lower content of Mn and the values are similar to those obtained for n=0.75. In reducing conditions the overall conductivity increases at lower content of Mn. However the conductivity in 5%$H_2$ for n=0.25 and 0.50 is lower than the conductivity for their counterparts n=1 and n=0.75.

## 4.3. Magnetic measurements

Magnetic susceptibility measurements can provide further information about the oxidation state of the manganese discussed in the previous chapter.

As it has been said in Chapter 2 the molar susceptibility ($\chi_M$) is a function of the reciprocal temperature (Curie-Weiss law):

$$\chi_M = \frac{C}{T + \Theta} \quad [4.3]$$

C is the Curie constant that is one of the parameters calculated in the regression to fit the experimental and Θ is the Weiss temperature. When there is no spin-orbital coupling, the constant C can be related with the effective magnetic momentum by the Curie-Langevin law:

$$\mu_{eff}^{\ 2} = \frac{3k_B C}{N\mu_B} \quad [4.4]$$

where $\mu_{eff}$ is the effective magnetic momentum, $k_B$ is Boltzmann constant, N is Avogadro's constant and $\mu_B$ is Bohr magneton. Thus, by estimating C from the experimental data it is possible to calculate the $\mu_{eff}$, which is related to the oxidation state of the manganese.

### 4.3.1. $La_4Sr_8Ti_{11.5}Mn_{0.5}O_{38-\delta}$ (n=0.5)

The temperature variation of molar magnetic susceptibility measured by the zero-field-cooling (ZFC) mode and the fitting using equation 4.3 are shown in Figure 4.23(a). To perform the ZFC measurement the procedure was to cool the

sample under zero applied field down to 5 K, and then applied a small field of 50 Oe for data collection in the warming process. It showed paramagnetic behaviour over the whole temperature range. The Weiss temperature (Θ) calculated was -2.10 K, which indicates a tendency to antiferromagnetic order. Figure 4.23(b) depicts the inverse magnetic susceptibility as a function of temperature and in the inset a detail of the low temperature region is shown.

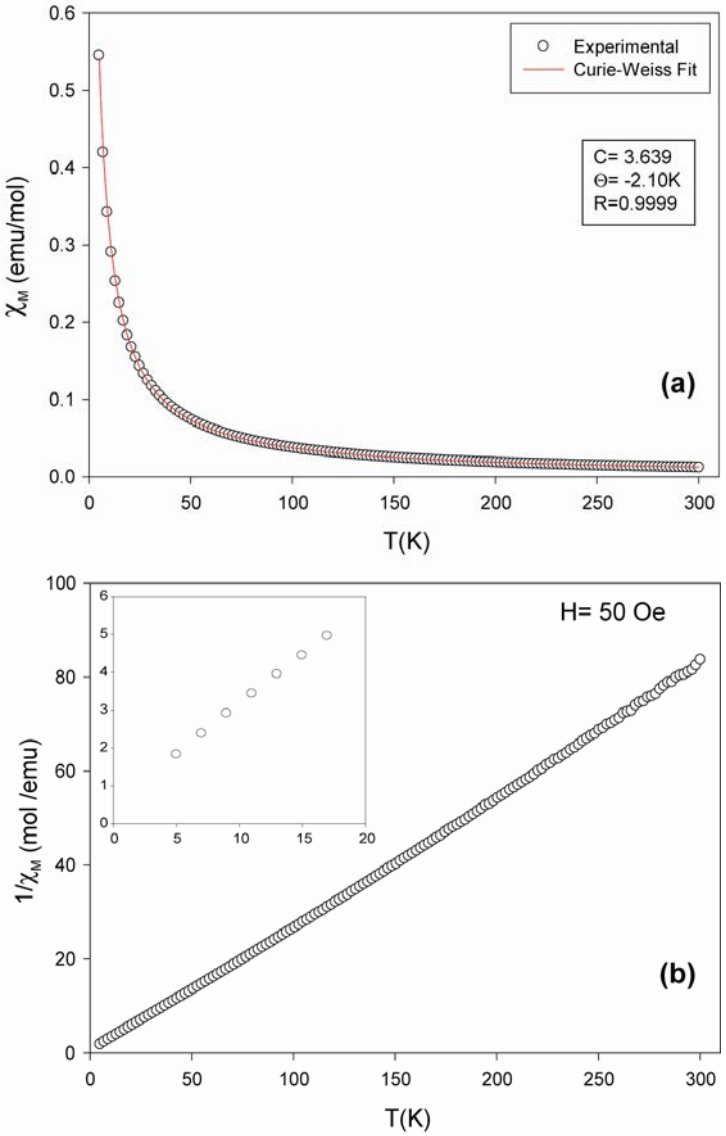


**Figure 4.23 (a) Temperature variation of molar magnetic susceptibility and fitting obtained using the Curie-Weiss law for n=0.5 and (b) Temperature dependence of the inverse molar magnetic susceptibility (Inset) Detail of the low temperature range.**

We can observe that at the lowest temperatures the strict Curie-Weiss behaviour is maintained, with the Weiss temperature (Θ) value relatively quite small, on the order of -2 K.

The calculated effective magnetic moment, $\mu_{eff}$, from equation 4.4 is $\mu_{eff}$=5.39 $\mu_B$, which is comparable to the high spin state value for $Mn^{3+}$ equal to 4.90 $\mu_B$.

Figure 4.24 shows magnetisation (M) versus applied magnetic field (H) at 5 K for n=0.5. No hysteresis was found, which also confirms that the sample is paramagnetic up to 5K.

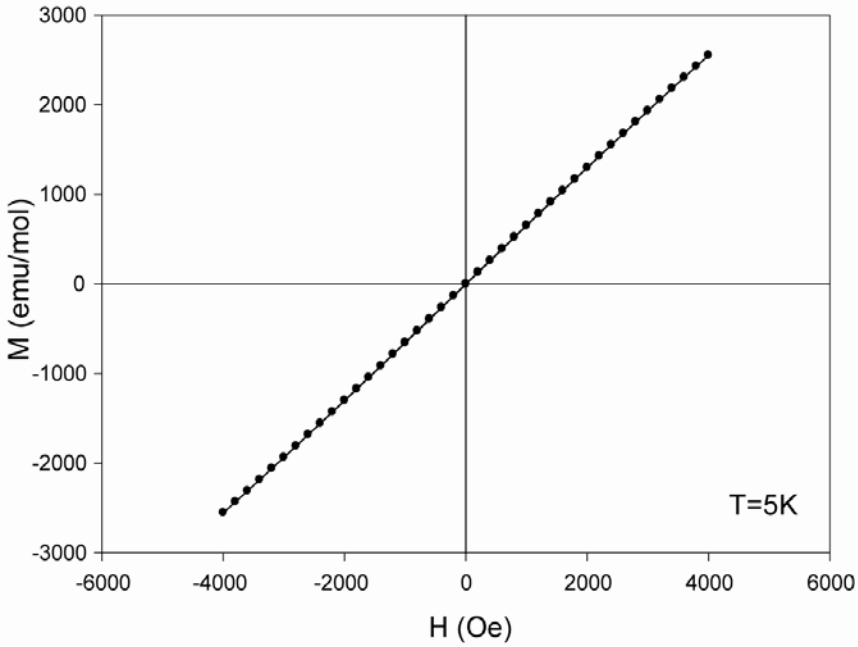


**Figure 4.24 Magnetisation (M) versus applied magnetic field (H) at 5 K for n=0.5.**

### 4.3.2. $La_4Sr_8Ti_{11}Mn_1O_{38-\delta}$ (n=1)

In Figure 4.25(a) the molar magnetic susceptibility versus temperature is shown as well as the fitting obtained using the Curie-Weiss law. The sample showed paramagnetic behaviour over the whole temperature range. The Weiss temperature (Θ) calculated was -2.18 K, which indicates a tendency to antiferromagnetic order. Figure 4.25(b) shows the inverse magnetic susceptibility as a function of temperature and in the inset a detail of the low

temperature region is shown. At the lowest temperatures the Curie-Weiss behaviour is maintained, with the Weiss temperature (Θ) value relatively quite small, on the order of -2 K, as it happened for n=0.5.

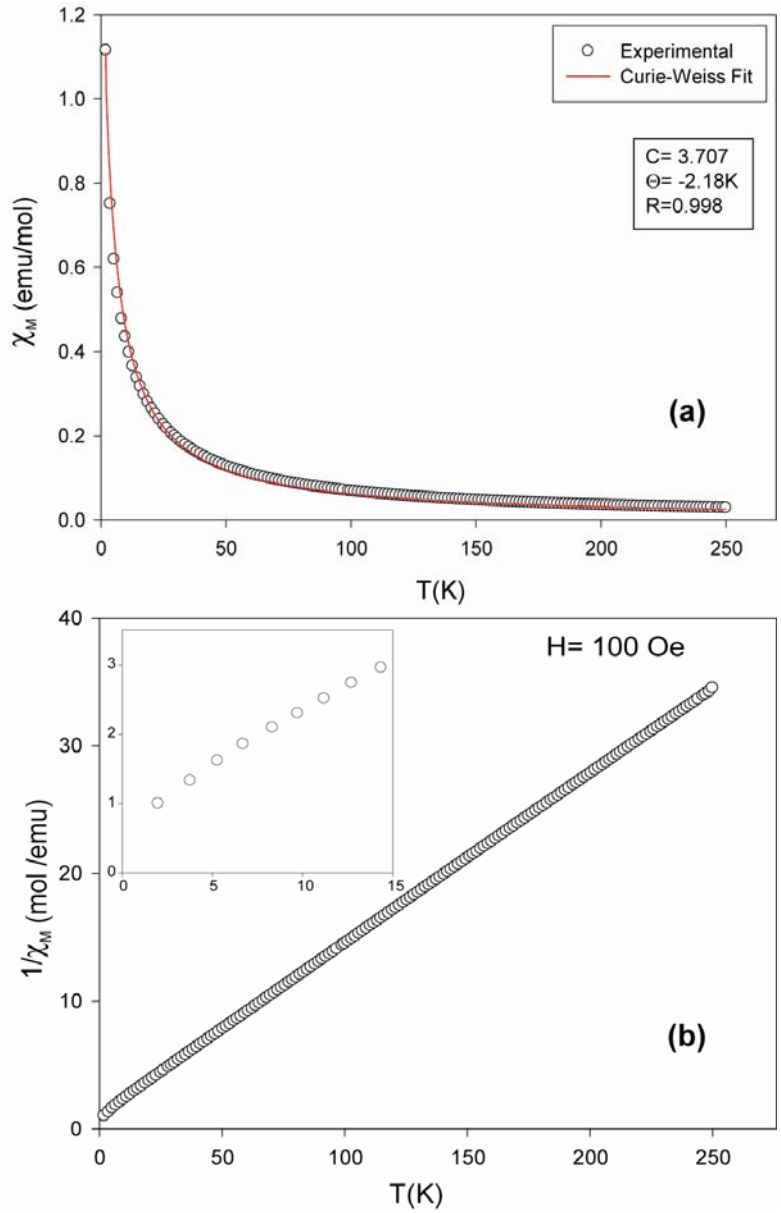


**Figure 4.25 (a) Temperature variation of molar magnetic susceptibility at 100Oe and fitting obtained using the Curie-Weiss law for n=1 and (b) Temperature dependence of the inverse molar magnetic susceptibility (Inset) Detail of the low temperature range.**

The calculated effective magnetic moment, $\mu_{eff}$, from equation 3.4 is $\mu_{eff}$=5.44 $\mu_B$, which is comparable to the high spin state value for $Mn^{3+}$ equal to 4.9 $\mu_B$.

### 4.3.3. $La_4Sr_8Ti_{10}Mn_2O_{38-\delta}$ (n=2)

The temperature variation of molar magnetic susceptibility measured under ZFC conditions is shown in Fig. 4.26(a). The plot shows an antiferromagnetic (AF) transition around 7K. Curie-Weiss behaviour is seen at high temperatures (above 170K) which yield a Weiss temperature (Θ) of -6.10K and an effective magnetic moment, $\mu_{eff}$=5.61$\mu_B$. Figure 4.26(b) depicts the inverse magnetic susceptibility as a function of temperature.

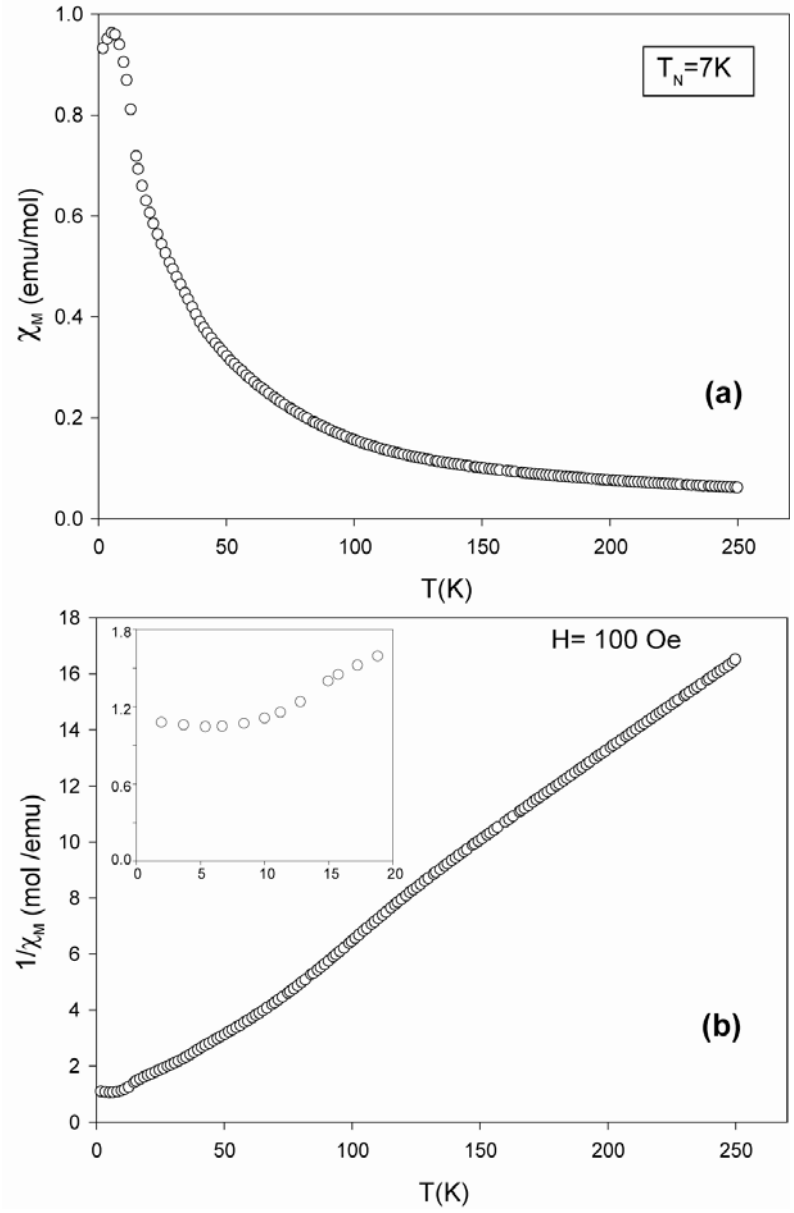


**Figure 4.26 (a) Magnetic susceptibility *vs.* temperature for n=2 and (b) T dependence of the inverse susceptibility. (Inset) Detail of the low T range.**

### 4.3.4. $La_4Sr_8Ti_8Mn_4O_{38-\delta}$ (n=4)

The temperature variation of molar magnetic susceptibility measured under ZFC conditions is shown in Fig. 4.27(a). The plot shows an antiferromagnetic (AF) transition around 9K. Figure 4.27(b) depicts the inverse magnetic susceptibility as a function of temperature. Curie-Weiss behaviour is seen at high temperatures (above 200K) which yield a Weiss temperature (Θ) of -7.83K and an effective magnetic moment, $\mu_{eff}=5.02\mu_B$,

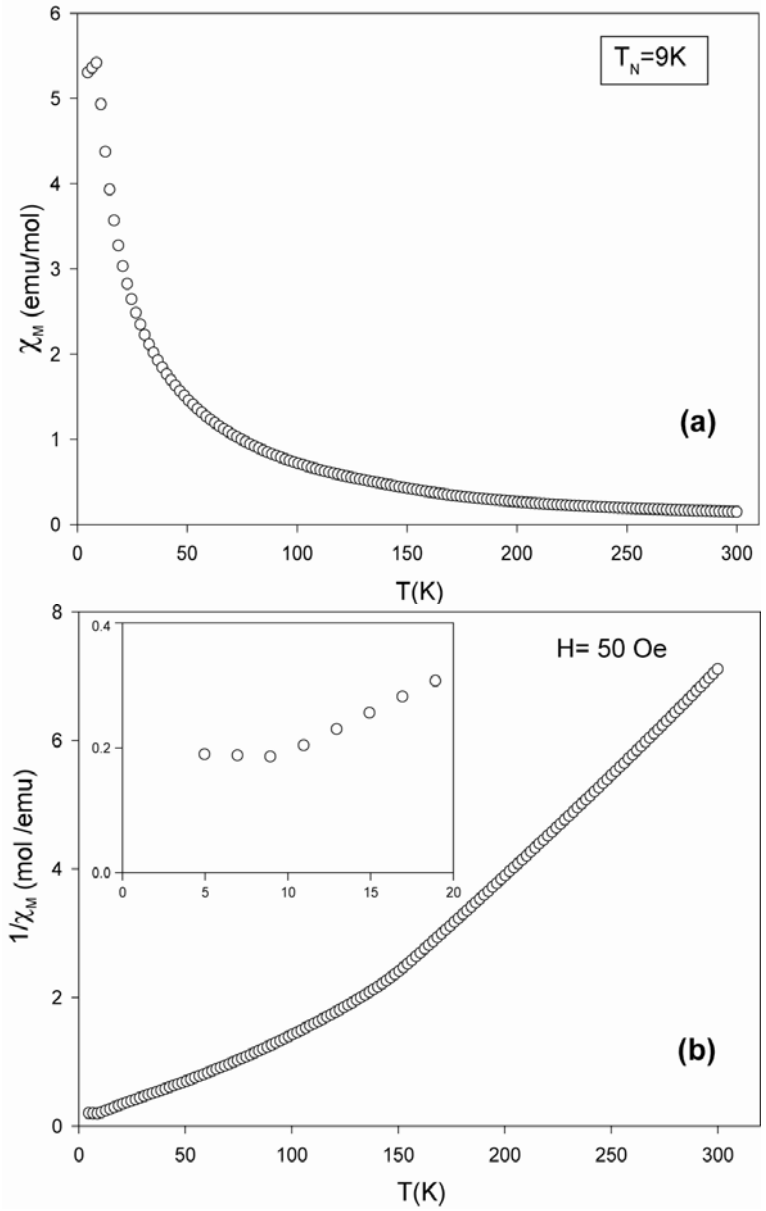


**Figure 4.27 (a) Magnetic susceptibility *vs.* T for n=4 and (b) Temperature dependence of the inverse molar magnetic susceptibility. (Inset) Detail of the low temperature range.**

Figure 4.28 shows magnetisation (M) versus applied magnetic field (H) at 5 K for n=4. Small magnetic hysteresis was found, revealing the presence of weak ferromagnetic behaviour.

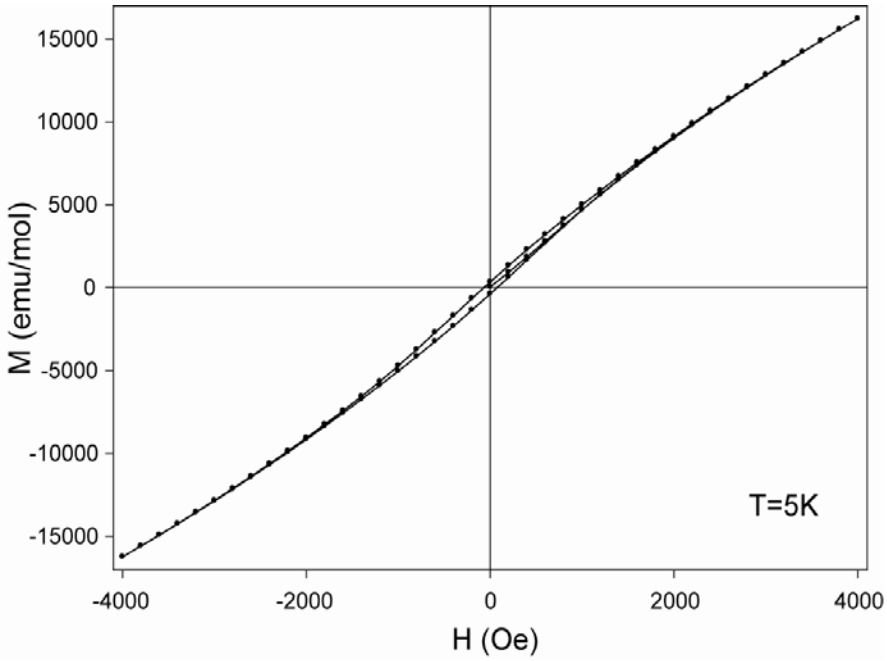


**Figure 4.28 Magnetisation (M) versus applied magnetic field (H) at 5 K for n=4.**

### 4.3.5. Summary of magnetic properties

Magnetic studies under ZFC have been carried out in some compounds of the series and the results obtained are presented in Table 4.1.

| n | Magnetic behaviour | $\mu_{eff}/\mu_B$ | Θ/K | $T_N$/K |
|---|---|---|---|---|
| 0.5 | Paramagnetic | 5.39 | -2.10 | - |
| 1 | Paramagnetic | 5.44 | -2.18 | - |
| 2 | Antiferromagnetic | 5.61 | -6.10 | 7 |
| 4 | Antiferromagnetic | 5.65 | -7.83 | 9 |

**Table 4.1 Magnetic behaviour, effective moments, Weiss temperature and Néel temperature for samples of the series $La_4Sr_8Ti_{12-n}Mn_nO_{38-\delta}$. The negative values of Weiss temperature remark the antiferromagnetic nature of the samples.**

For n=0.5 and n=1 a paramagnetic behaviour has been found in the whole range of temperatures studied. Negative Weiss constant values were found which indicates the presence of predominant antiferromagnetic interaction. The effective moments were 5.39 $\mu_B$ and 5.44 $\mu_B$ respectively. The expected effective moment for $Mn^{3+}$ is equal to 4.9 $\mu_B$. We are assuming that all the magnetic contribution is due to manganese but as we have seen in previous sections some $Ti^{3+}$ is also present. Then the effective magnetic moment of the compounds ($\mu_{eff}$) is given by $\mu_{eff}^2 = \mu_{eff}(Mn^{3+})^2 + \mu_{eff}(Ti^{3+})^2$. For $Ti^{3+}$ the value of the effective moment is $\mu_{eff}$ =1.73 $\mu_B$. The presence of some $Ti^{3+}$ could explain the effective magnetic moment values obtained for these two samples, a bit higher than the value for only $Mn^{3+}$.

For n=2 and n=4 an antiferromagnetic behaviour has been observed. The Néel temperatures are 7 and 9K respectively. At high temperatures Curie-Weiss behaviour was observed and the effective moments calculated were 5.61 $\mu_B$ and 5.65 $\mu_B$ respectively. The negative Weiss constant temperatures remark the presence of predominant antiferromagnetic interaction. Magnetic hysteresis is seen at 5K for n=4 revealing the presence of weak ferromagnetic behaviour. We have realized conductivity as a function of the $pO_2$ studies to complement the magnetic studies and the results are presented in next section.

### 4.4. Conductivity as a function of the $pO_2$

Electrical tests varying oxygen partial pressure under controlled leakage were performed on some samples of the series in the range from $10^{-1}$ to $10^{-20}$ atm at 900°C.

Data points for $pO_2$ in the range $10^{-6}$ - $10^{-13}$ have generally been omitted as they displayed conductivity values quite different from expected defect behaviour. As the actual partial pressure of the redox active agents such as $O_2$ or $H_2$ will be very low, e.g. $10^{-10}$ atm, it is not surprising that stable exchange is not observed

or perhaps more accurately the sample and sensor do not experience the same $pO_2$ values. The use of a suitable buffer could rectify this problem.

### 4.4.1. $La_4Sr_8Ti_{11.75}Mn_{0.25}O_{38-\delta}$ (n=0.25)

The sample was reduced for 18 hours at 900°C and then the oxidation step was recorded. Figure 4.29 shows the conductivity as a function of oxygen partial pressure. The $pO_2$ changed very slowly from $10^{-20}$ atm down to $10^{-15}$ atm, i.e. 14 hours. That means we should be very close to equilibrium in that oxygen partial pressure range. It is clear that the conductivity increases with decreasing oxygen partial pressure. Therefore, is evident that this phase is an n-type electronic conductor as indicated from the slope of -1/4.

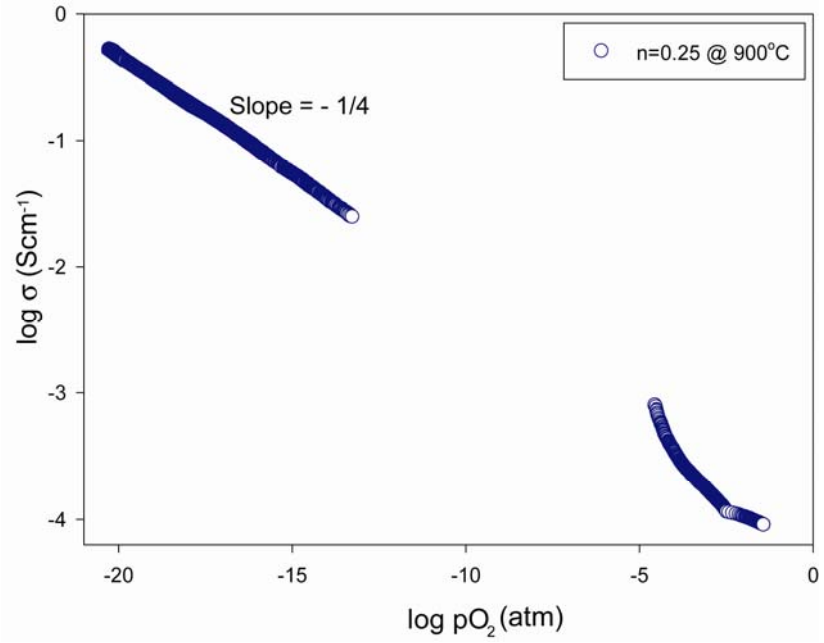


**Figure 4.29 Variation of the conductivity vs. oxygen partial pressure for n=0.25**

### 4.4.2. $La_4Sr_8Ti_{11.25}Mn_{0.75}O_{38-\delta}$ (n=0.75)

The reoxidation step was recorded, as shown in Figure 4.30, after the sample had been reduced for several hours. The $pO_2$ changed very slowly from $10^{-20}$ atm down to $10^{-15}$ atm, i.e. 24 hours. That means we should be very close to equilibrium in that oxygen partial pressure range. The change in the higher

values of $pO_2$ was faster, i.e. 8 hours and equilibrium was not achieved. The results confirm that this phase is an n-type electronic conductor as indicated from the slope of -1/4.

No evidence of changes in the conduction mechanism from n-type to p-type were distinguishable even for the higher $pO_2$ data.

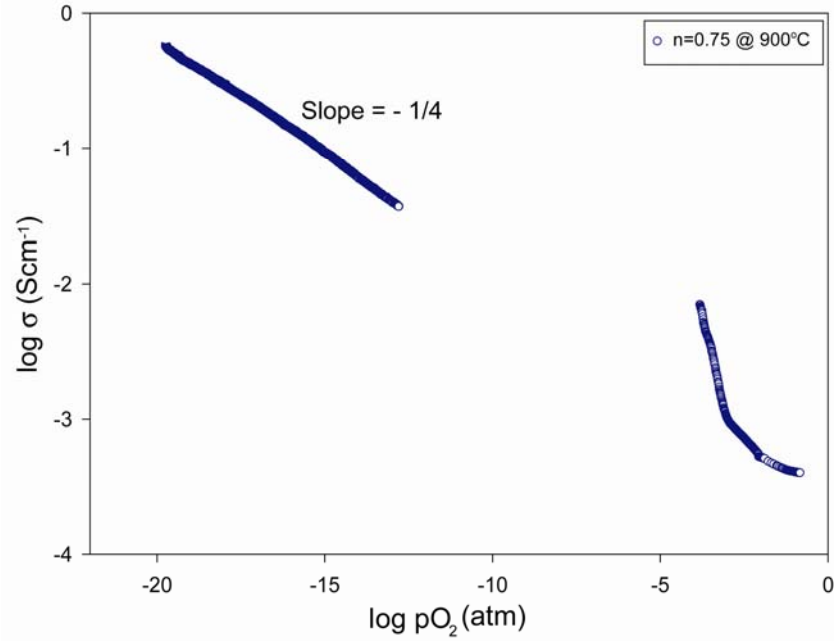


**Figure 4.30 Variation of the conductivity vs. oxygen partial pressure for n=0.75 which confirm n-type electronic conductivity.**

### 4.4.3. $La_4Sr_8Ti_{11}Mn_1O_{38-\delta}$ (n=1)

The sample was reduced for several hours and then the oxidation step was recorded, as shown in Figure 4.31. This time the change in the $pO_2$ was quicker. Only took around 6 hours going down from $10^{-20}$ atm to $10^{-15}$ atm hours. That means we probably are not close to equilibrium in that oxygen partial pressure range. This fast oxidation could explain the value of -1/5 for the slope instead of the typical -1/4 for n-type conductivity. We believe this behaviour is more related to non equilibrium process than changes in mechanism.

At higher values of $pO_2$, i.e. $10^{-3}$ atm to $10^{-1}$ atm, the calculated value of the slope was -0.23. In this range the oxidation took a higher average of time than it

took it for low values of $pO_2$. This means conditions closer to equilibrium. We can conclude that this phase is an n-type electronic conductor.

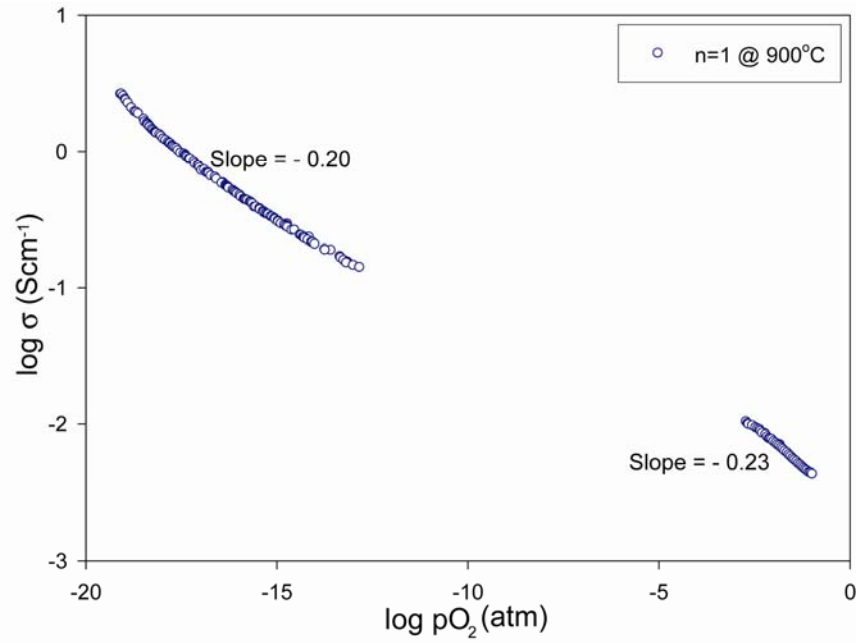


**Figure 4.31 Variation of the conductivity vs. oxygen partial pressure for n=1. The high value of the slope at low values of $pO_2$ is associated to a non equilibrium oxidation.**

### 4.4.4. $La_4Sr_8Ti_{10}Mn_2O_{38-\delta}$ (n=2)

The reoxidation step was recorded, as shown in Figure 4.32, after the sample had been reduced for several hours.

The results confirm that this phase is an n-type electronic conductor in reducing conditions as indicated from the slope of -1/4. At higher values of $pO_2$ the slope changes to a positive value of 1/4 which is an indication of p-type conductivity. It should be interesting to study intermediate $pO_2$ conditions using $MnO_x$ buffers as done for Plint *et al.*[6] As the conductivity is proportional to the concentration of charge carriers, their charge and mobility, one can obtain the classical power dependencies for partial p- and n-type electronic conductivities:

$$\sigma_p = \sigma_p^0 . pO_2^{1/4} \qquad \sigma_n = \sigma_n^0 . pO_2^{-1/4} \qquad [4.5]$$

where $\sigma^0_p$ and $\sigma^0_n$ are temperature-dependent constants.

Assuming that the ionic conductivity ($\sigma_0$) in the $pO_2$ range $10^{-15}$-$10^{-5}$ is independent of the oxygen pressure, the total conductivity may be approximated by the model:

$$\sigma = \sigma_0 + \sigma_p^0 . pO_2^{1/4} + \sigma_n^0 pO_2^{-1/4} \qquad [4.6]$$

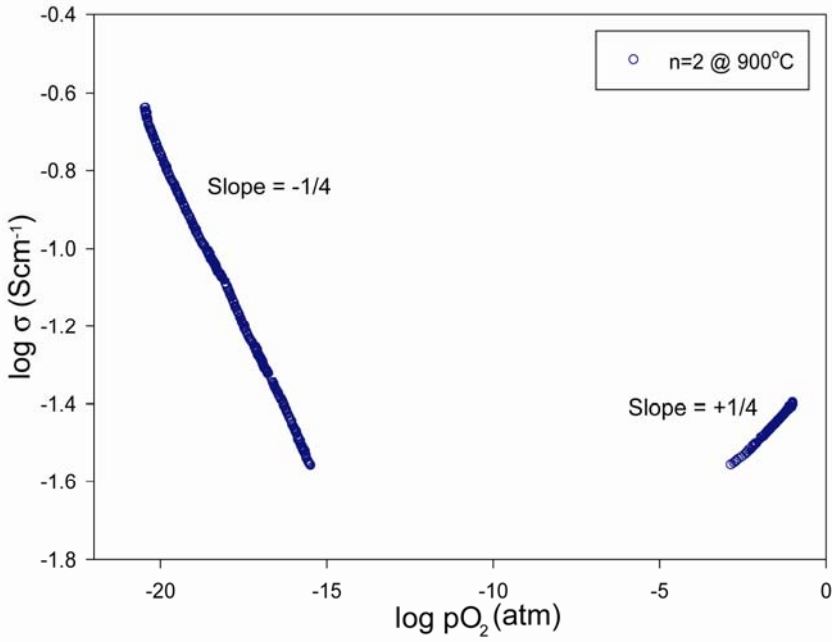


**Figure 4.32 Variation of the conductivity vs. oxygen partial pressure for n=2 which confirm a change in the conduction mechanism from n-type to p-type.**

### 4.4.5. $La_4Sr_8Ti_9Mn_3O_{38-\delta}$ (n=3)

The sample was reduced for several hours and then the oxidation step was recorded, as shown in Figure 4.33. The $pO_2$ changed slowly from $10^{-20}$ atm down to $10^{-15}$ atm, i.e. 12 hours. That means we should be very close to equilibrium in that oxygen partial pressure range. The change at higher values of $pO_2$ was faster, i.e. 8 hours and equilibrium was not achieved.

$La_4Sr_8Ti_9Mn_3O_{38-\delta}$ (n=3) remains p-type over the $pO_2$ stability range but the value of the slope is far from ¼. Plint *et al.* have reported[6] recently that this behaviour requires a defect model incorporating co-existent $Mn^{2+}$, $Mn^{3+}$ and

$Mn^{4+}$ states. Previous studies[7, 8] have indicated that $Mn^{3+}$ in crystalline solids is subject to a thermally activated disproportionation,

$$2Mn^{3+} \leftrightarrow Mn^{4+} + Mn^{2+} \qquad [4.7]$$

Stevenson *et al.* have reported[9] that $Mn^{2+}$ cations act as site-blockers for conduction. This can explain that the conductivity decreases in reducing conditions for n=3.

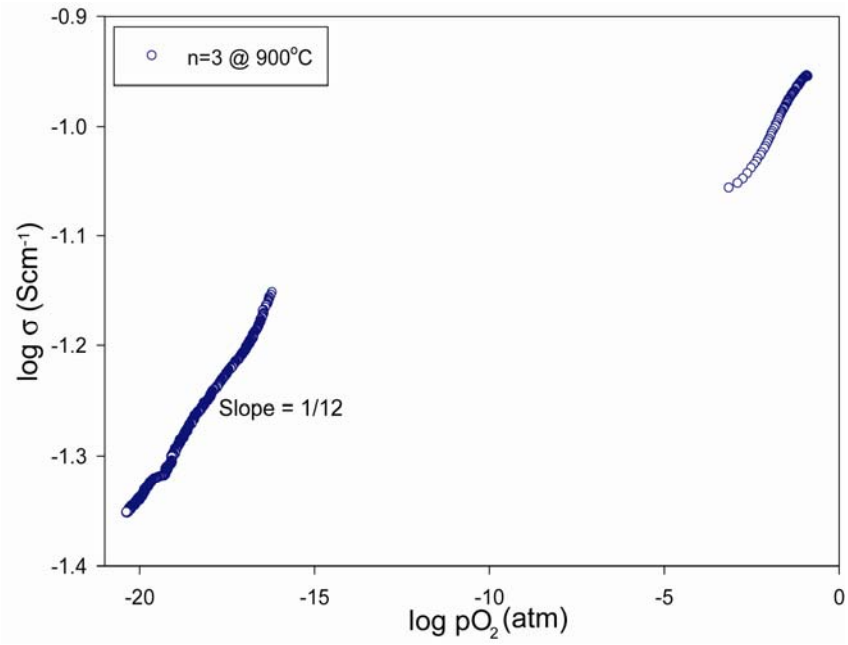


**Figure 4.33 Variation of the conductivity vs. oxygen partial pressure for n=3 which confirms p-type electronic conductivity.**

### 4.4.6. $La_4Sr_8Ti_8Mn_4O_{38-\delta}$ (n=4)

The reoxidation step was recorded, as shown in Figure 4.34, after the sample had been reduced for several hours. The $pO_2$ changed slowly from $10^{-19}$ atm down to $10^{-15}$ atm. That means we should be very close to equilibrium in that oxygen partial pressure range. However equilibrium was not really established in the rest of the range.

We can observe p-type conduction in both reducing and oxidised conditions. The slope is now higher than for n=3 and that value is still related to

disproportion of $Mn^{3+}$ to $Mn^{2+}$ and $Mn^{4+}$. This can explain the high value obtained in the magnetic studies for the effective moment (5.65 $\mu_B$) as the value for $Mn^{2+}$ is 5.9 $\mu_B$.

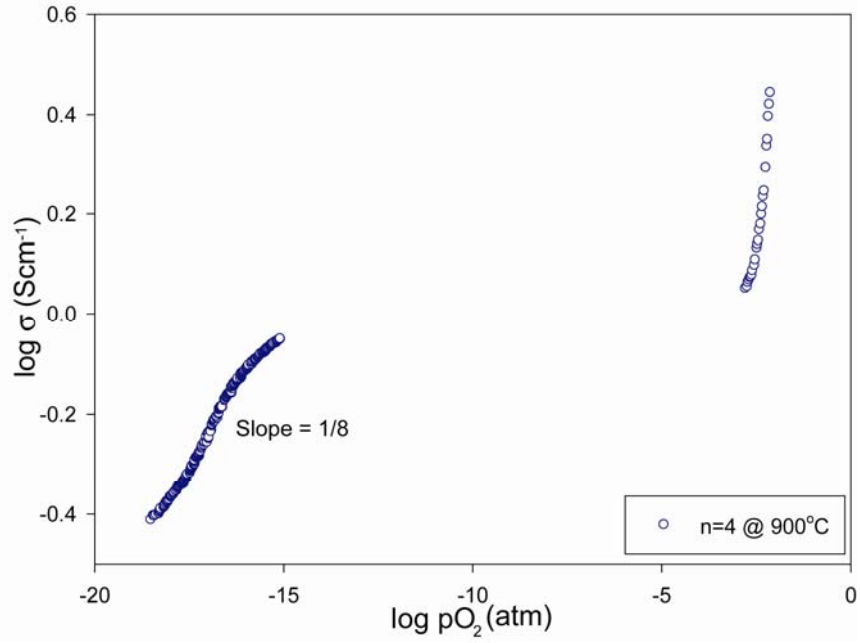


**Figure 4.34 Variation of the conductivity vs. oxygen partial pressure for n=4 which confirm p-type electronic conductivity.**

## 4.5. Conclusions

Electrical and magnetic properties have been investigated for a new family of perovskite titanates with formula $La_4Sr_8Ti_{12-n}Mn_nO_{38-\delta}$. The electrical properties have been studied using ac impedance spectroscopy and four terminal dc measurements.

AC impedance studies have shown that Mn substitution does not have a large impact on the bulk conductivity of the lower phases studied in static air, which remain close to the values observed in other related titanates.[2] However the grain boundary contributions are largely improved. The overall conductivity of the series increases with increasing content of manganese in static air. In reducing conditions the overall conductivity is higher at lower content of

manganese, Figure 4.35. The best conductivity value in reducing conditions has been obtained for n=1.

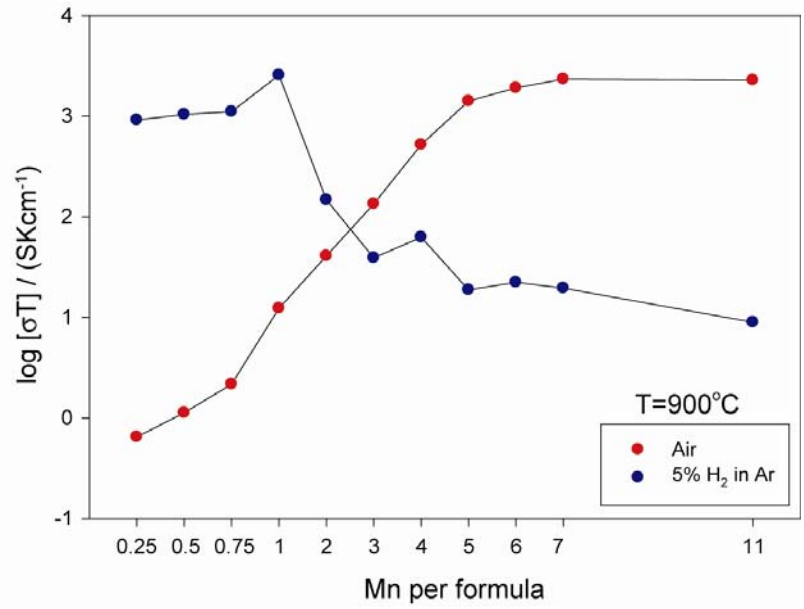


**Figure 4.35 Variation of the conductivity vs. manganese per formula unit in air and in 5%$H_2$ in Ar at 900°C.**

The replacement of $Ti^{4+}$ by lower valence cations would force the removal of oxygen from the structure to maintain the electroneutrality in the crystal, thus creating local oxygen vacancies that might favour ionic transport. This effect may lead to the observed gradual decrease of the lattice parameters with manganese content. Manganese has been previously shown to promote electroreduction under SOFC conditions[10, 11] Furthermore, Mn is known to accept lower coordination numbers in perovskites[12], especially for $Mn^{3+}$, and thus it may facilitate oxide-ion migration.

$SrTiO_3$ or La-substituted $SrTiO_3$ is known as an n-type semiconducting material, in which the electrical conductivity increases with decreasing $pO_2$.[13] The electrical conductivity is essentially controlled by the concentration of the electronic defect, $Ti^{3+}$ or $Ti'_{Ti}$. Instead, $LaMnO_3$ or Sr-substituted $LaMnO_3$ is a p-type conductor, and its electronic conductivity is determined by the mean Mn

valence.[14] After reduction, the electronic conductivity of (La,Sr)$MnO_3$ is decreased due to the lowered mean Mn valence, but its oxide ionic conductivity is increased due to the significantly increased oxygen vacancy concentration.[15]

Under oxidizing conditions, the electrical conductivity of the series increases with Mn content. It can be concluded that the electrical conductivity of the series in the oxidizing atmosphere is dominated by the p-type conduction related to Mn. In reducing atmosphere, however, the n-type conductivity related to $Ti^{3+}$ is greatly improved for n≤2 and the p-type conductivity related to manganese decreases at higher content of Mn.

For n≥3 indications of disproportion of $Mn^{3+}$ to $Mn^{2+}$ and $Mn^{4+}$ has been found which can explain the high values obtained for the effective moments as well as the decrease in total conductivity.

Evidence of ionic conductivity has been found and it is related to the removal of oxygen excess when Mn content increases. The possibility of mixed ionic/electronic conduction is very important, because it would allow the electro-oxidation process to move away from the three-phase electrode/electrolyte/gas interface onto the anode surface, with considerable catalytic enhancement[16].

Small changes in the slopes of the Arrhenius plots have been found. We have focused on samples n=1 and n=2. We believe that these changes are associated to a transition phase, i.e. insulator to metal-like in the compounds. It is corroborated by the neutron studies carried out on these samples since the transition phase temperatures match the change in conductivity for the samples, in air and in reducing conditions.

Magnetic studies for n=0.5 and n=1 have revealed paramagnetic behaviour across the whole range of temperatures studied. The oxidation state of manganese is mainly $Mn^{+3}$. For higher values of n we have found an antiferromagnetic behaviour.

## 4.6. References


[1] O.A.Marina,N.Canfield and J.Stevenson,*Solid State Ionics*, 2002, **149**,21

[2] J. Canales-Vazquez, S. W. Tao, and J. T. S. Irvine, *Solid State Ionics*, 2003, **159**, 159.

[3] Q. X. Fu, F. Tiezt, P. Lersch, and D. Stöver, *Solid State Ionics*, 2006, **177**, 1059.

[4] Q. X. Fu, F. Tiezt, and D. Stöver, *Solid State Ionics*, 2006, **177**, 1819.

[5] J. C. Ruiz-Morales, J. Canales-Vazquez, C. Savaniu, David Marrero-Lopez, W. Zhou, and J. T. S. Irvine, *Nature*, 2006, **439**, 568.

[6] S.Plint, P.Connors,S.Tao and J.Irvine,*Solid State Ionics*, 2006, **177**,2005.

[7] R. Raffaelle, H. U. Anderson, D. M. Sparklin, and P. E. Parris, *Phys. Rev. B*, 1991, **43**, 7991.

[8] S. E. Dorris and T. O. Mason, *J. Am. Ceram. Soc.*, 1988, **71**, 379.

[9] J. W. Stevenson, M. M. Nasrallah, H. U. Anderson, and D. M. Sparlin, *J. Solid State Chem.*, 1993, **102**, 175.

[10] P. Holtappels, J. L. Bradley, J. T. S. Irvine, A. Kaiser, and M. Mogensen, *Journal of Electrochemistry Society* 2001, **148**, A923.

[11] J. T. S. Irvine, P. R. Slater, A. Kaiser, J. L. Bradley, P. Holtappels, and M. Mogensen, 4th European SOFC Forum, Switzerland, 2000.

[12] K. Poeppelmeier and J.M.Longo, *J. Solid State Chem.*, 1982, **44**, 89

[13] U. Balachandran and N. G. Eror, *J. Electrochem. Soc.*, 1982, **129**, 1021.

[14] J. Mizusaki, Y. Yonemura, H. Kamata, K. Ohyama, M. Mori, H. Takai, H. Tagawa, M. Dokiya, K. Nayara, T. Sasamoto, H. Inaba, and T. Hashimoto, *Solid State Ionics*, 2000, **10**, 145.

[15] I. Yasuda and J. Hishinuma, *J. Solid State Chem.*, 1996, **123**, 382.

[16] A. Atkinson, S. Barnett, R. J. Gorte, J. T. S. Irvine, A. J. McEvoy, M. Mogensen, S. C. Singhal, and J.Vohs, *Nature materials*, 2004.

# 5

# Fuel Cell Tests

## 5.1. Introduction

The lowest members of the series $La_4Sr_8Ti_{12-n}Mn_nO_{38-\delta}$ have been investigated as fuel electrode materials for SOFCs. Relatively low polarisation resistances and anodic overpotentials have been observed under both hydrogen and methane conditions, especially for n=1.

## 5.2. Fuel cell tests

### 5.2.1. $La_4Sr_8Ti_{11.25}Mn_{0.25}O_{38-\delta}$ (n=0.25)

Figure 5.1 shows the polarisation resistances obtained for the half-cell tests performed using $La_4Sr_8Ti_{11.25}Mn_{0.25}O_{38-\delta}$ as anode material.

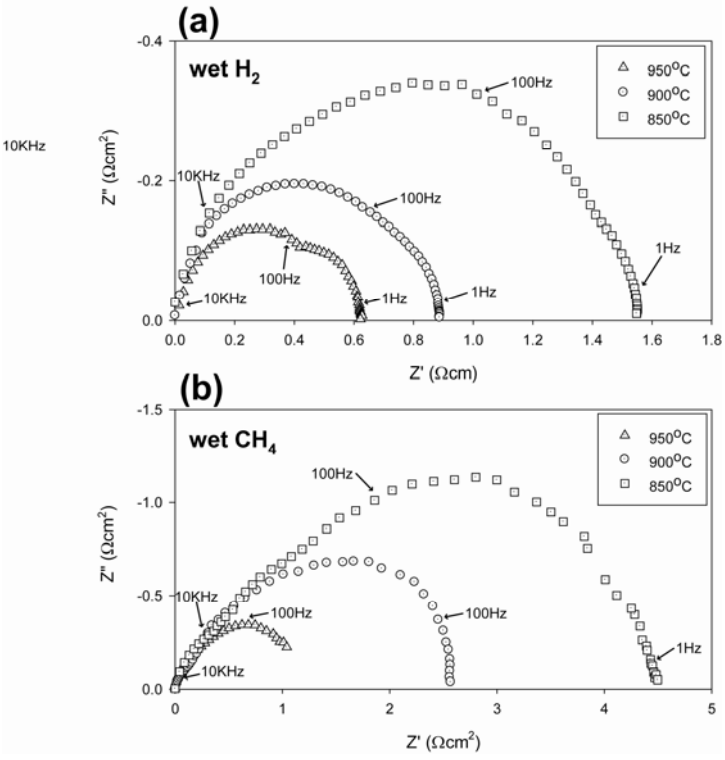


**Figure 5.1 Polarisation resistances of $La_4Sr_8Ti_{11.75}Mn_{0.25}O_{38-\delta}$ (n=0.25) anode at different temperatures a) under wet hydrogen and (b) methane.**

The polarisation resistances in wet $H_2$ (97.7% $H_2$, 2.3% $H_2O$) were 0.6 $\Omega cm^2$ at 950°C, 0.88 $\Omega cm^2$ at 900°C and 1.55 $\Omega cm^2$ at 850°C. The values in wet $CH_4$ (97.7% $CH_4$, 2.3% $H_2O$) were higher, i.e. 1.20 $\Omega cm^2$ at 950°C, 2.55 $\Omega cm^2$ at 900°C and 4.50 $\Omega cm^2$ at 850°C. These values are much lower than those reported[1] for the sample without manganese (n=0). For n=0 at 900°C the polarisation resistances in $H_2$ and $CH_4$ were 2.97 $\Omega cm^2$ and 8.93 $\Omega cm^2$ respectively.

The anodic overpotentials at 950°C under wet hydrogen and methane were respectively 124 mV at 0.5 $Acm^{-2}$ and 73 mV at 0.1 $Acm^{-2}$, Figure 5.2. At lower temperatures these values increase considerably.

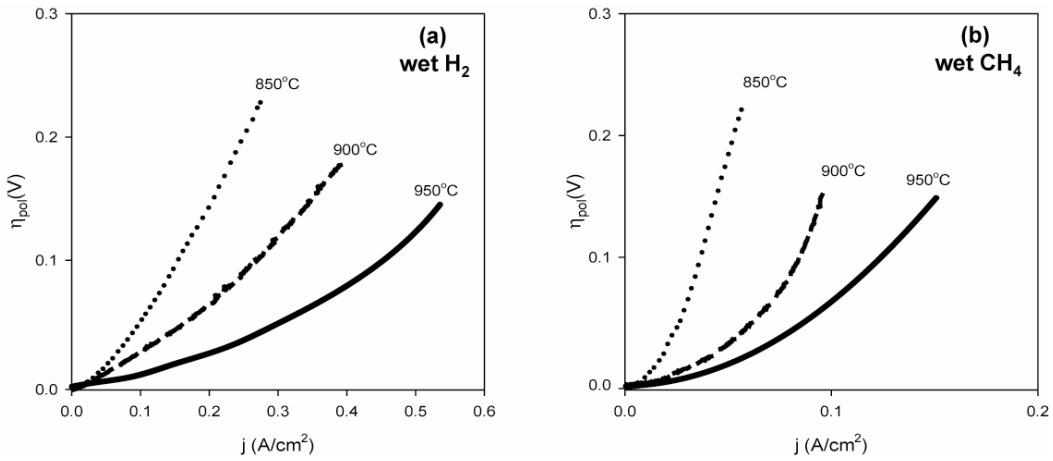


**Figure 5.2 Anodic overpotential of n=0.25 at different temperatures and (a) under wet hydrogen and (b) wet methane.**

The fuel cell performances using an n=0.25 anode, a rather thick (2 mm) YSZ electrolyte, and LSM cathode are shown in Figure 5.3. The maximum power density in wet $H_2$ was 0.14 W at 950°C. At the same temperature the maximum power density in methane was just close to 0.06 W. Current densities of 231, 184 and 133 $mA/cm^2$ at 600 mV were achieved at 950, 900 and 850°C respectively using $H_2$ as fuel.

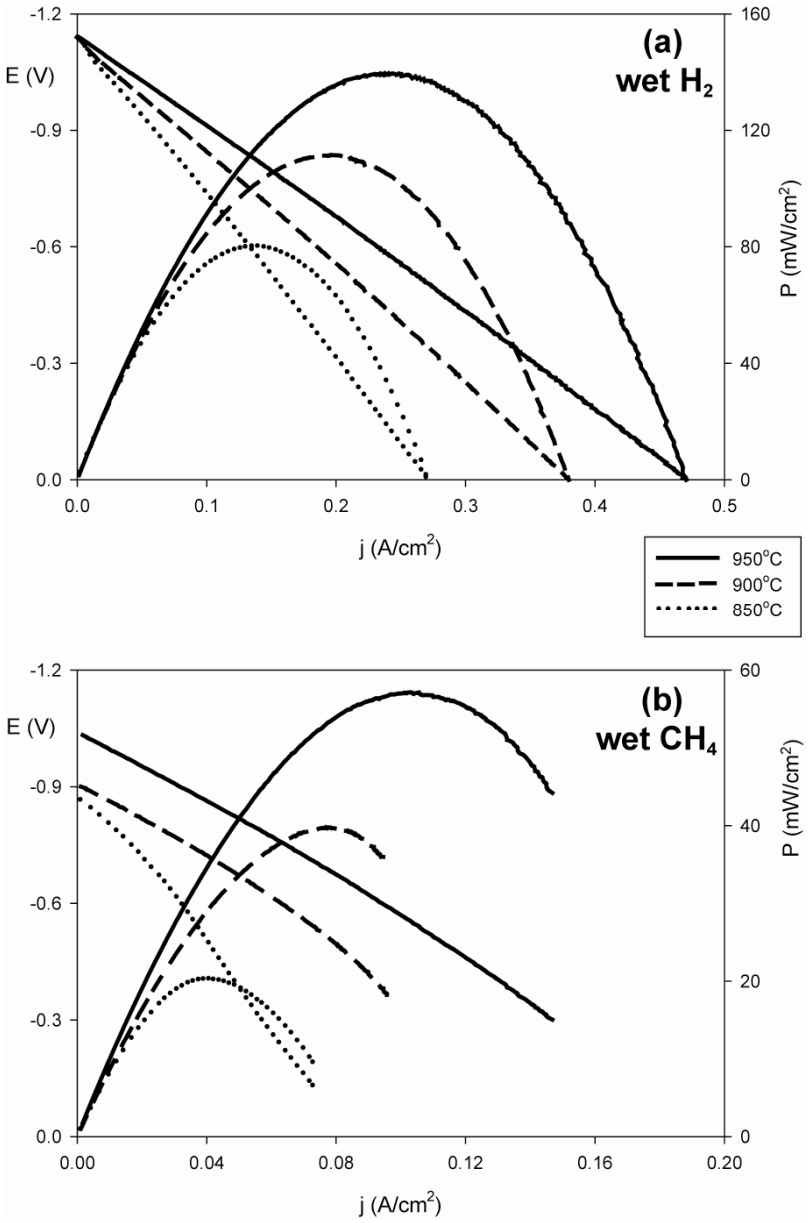


**Figure 5.3 Performance plots for $La_4Sr_8Ti_{11.75}Mn_{0.25}O_{38-\delta}$ (n=0.25) anode in thick electrolyte (a) under wet $H_2$ (b) under wet $CH_4$.**

Using methane as fuel current densities of 32, 63 and 94 mA/cm$^2$ at 600 mV were achieved at 950, 900 and 850°C respectively.

The open circuit voltages almost matched those predicted thermodynamically in hydrogen atmosphere. The theoretical values are: 1.104V, 1.111V and 1.119V, at 950, 900 and 850°C, respectively. The experimental values were 1.105V, 1.116 and 1.116V, in the same conditions, indicating good sealing in any case.

In methane the interpretation is rather complicated because in the presence of steam a number of alternative routes are possible for methane oxidation. The OCV under methane flow decreases with decreasing temperature. The OCV values in $CH_4$ are 1.030, 0.902 and 0.870 at 950, 900 and 850°C, respectively. This indicates that the fuel oxidation probably involves direct or partial oxidation of the methane. No carbon deposits were detected after our tests.

### 5.2.2. $La_4Sr_8Ti_{11.5}Mn_{0.5}O_{38-\delta}$ (n=0.5)

Figure 5.4 shows the polarisation resistances obtained for the half-cell tests performed using $La_4Sr_8Ti_{11.5}Mn_{0.5}O_{38-\delta}$ as anode material.

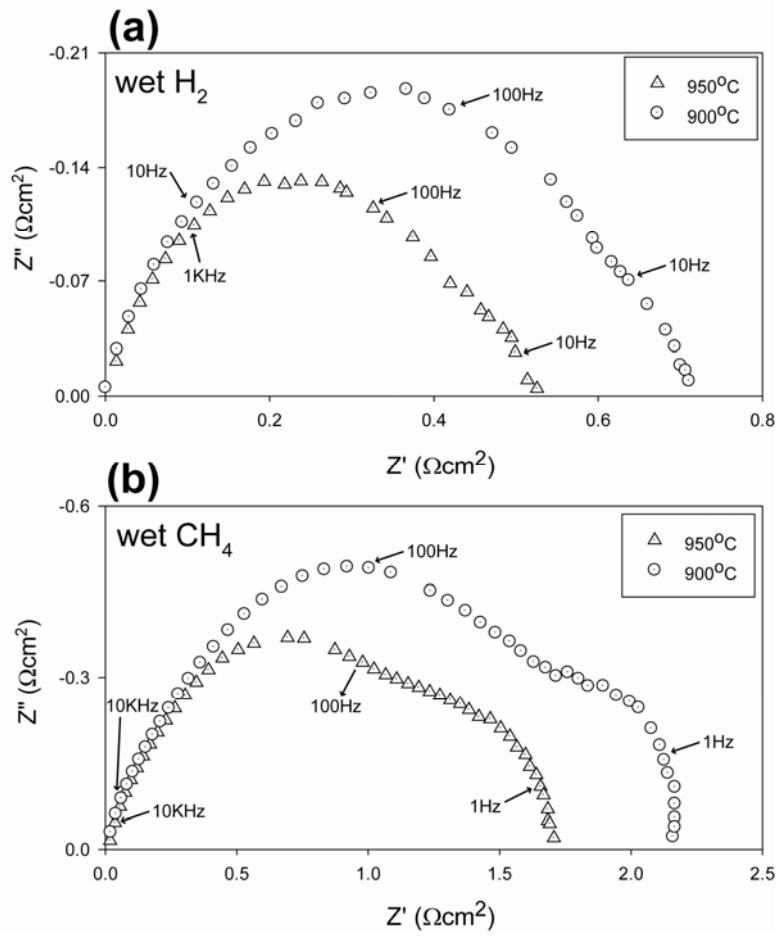


**Figure 5.4 Polarisation resistances of $La_4Sr_8Ti_{11.5}Mn_{0.5}O_{38-\delta}$ (n=0.5) anode at different temperatures a) under wet hydrogen and (b) methane.**

The polarisation resistances in wet $H_2$ (97.7% $H_2$, 2.3% $H_2O$) were 0.53 $\Omega cm^2$ at 950°C and 0.71 $\Omega cm^2$ at 900°C. The values in wet $CH_4$ (97.7% $CH_4$, 2.3% $H_2O$) were higher, i.e. 1.7 $\Omega cm^2$ at 950°C and 2.16 $\Omega cm^2$ at 900°C. The results in wet hydrogen are slightly better than those obtained for n=0.25. In wet methane the polarisation resistance is lower at 900°C but slightly higher at 950°C. This could be a problem of sealing as the OCV was lower for n=0.50 at this temperature.

The anodic overpotentials at 950°C under wet hydrogen and methane were respectively 189 mV at 0.3 $Acm^{-2}$ and 185 mV at 0.2 $Acm^{-2}$, Figure 5.5. At lower temperatures these values increase.

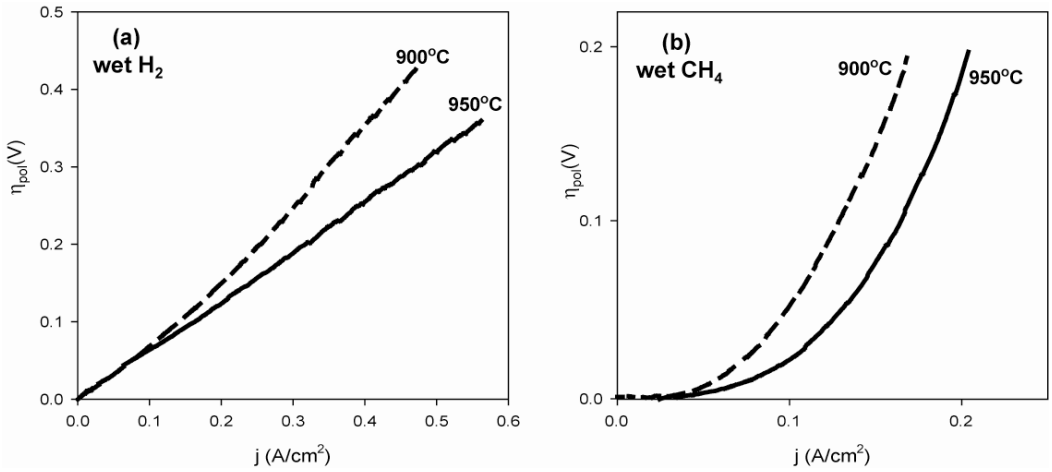


**Figure 5.5 Anodic overpotential of n=0.5 at different temperatures (a) under wet hydrogen and (b) wet methane.**

Figure 5.6 shows the performance of the n=0.5 anode in different atmospheres at different temperatures using a two-electrode set-up. The maximum power densities in wet $H_2$ were 0.11 W at 950°C and 0.09 W at 900°C. At the same temperatures the maximum power densities in $CH_4$ were 0.05 W and 0.03 W respectively. Current densities of 185 and 166mA/$cm^2$ at 600 mV were achieved at 950 and 900°C respectively using $H_2$ as fuel. In methane current densities of 82 and 50 mA/$cm^2$ at 600 mV were achieved at 950 and 900°C respectively.

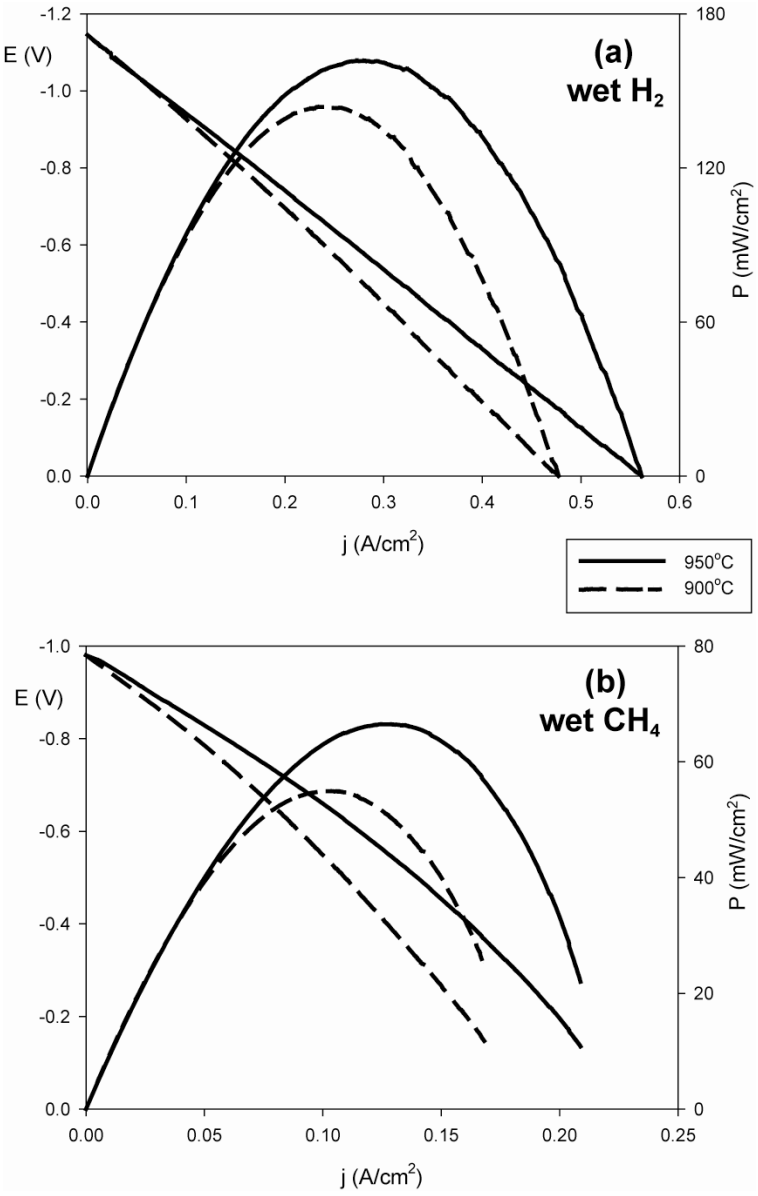


**Figure 5.6 Performance plots for $La_4Sr_8Ti_{11.5}Mn_{0.5}O_{38-\delta}$ (n=0.5) anode in thick electrolyte, (a) under wet $H_2$ (b) under wet $CH_4$.**

The open circuit voltages are slightly lower than those predicted thermodynamically in hydrogen atmosphere. The theoretical values are: 1.104V and 1.111V at 950 and 900°C, respectively. The experimental values were 1.091V and 1.099 in the same conditions. The OCV under methane flow decreases with decreasing temperature, i.e. 0.950 and 0.86 at 950, 900°C, respectively. This indicates that the fuel oxidation probably involves direct or partial oxidation of the methane.

### 5.2.3. $La_4Sr_8Ti_{11.25}Mn_{0.75}O_{38-\delta}$ (n=0.75)

The polarisation resistances obtained for the half-cell tests performed using n=0.75 as anode material are shown in Figure 5.7.

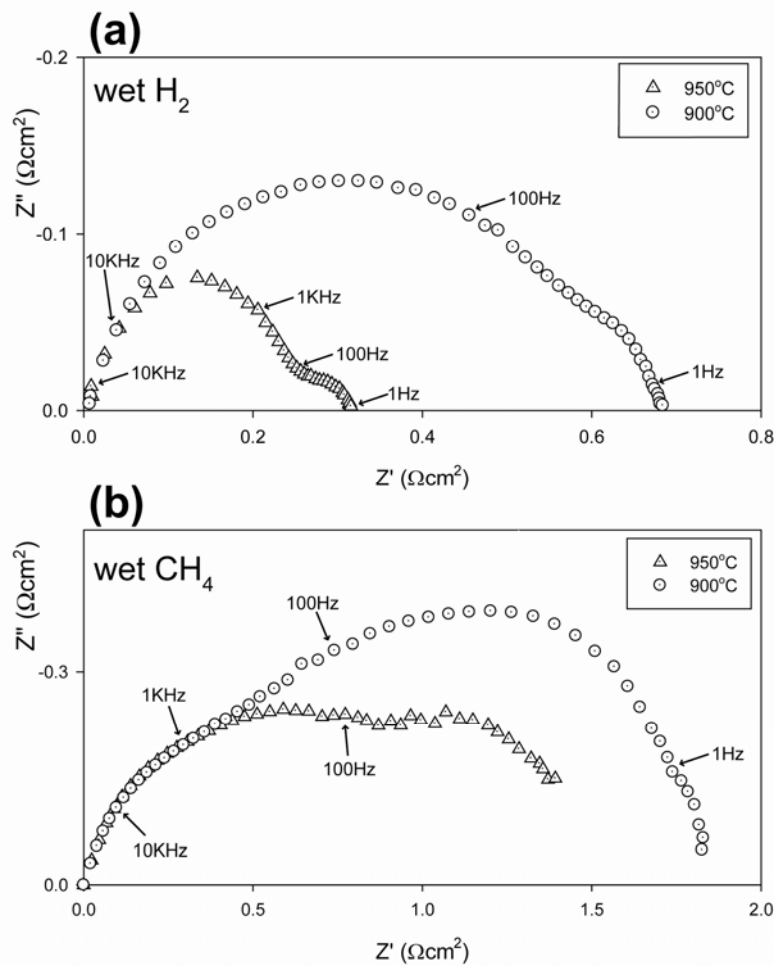


**Figure 5.7 Polarisation resistances of $La_4Sr_8Ti_{11.25}Mn_{0.75}O_{38-\delta}$ (n=0.75) anode at different temperatures a) under wet hydrogen and (b) methane.**

The polarisation resistances in wet $H_2$ (97.7% $H_2$, 2.3% $H_2O$) were 0.35 $\Omega cm^2$ at 950°C and 0.67 $\Omega cm^2$ at 900°C. The values in wet $CH_4$ (97.7% $CH_4$, 2.3% $H_2O$) were 1.5 $\Omega cm^2$ at 950°C and 1.80 $\Omega cm^2$ at 900°C. The results in wet hydrogen are better than those obtained for n=0.5 especially at 950°C. In wet methane the polarisation resistances are slightly lower at both temperatures.

The anodic overpotentials at 950°C under wet hydrogen and methane were respectively 146 mV at 0.3 $Acm^{-2}$ and 137 mV at 0.2 $Acm^{-2}$, Figure 5.8. These results are better than those obtained for n=0.5 and for Sc-substituted titanates[2].

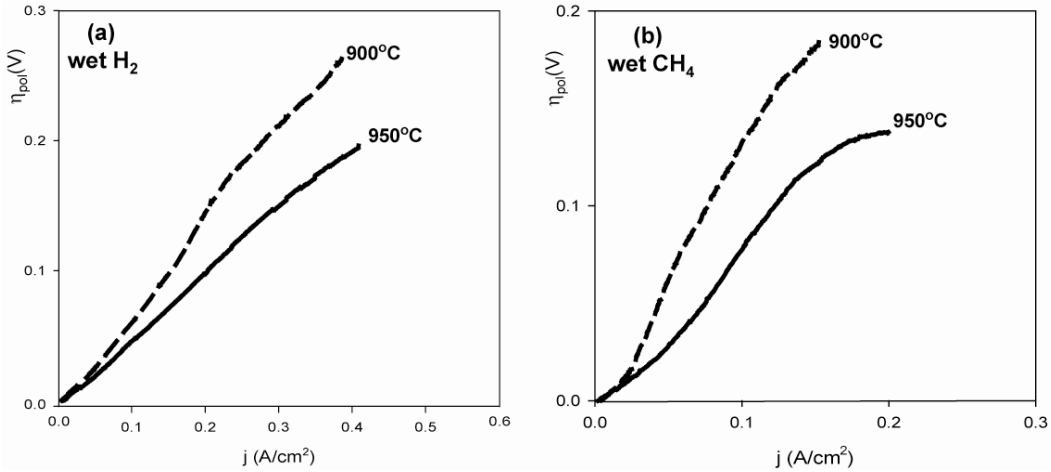


**Figure 5.8 Anodic overpotential of n=0.75 at different temperatures (a) under wet hydrogen and (b) wet methane.**

The fuel cell performances in different atmospheres using n=0.75 as anode material are shown in Figure 5.9. The maximum power densities in wet $H_2$ were 0.16 W at 950°C and 0.14 W at 900°C. At the same temperatures the maximum power densities in $CH_4$ were 0.07 W and 0.05 W respectively. Current densities of 270 and 240mA/cm$^2$ at 600 mV were achieved at 950 and 900°C respectively using $H_2$ as fuel. In $CH_4$ current densities of 116 and 90 mA/cm$^2$ at 600 mV were achieved at 950 and 900°C respectively

The open circuit voltages are slightly higher than those predicted thermodynamically in hydrogen atmosphere. The theoretical values are: 1.104V and 1.111V at 950 and 900, respectively. The experimental values were 1.130V and 1.140 in the same conditions. The open circuit voltages under methane flow are 0.951 and 0.973 at 950, 900°C, respectively.

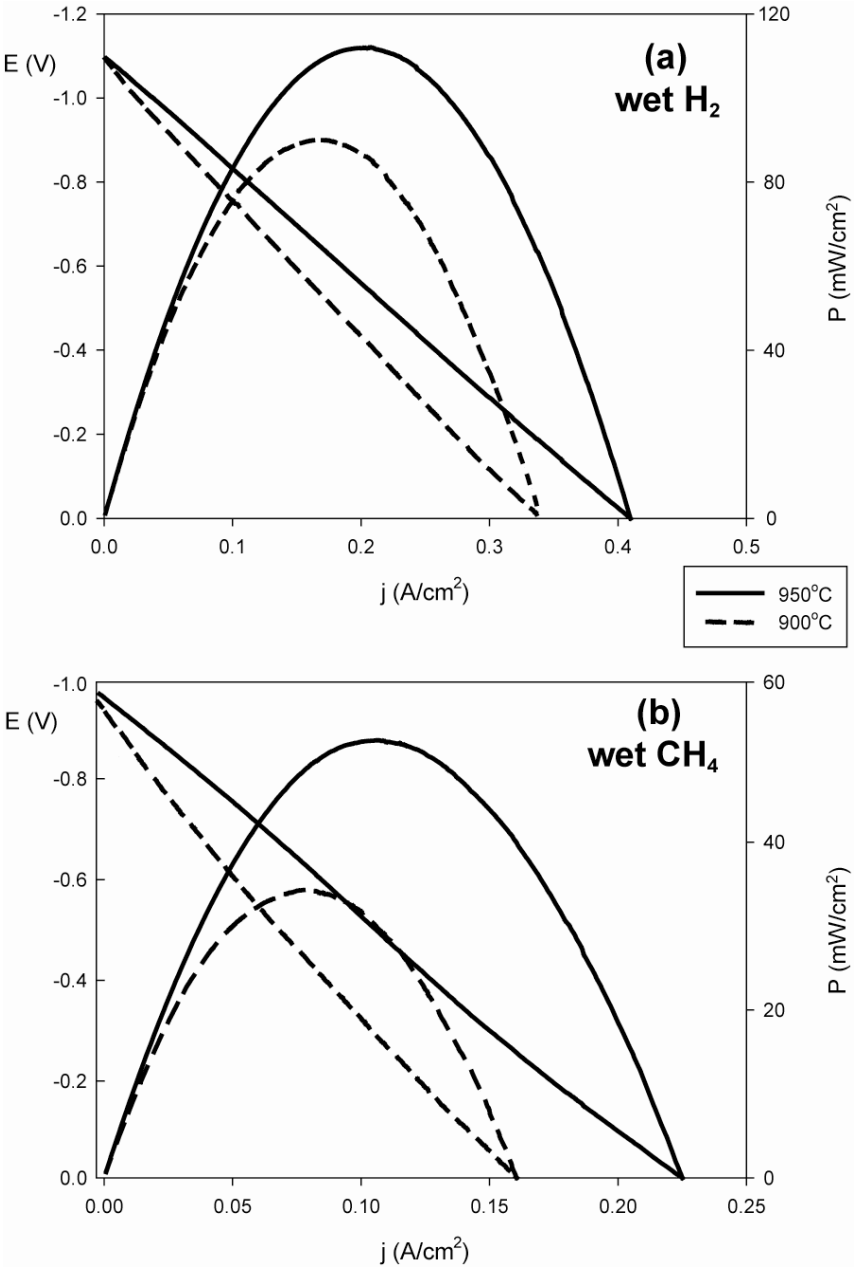


**Figure 5.9 Performance plots for $La_4Sr_8Ti_{11.25}Mn_{0.75}O_{38-\delta}$ (n=0.75) anode in thick electrolyte, (a) under wet $H_2$ (b) under wet $CH_4$.**

### 5.2.4. $La_4Sr_8Ti_{11}Mn_1O_{38-\delta}$ (n=1)[3]

The half-cell tests performed using $La_4Sr_8Ti_{11}MnO_{38-\delta}$ as anode material revealed rather low polarisation resistances in wet $H_2$ and $CH_4$, i.e. 0.3 and 0.7 $\Omega cm^2$ at 950ºC respectively, Figure 5.10. It is especially interesting to note that the results in methane, at least at 950°C, are fairly comparable to those in $H_2$.

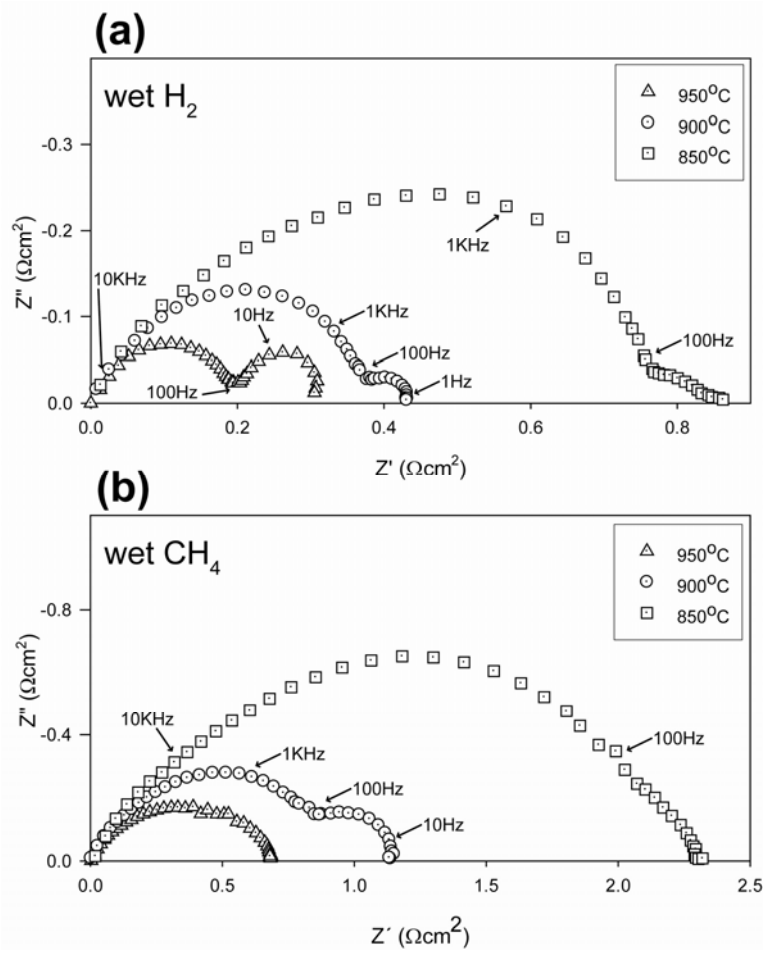


**Figure 5.10 Polarisation resistances of $La_4Sr_8Ti_{11}Mn_1O_{38-\delta}$ anode at different temperatures a) under wet hydrogen and (b) methane.**

The plots in $H_2$ and $CH_4$ clearly show different processes at each temperature. The high frequency region is associated to charge transfer process. Diffusion and mass transfer processes must therefore be associated to the slower frequencies.[4]

The anodic overpotentials under hydrogen, Figure 5.11 are better than the best results reported[2] for Sc-substituted titanates and much better than those corresponding to the non-substituted counterpart. The values obtained at 950°C and 900°C, at 0.5A/cm$^2$ under wet hydrogen were just 55mV and 116mV, respectively. These are rather low compared to the 250mV of anodic polarisation obtained for the Sc-doped titanates under the same conditions.

In methane the low values of polarisations are only obtained just at 950°C, i.e. 72mV at 0.5A/cm$^2$. At lower temperatures there is a large increase in the polarisation, i.e. a value of 116mV at 0.2A/cm$^2$ is obtained at 900°C. That could be related with a change in the methane oxidation mechanism, even a ~10% decrease in the OCV is observed at that temperature. This corroborates the low polarisation resistance values and the applicability of these materials as anodes for direct methane fuel cells.

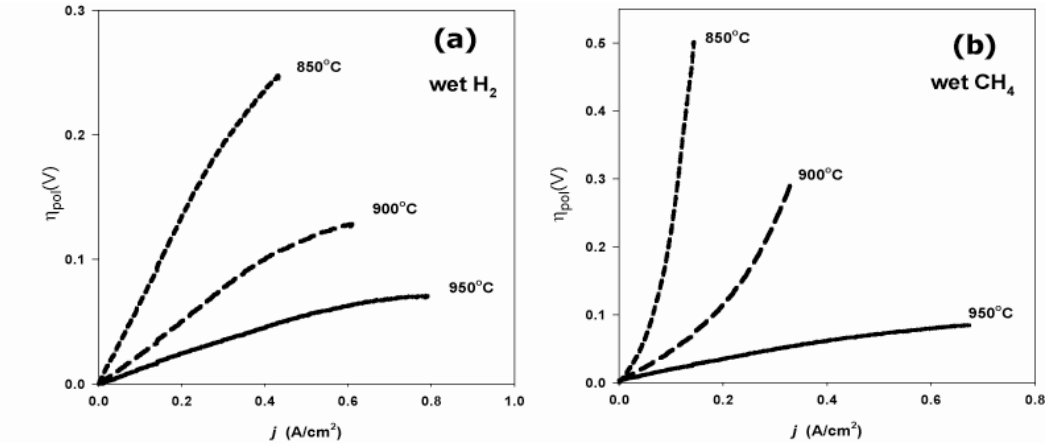


**Figure 5.11 Anodic overpotential of n=1 at different temperatures and (a) under wet hydrogen and (b) wet methane. Values as surprisingly low as 55mV in $H_2$ and 72mV in $CH_4$, at 0.5A/cm$^2$, at 950°C, were obtained. Thus, a good performance for this anode can be expected**

Figure 5.12 shows the performance of the n=1 anode, thick (2mm) YSZ electrolyte and LSM cathode in different atmospheres at different temperatures using a two-electrode set-up. The maximum power densities in wet $H_2$ were 0.22 W at 950°C and 0.16 W at 900°C. At the same temperatures the maximum power densities in $CH_4$ were 0.18 W and 0.11 W respectively. The open circuit voltages almost matched those predicted thermodynamically in hydrogen atmosphere. The theoretical values are: 1.104V, 1.111V and 1.119V, at 950, 900 and 850°C, respectively. The experimental values were 1.101V, 1.105 and

1.112V, in the same conditions, indicating good sealing in any case. In methane the interpretation is rather complicated because in the presence of steam a number of alternative routes are possible for methane oxidation. The OCV under methane flow decreases with decreasing temperature are 1.080, 0.980 and 0.920 at 950, 900 and 850°C, respectively. That could be related with a change in the methane oxidation mechanism. It probably involves direct or partial oxidation of the methane. No carbon deposits were detected after our tests.

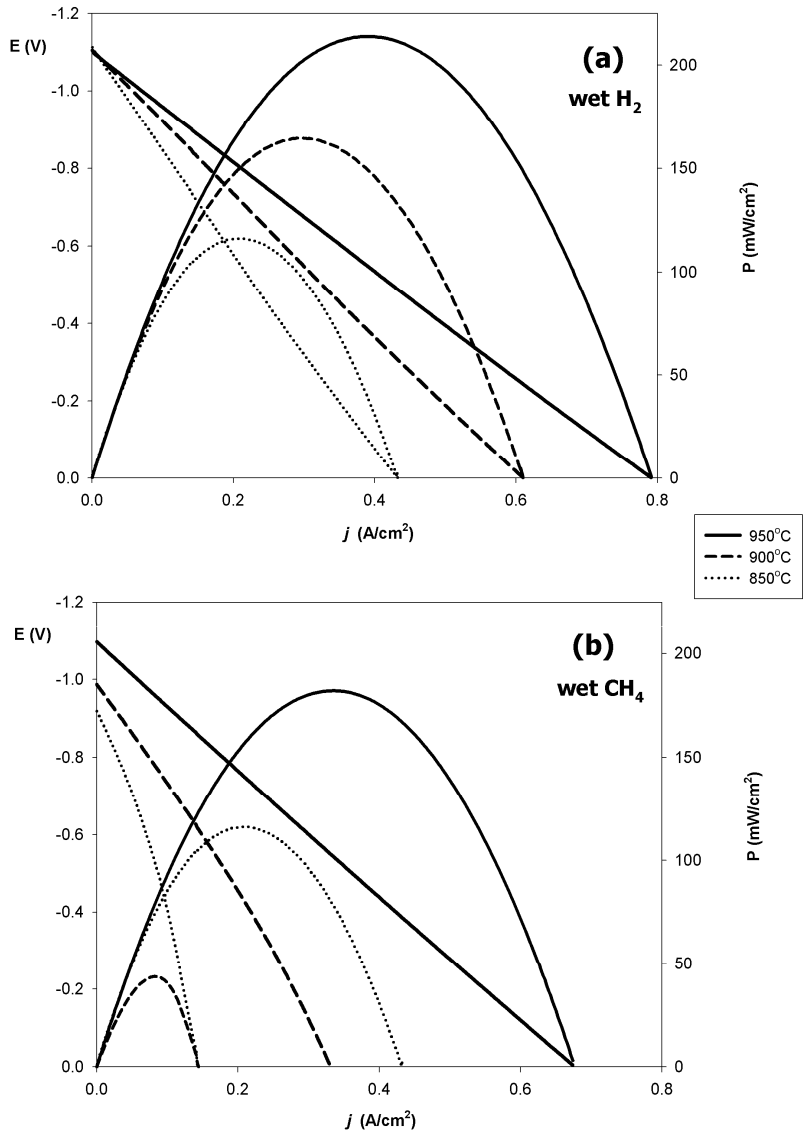


**Figure 5.12 Performance plots for $La_4Sr_8Ti_{11}Mn_1O_{38-\delta}$ (n=1) anode in thick electrolyte, (a) under wet $H_2$ (b) under wet $CH_4$. The performances in both cases, at 950°C were roughly 0.2W/cm$^2$.**

SEM performed on fuel cells after testing revealed a very good adherence between the anode and the electrolyte, Figure 5.13. Thus no contact resistances losses are expected. Despite of the low polarisation resistances obtained further optimisation of the microstructure seems to promise an enhanced catalytic activity towards the methane oxidation at lower temperatures.

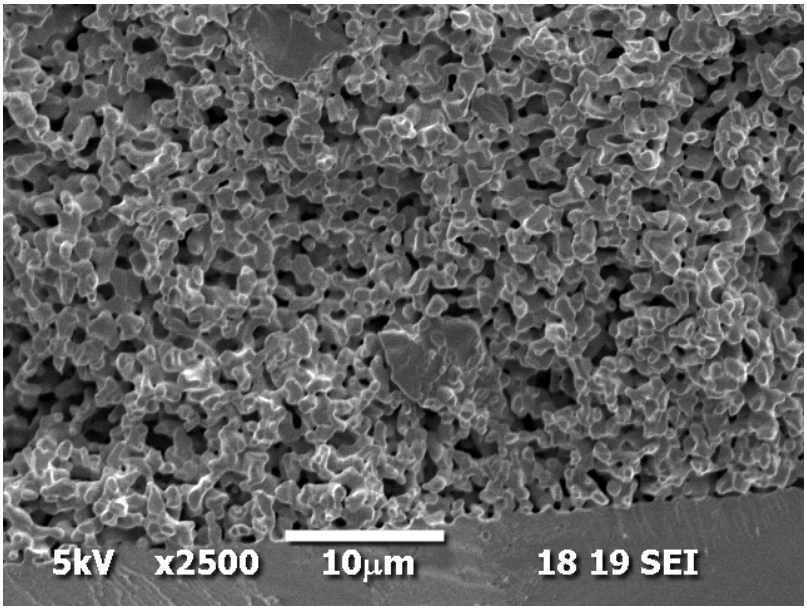


**Figure 5.13 Cross-sectional view of an interface of n=1 anode and YSZ. The contact between the two materials is really good, thus no contact resistances losses are expected.**

### 5.2.5. $La_4Sr_8Ti_{11}Mn_1O_{38-\delta}$ (n=2)

The polarisation resistances obtained for the half-cell tests performed using n=2 as anode material are showed in Figure 5.14.

The polarisation resistances in wet $H_2$ (97.7% $H_2$, 2.3% $H_2O$) are 0.8 $\Omega cm^2$ at 900°C and 1.55 $\Omega cm^2$ at 850°C. These values are much higher than those obtained for n=1. They are similar to those reported for n=0.25. This fact matches with the similar total conductivity obtained for these two samples under reducing conditions.

The values in wet methane (97.7% $CH_4$, 2.3% $H_2O$) are 5.5 $\Omega cm^2$ at 900°C and 14 $\Omega cm^2$ at 900°C. The results in wet $CH_4$ are very poor although they are slightly better than those obtained for the non-substituted counterpart (n=0).

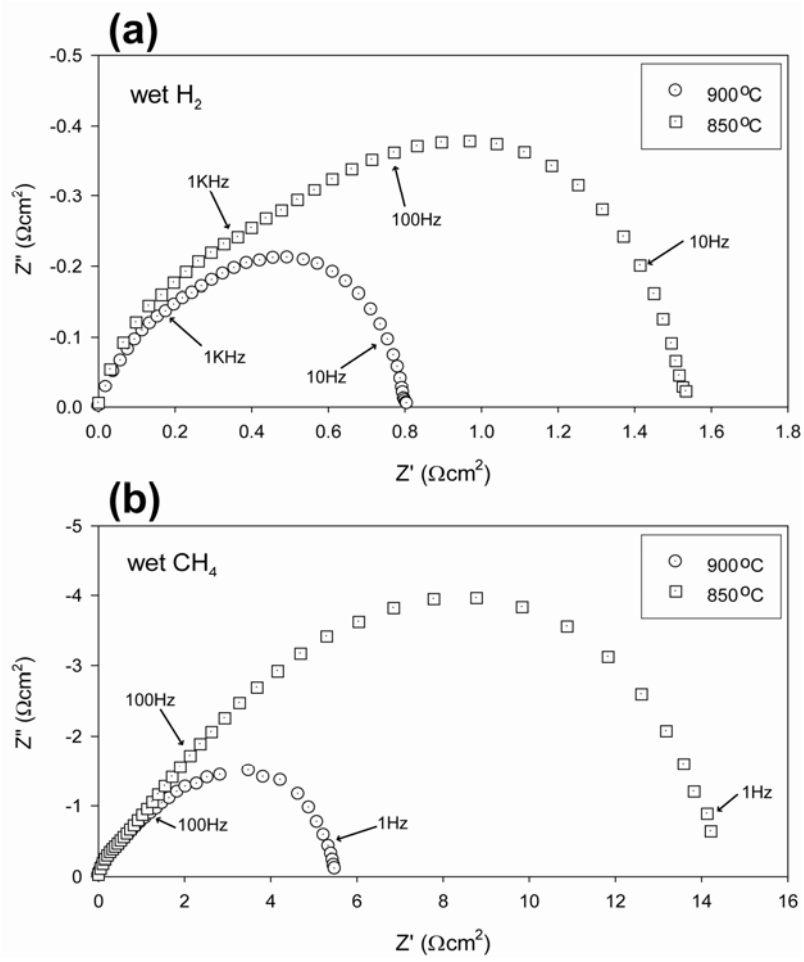


**Figure 5.14 Polarisation resistances of $La_4Sr_8Ti_{10}Mn_2O_{38-\delta}$ anode at different temperatures a) under wet hydrogen and (b) methane. The values in methane are comparable to those obtained for the non-substituted counterpart (n=0).**

The anodic overpotentials under wet hydrogen are 109 mV at 0.3 $Acm^{-2}$ at 950°C and 117 mV at 0.2 $Acm^{-2}$ at 900°C, Figure 5.15. The results in wet methane were very poor.

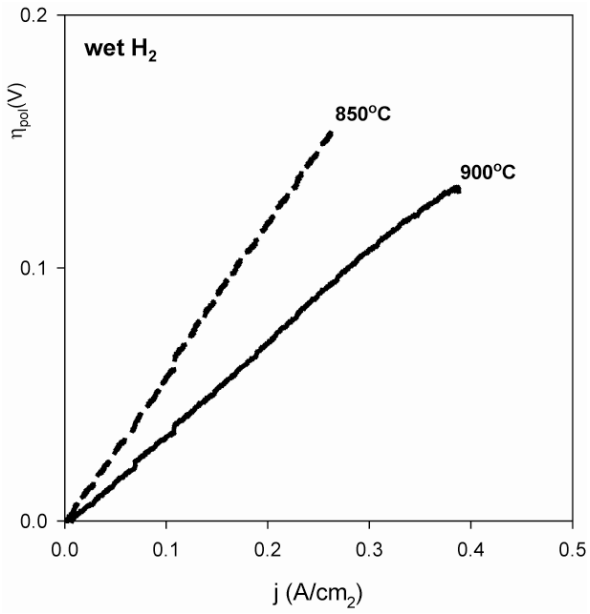


**Figure 5.15 Anodic overpotential of n=2 at different temperatures under wet hydrogen.**

The fuel cell performances in wet $H_2$ using n=2 as anode material are shown in Figure 5.16. The maximum power densities were 108 mW at 950°C and 73 mW at 900°C.

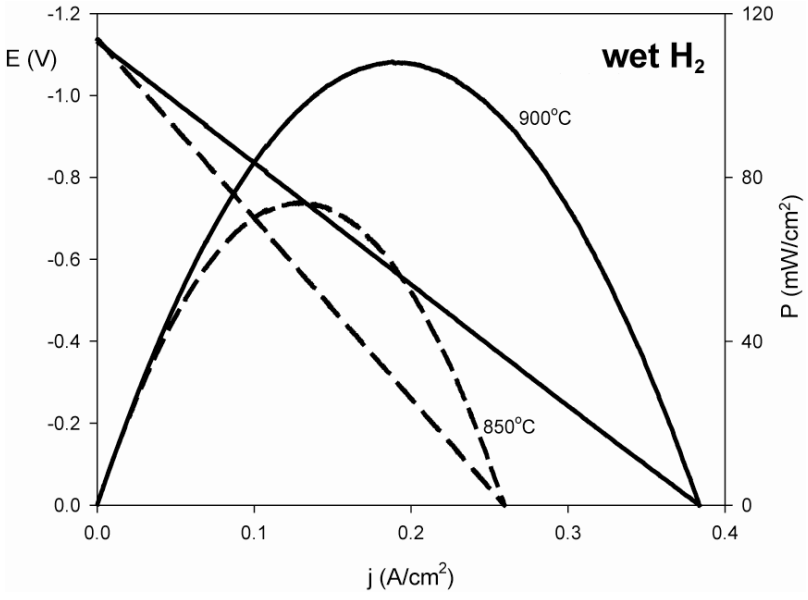


**Figure 5.16 Performance plots for $La_4Sr_8Ti_{10}Mn_2O_{38-\delta}$ (n=2) anode in thick electrolyte under wet $H_2$. The performances under wet $CH_4$ were very low compared to n=1.**

Current densities of 179 and 122mA/cm$^2$ at 600 mV were achieved at 950 and 900°C using $H_2$ as fuel. The open circuit voltages almost matched those predicted thermodynamically in hydrogen atmosphere, i.e. 1.110V and 1.131V at 900 and 850°C, respectively.

SEM performed on fuel cells after testing revealed a good adherence between the anode and the electrolyte, Figure 5.17. However an optimisation of the microstructure could improve the performance.

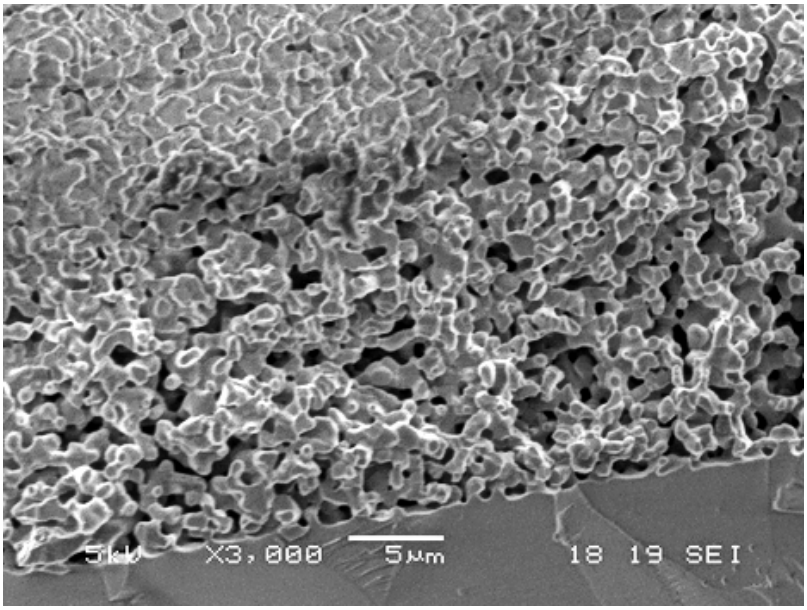


**Figure 5.17 Cross-sectional view of an interface of n=2 anode and YSZ.**

## 5.3. Summary

The lowest compounds of the series $La_4Sr_8Ti_{12-n}Mn_nO_{38-\delta}$, i.e. from n=0.25 to n=2, have been investigated under fuel cell conditions in pure hydrogen and methane. Table 5.1 shows the values of the polarisation resistances obtained for these samples in both atmospheres and at different temperatures. These values were obtained after passing 5%$H_2$ in Ar for 12-18 hours to achieve the full reduction of the samples.

| Anode | Rp(Ωcm$^2$) at 950°C | | Rp(Ωcm$^2$) at 900°C | | Rp(Ωcm$^2$) at 850°C | |
|---|---|---|---|---|---|---|
| n | wet $H_2$ | wet $CH_4$ | wet $H_2$ | wet $CH_4$ | wet $H_2$ | wet $CH_4$ |
| 0 | - | - | 2.97 | 8.93 | - | - |
| 0.25 | 0.60 | 1.20 | 0.88 | 2.55 | 1.55 | 4.5 |
| 0.5 | 0.53 | 1.70 | 0.71 | 2.16 | - | - |
| 0.75 | 0.35 | 1.50 | 0.67 | 1.80 | - | - |
| 1 | 0.30 | 0.68 | 0.43 | 1.14 | 0.86 | 2.3 |
| 2 | - | - | 0.80 | 5.50 | 1.55 | 14 |

**Table 5.1 Polarisation resistances $La_4Sr_8Ti_{12-n}Mn_nO_{38-\delta}$ anodes in hydrogen and methane at different temperatures. $La_4Sr_8Ti_{11}Mn_1O_{38-\delta}$ exhibits the best properties as an anode material for SOFCs. Despite the polarisation resistance in methane being nearly 2 times larger than in hydrogen, the performances are very similar.**

The lowest values for the polarisation resistance were obtained for n=1. Despite the polarisation resistance in methane being nearly 2 times larger than in hydrogen at 950°C, the performances are very similar, which might indicate certain methane activation at that temperature.

The experimental OCV values matched generally those predicted thermodynamically in hydrogen atmosphere. However the OCV under methane flow decreases with decreasing temperature. There exist a number of possible mechanisms for the oxidation of methane in wet atmospheres, *i.e.*, methane reforming, direct oxidation, or partial oxidation in addition to gas shift and cracking. If the process involves hydrogen production the theoretical OCV would decrease with increasing temperature. In these phases the OCV increases with increasing temperature so we think the process does not involve methane cracking or reforming. Hence we assume that the mechanics involves direct or partial oxidation. Furthermore no carbon deposits were detected after our tests.

Figure 5.18 shows the evolution of the OCV values and polarisation resistances obtained in methane at 900°C. For n=1 we have got the highest value for the OCV, i.e. 1V.

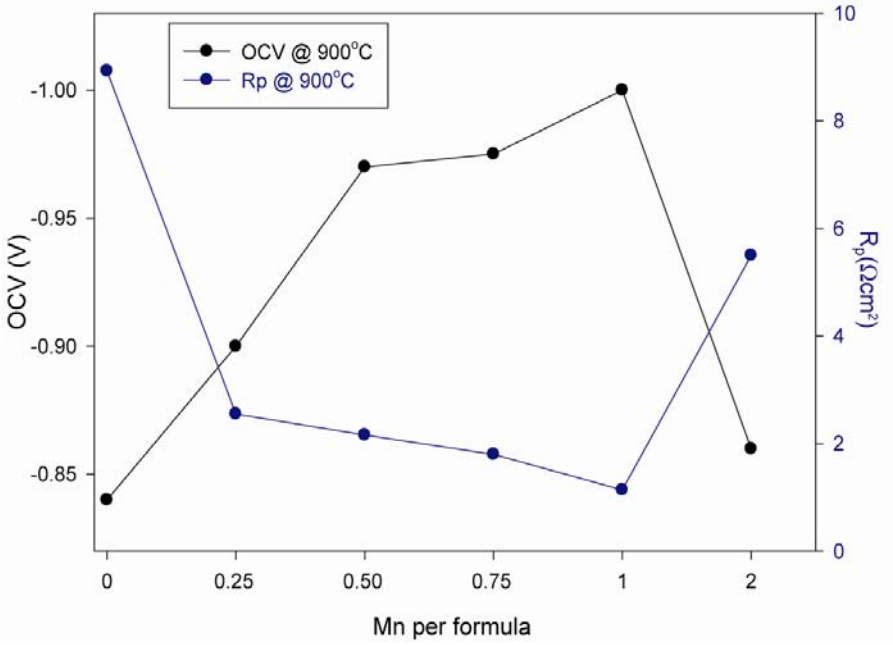


**Figure 5.18 OCV values and polarisation resistances at 900°C in methane for the $La_4Sr_8Ti_{12-n}Mn_nO_{38-\delta}$ series. For n=1 we have obtained the lowest polarisation resistance (1.14 Ωcm$^2$) and the highest OCV (1.0V).**

## 5.4. Conclusions

Half-cell tests were performed using $La_4Sr_8Ti_{12-n}Mn_nO_{38-\delta}$ as anode material for the lowest members of the series. The best results were found for n=1. These studies revealed rather low polarisation resistances in wet $H_2$ and $CH_4$ at 950ºC respectively for n=1. It is especially interesting to note that the results in methane, at least at 950°C, are fairly comparable to those in hydrogen.

The anodic overpotentials under hydrogen are much better than those corresponding to the non-substituted counterpart and better than the results reported for Sc-substituted titanates. The substitution of Ti by cations with preference for coordination other than octahedral such as Mn has improved the performance of these phases as anodes for SOFC. Good results have been

obtained with the substitution of Mn and Ga for Ti.[5] In methane the low values of polarisations for n=1 are only obtained at 950$^{o}$C.

The open circuit voltages almost matched those predicted thermodynamically in hydrogen atmosphere for all the samples studied. In methane the interpretation is rather complicated because in the presence of steam a number of alternative routes are possible for methane oxidation. The OCV under methane flow decreases with decreasing temperature. We think the process involves direct or partial oxidation. Furthermore no carbon deposits were detected after our tests.

SEM pictures were taken after performing the fuel cell tests. The anode shows a homogeneous distribution of particles and pores with grain size ~ 0.8 μm. Thus, the ohmic overpotential due to the contact resistance can be neglected because the adherence seems to be good. Nevertheless an optimisation of the microstructure could enhance catalytic activity towards the $CH_4$ oxidation at lower temperatures

Because of these results these materials are a good potential candidate for anode for SOFCs.

## 5.5. References

[1] J. Canales-Vazquez, 'Studies on oxygen excess perovskite-based titanates for SOFC fuel electrodes', PhD thesis, St Andrews, 2003.

[2] J. Canales-Vazquez, J. C. Ruiz-Morales, J. T. S. Irvine, and W. Z. Zhou, *Journal of the Electrochemical Society*, 2005, **152**, A1458.

[3] A. Ovalle, J. C. Ruiz-Morales, J. Canales-Vazquez, D. Marrero-Lopez, and J. T. S. Irvine, *Solid State Ionics*, 2006, **177**, 1997.

[4] S. C. Singhal and K. Kendal, in 'High Temperature Solid Oxide Fuel Cells: Fundamentals, Design and Applications', Oxford, 2003.

[5] J. C. Ruiz-Morales, J. Canales-Vazquez, C. Savaniu, David Marrero-Lopez, W. Zhou, and J. T. S. Irvine, *Nature*, 2006, **439**, 568.

# 6

# Conclusions and future work

## 6.1. Conclusions

A new series of compounds with general formulas $La_{4+n}Sr_{8-n}Ti_{12-n}O_{38}$ and $La_4Sr_8Ti_{12-n}Mn_nO_{38-\delta}$ have been made and investigated in the search for new anode materials for fuel cells. The goal of this project was to improve the performance of $La_4Sr_8Ti_{12}O_{38}$ as an anode material for SOFCs using $H_2$ and methane as fuels.

The phases belonging to the $La_{4+n}Sr_{8-n}Ti_{12-n}Mn_nO_{38}$ series gave reflections at $2\theta$ 28-31º on the XRD patterns, which are characteristic of layered domains. Additionally preliminary TEM studies corroborated the presence of these layered domains in these phases. These layered domains are coupled with the presence of $Mn^{4+}$. As the appearance of such layers has a large negative effect on the electrochemical properties of the materials only a few compounds of these series were characterised.

The series $La_4Sr_8Ti_{12-n}Mn_nO_{38-\delta}$ are all simple perovskites but they no longer exhibit the simplest cubic form. Even at low levels of Mn substitution (n=0.75) the combined NPD and XRD patterns were better refined as a rhombohedral structure (R−3c). As Mn substitution increased the rhombohedral splitting became more pronounced. Rhombohedral distortions are common in perovskite manganites and cobaltites and can be ascribed to the R−3c space group as the result of equivalent antiphase octahedra tilting along all the three crystallographic axes. The replacement of $Ti^{4+}$ by $Mn^{3+}$ forces the removal of oxygen from the structure to maintain the electroneutrality in the crystal, thus creating local oxygen vacancies that might favour ionic transport. This effect

leads to the observed gradual decrease of the lattice parameters with manganese content in oxidizing conditions. The volume of the unit cell gradually decreases with increasing the Mn content following Vegard's law, which indicates a random distribution of Mn in the B-sites. Under reducing conditions, substitution of Mn for Ti leads to a gradual lattice expansion until n=2 and further substitution causes a lattice shrinkage. The primitive cell volumes correlate with the oxygen content.

Clearly the rhombohedral distortion may influence how the oxygen excess is accommodated within the perovskite but this must still involve some short-range defects. Preliminary HRTEM investigations revealed that some crystallographic shears distributed randomly within the perovskite matrix remain in the structure, which implies that the oxygen overstoichiometry is compatible with rhombohedral distortions in the oxygen sublattice.

AC impedance studies have shown that Mn substitution does not have a large impact on the bulk conductivity of the lower phases studied in static air, which remain close to the values observed in other related titanates. However the grain boundary contributions are largely improved. The overall conductivity of the series increases with increasing content of manganese in static air. In reducing conditions the overall conductivity is higher at lower content of manganese. Conductivity measurements under oxygen partial pressure revealed that for low degree of Mn substitution ($n \leq 1$) the total conductivity is mainly n-type electronic under oxidizing and reducing conditions. Magnetic studies for n=0.5 and n=1 have revealed paramagnetic behaviour across the whole range of temperatures studied. The oxidation state of manganese is mainly $Mn^{3+}$.

Further substitution of Mn creates oxygen vacancies and for n=2 mixed ionic/electronic conduction was observed. Mixed conduction is very important, because it would allow the electro-oxidation process to move away from the

three-phase electrode/electrolyte/gas interface onto the anode surface, with considerable catalytic enhancement.

For higher values of Mn substitution (n≥3) the total conductivity is mainly p-type. The slopes founded are smaller than expected, i.e. 1/12 and 1/8 for n=3 and n=4 respectively, and it can be associated to a process of disproportion of $Mn^{3+}$ to $Mn^{2+}$ and $Mn^{4+}$. Magnetic studies for these samples revealed an antiferromagnetic behaviour and values of effective moments higher than expected for $Mn^{3+}$, which corroborates the disproportionation process.

Small changes in the slopes of the Arrhenius plots were found especially for samples n=1 and n=2. These changes were assigned to a transition phase, i.e. insulator to metal-like in the compounds. Neutron studies carried out on these samples corroborated this assignment as the phase transition temperatures match the change in conductivity for the samples, in air and in reducing conditions.

The half-cell tests performed using $La_4Sr_8Ti_{12-n}Mn_nO_{38-\delta}$ as anode material revealed rather low polarisation resistances in wet $H_2$ and $CH_4$ at 950ºC for n=1. It is especially interesting to note that the results in methane, at least at 950$^oC$, were fairly comparable to those in hydrogen.

These results obtained for n=1 were expected. We have seen during the course of this work that under reducing conditions the composition n=1 presents the higher conductivity. The total conductivity of n=1 is mainly n-type electronic although some ionic conductivity is expected as the substitution of Ti for Mn creates some oxygen vacancies by removing the oxygen excess characteristic of these materials.

The anodic overpotentials for n=1 under hydrogen are better than those corresponding to the non-substituted counterpart and better than the results reported for Sc-substituted titanates.

The open circuit voltages almost matched those predicted thermodynamically in hydrogen atmosphere for all the samples studied. In methane the interpretation of the OCV is rather complicated because in the presence of steam a number of alternative routes are possible for methane oxidation. The OCV under methane flow decreases with decreasing temperature and probably the process involves direct or partial oxidation. Furthermore no carbon deposits were detected after our tests.

SEM micrographs were recorded after performing the fuel cell tests. The anode shows a homogeneous distribution of particles and pores. Thus, the ohmic overpotential due to the contact resistance can be neglected because the adherence seems to be good.

As a final conclusion the substitution of Ti by cations with preference for coordination other than octahedral such as Mn has improved the performance of these phases as anodes for SOFCs especially under methane.

## 6.2. Future work

There are several areas that can be addressed for future work. The synthesis of the materials trying to improve the microstructure using sol-gel methods. Studies at intermediate $pO_2$ conditions using $MnO_x$ buffers to determine whether ionic conductivity is present or not will help understand conductivity and defect mechanism. It would also be interesting to test magnetic properties for possible magneto-resistance applications. These materials are stable phases under oxidising conditions so it seems possible that they may also be an effective cathode for SOFC operation. Consequently the series $La_4Sr_8Ti_{12-n}Mn_nO_{38-\delta}$ could be investigated as cathode and anode simultaneously in symmetrical SOFCs. Catalytic studies would also need to be done on the system.